CORA Cork Open Research Archive
Cartlann Taighde Oscailte Chorcaí

Title	Thermal properties of germanium telluride close to the ferroelectric phase transition
Authors	Dangic, Dorde
Publication date	2021-05-07
Original Citation	Dangic, D. 2021. Thermal properties of germanium telluride close to the ferroelectric phase transition. PhD Thesis, University College Cork.
Type of publication	Doctoral thesis
Rights	© 2021, Dorde Dangic. - https://creativecommons.org/licenses/by-nc-nd/4.0/
Download date	2024-04-19 02:56:42
Item downloaded from	https://hdl.handle.net/10468/11845

UCC
University College Cork, Ireland
Coláiste na hOllscoile Corcaigh

Thermal properties of germanium telluride close to the ferroelectric phase transition

Đorđe Dangić
MSc
116220882

NATIONAL UNIVERSITY OF IRELAND, CORK

School of Science

Department of Physics

Thesis submitted for the degree of Doctor of Philosophy

7 May 2021

Head of Department: Prof. John G. McInerney

Supervisors: Dr. Ivana Savić
Prof. Stephen Fahy

Contents

List of Figures iv
List of Tables xiv
Acknowledgements xvi
Abstract xvii

1 Introduction **1**
1.1 Thermoelectric materials 1
1.2 Improving thermoelectric figure of merit 4
1.2.1 Reducing lattice thermal conductivity 4
1.2.2 Improving Seebeck coefficient 7
1.3 Phase transitions 9
1.4 Outline of the thesis 10

2 Computational methods **14**
2.1 Density functional theory 14
2.1.1 Plane waves 18
2.1.2 Pseudopotentials 19
2.2 Molecular dynamics simulation 20
2.3 Gaussian Approximation Potentials 22
2.4 Temperature dependent effective potential method 25
2.5 Boltzmann transport equation 29
2.5.1 Boltzmann transport equation for phonons 32
2.6 Thermal conductivity from the Green-Kubo formalism 32

3 Negative thermal expansion of GeTe close to the phase transition **40**
3.1 Introduction 40
3.1.1 General comments 40
3.1.2 Quasiharmonic theory of thermal expansion close to the ferroelectric phase transition 43
3.1.3 Computational details 48
3.2 Results 49
3.3 Conclusion 57

4 Phonon spectral functions of GeTe close to the ferroelectric phase transition **59**
4.1 Introduction 59
4.2 Computational details 61
4.3 Results 62
4.3.1 Soft phonon mode at the phase transition 62
4.3.2 Phonon spectral function 64
4.4 Conclusion 68

5 Lattice thermal conductivity of GeTe close to the ferroelectric phase transition **69**
5.1 Introduction 69

5.2 Computational details . . . 71
5.3 Results . . . 71
5.3.1 Lattice thermal conductivity in the Boltzmann transport approach . . . 71
5.3.2 Lattice thermal conductivity using the Green-Kubo method . . . 78
5.4 Conclusion . . . 83

6 Structural, electronic and transport properties of ferroelectric domain walls in GeTe 84
6.1 Introduction . . . 84
6.1.1 Domain walls - general comments . . . 85
6.2 Results . . . 90
6.2.1 Construction of domain walls in germanium telluride . . . 90
6.2.2 Technical details of electronic structure calculations . . . 96
6.2.3 Structural properties of domain walls . . . 96
6.2.3.1 Structural properties of $(11\bar{1})$ domain walls . . . 96
6.2.3.2 Structural properties of (111) and $(1\bar{1}0)$ domain walls 99
6.2.4 Electronic properties of domain walls . . . 100
6.2.5 Lattice thermal conductivity . . . 108
6.2.6 Electronic transport properties . . . 112
6.2.6.1 Results . . . 115
6.3 Conclusion . . . 120

7 Molecular dynamics simulation of the ferroelectric phase transition in GeTe 122
7.1 Introduction . . . 122
7.1.1 Fitting of the Gaussian Approximation Potential . . . 124
7.1.1.1 Comparison of GAP results with DFT . . . 125
7.2 Results . . . 128
7.2.1 Thermal expansion of GeTe from molecular dynamics simulations . . . 128
7.2.2 Order parameter at the phase transition . . . 131
7.2.3 Vibrational properties of GeTe from MD simulations . . . 135
7.2.4 Lattice thermal conductivity from molecular dynamics . . . 138
7.3 Conclusion . . . 142

8 Conclusions 143
8.1 Summary . . . 143
8.2 Outlook . . . 145

A Convergence of the lattice thermal conductivity results 147

B Convergence of domain wall properties 149
B.1 Domain wall widths and energies . . . 149
B.2 Convergence of the Seebeck coefficient with respect to the number of k points . . . 150

C Convergence issues with molecular dynamics simulations 152

D Comparison of the results with two different heat current definitions 157

List of Figures

1.1 Schematics of the thermoelectric device for power generation. The yellow and green blocks represent n- and p- type doped thermoelectric materials. The large arrows show the direction of free charge carrier diffusion and heat flow, while the line arrows through the load show the electric current direction. 2
1.2 Efficiency of a thermoelectric generator as a function of temperature for different thermoelectric figures of merit of the material. The light-blue region shows the range of existing, state-of-the-art thermoelectric materials. The orange region represents the efficiencies of different types of power generators that are currently in use [1]. 4
1.3 The density of states of a parabolic band for systems with different dimensionality. One-dimensional systems have the biggest change in the free charge concentration at the Fermi level, which decreases with increased dimensionality of the system. Zero energy represents the conduction band minimum. 8

3.1 Thermal expansion in Lennard-Jones potential. Equipotential points are shown as dashed lines and the average of them is the blue point. The temperature dependence of the bond length is shown in the inset. 41
3.2 Primitive unit cell of GeTe at (a) 0 K and (b) above the Curie temperature, generated using VESTA software [2]. The low-temperature rhombohedral structure becomes more similar to the rocksalt structure as temperature increases: the angle between the primitive lattice vectors θ becomes closer to 60° and the Te internal atomic position τ approaches 0.5. 44
3.3 The first Brillouin zone of GeTe with notation of high symmetry points. 49
3.4 (a) Phonon dispersion of GeTe calculated using the GGA-PBE exchange-correlation functional neglecting and accounting for carrier screening (solid black lines and red lines, respectively). The frequencies of the zone centre Raman active modes were taken from the measurements of Ref. [3] (blue circles) and Ref. [4] (black circles). (b) Phonon density of states of GeTe calculated excluding screening (solid black line) and measured by Ref. [5] (blue filled squares and red empty squares) and Ref. [6] (green circles). 51
3.5 Structural parameters of GeTe as a function of temperature: (a) the lattice constant a, (b) the angle θ, and (c) the internal atomic coordinate τ. Solid black lines represent our calculations. Red and blue circles correspond to the measurements of Refs. [7] and [8], respectively. Dashed black lines represent our calculations shifted by the difference between our calculated values and the experimental values of Ref. [7] at 300 K. (d) TO mode frequency versus temperature: our calculation (solid black line) and experiment [3] (blue circles). 52

3.6 Structural parameters of GeTe as a function of temperature: (a) lattice constant, (b) angle, and (c) internal atomic coordinate. Solid black lines represent the results obtained using our approach, while dashed red lines correspond to the standard method (see text for full explanation). 54
3.7 (a) Volumetric thermal expansion of GeTe: our calculation (solid black line), experiment [7] (red circles), and our calculation shifted by the difference between our and the experimental value at 300 K (dashed black line). (b) Computed volumetric thermal expansion including and neglecting acoustic-soft optical mode coupling, shown in solid black and dashed red lines, respectively. 55
3.8 Elastic constants of GeTe as functions of temperature: (a) $C_{11} + C_{12}$, (b) C_{13} (solid black line) and C_{33} (dashed red line). 56
3.9 Temperature dependence of: (a) average generalized Grüneisen parameters defined for each structural parameter (a - lattice constant, θ - angle, τ - internal atomic coordinate), and (b) normalized compliance matrix elements (see text for full explanation). 56

4.1 Temperature dependence of the zone centre transverse optical phonon frequencies. (a) The lower transverse optical (TO) mode (E) and (b) the higher TO mode (A_1) at the zone centre (as we approach Γ in the $X-\Gamma$ direction, which is perpendicular to the anisotropy axis). Red circles and blue squares represent the calculated TDEP and anharmonic phonon frequencies respectively, while other symbols represent the experimental results from Refs. [3, 9, 4]. The TDEP frequency is the square root of the eigenvalue of the dynamical matrix for $\vec{q} = 0$ at a particular temperature, while the anharmonic frequency is the peak of the phonon mode power spectrum, defined in Eq. (4.3). The black vertical line represents the phase boundary between the rhombohedral and rocksalt structures in our calculations (≈ 634 K). 64
4.2 Phonon spectral function defined in Eq. (4.3) along high symmetry lines in GeTe at phase transition. Black lines represent the TDEP frequencies calculated at 631 K (close to the critical temperature 634 K) and dashed cyan lines are the TDEP phonon band structure at 300 K. The darker shades of purple show regions with higher phonon spectral function values, while pale yellow regions have the lowest values of phonon spectral function. 66

4.3 (a) Spectral function for the zone centre higher transverse optical mode (A_1) in GeTe at different temperatures. Vertical lines represent the values of the TDEP $A_1(\Gamma)$ frequencies at different temperatures. A drastic deviation from the Lorentzian shape is evident for the entire temperature range and most prominent in the vicinity of the phase transition (at 631 and 637 K). (b) Spectral function of the zone centre A_1 mode at 631 K including all phonon-phonon interactions ("Full calc."), excluding the coupling to transverse acoustic (TA) modes ("Without TA modes"), and excluding the interaction with the first transverse acoustic mode and the second transverse optical mode ("Without TA1 and TO2 mode"). The vertical line represents the TDEP frequency of the A_1 (Γ) mode at 631 K. 67

4.4 (a) Spectral function of the zone centre E mode at different temperatures. (b) Spectral function of the E (Γ) mode at 631 K including all phonon-phonon interactions ("Full calc."), excluding the coupling to transverse acoustic modes ("Without TA modes") and excluding the coupling between the second transverse acoustic and first transverse optical modes ("Without TA2 and TO1 modes"). The vertical lines represent the TDEP frequencies of the E (Γ) mode at various temperatures. 68

5.1 Temperature dependence of the lattice thermal conductivity of GeTe. Red and blue lines represent the calculated values using the Boltzmann transport approach in the directions perpendicular and parallel to the trigonal [111] axis, respectively. Dashed line represents the average values of the computed lattice thermal conductivity. Grey region represents the experimental results collected from Refs. [10, 11, 12, 13, 14, 15, 16, 17]. 72

5.2 Spectral lattice thermal conductivity (see Eq. (5.1)) of GeTe at (a) 300 K and (b) 631 K. Shaded regions show the contribution of a particular phonon branch. 74

5.3 Frequency dependence of phonon transport properties. (a) Average phonon group velocities and (b) average phonon lifetimes of GeTe versus phonon frequency for different temperatures. Averaging is carried out by convolving the calculated values of these quantities with a Gaussian (see Eq. (5.2)). 75

5.4 Average phonon lifetimes of GeTe scaled by T/300 K, where T is the temperature. Averaging is carried out by convolving the calculated phonon lifetimes with a Gaussian, see Eq. (5.2). 76

5.5 Change of the anharmonic force constants of (a) Ge-Ge-Ge and (b) Ge-Ge-Te triplets with temperature. The bars in the figure show the maximum and minimum norm of the force constants for the specific temperature and bond length. 77

5.6 Phonon scattering phase space scaled by T/300 as a function of TDEP frequency at different temperatures. 78

5.7 Green-Kubo lattice thermal conductivity. (a) Difference in the calculated lattice thermal conductivity using the Green-Kubo method (Eq. (2.39)) and the Boltzmann transport equation. (b) Phonon lifetimes of GeTe (see text for explanation) in the Green-Kubo and Boltzmann transport equation approach plotted versus TDEP frequencies of phonon modes. Inset shows the region of soft phonon modes where the change is most noticeable. 79
5.8 Displacement autocorrelation function of optical modes at the zone center at (a) 300 K and (b) 631 K. Displacement autocorrelation function has been normalized to be 1 at time 0. 80
5.9 (a) Phonon lifetimes and (b) phonon frequency shifts obtained through the fitting procedure compared to the ones obtained by the standard method at 631 K (see text for more information). 81
5.10 (a) Phonon populations obtained using the phonon displacement autocorrelation function at 631 K. The line represents the Bose-Einstein factor at 631 K. (b) Differences between the calculated values of phonon populations and the Bose-Einstein factor along the high symmetry lines. The size of the point is proportional to the log of the difference. 82

6.1 An example of the domain structure in a ferroelectric material. Different polarization directions in a single domain are color coded (top) and the boundaries between these domains correspond to different types of domain walls (bottom). The domain wall boundary for this configuration of domains is one of the faces of the cube, (001) plane. Tail-to-tail, head-to-head and tail-to-head domain walls are labeled as T-T, H-H and T-H, respectively. 86
6.2 Illustration of a ferroelectric material containing charged domain walls (DWs). Coloured arrows denote the polarization orientations. DWs are the interfaces between domains with different polarization orientations. There are head-to-head (H-H) and tail-to-tail (T-T) charged DWs, depending on the polarization orientation with respect to the DW plane. In this figure, different polarization changes at DWs only give a qualitative illustration of the actual polarization differences between DWs. The polarization changes at these DWs form bound charge (labelled by plus and minus). The direction of the electric field induced by the bound charge is given with the black arrow. The electric field localizes free charge carriers on the DWs (green - holes, yellow - electrons). In the 39° $(11\bar{1})$ DWs considered here, the angle between the polarizations in neighbouring domains is 39°, and the DWs are in the $(11\bar{1})$ plane. 90

6.3 Geometry of GeTe domain structure containing 39° or 141° $(11\bar{1})$ domain walls for the case where domains are one unit cell long. Blue lines are the unit cell vectors of the domain structure, while green vectors represent the third primitive lattice vectors of individual domains. Red dashed lines represent polarization directions in different domains. The positions of Ge atoms are labeled as Ge_1 and Ge_2. The lattice constants of the two primitive unit cells that constitute this supercell are labeled as a_1 and a_2. 93
6.4 Polarization directions inside each domain for GeTe structures containing 71° or 109° $(11\bar{1})$ domain walls (illustration for 39°/141° DW is the same with appropriate angle between $P_{\parallel}$ and $P'_{\parallel}$). Polarization directions in two neighboring domains are labeled as primed and non-primed. $P_{\parallel}$ is the direction along the trigonal axis. P_n is the direction normal to the plane of the trigonal axes in neighboring domains and corresponds to the Bloch character of polarization. The third direction, $P_{\perp}$, is perpendicular to the other two directions and quantifies the Néel character of polarization. 94
6.5 Polarization profiles for GeTe structures containing (a) 39°, (b) 141° and (c) 180° $(11\bar{1})$ domain walls (DWs). Red line represents polarization in the direction of trigonal axes of each domain ($P_{\parallel}$), and blue line red shows the Néel component of polarization ($P_{\perp}$). DW boundaries are indicated by black vertical lines and labeled T-T for tail-to-tail, H-H for head-to-head, H-T for head-to-tail and T-H for tail-to-head DWs. For 39° T-T DW, $P_{\parallel}$ values in one of the domains are plotted as negative (orange line) to aid visualization. 97
6.6 Local lattice constant (blue line) and local rhombohedral angle (red line) for GeTe structures containing (a) 39°, (b) 141° and (c) 180° $(11\bar{1})$ domain walls (DWs). DW boundaries are indicated by black vertical lines and labeled T-T for tail-to-tail, H-H for head-to-head, H-T for head-to-tail and T-H for tail-to-head DWs. 98
6.7 Polarization profiles for GeTe structures containing (a) (111) and (b) $(1\bar{1}0)$ domain walls (DWs). Red line represents polarization in the direction of the trigonal axis ($P_{\parallel}$), while blue and black lines represent the Néel ($P_{\perp}$) and Bloch (P_B) components of polarization (multiplied by constant values to make them visible on the graph). DW boundaries are indicated by black vertical lines and labeled T-T for tail-to-tail, H-H for head-to-head, H-T for head-to-tail and T-H for tail-to-head DWs. 100
6.8 Local lattice constant (blue line) and local rhombohedral angle (red line) for GeTe structures containing (a) (111) and (b) $(1\bar{1}0)$ domain walls (DWs). DW boundaries are indicated by black vertical lines and labeled T-T for tail-to-tail, H-H for head-to-head, H-T for head-to-tail and T-H for tail-to-head DWs. 101

6.9 Total potential along the domain structure for (a) 141° and (b) 180° ($11\bar{1}$) domain walls. The red lines represent the plane average of the local potential in the plane parallel to the domain wall plane and blue lines are the unit cell average. Positions of the domain walls are represented by the vertical black lines and noted H-H for head-to-head, T-T for tail-to-tail and H-T for head-to-tail domain wall. 102
6.10 Total potential along the 39° ($11\bar{1}$) domain structure for (a) relaxed electronic occupations and (b) semiconducting electronic occupations. Red lines represent the plane average of the local potential in the plane parallel to the domain wall plane and blue lines are the unit cell average. Positions of the domain walls are represented by the vertical black lines and noted H-H for head-to-head and T-T for tail-to-tail. 102
6.11 Local density of states for the structures with (a) 39°, (b) 141° and (c) 180° domain walls. Black vertical lines represent the intrinsic value of the Fermi level. 103
6.12 Projected electronic band structure along specific lines in the Brillouin zone for the structures with (a) 39° and (b) 141° domain walls. Blue lines are energies of electronic states with $k_3 = 0$, while the red broadening represents the dispersion of these states in the direction perpendicular to the domain wall. Horizontal lines are the values of the intrinsic Fermi level. The side plot in figure (a) represents local density of states for 39° T-T domain wall. 105
6.13 (a) Projected electronic band structure along specific lines in the Brillouin zone for the structures with 180° domain wall. Blue lines are energies of electronic states with $k_3 = 0$, while the red broadening represents the dispersion of these states in the direction perpendicular to the domain wall. (b) Electronic band structure of the same domain system resolved by a domain wall. The left side shows the 180° domain wall local density of states. 105
6.14 (a) Charge densities for the states labeled 1. and 2. in the electronic band structures Fig. 6.12 (a). (b) Charge densities for the states labeled 1. and 2. in the electronic band structures Fig. 6.12 (b). (c) Charge densities for the states labeled 1. and 2. in the electronic band structures Fig. 6.13 (a). Localization of electronic states at the domain walls is clearly shown in these figures. The x-axis is the coordinate perpendicular to the domain wall. 107

6.15 (a) 2D electronic band structure and Van Hove singularities of the tail-to-tail domain wall. Energy of the top valence band for 39° $(11\bar{1})$ tail-to-tail domain wall (in eV) in the interface Brillouin zone. Black arrows represent the directions of the in-plane reciprocal lattice vectors. The blue arrow corresponds to the projection of the polarization change onto the domain wall plane. Van Hove singularities are indicated by blue points. (b) Energy (in eV) of the top valence band of bulk GeTe projected onto the $(11\bar{1})$ domain wall (DW) plane, with the reciprocal lattice vector normal to the DW plane set to zero. Black arrows represent the directions of the in-plane reciprocal lattice vectors. Van Hove singularities are indicated by blue points. 108

6.16 (a) Lattice thermal conductivity of bulk GeTe and GeTe structure with 39° head-to-head (H-H) domain walls (DWs) and the domain size of 160 nm at 300 K, showing the contribution of each scattering mechanism due to the DW. (b) Dependence of the lattice thermal conductivity of GeTe with 39° H-H DWs on the domain size at 300 K. Black horizontal line represents the bulk value of lattice thermal conductivity in GeTe. 111

6.17 a) Calculated Seebeck coefficient for p-type bulk GeTe and 39° $(11\bar{1})$ tail-to-tail (T-T) domain walls (DWs) for various directions at 300 K. Experimental data for bulk GeTe from Refs. [18, 12] are shown by red squares and stars, respectively. The top x-axis shows the DW interface free charge density, while the bottom x-axis corresponds to the volume charge concentration for the DW separation of 5.6 nm. Black vertical line shows the intrinsic doping concentration of DWs for this DW separation due to charge transfer between the head-to-head and T-T DWs. b) Calculated Seebeck coefficient along same directions for the H-H DWs. 116

6.18 (a) Seebeck coefficient of p-type 39° $(11\bar{1})$ tail-to-tail (T-T) domain walls at 300 K calculated using the constant relaxation time approximation and the constant group velocity approximation (CGVA). Experimental data from Refs. [18, 12] are shown by red squares and stars, respectively. The bottom x-axis corresponds to the volume charge concentration for the DW separation of 5.6 nm. Black vertical line shows the intrinsic doping concentration of the T-T DW for this DW separation due to charge transfer between the head-to-head and T-T DWs. (b) Average value of transport coefficient $v^2(E)\tau(E)$ at T-T DW for three directions noted in the figure (a). Maximum value of the Seebeck coefficient strongly correlates with the relative slope of this transport coefficient. 117

6.19 Calculated electrical conductivity of p-type bulk GeTe and (a) 39° $(11\bar{1})$ tail-to-tail (T-T) domain walls (DWs) and (b) n-type head-to-head DW for various directions at 300 K. The top x-axis shows the DW interface free charge density, while the bottom x-axis corresponds to the volume charge concentration for the DW separation of 5.6 nm. Black vertical line shows the intrinsic doping concentration of the T-T DW for this DW separation due to charge transfer between the head-to-head and T-T DWs. 118
6.20 Calculated power factor of p-type bulk GeTe and (a) 39° $(11\bar{1})$ tail-to-tail (T-T) domain walls (DWs) and (b) n-type head-to-head DW for various directions at 300 K. The top x-axis shows the DW interface free charge density, while the bottom x-axis corresponds to the volume charge concentration for the DW separation of 5.6 nm. Black vertical line shows the intrinsic doping concentration of the T-T DW for this DW separation due to charge transfer between the head-to-head and T-T DWs. 119
6.21 Proposed design of the nano-thermoelectric device based on domain walls. White regions represent domains with different polarization orientations, acting as electrical insulators. Head-to-head and tail-to-tail domain walls, shown by red and blue regions, act as an n- and p-type leg of the thermoelectric device, respectively. Electrodes and insulating parts are shown in black and green, respectively. Heating up the top electrodes causes electron and hole diffusion in n- and p-type domain walls, respectively, which produces electrical current. 120

7.1 (a) Average atomic energies and (b) atomic forces, calculated using DFT and GAP. The test set in this case is the data we use to fit TDEP force constants in Chapter 5. The insets show the distributions of errors (differences of computed energies/forces with DFT and GAP.), where p is the percentage of the energies/forces with errors smaller than indicated by the x-axis. 126
7.2 (a) Comparison of the phonon band structure and phonon density of states (side plot) of GeTe calculated using DFT and GAP. (b) Mode resolved Grüneisen parameters of GeTe calculated using DFT and GAP. (c) Comparison of the energy profile of the interatomic displacement parameter calculated with GAP and DFT 128
7.3 Thermal expansion of (a) lattice constant, and (b) rhombohedral angle using different methods. The error bars associated with the GAP model are not visible on the graph (smaller than experimental points). Experiments correspond to Refs. [7, 19, 20]. 129
7.4 (a) Thermal expansion of volume in germanium telluride using different methods. Experiments correspond to Refs. [7, 19, 20]. (b) The volume-order parameter correlation coefficient at different temperatures. We can see a large increase at the phase transition, which is a sign of an increased coupling between strain and order parameter. . 130

7.5 (a) Calculated temperature dependence of the polarization in GeTe compared to experiments. Full red points represent the average polarization at a certain temperature, while empty points are the average absolute values of the polarization. Experimental results are from Refs. [7, 19, 20]. (b) Calculated temperature dependence of the soft TO mode in GeTe compared to experiments [3, 9]. Full lines in both panels represent the function $f(T) = A(T_C - T)^{\alpha}$ fitted to the calculated values of polarization and soft TO mode. 132
7.6 (a) Dynamical properties of the order parameter at different temperatures. The figure shows the Fourier transform of the polarization correlation function for different temperatures. (b) Switching behavior of the polarization close to the phase transition (631 K). The side plot shows the probability distribution function of the order parameter along the MD trajectory shown in the larger part of the figure. 133
7.7 (a) Probability distribution function (PDF) of the local order parameter at 631 K at three different timesteps. (b) PDF of the local order parameter at 637 K at three different timesteps. 134
7.8 Variance of the local polarization averaged over time as a function of temperature. 135
7.9 Phonon density of states in germanium telluride at (a) 300 K and (b) 631 K calculated with three different methods: the velocity autocorrelation function power spectrum from molecular dynamics (MD), lattice dynamics (TDEP), from frequencies obtained by fitting the velocity autocorrelation function (fitted). 136
7.10 Zone center optical phonon mode spectral functions at (a) 300 K and (b) 631 K, calculated with two different methods (full lines are molecular dynamics simulations, while dashed lines are the lattice dynamics calculations implemented in the temperature dependent effective potential method). 137
7.11 Phonon populations calculated from molecular dynamics simulations at (a) 300 K and (b) 631 K, and compared to the values extracted from the equipartition law ($n_{\vec{q}s} = \frac{k_B T}{\hbar \omega_{\vec{q}s}}$). 138
7.12 Lattice thermal conductivity of germanium telluride calculated using molecular dynamics (MD) (red lines and dots), the Boltzmann transport equation (BTE) with the temperature dependent effective potential (TDEP) method and the GAP forces (blue lines and dots), and BTE with phonon lifetimes fitted to MD simulations (green lines and dots) and compared to experiment (gray region). The lines with squares represent the lattice thermal conductivity along directions perpendicular to trigonal axis (in-plane directions), while lines with dots are results along direction parallel to trigonal axis. The dashed lines are average values of the lattice thermal conductivity. 140
7.13 Phonon lifetimes calculated from molecular dynamics (see Eq. (7.7)) and the temperature dependent effective potential (TDEP) method at (a) 300 K and (b) 631 K. 140

7.14 (a) Average phonon lifetimes from molecular dynamics at three different temperatures closest to the phase transition (see Eq. (7.7)). (b) The heat capacity of GeTe calculated from energy fluctuation at different temperatures (see Eq. (7.8)). 141

A.1 Convergence study of lattice thermal conductivity with respect to (a) the third order force constant cutoff and (b) the $\vec{q}$ point grid. 147
A.2 Convergence study of the integral of the phonon spectral function of the A_1 phonon mode with respect to the number of points in the sampling of Ω. 148

B.1 (a) Domain wall width and (b) domain wall energy for (111) and $(1\bar{1}0)$ domain walls (DWs) as a function of the supercell size. 150
B.2 Convergence study of transport properties with respect to the number of $\vec{k}$ points for (a) bulk GeTe and (b) T-T 39° $(11\bar{1})$ domain wall. . . . 151

C.1 Probability distribution function (PDF) of the elements in the sum in Eq. (C.2). (a) Calculated PDF and the Gaussian and Cauchy fits to the data with the Gaussian noise. (b) PDF of the same quantity at lower correlation times is a skewed distribution. 154
C.2 (a) Original and filtered power spectrum of the heat current of GeTe at 300 K. (b) Lattice thermal conductivity of GeTe at 300 K as a function of the maximum correlation time, see Eq. (C.2). 154

D.1 Relative difference in the lattice thermal conductivity calculated using Eqs. (D.1) and (2.39) 158

List of Tables

3.1 Lattice parameters of GeTe at 0 K, calculated using the LDA and GGA-PBE functionals, and compared with experimental results [7]. a stands for the lattice constant, θ for the angle, τ for the internal atomic coordinate, and V_0 is the volume of the primitive unit cell. 49
3.2 Calculated elastic constants of GeTe using density functional perturbation theory (DFPT), and density functional theory (DFT) combined with a finite difference method. $C_{11}+C_{12}$, C_{13} and C_{33} were calculated directly using DFPT and expressed in GPa, and transformed into K_{aa}, $K_{a\theta}$ and $K_{\theta\theta}$ using Eq. (3.10). K_{aa}, $K_{a\theta}$ and $K_{\theta\theta}$ were computed using DFT and expressed in eV, and transformed into $C_{11}+C_{12}$, C_{13} and C_{33} by inverting Eq. (3.10). 50

6.1 Domain wall (DW) widths and energies for $(11\bar{1})$ DWs. H-H and T-T denote head-to-head and tail-to-tail DWs, respectively. H-T and T-H denote head-to-tail and tail-to-head DWs, respectively. 97
6.2 Domain wall (DW) widths and energies for 180° (111) and $(1\bar{1}0)$ DWs. H-H and T-T denote head-to-head and tail-to-tail DWs, respectively. H-T and T-H denote head-to-tail and tail-to-head DWs, respectively. . 99
6.3 Lattice thermal conductivity of GeTe structure with a particular type of domain walls (DWs) at 300 K and DW density of 1/160 nm^{-1}, given as a percentage of the bulk value. H-H and T-T denote head-to-head and tail-to-tail DWs, respectively. 141° and $(1\bar{1}0)$ DW only have head-to-tail DWs. 111

7.1 The Gaussian Approximation Potential hyperparameters used to fit the interatomic potential for GeTe. 125
7.2 Lattice parameters of GeTe at 0 K, calculated using the GAP interatomic potential, DFT LDA and GGA-PBE functionals, and compared with experimental results [7]. a stands for lattice constant, θ for angle, and τ for internal atomic coordinate. 126
7.3 Elastic properties of germanium telluride calculated using the GAP interatomic potential and DFPT with the GGA-PBE exchange-correlation functional. 127

B.1 Domain wall (DW) widths and energies for different sizes of the simulation supercell relaxing only Te atom positions. 150

C.1 Dependence of the calculated lattice thermal conductivity on the size of the MD simulation cell. The errors are determined as the standard errors from the set of calculated values. 155

I, Đorđe Dangić, certify that this thesis is my own work and I have not obtained a degree in this university or elsewhere on the basis of the work submitted in this thesis.

Đorđe Dangić

Acknowledgements

First and foremost, I would like to thank my supervisor Ivana Savić for giving me an opportunity to work on such a fruitful and interesting topic. She allowed me to explore the topics I found interesting and provided a context for these scientific excursions within the ongoing research project.

Secondly, I would like to thank my co-supervisor Stephen Fahy, whose key insights inspired me to explore the subjects adjacent to the main research project.

Thirdly, I would like to thank my collaborators Aoife Murphy, Éamonn Murray, and Olle Hellman for helping me with the research projects we worked jointly on.

I acknowledge the help from my friends and colleagues Shane, Amy, Christian, Ransell, Jose, Jiang, Aoife M., Aoife L., Shima, and many more who made my stay in Cork extremely pleasant.

I would also like to thank Giulia for making the last year, which was supposed to be the loneliest and the most stressful, one of the best years of my life.

Finally, I would like to thank my parents for their ongoing support and encouragement.

Abstract

Improving thermoelectric efficiency is one of the most challenging problems in materials science. Recent work made a connection between increased phonon anharmonicity in the vicinity of the structural phase transition and the reduction of the lattice thermal conductivity κ, which could increase the thermoelectric performance of materials near structural phase transitions. In this thesis, we investigate the influence of the phase transition on the material properties in germanium telluride, an excellent thermoelectric material that undergoes a structural phase transition at around 700 K. We find that the enhanced acoustic - soft optical mode coupling causes negative thermal expansion close to the structural phase transition. Unexpectedly, the negative thermal expansion boosts phonon group velocities in this temperature region, countering the increased phonon anharmonicity and leading to an increase in κ near the structural phase transition. The increased phonon anharmonicity in the vicinity of the phase transition causes non-Lorentzian shapes of the phonon spectral functions, questioning the traditional Boltzmann transport approach for calculation of κ. To address this issue, we implement a novel method of calculating lattice thermal conductivity, combining the Green-Kubo approach and the lattice (phonon) dynamics. We find that the Boltzmann transport equation underestimates the lattice thermal conductivity close to the phase transition. We perform molecular dynamics simulations of GeTe at different temperatures to confirm these findings.

The phase transition in GeTe has a ferroelectric character as well. The formation of ferroelectric domains in GeTe has been observed experimentally. Here we also investigate the influence of ferroelectric domain walls on the thermoelectric properties of GeTe. We recognize several different types of domain walls that can occur in GeTe. We calculate the structural, electronic, and transport properties of a few selected domain wall types. We find that domain walls offer a promising alternative for the reduction of lattice thermal conductivity in GeTe. Wider domain walls are shown to scatter phonons more efficiently, causing up to a 40% reduction of κ. Additionally, we investigate the electronic transport properties of domain walls and find a two-fold enhancement of the Seebeck coefficient in the in-plane directions of domain walls. While significantly increasing the Seebeck coefficient, domain walls do not drastically suppress the electrical conductivity, leading to a significant increase of the power factor at charged domain walls in GeTe with respect to bulk (by a factor of 5). Finally, we propose a novel design of a nano-thermoelectric device that maximizes the beneficial transport properties of domain walls.

Chapter 1

Introduction

1.1 Thermoelectric materials

Energy sustainability is one of the most important problems our society faces. As fossil fuels have been being recognized as one of the biggest contributors to global warming [21, 22], we need to find a way to reduce their use and increase their efficiency. A big part of the energy that is emitted by burning fossil fuels is being lost to the environment in the form of waste heat. Thermoelectric devices are the most promising way of scavenging this lost energy [23, 24, 25, 26]. Until now they have found use in some niche applications, such as fuel cells in deep space missions [27, 28], remote research stations [29], and cooling devices [30, 31], but their widespread use is seriously limited due to low efficiency [1, 32, 33, 34]. Improving the performance of these devices could lead to a revolution in the energy sector by finally breaking away from reliance on fossil fuels.

Thermoelectric devices utilize the effect of thermoelectricity [35, 36, 37]. This phenomenon encompasses three historically different, but mutually connected effects, Seebeck [35], Peltier [36], and Thompson [37] effect, all known from the nineteenth century. The Seebeck effect, which we will use interchangeably with thermoelectricity in the rest of the thesis, is the occurrence of an electrical potential gradient in the material due to a temperature gradient. Experimentally this can be observed by making a junction of two materials (A and B, usually conductors), called a thermocouple, and placing a temperature difference between two such junctions. In the steady-state (with zero current), the voltage between junctions (ΔV) is proportional to the temperature

difference (ΔT) [38]:

$$\Delta V = S\,\Delta T.$$

The Peltier effect can be understood as the counterpart of the Seebeck effect. For the system in the example above, if we drive a current through the thermocouple, one of the junctions would cool and the other would heat up. The absorption (emission) of heat is empirically determined to be [38]:

$$\dot{Q} = (\Pi_A - \Pi_B)I,$$

where Π is the Peltier coefficient of each material, I is the electrical current, and $\dot{Q}$ is the rate of heat absorption (generation). This effect is utilized in cooling devices, the previously mentioned niche application of thermoelectric devices. The connection between the Seebeck and Peltier effect can be shown to be [38]:

$$\Pi = S\,T.$$

The last thermoelectric effect, the Thompson effect, is the last one discovered and it explains the heating or cooling of the conductor with the current passing through it.

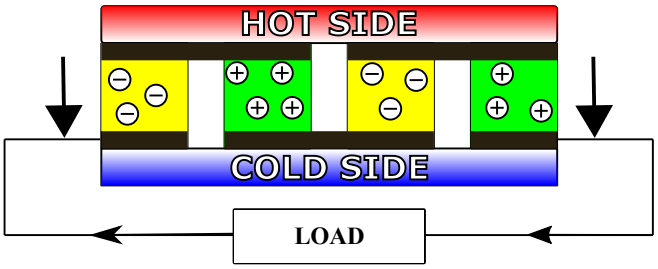

Figure 1.1: Schematics of the thermoelectric device for power generation. The yellow and green blocks represent n- and p- type doped thermoelectric materials. The large arrows show the direction of free charge carrier diffusion and heat flow, while the line arrows through the load show the electric current direction.

A simplified schematic of the thermoelectric device is given in Fig. 1.1. Usually, thermoelectric devices consist of a large number of alternating p and n type semiconductor bulk elements connected at top and bottom by conducting layers. This type of device uses the longitudinal Seebeck effect where current and temperature gradient are parallel to each other. We define the efficiency of the device as [38]:

$$\eta = \frac{W}{Q_1 + Q_2}, \tag{1.1}$$

where W is the useful power generated in the load R by the thermoelectric device:

$$W = I^2R = \left(\frac{\Delta V}{R+r}\right)^2 R = \frac{\sigma S^2 \Delta T^2 m}{(m+1)^2}.$$

Here we denote the electronic conductivity of the material as $\sigma = 1/\rho$, and the ratio between the resistivities of the load and the material as $m = \frac{R}{r}$. The wasted heat power is given by the Peltier heat Q_1:

$$Q_1 = \Pi I = \frac{\sigma S^2 T \Delta T}{m+1},$$

and the heat transferred through the material due to the temperature gradient is:

$$Q_2 = \kappa \Delta T,$$

where κ is total thermal conductivity of the material. The ratio $m = m_{max}$ that maximizes the efficiency of the thermoelectric device is found by solving the equation $\frac{\partial \eta}{\partial m} = 0$:

$$m_{max} = \sqrt{1 + \frac{\sigma S^2 T}{\kappa}}.$$

Substituting this result in Eq. (1.1) gives us the maximum efficiency of the thermoelectric device that is the function of only the transport properties of the material:

$$\eta = \frac{\Delta T}{T_H} \frac{\sqrt{1+zT}-1}{\sqrt{1+zT}+\frac{T_C}{T_H}}, \tag{1.2}$$

where the quantity zT is called the thermoelectric figure of merit:

$$zT = \frac{\sigma S^2 T}{\kappa_e + \kappa_{latt}}, \tag{1.3}$$

where the total thermal conductivity contains both electronic and lattice contributions, κ_e and κ_{latt} respectively.

To gain some perspective on what these numbers mean, we show the efficiency of a thermoelectric generator versus the hot side temperature for a number of materials with different zTs (see Fig. 1.2). Light-blue regions represent the range of efficiencies of existing thermoelectric materials, while the orange region roughly represents other types of power generation currently in use [1]. We can see that even the best thermoelectric materials can not compete with conventional power sources. This can be seen

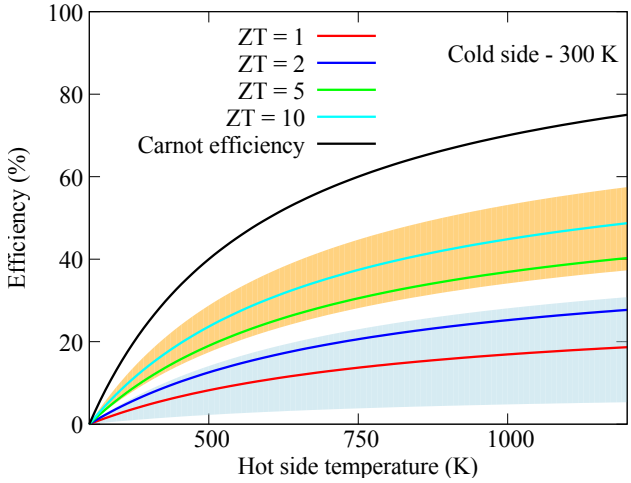

Figure 1.2: Efficiency of a thermoelectric generator as a function of temperature for different thermoelectric figures of merit of the material. The light-blue region shows the range of existing, state-of-the-art thermoelectric materials. The orange region represents the efficiencies of different types of power generators that are currently in use [1].

as a discouraging fact, or as an opportunity to substantially increase the efficiency of thermoelectric materials. This graph, however, does not represent the suitability of different power sources for niche applications and this is where thermoelectric materials can find their use [29, 32].

1.2 Improving thermoelectric figure of merit

Thermoelectric figure of merit depends on the electronic and vibrational properties of the material through Eq. (1.3). One can immediately notice that Seebeck coefficient (S), electronic conductivity (σ), and electronic thermal conductivity (κ_e) all depend on the electronic properties of the material. Changing and optimizing one of these electronic quantities will change others as well. Usually what happens is that improving one of these quantities makes others worse, so that there is a delicate balance that needs to be achieved in order to improve zT. However, the lattice thermal conductivity (κ_{latt}) is mostly decoupled from other properties and its reduction represents the most promising way of improving zT.

1.2.1 Reducing lattice thermal conductivity

Lattice thermal conductivity describes how well heat is transferred through a material by atomic vibrations [39]. A crystalline material can be described as an infinite

repetition of the pattern called a primitive unit cell. This unit cell is determined by a set of lattice vectors that represent the translational symmetry of the crystal structure, and the atomic basis (the positions and types of atoms within a unit cell) [40, 39, 41]. Atoms in real materials are not stationary, they vibrate around their equilibrium positions. The restoring forces in these vibrations can be approximated as arising from a simple harmonic potential leading to a set of normal modes of oscillation in the crystal called phonons [39, 41]. Phonons in this particular case of harmonic interaction have infinite lifetimes and consequently infinite mean free paths, leading to an infinite lattice thermal conductivity. However, this is not a realistic picture. The atomic interaction in a crystal is only crudely approximated by the harmonic potential and, in general, has an anharmonic contribution. The anharmonic contribution leads to the coupling or interaction between phonons which instigates scattering between them, limiting lattice thermal conductivity. Furthermore, realistic materials are not perfect crystals. They contain impurities such are interstitial atoms, vacancies, dopants, grain boundaries, etc. All of these scatter phonons, decreasing lattice thermal conductivity even further.

According to Eq. (1.3), reducing lattice thermal conductivity would lead to an overall increase in thermoelectric figure of merit. As we can see from the previous paragraph, lattice thermal conductivity depends mostly on the vibrational properties of the material, and because of that modifying it requires changing the vibrational, rather than the electronic properties of the material. Furthermore, the best thermoelectrics are usually semiconductor materials, for which the lattice thermal conductivity is much more important than the electronic thermal conductivity. This makes the reduction of the lattice thermal conductivity the most promising pathway for increasing the efficiency of thermoelectric materials.

Since anharmonicity is the main reason for the finite lattice thermal conductivity, one might expect that materials with highly anharmonic interaction will have low lattice conductivity. Materials with large anharmonicity usually have very large unit cells with light atoms loosely bonded. This causes a rattling like motion that gives very flat and localized phonon modes that scatter other, propagating, phonon modes [42, 43, 44]. These rattling modes do not conduct heat themselves because of their very low group velocities due to localization, but provide a large scattering density of states for other modes. Examples of these materials are various clathrates [45, 42, 46], skutterudites [43, 47], cobaltates [48], etc.

Another physical mechanism that gives rise to large anharmonicity is the resonant bonding effect in some types of materials. In IV-VI, group V and V_2-VI_3 materials, unsaturated covalent bonds lead to the resonant bonding effect [49, 50]. This effect

manifests itself through slowly decaying, long-range interatomic force constants along particular directions. This can be explained as a long-range interaction coming from electronic, rather than ionic polarizability. These increased interactions lead to higher anharmonicity of these materials and consequently lower lattice thermal conductivity.

Resonant bonding causes softening of the transverse optical (TO) mode in some of the mentioned materials, which in the most extreme cases can lead to a change of the crystal structure. Most structural displacive phase transitions have a similar feature of particular soft phonon modes [3, 51, 52]. The name soft mode comes from the low frequency of that mode, which becomes even smaller as we approach the phase transition [53]. At the phase transition, this frequency becomes zero and that mode freezes, creating the displacement of a crystal lattice that is recognized as a structural phase transition [54].

Recent work in our group showed that low lattice thermal conductivity can be achieved by pushing lead telluride (PbTe) closer to the phase transition, either through strain engineering or alloying with germanium telluride [50, 55]. The Refs. [50, 55] investigated the phase transition in PbTe at 0 K, so by construction the phase transition in these cases is of the displacive type. As we approach the phase transition in this material, soft TO mode becomes zero. That means the overlap of this mode with acoustic zone center phonons becomes larger, leading to larger scattering between these modes. Since most of the heat is being conducted by these acoustic modes, reducing their lifetimes leads to a large reduction of the lattice thermal conductivity. The softening of the TO mode also tends to increase its anharmonic coupling strength. Scattering rates are inversely proportional to the phonon frequency, meaning softening of this phonon mode will lead to the divergence of the scattering rates. The added benefit of reducing lattice thermal conductivity through the phase transition engineering, compared to other approaches, is that the phase transition might not affect the electronic properties of material negatively, while nanostructuring or alloying might.

Another pathway for reducing lattice thermal conductivity is nanostructuring [56, 57]. Including impurities in the otherwise perfect crystal structure leads to phonon scattering by these structures. Different types of impurities will scatter different phonons [56]. For example, while impurity atoms will scatter short-wavelength phonons (the Brillouin zone edge phonons), mid to large wavelength phonons will not be scattered [58]. On the other hand, inclusions with larger characteristic lengths will scatter phonons of larger wavelengths [59]. These effects can be achieved by solid solutions where phase separation forms structures on nanometer scales [59]. The disadvantage of this method is the degradation of electronic properties since larger impurity structures can

effectively reduce electronic mobility as well. This is the case especially in materials with random orientation of grain boundaries.

1.2.2 Improving Seebeck coefficient

Another possible pathway for increasing the thermoelectric figure of merit is the enhancement of the Seebeck coefficient. The Seebeck coefficient enters as a square in the expression for zT (see Eq. (1.3)), meaning that increasing the Seebeck coefficient could substantially increase the zT of a material. Here, however, we have to be careful not to degrade the mobility of electrons significantly. There are several ways of improving the Seebeck coefficient and all of them could be understood by examining the Mott expression for the Seebeck coefficient [60]:

$$S = \frac{\pi^2 k_B^2 T}{3e} \left(\frac{N'(E)}{N(E)} + \frac{\left\langle v^2(E) \right\rangle'}{\langle v^2(E) \rangle} + \frac{\tau'(E)}{\tau(E)} \right) \Bigg|_{E=\mathrm{E_F}}, \tag{1.4}$$

where k_B is the Boltzmann constant, T is the temperature, e is the electron charge, $N(E)$ is the electronic density of states, $\left\langle v^2(E) \right\rangle$ is the squared carrier group velocities average, $\tau(E)$ is their relaxation time and E_F is the Fermi level. Primed quantities represent the first derivatives with respect to energy. This equation clearly shows that the Seebeck coefficient depends on the relative change of the transport properties of a material with energy.

Equation (1.4) shows that increasing the density of states or the concentration of the free charge carriers at the Fermi level is beneficial to the Seebeck coefficient. This can be achieved by reducing the dimensionality of the system [61, 62]. Systems such as quantum wells, quantum wires, and quantum dots have an increased density of states close to Fermi level as shown in Fig. 1.3.

Computational studies done on quantum wires and wells of bismuth telluride (Bi_2Te_3) [61, 62] showed that the thermoelectric figure of merit can be an order of magnitude higher compared to the bulk material. Experimental realization of these effects was achieved in superlattices [63, 64, 65] or gated structures [66, 67]. In both of these cases, localization in 2D was achieved by the electric field, intrinsically in the case of superlattices, and by applying voltage in gated structures.

The optimal doping level for the Seebeck coefficient would be where the Fermi level is close to the maximum of the density of states (DOS). This is best observed in the case when DOS resembles a Dirac delta function. Bulk materials usually do not exhibit

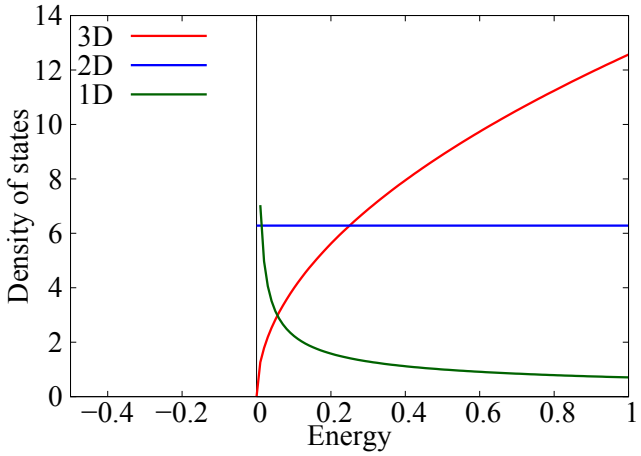

Figure 1.3: The density of states of a parabolic band for systems with different dimensionality. One-dimensional systems have the biggest change in the free charge concentration at the Fermi level, which decreases with increased dimensionality of the system. Zero energy represents the conduction band minimum.

this type of energy dependence of DOS, but 0 D structures by construction have that. However, it is possible to engineer a material with highly localized impurity states that give a Dirac delta-like distortion of the bulk DOS. This is achieved in thallium doped PbTe [68], where zT is doubled compared to the bulk material, and indium doped GeTe [69].

Sharp increases in the electronic density of states close to the Fermi level can be also achieved by band convergence. Most of the semiconductors considered for thermoelectric applications have a single parabolic band that can participate in transport. Doping can shift other bands that are further from the Fermi level closer to this primary band i.e. they converge towards the same energy. This is achieved in selenium doped PbTe [70], MgTe doped PbTe [71], $CoSb_3$ [43], MgTe doped SnTe [72] etc.

The Seebeck coefficient can be increased also by modifying the energy dependence of group velocities and relaxation times, as shown in Eq. (1.4). A representative of these methods is the energy filtering effect that is observed in some samples with a complex internal structure, meaning a large number of grain boundaries and impurities. Grain boundaries represent scattering potentials of a certain height and predominantly scatter the electronic states with energies lower than that height. This changes the energy dependence of the relaxation time, leading to an increase in the observed Seebeck coefficient. These effects were first theoretically predicted [73, 74], and then experimentally observed in nanostructured PbTe [75, 76]. However, in real samples this increase in the Seebeck coefficient is followed by a reduction of the electronic conductivity, leading to an overall decrease of the thermoelectric efficiency.

1.3 Phase transitions

The second order phase transition is the point in some parameter space (usually pressure or temperature) at which the order parameter becomes non zero [54]. Phase transitions are usually recognized by spontaneous symmetry breaking, where a single minimum in the free energy of one phase (a high symmetry phase) splits into a number of degenerate minima of the second phase (a lower symmetry phase).

The order parameter in the ferroelectric phase transition is the local dipole moment of the unit cell or polarization. For example, in the cubic phase, GeTe (one of the best thermoelectric materials that we will investigate in this thesis) crystallizes in the rocksalt structure [7, 8]. Since this structure has the inversion symmetry, the polarization (order parameter) value is zero. During the phase transition, GeTe changes its crystal structure and becomes rhombohedral. The rhombohedral structure is characterized by the elongation of one of the body diagonals of the rocksalt cubic conventional unit cell. This spontaneous strain can be regarded as a secondary order parameter, meaning that this phase transition has a ferroelastic character as well [77]. Simultaneously, there is a displacement of the tellurium sublattice along this direction which creates a non-zero polarization of the unit cell.

There are two possible mechanisms that drive the ferroelectric phase transition in GeTe. These mechanisms determine the nature of the phase transition, whether the phase transition is displacive or order-disorder. It is easy to make a distinction between these two mechanisms in the Landau mean field theory of the second order phase transition [54]. The total free energy of the material in this approximation takes the form of the quartic polynomial with even powers:

$$\Phi = \Phi_0 + \frac{A}{2}\tau^2 + \frac{B}{4}\tau^4, \tag{1.5}$$

where τ is the order parameter and A, B are coefficients that depend on the pressure and temperature. When $A < 0$, we have two degenerate minima of the total free energy.

Let us assume that this form of the potential holds for the local order parameters as well. The displacive phase transition is then described by the increase of the parameter A with temperature. The phase transition happens when $A = 0$, and two minima merge at $\tau = 0$. Consequently, all of the local τ become zero at the same moment (A is universal by construction), which implies that the correlation length is infinitely long at the phase transition. This means that this phase transition is of the second order.

However, let us imagine a situation where softening of the parameter A with tempera-

ture is so slow, that the thermal energy of the system is large enough to allow transition of τ between two degenerate minima. At some point the average τ of the system will be zero. This is the point where the system undergoes the phase transition. Since the "jumping" of τ between two minima is completely random, the correlation length at this phase transition is finite. In other words, this is the first order phase transition.

Finally, the situation drastically complicates if we add another term (C) in the total free energy that will describe interaction between local order parameters:

$$\Phi = \Phi_0 + \frac{A}{2}\tau^2 + \frac{B}{4}\tau^4 + C\sum_{i>j}(\tau_i - \tau_j)^2. \tag{1.6}$$

The parameter C is usually called local mode coupling and it is the equivalent of the exchange interaction of the Ising model (this is easily seen by expanding the square of the binomial) [78]. Now we have a many body problem for which we do not have the exact solution. In this model, the order-disorder phase transition can be of the second order, since the interaction between local order parameters allows for the infinite correlation lengths. This is exactly what happens, for example, in the Ising model.

The real systems, however, are much more complicated than the simple models outlined above. Because of this, it is very hard determine the nature of the phase transition, either with computational or experimental techniques. A part of this thesis will be focused on trying to elucidate the nature of the phase transition in GeTe.

1.4 Outline of the thesis

The main objective of this thesis was to understand if the ferroelectric phase transition occurring in germanium telluride might positively affect its thermoelectric performance. Strong acoustic-soft TO mode coupling responsible for the low lattice thermal conductivity in strained PbTe [50] and PbTe-GeTe alloys [55] was expected also to exist in GeTe close to the ferroelectric phase transition. We showed that this coupling is indeed strong and that it is responsible for negative thermal expansion observed at the phase transition [79]. On the other hand, contrary to what we expected, the lattice thermal conductivity actually increases at the phase transition due to increased phonon group velocities induced by large lattice contraction. However, anharmonicity of the phonon modes is large at the ferroelectric phase transition, as evidenced by a large deviation from the Lorentzian shape of the phonon spectral functions. Calculated spectral functions show that phonon modes further soften due to phonon-phonon interaction.

We implemented a method for the calculation of lattice thermal conductivity that takes into account non-Lorentzian shapes of the phonon spectral functions and show that this softening leads to even larger lattice thermal conductivity. We confirmed our results for thermal properties of GeTe at the ferroelectric phase transition by performing a molecular dynamics simulation using a very accurate interatomic potential.

We have noticed that in experiments the GeTe structure in the rhombohedral phase organizes in a fairly ordered domain pattern called herringbone structure [80]. These domains are separated by ferroelectric domain walls which, depending on the nature of polarization change between domains, can be charged or neutral. We have found that the charged domain walls host a 2D free electron gas. Investigation of transport properties of these systems showed a substantial increase in both the Seebeck coefficient(a factor of 2) and the power factor (a factor of 5) compared to the bulk material at 300 K [81]. Ferroelectric domain walls, both charged and neutral, can be used as phonon scattering centers in an effort to reduce lattice thermal conductivity. Our results show that the reduction can be as high as 40 % at room temperature [82]. These findings clearly show the potential of ferroelectric domain walls for thermoelectric applications.

The thesis is structured as follows.

In Chapter 2, we first review the theoretical background behind density functional theory, which we used as our primary computational tool. We then briefly discuss main features of molecular dynamics simulations. Next, we summarize the theory behind the Gaussian Approximation Potentials we used to fit interatomic potential for GeTe. We also discuss the application of the temperature dependent effective potentials method. We follow with a derivation of the solution of Boltzmann transport equation in the relaxation time approximation, for both electrons and phonons. We finalize with the derivation of the expression for the lattice thermal conductivity from the Green-Kubo theory.

In Chapter 3, we present a method for calculating the thermal expansion of solids close to the ferroelectric phase transition. Changes in structural parameters as we increase temperature are shown, as well as the influence of temperature and phase transition on elastic constants and soft TO mode. We elucidate the origin of negative thermal expansion at the ferroelectric phase transition in GeTe.

Chapter 4 shows the results for the phonon spectral functions of GeTe close to the ferroelectric phase transition. We show the reason behind the anomalous behavior of the phonon spectral functions in this region.

Chapter 5 is based on the calculation of the lattice thermal conductivity of GeTe close

to the phase transition. We show the reason behind the increase in the lattice thermal conductivity at the phase transition using results obtained from Boltzmann transport equation. We discuss the results of the Green-Kubo method for calculating lattice thermal conductivity.

Chapter 6 contains the predictions of the structural and electronic properties of ferroelectric domain walls in GeTe. We provide a recipe for the construction of domain walls. We calculate the structural properties of domain walls and show their influence on the lattice thermal conductivity of GeTe. We investigate the electronic properties of charged domain walls. We introduce a model for calculating the energy and momentum dependent relaxation times of electronic states. This is followed by the results on the electronic transport properties of domain walls with a discussion on possible applications.

Chapter 7 contains a study of the ferroelectric phase transition in GeTe using molecular dynamics (MD) simulations. We provide of the fitting procedure of the Gaussian Approximation Potentials. We confirm the results of Chapters 3 and 5 on the negative thermal expansion and an increase of the lattice thermal conductivity at the phase transition by use of MD simulations. We also provide a study of vibrational properties of GeTe at the phase transition directly from the MD simulation.

We conclude in Chapter 8 with overall conclusions and the outlook for future investigations.

The original work presented in this thesis has been published in the following papers:

- Đorđe Dangić, Aoife R. Murphy, Éamonn D. Murray, Stephen Fahy, and Ivana Savić, "Coupling between acoustic and soft transverse optical phonons leads to negative thermal expansion of GeTe near the ferroelectric phase transition", *Phys. Rev. B* **97**, 224106 (2018).
- Đorđe Dangić, Éamonn D. Murray, Stephen Fahy, and Ivana Savić, "Structural and thermal transport properties of ferroelectric domain walls in GeTe from first principles", *Phys. Rev. B* **101**, 184110 (2020).
- Đorđe Dangić, Stephen Fahy, and Ivana Savić, "Giant thermoelectric power factor in charged ferroelectric domain walls of GeTe with Van Hove singularities", *npj Computational Materials* **6**, 195 (2020).
- Đorđe Dangić, Olle Hellman, Stephen Fahy, and Ivana Savić, "The origin of the lattice thermal conductivity enhancement at the ferroelectric phase transition in GeTe", *npj Computational Materials*, **7**, 57 (2021).

- Đorđe Dangić, Stephen Fahy, and Ivana Savić, "Structural phase transition in GeTe from molecular dynamics simulations", in preparation.

Chapter 2

Computational methods

Here we will summarize the underlying theory behind the first-principles calculations carried out in this thesis. In the first section we briefly introduce the density functional theory, which we used to obtain most of the microscopic material properties. The second section is the overview of molecular dynamics simulations, focusing on the parts relevant to our studies. The third section introduces Gaussian Approximation Potentials, a method for parametrizing interatomic potentials using machine learning techniques. We then summarize the temperature dependent effective potential method for obtaining interatomic force constants from first principles data. The fifth section presents the relaxation time solution of the Boltzmann transport equation for both electrons and phonons. Finally, the sixth section contains derivation of the Green-Kubo relation for lattice thermal conductivity using phonon spectral functions.

2.1 Density functional theory

A general Hamiltonian for the system of interacting electrons and nuclei is [83]:

$$\hat{H} = -\frac{\hbar^2}{2m_e}\sum_i \nabla_i^2 + \sum_{i,I}\frac{Z_I e^2}{|\vec{r}_i - \vec{R}_I|} + \frac{1}{2}\sum_{i\neq j}\frac{e^2}{|\vec{r}_i - \vec{r}_j|} - \sum_I \frac{\hbar^2}{2M_I}\nabla_I^2 + \\ + \frac{1}{2}\sum_{I\neq J}\frac{Z_I Z_J e^2}{\vec{R}_I - \vec{R}_J} = \hat{T}_e + \hat{V}_{ext} + \hat{V}_{int} + \hat{T}_{ion} + E_{II}. \tag{2.1}$$

Here the masses of electrons and nuclei are denoted as m_e and M_I respectively, the fundamental electron charge as e, the positions of electron and nuclei as $\vec{r}_i$ and $\vec{R}_I$, and the atomic number of nuclei as Z_I. Here $\hat{T}_{e/ion}$ represents the kinetic energy of elec-

trons and nuclei respectively, $\hat{V}_{ext}$ is the external potential of nuclei acting on electrons, $\hat{V}_{int}$ the interaction energy of electrons between themselves and E_{II} is the interaction energy between nuclei. In most cases, one can use the Born-Oppenheimer approximation which states that nuclei and electron degrees of freedom are separated and that electrons have a negligible effect on the nuclei motion. That means the term T_{ion} can be to zero and the variables R_I are considered to be fixed.

However, even after this approximation, Eq. (2.1) is almost impossible to solve, especially for large systems. The need for an exact solution of the above equation can be avoided by utilizing the Hohenberg-Kohn theorems with the Kohn-Sham ansatz (the basis of density functional theory (DFT)).

The Hohenberg-Kohn theorems [84, 83] state:

- **Theorem I** *For any system of interacting particles in an external potential $\hat{V}_{ext}(\vec{r})$, the potential $\hat{V}_{ext}(\vec{r})$ is determined uniquely, except by a constant, by the ground state particle density $n_0(\vec{r})$.*
- **Theorem II** *An universal functional of the energy $E[n]$ in terms of the density $n(\vec{r})$ can be defined, valid for any external potential $V_{ext}(\vec{r})$. For any particular $V_{ext}(\vec{r})$, the exact ground state energy of the system is the global minimum value of this functional, and the density $n(\vec{r})$ that minimizes the functional is the exact ground state density $n_0(\vec{r})$.*

Proofs of these theorems are fairly straightforward and will be omitted here [84, 83]. We will only comment on the significance and consequence of these statements. The first theorem tells us that if we have a well defined $V_{ext}(\vec{r})$, as it is the case for the solid without an external field, we have a unique ground-state electron density $n_0(\vec{r})$. This means we do not have to actually solve Eq. (2.1), and we do not need to know the actual wave functions of the system to fully describe it. All the information we need to know is the ground state electronic density to get the total energy of the system. The second theorem gives us a recipe for how to actually find this ground state electronic density. The ground state density is the function that minimizes the total energy functional $E_{HK}[n]$:

$$E_{HK}[n] = F_{HK}[n] + \int \mathrm{d}^3\vec{r}\, V_{ext}(\vec{r})n(\vec{r}) + E_{II}, \tag{2.2}$$

where the functionals of electronic kinetic energy and electron-electron interaction energy are folded into $F_{HK}[n]$.

This is still a many-body problem which is very difficult to solve. In order to utilize

the above theory, one uses the Kohn-Sham ansatz [85]. The Kohn-Sham ansatz maps an interacting system of particles to a non-interacting system that has the same electronic density. Going from a system of equations for a many-body interacting system to an equation for a non-interacting system considerably simplifies the numerical part of the calculation. The many-body part of the equation is folded into the exchange-correlation functional of the density. The exact form of the exchange-correlation functional is not known. The approximate formulation of the exchange-correlation functional is the first approximation made in this discussion. To get an exact form of the exchange-correlation potential, Eq. (2.2) is rewritten in a slightly different way:

$$E_{KS}[n] = T_s[n] + \int \mathrm{d}\vec{r} V_{ext}(\vec{r}) n(\vec{r}) + E_{Hart}[n] + E_{II} + E_{xc}[n]. \tag{2.3}$$

The non-interacting parts of Eq. (2.2) are pulled outside and everything else has been incorporated into the exchange-correlation functional $E_{xc}[n]$:

$$E_{xc}[n] = F_{HK}[n] - (T_s[n] + E_{Hart}[n]) = \langle \hat{T} \rangle - T_s[n] + \langle \hat{V}_{int} \rangle - E_{Hart}[n], \tag{2.4}$$

where the independent particle kinetic energy $T_s[n]$ is defined as:

$$T_s[n] = \frac{1}{2} \sum_i |\nabla \psi_i|^2,$$

where ψ_i is a single particle wave function (the eigenfunction for a single electron in the Kohn-Sham potential Eq. (2.6)). The Hartree energy term (giving the energy of the interaction of the electron density with itself) is:

$$E_{Hart}[n] = \frac{1}{2} \int \mathrm{d}\vec{r} \mathrm{d}\vec{r}' \frac{n(\vec{r}) n(\vec{r}')}{|\vec{r} - \vec{r}'|}.$$

Equation (2.3) tells us that the exchange-correlation functional is the difference of the kinetic and electron-electron interaction energies of a fully interacting system and a non-interacting system with the same ground state density, in which the electron-electron interaction is substituted by the Hartree energy. To obtain the Kohn-Sham equations, one has to apply the minimization procedure of the functional given by Eq. (2.3). Since all of the terms are functionals of wave functions, either explicitly or implicitly through the electronic density, a variational approach with respect to wave functions is used:

$$\frac{\delta E_{KS}}{\delta \psi_i^*(\vec{r})} = \frac{\delta T_s}{\delta \psi_i^*(\vec{r})} + \left[\frac{\delta E_{ext}}{\delta n(\vec{r})} + \frac{\delta E_{Hart}}{\delta n(\vec{r})} + \frac{\delta E_{xc}}{\delta n(\vec{r})} \right] \frac{\delta n(\vec{r})}{\delta \psi_i^*(\vec{r})} = 0.$$

This further can be simplified (by directly taking the derivatives with respect to wave functions) to a Kohn-Sham Schrödinger like equation:

$$(H_{KS} - \epsilon^i)\psi_i(\vec{r}) = (-\frac{1}{2}\nabla^2 + V_{KS}(\vec{r}) - \epsilon^i)\psi_i(\vec{r}) = 0. \tag{2.5}$$

Here the Kohn-Sham potential V_{KS} contains the external potential, Hartree and exchange-correlation parts:

$$V_{KS}(\vec{r}) = V_{ext}(\vec{r}) + \frac{\delta E_{Hart}}{\delta n(\vec{r})} + \frac{\delta E_{xc}}{\delta n(\vec{r})} = V_{ext}(\vec{r}) + V_{Hart}(\vec{r}) + V_{xc}(\vec{r}). \tag{2.6}$$

Equation (2.5) maps a many body system of interacting particles to an equivalent system of non-interacting particles. Eq. (2.6) confirms once more that the only approximation coming into this approach is through the definition of the exchange-correlation potential $V_{xc}(\vec{r})$.

There are various approaches to approximate the term $V_{xc}(\vec{r})$ in the above equations. The first and the most simple way is the local density approximation (LDA) [85] which, as its name suggests, assumes that the exchange-correlation potential at a point $\vec{r}$ depends only on the electronic density at that point and is equal to the potential in the homogeneous electron gas with the same density. This approximation works surprisingly well, even for the systems that are not metals and have almost free electrons. However, over the years many other methods of treating $V_{xc}(\vec{r})$ arose, in an attempt to give DFT more transferability and reliability. First of these are generalized gradient approximations (GGA) [86], which we use in this work.

To derive an expression for the generalized gradient approximation, one starts by assuming that the long-range electron-electron interaction is handled with the Hartree term. Hence, the exchange-correlation part will need to account for the local part of the electron-electron interaction. This means that one can represent the exchange-correlation energy as:

$$E_{xc}[n] = \int \mathrm{d}\vec{r}\, n(\vec{r})\epsilon_{xc}(n(\vec{r}), \vec{r}).$$

Here we can see that while E_{xc} is still a functional of the electronic density, the property of interest $\epsilon_{xc}(n(\vec{r}), \vec{r})$ is the functional of the electronic density and only depends on the value of density at $\vec{r}$. To generalize this, as in the GGA approach, we introduce the dependence of ϵ_{xc} on the gradient of the density as well:

$$E_{xc}[n] = \int \mathrm{d}\vec{r}\, n(\vec{r})\epsilon_x^{hom}(n)F_{xc}(n, \nabla n),$$

where $\epsilon_x^{hom}(n)$ is the exchange energy per electron of the homogeneous electron gas and $F_{xc}(n, \nabla n)$ is a dimensionless function that needs to be parametrized in a certain way. We use the Perdew-Burke-Ernzerhof (PBE) parameterization [86]. The GGA approach corrects energy characteristics of the modeled systems, expands and softens bonds, sometimes correcting the LDA predictions. However, some parametrizations are plagued by complexities of the chosen functional leading to over parameterization and reduced smoothness of the potential. These inaccuracies are somewhat corrected by GGA-PBE, leading to better agreement of the modeled system to the experiment [83].

To perform density functional theory calculations, we used ABINIT code [87, 88]. ABINIT's main program allows one to find the total energy, charge density and electronic structure of systems made of electrons and nuclei (molecules and periodic solids) within Density Functional Theory (DFT), using pseudopotentials and a planewave basis representation for the electron wave functions [89]. We used ABINIT to perform structural relaxation, calculation of energies and forces needed for fitting TDEP and GAP potentials, run a small scale MD simulations with a Verlet algorithm and perform density functional perturbation theory calculations.

2.1.1 Plane waves

When considering condensed matter systems, we most commonly consider only crystalline materials. Crystals have a periodic structure defined by a set of lattice vectors. Mathematically this is reflected in the Hamiltonian for which the following equation holds: $V(\vec{r}) = V(\vec{R} + \vec{r})$. Here $\vec{R}$ is a linear combination of the lattice vectors. A consequence of this is Bloch's theorem for the single-particle wavefunctions:

$$\psi_{i,\vec{k}}(\vec{r} + \vec{R}) = \exp(i\vec{k} \cdot \vec{R})\psi_{i,\vec{k}}(\vec{r}).$$

To derive Bloch's theorem one starts by taking a Fourier transform of the electronic wave function. Because the system is periodic, the reciprocal space is periodic as well and one can take that the inverse variable of the Fourier transform is $\vec{k} + \vec{G}_m$, where $\vec{G}_m$ is a linear combination of the reciprocal lattice vectors:

$$\psi_{i,\vec{k}}(\vec{r}) = \sum_m c_{i,m}(\vec{k}) \frac{1}{\sqrt{V}} \exp(i(\vec{k} + \vec{G}_m) \cdot \vec{r}) = \frac{1}{\sqrt{N}} \exp(i\vec{k} \cdot \vec{r}) u_{i,\vec{k}}(\vec{r}).$$

Here V is the volume of the crystal and $u_{i,\vec{k}}(\vec{r})$ is the periodic part of the wave function:

$$u_{i,\vec{k}}(\vec{r}) = \frac{1}{\sqrt{V_{cell}}} \sum_m c_{i,m}(\vec{k}) \exp(i\vec{G}_m \cdot \vec{r}).$$

The advantage of the approach for representing wave functions as a linear combination of plane waves (i.e as Fourier series) is that it does not depend on a particular atomic basis. On the other hand, the applicability of this approach is plagued by the need to introduce pseudopotentials, which give much more rapid convergence of the Fourier series than the true electron-nuclear potential, as we will note later. The plane-wave basis is easy to implement and convergence is straightforward. Plane waves are numbered by reciprocal lattice vectors $\vec{G}_m$ and one can reach convergence simply by increasing the number of plane waves m. The number of plane waves is usually determined by the plane wave cutoff E_{cutoff} which has the dimension of energy (here in units of $\hbar$):

$$\frac{1}{2}|\vec{k} + \vec{G}_m|^2 < E_{cutoff}.$$

As one can see from the equation above, the plane waves needed to describe the wave function are in a certain sphere of radius E_{cutoff}. However, to use the Fast Fourier Transform (FFT) (which is another advantage of this approach), we have to take a uniform grid of $\vec{G}_m$ vectors. Thus, while the convergence of wavefunctions in the plane wave basis is defined in terms of E_{cutoff}, the actual number of plane waves is determined by the size of the FFT grid.

2.1.2 Pseudopotentials

Most of the physical properties of solids we are interested in are determined by the interaction and bonding of valence electrons. Core electrons are tightly bound to nuclei and weakly interact, or not at all, with valence states. Considering that we have to treat all electronic states in Eq. (2.1), a large amount of work is done without actually contributing to the result of interest. A way to circumvent this problem is the introduction of pseudopotentials which represent an auxiliary potential to the real one. Another advantage of this approach is that it lowers the number of plane waves in the plane-wave expansion needed to describe valence states. Valence states oscillate rapidly as the radial component goes to zero due to the diverging kinetic energy part. In the pseudopotential model, this $1/r$ potential is substituted by a better behaving one which gives a smoother electron wave function with fewer nodes and the same properties as

the original, real, one. The main difficulty when constructing a good pseudopotential is its transferability, or the ability to perform equally well in a number of different bonding environments.

To satisfy this extremely important condition of transferability, we use so-called norm-conserving pseudopotentials [83, 90]. The pseudopotential wavefunctions satisfy the same orthonormality conditions as the real wavefunctions and are the solutions of the Kohn-Sham equation Eq. (2.5) where the external potential is substituted for the pseudopotential. These potentials are created from first-principles or *ab-initio*, meaning that they are fitted to all-electron calculations for the atom. Accurate pseudopotentials satisfy a number of conditions:

- All-electron and pseudopotentials wavefunctions agree beyond some core region R_c, as well as their eigenvalues.
- Pseudopotential's wavefunctions satisfy a norm-conserving property, meaning that their integrated charge within the radius R_c agrees with the all-electron wave function.

A consequence of the first condition is that also the logarithmic derivatives of the wavefunctions agree at R_c. The second condition implies that also the energy derivative of the logarithmic energy derivatives of the wavefunctions agrees at the cutoff radius. This further gives us a certain confidence that energy values calculated for different bonding environments will agree to the first derivative of the energy.

2.2 Molecular dynamics simulation

Classical molecular dynamics (MD) simulations evolve the system of atoms or molecules in time according to Newton's equations of motion. This means that we integrate the Newton's equations of motion at a discrete time step for each particle in the system. Forces exerted on atoms are usually calculated either fully ab initio (from density functional theory) or from some interatomic potential having a relatively simple functional form.

The most common algorithm used for the integration of Newton's equations is the velocity Verlet algorithm [91]. It updates the particle position and velocity at each time step using positions and velocities from the previous time step. Generally the algorithm follows the recipe:

1. Calculate $\vec{x}(t+\Delta t) = \vec{x}(t) + \vec{v}(t)\Delta t + \frac{1}{2}\vec{a}(t)\Delta t^2$.

2. Calculate $\vec{a}(t+\Delta t)$ from forces calculated using new particle positions ($\vec{x}(t+\Delta t)$).

3. Calculate $\vec{v}(t+\Delta t) = \vec{v}(t) + \frac{1}{2}\left(\vec{a}(t) + \vec{a}(t+\Delta t)\right)\Delta t$.

The reason why we run molecular dynamics simulations is to obtain certain thermodynamic properties of the system, which show up as emergent properties from the underlying microscopic interactions between constituent particles. Statistical mechanics gives us values of these thermodynamics properties of interest as the ensemble averages of the system. To use MD simulations as a way of obtaining these ensemble averages, we implicitly assume the ergodicity of the system. This means that in the limit of an infinitely long MD simulation, the system will visit all states accessible by it. Practically, this means that we can use the average of some quantity over time as the average over ensembles.

When we talk about thermodynamic properties, we usually assume they are measured at a constant temperature, particle number, energy, pressure etc. To model this explicitly in MD simulations, we add a certain thermostat to the system with which the particles can interact. We set up interaction of the particles with a thermostat in a way that it conserves the thermodynamic property of interest (most usually pressure or temperature) [92].

For example, when we think of structural properties of materials, we usually think of them at a constant zero pressure and a certain temperature. To get structural properties of a material in an MD simulation, we then need to use the NPT ensemble and set as a target pressure zero Pascal. As a response to that constraint, the simulation cell in MD will change to accommodate the condition that the average pressure along the trajectory is close to zero. The MD simulation cell in that case fluctuates around some mean value that we recognize as the structure of the material at that temperature.

Similarly, if we are interested in some thermodynamic properties of the system at a constant volume and temperature, we would use the NVT ensemble. Here we fix the MD simulation cell and only thermostat the temperature. The temperature is kept approximately constant by appropriately scaling the velocities of the constituent particles.

All of the above features of the molecular dynamics simulation are already available in the LAMMPS code [93]. The input information for the LAMMPS code are the initial positions of atoms, the targeted temperature and pressure, the choice of the interatomic potential, the time step length and the total simulation time. The output from the code are instantaneous values of thermodynamics properties of the system and the atomic positions and velocities.

2.3 Gaussian Approximation Potentials

During MD simulations atoms change their velocities due to the interaction with other atoms and a thermostat. The forces exerted on an atom would ideally come from DFT calculations. However, DFT is too slow to be useful as the force calculator during MD simulations. Because of that, parametrized interatomic potentials (force fields) are used instead. Here we present an overview of recently developed Gaussian Approximation Potentials that rely on machine learning techniques to model interatomic interaction.

The underlying approximation that governs the use of interatomic potentials is that the total energy of the system can be represented as the sum of individual atomic contributions [94]:

$$E_{TOT} = \sum_i \epsilon_i. \tag{2.7}$$

Here we note that the energy associated with one atom ϵ_i usually represents only the short-range interaction, while the long-range interaction is calculated on top of it. In the traditional, empirical, interatomic potentials ϵ_i usually has a closed functional form that is dependent on bond lengths and angles [95, 96]. This allows a fairly easy parametrization of those potentials and is the source of their great efficiency (compared to DFT). The fitting of empirical interatomic potentials is carried out with the goal of reproducing some macroscopic physical properties: lattice constant, phonon frequencies, thermal conductivity, etc. compared to experiments or DFT calculations. This approach, while giving a good precision of the modeled system targeted property, sometimes completely fails to reproduce results for the rest of the material properties. Our study of GeTe includes investigation of several different physical properties at two different crystallographic phases and different bonding arrangements (ferroelectric domain walls), hence the use of traditional interatomic potentials is hard to justify.

Another way of obtaining interatomic potentials that became popular fairly recently is the machine learning approach. It is characterized by the use of large datasets of atomic energies and forces (calculated from DFT) for fitting purposes and a nonparametric form of the interatomic potential [97, 98, 99, 100, 101]. This makes the interatomic potentials obtained in this way extremely accurate and transferable. In our work, we used the Gaussian Approximation Potentials (GAP) framework to fit the interatomic potential for germanium telluride [99, 100].

Gaussian Approximation Potentials use the principles of the Bayesian statistics to infer

the values of the Born-Oppenheimer energy surface given the set of already observed values. The statement of the problem is the following. Given the training set of N precomputed function values $f(x_i) = t_i$ (here we include a certain level of noise, which we assume is Gaussian), the joint posterior of the test ($\vec{f^*}$) and training ($\vec{f}$) function values can be calculated from the Bayes rule [102]:

$$P(\vec{f}\vec{f^*}|\vec{t}) = \frac{P(\vec{f}\vec{f^*})P(\vec{t}|\vec{f})}{P(\vec{t})}.$$

Here $P(\vec{f})$ is the Gaussian prior, which means that the function values are distributed according to a multivariate normal distribution with mean 0:

$$P(\vec{f}) \sim \mathcal{N}(0, \hat{K}),$$

where $\hat{K}$ is the covariance matrix whose entries are given by the covariance function $K_{ij} = Cov(x_i, x_j)$. $P(\vec{t}|\vec{f})$ is the likelihood of observing the function value t: $P(\vec{t}|\vec{f}) \sim \mathcal{N}(\vec{f}, \sigma_n^2 I)$, where σ_n^2 is the variance of noise. The desired probability distribution can be found using:

$$P(\vec{f^*}|\vec{t}) = \int P(\vec{f}\vec{f^*}|\vec{t})\mathrm{d}\vec{f}.$$

Since both the likelihood and the prior are Gaussian, the resulting probability distribution will be Gaussian. The result of the above integral is [102]:

$$P(\vec{f^*}|\vec{t}) = \mathcal{N}(K_{*,f}(K_{f,f} + \sigma_n^2)^{-1}\vec{t}, K_{*,*} - K_{*,f}(K_{f,f} + \sigma_n^2)^{-1}K_{f,*}). \tag{2.8}$$

Here $K_{*,f}$ is the submatrix of the covariance matrix between the set of training and test data points, $K_{f,f}$ is the covariance matrix between the training data and $K_{*,*}$ is the covariance of the test data [102]. Our predicted values of the function are given by the mean of the above probability distribution and the predicted errors are given with the variance.

Let us discuss what are the quantities considered above in our specific case. The function values t should be the local atomic energies (ϵ_i) [94]:

$$E_{TOT} = \sum_{i=1,N_a} \epsilon_i = \sum_{i=1,N_a} \sum_h w_h \phi_h(\vec{d_i}). \tag{2.9}$$

Here we decomposed the local energy of an atom as a sum over the set of the basis functions ϕ of the descriptor $\vec{d}$. The basis functions and the descriptor allow us to

uniquely describe the immediate environment of an atom. Assuming a Gaussian prior for the weights $\vec{w}$ we can recognize that the K is the covariance matrix of the basis functions. However, there is no unique way of partitioning the DFT total energy to specific atoms. Luckily, we do not really need to know the individual energies of atoms to use this approach. Let us imagine we want to know the local energy of the specific atom and let it be our test set. Instead of looking for covariances between individual local energies of test and training set, we study the covariance between the local energy of the test set and the total energy of the training set (for which we assume Eq. (2.9) holds). Of course, now we are troubled with an extremely large number of calculations needed to collect enough data to accurately fit the GAP model. To overcome this, we include forces in the fitting procedure as well [94].

The force on an atom is the derivative of the total energy with respect to the atomic position. The force in this approach can be included by calculating the covariance of the forces and energies [99]. This means that we calculate the local energy using the mean of the probability distribution (Eq. (2.8)), except in this case the vector $\vec{t}$ has the values of computed forces, and $K_{f,f}$ is the covariance between forces and total energies (their expansion to the functional basis as in Eq. (2.9) to be precise) in the training set (meaning f in the subscript can be force or the total energy). Here we need to know the derivative of the covariance matrix with respect to the atomic position which is obtained analytically. This methodology does not only allow us to fit an interatomic potential using DFT forces but also to obtain forces directly from the interatomic potential.

The second important part of any type of interatomic potential is the descriptor, the object used to describe the immediate environment of the atom [100, 98, 101, 103, 104] (the form of the basis functions in Eq. (2.9)). The first obvious choice for the descriptor could be the bond lengths and angles, which have been used for a large number of empirical interatomic potentials [96]. Ideally, the descriptor needs to satisfy several mathematical properties, for example invariance on the permutation of neighbours, rotation and rigid translation of the system. For example, it is obvious that an arbitrary list of bond lengths and angles does not satisfy the permutation condition, making it a poor choice of the descriptor.

Gaussian Approximation Potentials can make use of the descriptor based on the density of atomic positions in the neighborhood of the atom of interest $\rho_i(\vec{r})$ [100]. Each atom in the neighborhood is represented by a Gaussian centered at a position of the said

atom ($\vec{r}_{ij}$):

$$\rho_i(\vec{r}) = \sum_j^N \exp\left(-\frac{|\vec{r}-\vec{r}_{ij}|^2}{2\sigma_{atom}^2}\right).$$

The natural kernel for calculating the covariance of two samples[1] in this case is the Smooth Overlap of Atomic Positions (SOAP). Put simply, SOAP is the dot product between two descriptors. In this case it would calculate the overlap of the neighborhood atomic densities of the atom in the training set and the atom in the test set. In practice, the atomic density $\rho_i(\vec{r})$ (here $\vec{r} = r\vec{u}$, $\vec{u}$ is the unit vector) is expanded in the basis set of the orthonormal radial functions $g_n(r)$ and the spherical harmonics $Y_{lm}(\vec{u})$:

$$\rho_i(\vec{r}) = \sum_{nlm} c^i_{nlm} g_n(r) Y_{lm}(\vec{u}). \tag{2.10}$$

We obtain the expansion coefficients c^i_{nlm} and construct the rotationally invariant descriptor by taking their normalized power spectrum[100], $|c^i_{nlm}|^2$.

We used the QUIP code [99, 100] to fit the interatomic potential of GeTe.

2.4 Temperature dependent effective potential method

Now we briefly discuss temperature dependent effective potential method we used to calculate temperature dependent vibrational properties in Chapter 4, Chapter 5 and Chapter 7.

GeTe undergoes a structural phase transition at around 600−700 K [7, 8]. The quasi-harmonic phonon theory fails to describe vibrational properties of GeTe in the high symmetry, cubic, phase [105]. It predicts imaginary phonon frequencies for the zone center optical phonon modes, indicating a dynamical instability of the GeTe rock-salt structure at zero temperature. To overcome this difficulty, we have employed the temperature dependent effective potential (TDEP) [106, 107, 108] method to describe vibrational properties of GeTe at finite temperatures. In this subsection we will present the general features of this approach.

In general the crystal Hamiltonian can be written in the following form:

$$H = K + U,$$

[1] The sample is an element of the training or test set.

where K represents the kinetic energy of the ions and U is the potential energy. First we focus on the potential energy part of the total Hamiltonian and expand it in the Taylor series with respect to atomic displacements ($\vec{u}_i$) from equilibrium positions [108]:

$$U = U_0 + \frac{1}{2!}\sum_{i,j,\alpha,\beta}\Phi_{i,j}^{\alpha\beta}u_i^\alpha u_j^\beta + \frac{1}{3!}\sum_{i,j,k,\alpha,\beta,\gamma}\Phi_{i,j,k}^{\alpha\beta\gamma}u_i^\alpha u_j^\beta u_k^\gamma + \cdots, \tag{2.11}$$

where Greek indices label the atoms and Roman indices label the Cartesian coordinates of the atomic displacements from their minimum energy positions. If the equilibrium positions of the crystal are well defined, the first derivative of the potential energy (force acting on the atom) should be zero. The expansion coefficients $\Phi_{i_1,i_2,\ldots,i_n}$ are called the nth-order interatomic force constants:

$$\Phi_{i_1,i_2,\ldots,i_n}^{\alpha_1,\alpha_2,\ldots,\alpha_n} = \frac{\partial^n U}{\partial u_{i_1}^{\alpha_1}\partial u_{i_2}^{\alpha_2}\cdots\partial u_{i_n}^{\alpha_n}}.$$

The quasiharmonic theory truncates the above expansion in Eq. (2.11) at the second order [109], assuming that the potential energy of the crystal is perfectly harmonic. The advantage of this approach is that the Hamiltonian of this form can be diagonalized. The full Hamiltonian in the quasiharmonic approximation is:

$$H = \sum_{i,\alpha}\frac{(p_i^\alpha)^2}{2m_i} + \frac{1}{2}\sum_{i,j,\alpha,\beta}\Phi_{i,j}^{\alpha\beta}u_i^\alpha u_j^\beta,$$

where m_i and $\vec{p}_i$ are the mass and the momentum of the atom i. The force acting on the atom i ($\vec{F}_i$) can be calculated as the first derivative of the potential energy with respect to the atomic displacement:

$$F_i^\alpha = -\sum_{j,\beta}\Phi_{i,j}^{\alpha,\beta}u_j^\beta.$$

Knowing the force acting on the atom, we can write down the equation of motion:

$$m_i\frac{d^2u_i^\alpha}{dt^2} = -\sum_{j,\beta}\Phi_{i,j}^{\alpha,\beta}u_j^\beta. \tag{2.12}$$

The displacements can be represented as a sum of the plane waves [109]:

$$u_i = \frac{1}{\sqrt{m_i}}\sum_{\vec{q}}A_{\vec{q}}\epsilon_{\vec{q}}^i e^{i\vec{q}\cdot\vec{R}_i-\omega_{\vec{q}}t}.$$

Here $\vec{R}_i$ is the position of the unit cell where the atom i is situated and t is time. Substituting the above ansatz into Eq. (2.12), we obtain the frequencies at which each of these plane waves oscillate:

$$\omega^2_{\vec{q}}\vec{\epsilon}_{\vec{q}} = \Phi_{\vec{q}}\vec{\epsilon}_{\vec{q}} \tag{2.13}$$

where $\Phi_{\vec{q}}$ is Fourier transform of the second order force constant, also called the dynamical matrix:

$$\Phi_{\vec{q}} = \sum_{\vec{R}} \frac{\Phi(\vec{R})}{\sqrt{m_i m_j}} e^{i\vec{q}\cdot\vec{R}}.$$

In this notation $\vec{R}$ is the vector connecting unit cells containing atoms i, j.

In the harmonic approximation, the frequencies of the normal modes of the crystal are square roots of eigenvalues of the dynamical matrix. Nothing is preventing these eigenvalues from being negative. If the eigenvalue of the dynamical matrix is negative, that usually points to a dynamical instability of the system (the system is not in the local minimum of the total potential energy).

This is the case with the high symmetry rocksalt structure of GeTe at 0 K [105]. In this structure, the Γ point optical mode has an imaginary frequency. This mode is associated with the out-of-phase movement of Ge and Te atoms in the same unit cell along the trigonal axis and thus closely related to the polarization of the system. At temperatures higher than 600 K, anharmonic terms in Eq. (2.11) should cause the frequency of this mode to become positive, as observed in experiment [9]. This means that we have to somehow incorporate temperature effects in the above calculations to achieve the dynamical stability of the high symmetry phase of GeTe.

One way of doing this is the temperature effective potential (TDEP) method [106, 107, 108]. Experiments imply that the temperature renormalizes the local potential energy of the soft mode, making its curvature positive when averaged over the thermal ensemble of atomic configurations. The most straightforward way to account for temperature in a solid system is to run a molecular dynamics simulation where temperature can be determined as the average kinetic energy of the constituent atoms. The idea behind TDEP is to take the forces and displacements of the individual atoms during a molecular dynamics simulation and fit force constants to those forces using a least squares fitting procedure.

From our crystal Hamiltonian (see Eq. (2.11)) we can see that the force on the atom i

is given as [108]:

$$F_i^\alpha = \sum_{\beta,j} \Phi_{i,j}^{\alpha,\beta} u_j^\beta + \frac{1}{2} \sum_{\beta,\gamma,j,k} \Phi_{i,j,k}^{\alpha,\beta,\gamma} u_j^\beta u_k^\gamma. \tag{2.14}$$

Here we keep the expansion of the potential energy up to the third order everywhere, unless it is specifically mentioned differently. The molecular dynamics simulation performed at a specific temperature will give us actual forces and displacements, to which we can fit the expression in Eq. (2.14) to find the effective force constants Φ. Still the number of fitting parameters can be very large. For example, a system with two atoms per unit cell (like GeTe) and a $4\times4\times4$ supercell will have 128 atoms and thus 147456 parameters to fit just for the second order force constants. Luckily we can use some equalities for the force constants (for example the acoustic sum rule and the symmetry of the higher order derivatives), as well as the symmetries of the crystal structure. In the case of a cubic system, this would reduce the number of independent second order force constants to just 11 in the previous example [107]. The force constants in TDEP are chosen so that they minimize the mean-square error of predicted forces from Eq. (2.14) compared to explicitly calculated forces in MD.

Here we discuss the difference between TDEP and conventional force constants (and consequently the resulting vibrational properties). Harmonic frequencies are usually obtained as square roots of the eigenvalues of the dynamical matrix as defined in Eq. (2.13). Traditionally, the dynamical matrix is obtained from the force constants from the expansion of the potential energy in the Taylor series at 0 K [109]. On the other hand, TDEP harmonic frequencies or TDEP frequencies, although obtained through the same general process (see Eq. (2.13)), can not be regarded as conventional harmonic frequencies. Force constants in the TDEP method are not the derivatives of the potential of the ground state at 0 K and have a contribution of higher-order force constants in the expansion at 0 K[2]. So in principle, when we say we expand the potential energy up to the cubic order in TDEP, we effectively expand the potential energy of the traditional approach to a higher order than third. However, there is not a mapping of the TDEP method onto a truncation of the Taylor series of the potential energy U at a specific order.

Finally, we note that we have not included the LO/TO splitting in our calculations. GeTe intrinsically possesses a large number of Ge vacancies that dope the system ($\approx 10^{20}$ cm^{-3} free charge carriers). This large number of free charge carriers will com-

[2]This is similar to the approach we took in the thermal expansion study for the elastic coefficients K_{ij}.

pletely screen the long range electrostatic interactions responsible for LO/TO splitting [3]. To model this realistic situation we did not include LO/TO splitting in any of our calculations.

We use the TDEP code [106, 107, 108] to calculate phonon frequencies, group velocities and self energy (both real and imaginary part) on a given $\vec{q}$-point grid.

2.5 Boltzmann transport equation

In this section we will outline the derivation of the electronic and vibrational transport properties from the Boltzmann transport equation. As an example, we will use the system of electrons to show the derivation. Finally, we will apply the general result to phonons to obtain lattice thermal conductivity.

The Boltzmann transport equation (BTE) is a semiempirical approach which keeps track of the time evolution of the population of the electronic state $\vec{k}$ ($\vec{k}$ is the wave vector of the particular electron state and for now we are omitting the band number for simplicity) in the vicinity of some point $\vec{r}$. We assume that the time evolution of the electronic state population is influenced by a number of independent processes [110]:

$$\frac{\partial f_{\vec{k}}}{\partial t} = \frac{\partial f_{\vec{k}}}{\partial t}\Big|_{diff} + \frac{\partial f_{\vec{k}}}{\partial t}\Big|_{field} + \frac{\partial f_{\vec{k}}}{\partial t}\Big|_{scatt}. \tag{2.15}$$

Here $f_{\vec{k}}$ is the population of the electronic state $\vec{k}$ and t is the time.

The first term on the right hand side describes diffusion processes. If the velocity of that particular state is $\vec{v}_{\vec{k}}$, the population of the state at $\vec{r}$ after some small Δt is going to be the same as at the point $\vec{r} - \vec{v}_{\vec{k}}\Delta t$. From this, we get that the evolution of the electronic state population due to diffusion processes follows:

$$\frac{\partial f_{\vec{k}}}{\partial t}\Big|_{diff} = -\vec{v}_{\vec{k}} \cdot \frac{\partial f_{\vec{k}}}{\partial \vec{r}}. \tag{2.16}$$

The second term on the right hand side of the Eq. (2.15) comes from applied fields in the system. For simplicity, we will assume the existence of an electric field only. The time dependence of the electronic state population will come from the change of the momentum due to the force applied by the electric field ($\vec{E}$):

$$\frac{\partial f_{\vec{k}}}{\partial t}\Big|_{field} = -\frac{\partial \vec{k}}{\partial t}\frac{\partial f_{\vec{k}}}{\partial \vec{k}} = -\frac{e}{\hbar}\vec{E}\frac{\partial f_{\vec{k}}}{\partial \vec{k}}. \tag{2.17}$$

Here e is the elementary charge.

The final term in Eq. (2.15) comes from scattering processes. This is the most troublesome part of the equation to treat systematically. To calculate the population change in some state $\vec{k}$, we would have to sum the contributions over all other states, which will depend on their populations. It is clear that this leads to a complicated self-consistent system of equations. To get away from this, we use the linearized Boltzmann equation in the relaxation time approximation, which means we assume small changes of electron populations from the equilibrium population at that temperature:

$$\frac{\partial f_{\vec{k}}}{\partial t}\Big|_{scatt} = \frac{f_{\vec{k}} - f^0_{\vec{k}}}{\tau_k}, \tag{2.18}$$

where $f^0_{\vec{k}}$ is the equilibrium population of the state $\vec{k}$ and τ_k is the relaxation time of that state.

With the linearization of BTE, we can change populations in the terms describing diffusion and field induced changes to equilibrium populations. In Eq. (2.16) we notice that the spatial dependence of equilibrium populations can come only from the spatial dependence of temperature (if there is some thermal gradient in the system):

$$\frac{\partial f_{\vec{k}}}{\partial t}\Big|_{diff} = -\vec{v}_{\vec{k}} \cdot \frac{\partial f^0_{\vec{k}}}{\partial T} \nabla T. \tag{2.19}$$

Similarly, we notice that $\vec{k}$ dependence of the equilibrium populations can only come through the energy dependence. Employing this, we obtain:

$$\frac{\partial f_{\vec{k}}}{\partial t}\Big|_{field} = -\frac{e}{\hbar}\vec{E} \cdot \frac{\partial \epsilon_{\vec{k}}}{\partial \vec{k}} \frac{\partial f^0_{\vec{k}}}{\partial \epsilon_{\vec{k}}} = -\frac{e}{\hbar}\vec{E} \cdot \vec{v}_{\vec{k}} \frac{\partial f^0_{\vec{k}}}{\partial \epsilon_{\vec{k}}}, \tag{2.20}$$

where $\epsilon_{\vec{k}}$ is the energy of the electronic state $\vec{k}$.

Substituting these results to Eq. (2.15) and rearranging the terms, we get the expression:

$$f_{\vec{k}} = f^0_{\vec{k}} - \vec{v}_{\vec{k}} \left(\frac{\partial f^0_{\vec{k}}}{\partial T} \nabla T - e \frac{\partial f^0_{\vec{k}}}{\partial \epsilon_{\vec{k}}} \vec{E} \right) \tau_{\vec{k}}. \tag{2.21}$$

Now we will define transport coefficients. First we express the electron charge and

energy current in terms of the gradients of electric field and temperature:

$$\begin{aligned}\vec{J} &= K_{EE}\vec{E} + K_{ET}\nabla T,\\ \vec{Q} &= K_{TE}\vec{E} + K_{TT}\nabla T.\end{aligned} \tag{2.22}$$

We define the electrical conductivity tensor (σ_{ij}) as the coupling term between electron charge current and electric field at a constant temperature ($\nabla T = 0$). From this, it is easy to conclude that the electrical conductivity tensor is $\sigma = K_{EE}$.

The Seebeck coefficient (S_{ij}) is defined as the coupling term between thermal gradient and the electric field caused by it in an insulating system ($\vec{J} = 0$):

$$\vec{E} = S_{ij}\nabla T \quad \Rightarrow \quad S = -\frac{K_{ET}}{K_{EE}}. \tag{2.23}$$

For the same setup, the electrical thermal conductivity (κ_{ij}) is the coupling term between thermal current and temperature gradient. Substituting Eq. (2.23) to Eq. (2.22), we get:

$$\kappa = -\frac{Q}{\nabla T} = -\left(K_{TT} - \frac{K_{TE}\cdot K_{ET}}{K_{EE}}\right). \tag{2.24}$$

The microscopic definitions of charge and thermal current are:

$$\begin{aligned}\vec{J} &= \int e\vec{v}_{\vec{k}} f_{\vec{k}} d^3\vec{k},\\ \vec{Q} &= \int \epsilon_{\vec{k}}\vec{v}_{\vec{k}} f_{\vec{k}} d^3\vec{k}.\end{aligned} \tag{2.25}$$

Substituting Eq. (2.21) above and comparing the terms with electric field and thermal gradient, we can deduce the coefficients K in Eq. (2.22). Solving for electrical conductivity and Seebeck coefficient, we obtain the relations:

$$\begin{aligned}\sigma_{ij} &= L_0^{ij},\\ S_{ij} &= -L_1^{ij}/(eTL_0^{ij}),\end{aligned}$$

where we define the L_n^{ij} integral to be (changing from integration to sum over the

Brillouin zone):

$$L_n^{ij} = \frac{2e^2}{NV} \sum_{\vec{k}} \frac{\partial f^0_{\vec{k}}}{\partial \epsilon_{\vec{k}}} v^i_{\vec{k}} v^j_{\vec{k}} \tau_{\vec{k}} (\epsilon_{\vec{k}} - E_F)^n, \tag{2.26}$$

where E_F is the Fermi level, N is the number of k-points in the sum and V is the volume of the unit cell.

2.5.1 Boltzmann transport equation for phonons

Derivation for phonons follows the similar line as that for electrons. Phonons are charge neutral particles, hence an electric field do not exert the force on them. Following that conclusion, Eq. (2.21) has the form:

$$n_{\vec{q}s} = n^0_{\vec{q}s} - \vec{v}_{\vec{q}s} \frac{\partial n^0_{\vec{q}s}}{\partial T} \nabla T \tau_{\vec{q}s}. \tag{2.27}$$

Here we used $n_{\vec{q}s}$ to denote the population of the $(\vec{q}s)$ phonon mode, while $\vec{v}_{\vec{q}s}$ and $\tau_{\vec{q}s}$ are the phonon group velocity and phonon lifetime.

The phonon heat current $\vec{Q}$ has the following expression:

$$\vec{Q} = \frac{1}{NV} \sum_{\vec{q}s} \hbar \omega_{\vec{q}s} \vec{v}_{\vec{q}s} n_{\vec{q}s}. \tag{2.28}$$

Here N is the number of $\vec{q}$ points in the sum, V is the volume of the unit cell, $\hbar$ is the Planck's constant and $\omega_{\vec{q}s}$ is the phonon frequency. Comparing Eq. (2.22) with the above expression, we obtain the expression for the lattice thermal conductivity in the Boltzmann transport equation framework:

$$\kappa^{ij} = \frac{1}{NV} \sum_{\vec{q}s} \hbar \omega_{\vec{q}s} \frac{\partial n^0_{\vec{q}s}}{\partial T} v^i_{\vec{q}s} v^j_{\vec{q}s} \tau_{\vec{q}s}. \tag{2.29}$$

2.6 Thermal conductivity from the Green-Kubo formalism

In this section, we will derive the expression for the lattice thermal conductivity which should be a better approximation for a true lattice thermal conductivity at the phase

transition compared to the traditional Boltzmann transport theory approach. These results have been shown in Refs. [111, 112] with a different definition of the heat current for the diagonal part of the lattice thermal conductivity. The one phonon Green functions were calculated in Refs. [113, 114] using equation of motion techniques. We combined these two results to obtain the final expression for the lattice thermal conductivity.

We start from an expression of thermal conductivity given in the Green-Kubo theory of linear response [115]:

$$\kappa^{\alpha\beta} = \frac{NV}{k_B T^2} \int_0^\infty \langle J^\alpha(0) J^\beta(t) \rangle \mathrm{d}t, \tag{2.30}$$

where N is the number of unit cells in the system and V is the volume of the primitive unit cell, k_B is the Boltzmann constant, T is the temperature and $J^\alpha(t)$ is the heat current in the Cartesian direction α at time t. To use the above equation, we have to have a microscopic definition of heat current. We will use the one given by Hardy, obtained through the energy conservation law [116]:

$$J^\alpha(t) = \frac{1}{2NV} \sum_{\vec{q},s,s'} \hbar \omega_{\vec{q}s} v^\alpha_{\vec{q}ss'} A_{\vec{q}s}(t) B_{-\vec{q}s'}(t).$$

Here the $\hbar$ is the reduced Planck constant, $\omega_{\vec{q}s}$ is the frequency of the phonon mode with the wave vector $\vec{q}$ and branch s. $v^\alpha_{\vec{q}ss'}$ is the generalization of the phonon group velocity [116] (terms with $s = s'$ is what we call the phonon group velocities):

$$v^\alpha_{\vec{q}ss'} = \frac{i}{2\sqrt{\omega_{\vec{q}s}\omega_{\vec{q}s'}}} \sum_{\gamma,\beta} \epsilon^\alpha_{\vec{q}s} \left(\sum_l \frac{1}{\sqrt{m_{l+j} m_j}} \Phi^{\gamma,\beta}_{l+j,j} R^\alpha_l \exp(i\vec{q}\cdot\vec{R}_l) \right) \epsilon^\beta_{\vec{q}s'}.$$

The operators $A_{\vec{q}s}$ and $B_{\vec{q}s}$ are the scaled phonon displacement and momentum operators defined as (in the second quantization representation)[113]:

$$A_{\vec{q}s} = a_{\vec{q}s} + a^\dagger_{-\vec{q}s}, \qquad B_{\vec{q}s} = a_{\vec{q}s} - a^\dagger_{-\vec{q}s},$$

where $a_{\vec{q}s}$ and $a^\dagger_{\vec{q}s}$ are the phonon annihilation and creation operators.

Substituting the expression for heat current into Eq. (2.30), we obtain:

$$\kappa^{\alpha\beta} = \frac{\hbar^2}{4NVk_B T^2} \sum_{\vec{q},s,s'} \sum_{\vec{q}',s'',s'''} \int_0^\infty \omega_{\vec{q}s}\omega_{\vec{q}'s''} v^\alpha_{\vec{q}ss'} v^\beta_{\vec{q}'s''s'''} \times$$
$$\langle A_{\vec{q}s}(0) B_{-\vec{q}s'}(0) A_{\vec{q}'s''}(t) B_{-\vec{q}'s'''}(t) \rangle \mathrm{d}t. \tag{2.31}$$

The expectation value of the product of four operators can be decoupled using Wick's theorem [109, 112, 111]:

$$\langle A_{\vec{q}s}(0)B_{-\vec{q}s'}(0)A_{\vec{q}'s''}(t)B_{-\vec{q}'s'''}(t)\rangle = \langle A_{\vec{q}s}(0)B_{-\vec{q}s'}(0)\rangle\langle A_{\vec{q}'s''}(t)B_{-\vec{q}'s'''}(t)\rangle +$$
$$\langle A_{\vec{q}s}(0)A_{\vec{q}'s''}(t)\rangle\langle B_{-\vec{q}s'}(0)B_{-\vec{q}'s'''}(t)\rangle + \langle A_{\vec{q}s}(0)B_{-\vec{q}'s'''}(t)\rangle\langle B_{-\vec{q}s'}(0)A_{\vec{q}'s''}(t)\rangle.$$

We find the Fourier transform of the above correlation functions [117]:

$$\langle X(t')Y(t)\rangle = \int_{-\infty}^{\infty} J_{XY}(\Omega)e^{-i\hbar\Omega(t-t')}\mathrm{d}\Omega,$$
$$\langle Y(t)X(t')\rangle = \int_{-\infty}^{\infty} J_{XY}(\Omega)e^{\frac{\hbar\Omega}{k_BT}}e^{-i\hbar\Omega(t-t')}\mathrm{d}\Omega.$$

Substituting the transforms into Eq. (2.31), we obtain:

$$\kappa^{\alpha\beta} = \frac{\hbar^2\pi}{4NVk_BT^2}\sum_{\vec{q},s,s'}\sum_{\vec{q}',s'',s'''}\int_{-\infty}^{\infty}\omega_{\vec{q}s}\omega_{\vec{q}'s''}v^{\alpha}_{\vec{q}ss'}v^{\beta}_{\vec{q}'s''s'''}(J_{AA}J_{BB}+J_{AB}^2)e^{\frac{\hbar\Omega}{k_BT}}\mathrm{d}\Omega. \quad (2.32)$$

Here we noted the Fourier transforms of the correlation functions as:

$$J_{AA} = \frac{1}{2\pi}\int_{-\infty}^{\infty}\langle A^{\dagger}_{-\vec{q}s}(0)A_{\vec{q}'s''}(t)\rangle e^{i\hbar\Omega t}\mathrm{d}t,$$
$$J_{BB} = \frac{1}{2\pi}\int_{-\infty}^{\infty}\langle B^{\dagger}_{\vec{q}'s'''}(0)B_{-\vec{q}s'}(t)\rangle e^{i\hbar\Omega t}\mathrm{d}t,$$
$$J_{AB} = \frac{1}{2\pi}\int_{-\infty}^{\infty}\langle A^{\dagger}_{-\vec{q}s}(0)B_{-\vec{q}'s'''}(t)\rangle e^{i\hbar\Omega t}\mathrm{d}t.$$

The explicit dependence on Ω will be omitted in the rest of the section. We find these correlation functions through the spectral representation of appropriate retarded Green's functions [117, 118]. For example:

$$J_{AA} = -\frac{2}{e^{\frac{\hbar\Omega}{k_BT}}-1}\mathrm{Im}G_{AA}(\Omega \pm i\epsilon).$$

Here Im stands for the imaginary part. The retarded Green's function is defined as [117]:

$$G_{AA}(t) = -i\theta(t)\langle[A_{\vec{q}s}(0), A^{\dagger}_{\vec{q}'s'}(t)]\rangle, \quad (2.33)$$

where $\theta(t)$ is the Heaviside function and [...] stands for the commutator in the case of boson operators. We will obtain these Green's functions through the equation of

motion method. We will use the equation of motion in the Heisenberg picture:

$$i\frac{\mathrm{d}}{\mathrm{d}t}A(t) = [A, H],$$

where H is the Hamiltonian of the system. Our crystal Hamiltonian written in terms of the normal mode coordinates obtained in the harmonic approximation has the form [113]:

$$H = \sum_{\lambda} \hbar\omega_{\lambda}(a_{\lambda}^{\dagger}a_{\lambda} + \frac{1}{2}) + \sum_{\lambda_1,\lambda_2,\lambda_3} \Phi_{\lambda_1,\lambda_2,\lambda_3} A_{\lambda_1} A_{\lambda_2} A_{\lambda_3}.$$

Here $\Phi_{\lambda_1,\lambda_2,\lambda_3}$ is the Fourier transform of the third order force constants. We switched to shortened notation $\lambda = (\vec{q}, s)$ and ($\bar{\lambda} = (-\vec{q}, s)$). The equation of motion for Green's function is as follows:

$$i\frac{\mathrm{d}}{\mathrm{d}t}G_{AA}(t) = \delta(t)\langle[A_{\vec{q}s}, A^{\dagger}_{\vec{q}'s'}]\rangle - i\theta(t)\langle\Big[[A_{\vec{q}s}, H], A^{\dagger}_{\vec{q}'s'}\Big]\rangle.$$

Operators at different times do not have a general expression for their commutator. However, the first term in the equation above contains the Dirac delta function, so we can evaluate the commutator (which is 0). The second term has the commutator between the displacement operator and the Hamiltonian, which in general will give rise to higher Green's functions[3]. Calculating this commutator, we get a new Green's function:

$$\begin{aligned} i\frac{\mathrm{d}}{\mathrm{d}t}G_{AA}(t) &= \omega_{\vec{q}s}G_{BA}(t), \\ G_{BA}(t) &= -i\theta(t)\langle[B_{\vec{q}s}, A^{\dagger}_{\vec{q}'s'}]\rangle. \end{aligned} \tag{2.34}$$

This Green's function is of the same order as the first one. However, if we write the equation of motion for this Green's function, we will get higher Green's functions (because the operator $B_{\vec{q},s}$ does not commute with the anharmonic part of the Hamiltonian) [113]:

$$\begin{aligned} i\frac{\mathrm{d}}{\mathrm{d}t}G_{BA}(t) = \delta(t)\langle[B_{\vec{q}s}, A^{\dagger}_{\vec{q}'s'}]\rangle + \omega_{\vec{q}s}G_{AA}(t) + \\ 6\sum_{\lambda_1,\lambda_2} \Phi_{-\vec{q}s,\lambda_1,\lambda_2}G_{AAA}. \end{aligned}$$

[3] We will be using terms higher Green's functions and higher order Green's functions interchangeably. It just means that in our definition of the Green's function, Eq. (2.33), we have more than one operator on the left side of the commutator.

This third order Green's function is defined as:

$$G_{AAA}(t) = -i\theta(t)\langle[A_{\lambda_1}A_{\lambda_2}, A_{\vec{q}'s'}]\rangle.$$

It is clear at this point that we will get an infinite chain of higher and higher Green's functions if we continue with this method. Therefore, we have to find an appropriate scheme to terminate this infinite expansion. The best way to do this is to express higher Green's functions in terms of lower Green's functions. This method is equivalent to summing only the leading diagrams in the perturbative approach of Green's functions [119]. The lowest order Green's function that we can decouple is the one containing four phonon operators. To obtain it, we calculate the equation of motion of the third-order Green's function:

$$\begin{aligned}
i\frac{\mathrm{d}}{\mathrm{d}t}G_{AAA}(t) &= \omega_{\lambda_1}G_{BAA}(t) + \omega_{\lambda_2}G_{ABA}(t),\\
i\frac{\mathrm{d}}{\mathrm{d}t}G_{BAA}(t) &= \omega_{\lambda_2}G_{BBA}(t) + \omega_{\lambda_1}G_{AAA}(t) - 6\sum_{\lambda_3\lambda_4}\Phi_{\bar{\lambda}_1,\lambda_3,\lambda_4}i\theta(t)\langle[A_{\lambda_3}A_{\lambda_4}A_{\lambda_2}, A^{\dagger}_{\vec{q}'s'}]\rangle,\\
i\frac{\mathrm{d}}{\mathrm{d}t}G_{ABA}(t) &= \omega_{\lambda_2}G_{AAA}(t) + \omega_{\lambda_1}G_{BBA}(t) - 6\sum_{\lambda_3\lambda_4}\Phi_{\bar{\lambda}_2,\lambda_3,\lambda_4}i\theta(t)\langle[A_{\lambda_3}A_{\lambda_4}A_{\lambda_1}, A^{\dagger}_{\vec{q}'s'}]\rangle,\\
i\frac{\mathrm{d}}{\mathrm{d}t}G_{BBA}(t) &= \omega_{\lambda_2}G_{BAA}(t) + \omega_{\lambda_1}G_{ABA}(t).
\end{aligned}$$

We will do the Fourier transform of these Green's functions, so we get, instead of differential, regular algebraic equations. We can see that in the absence of the fourth order Green's function, these four third order Green's function form a closed system of equations. From this closed system of equations, we obtain the solution for $G_{AAA}(\Omega)$:

$$\begin{aligned}
G_{AAA} = &\frac{1}{2}(V_{12}(\Omega) + V_{21}(\Omega))\frac{\omega_{\lambda_1} + \omega_{\lambda_2}}{\Omega^2 - (\omega_{\lambda_1} + \omega_{\lambda_2})^2}\\
&-\frac{1}{2}(V_{12}(\Omega) - V_{21}(\Omega))\frac{\omega_{\lambda_1} - \omega_{\lambda_2}}{\Omega^2 - (\omega_{\lambda_1} - \omega_{\lambda_2})^2}.
\end{aligned}$$

Here we used a shorthand notation:

$$V_{12} = 6\sum_{\lambda_3,\lambda_4}\Phi_{\bar{\lambda}_1,\lambda_3,\lambda_4}\Pi_{\lambda_3\lambda_4\lambda_2\vec{q}'s'},$$

where $\Pi_{\lambda_3\lambda_4\lambda_2\vec{q}'s'}$ are higher Green's function in equations above [114]:

$$\Pi_{\lambda_3\lambda_4\lambda_2\vec{q}'s'} \equiv G_{AAAA} = -i\theta(t)\left\langle[A_{\lambda_3}(t)A_{\lambda_4}(t)A_{\lambda_2}(t), A^{\dagger}_{\vec{q}'s'}]\right\rangle.$$

We decouple the higher Green function as following to obtain ($G_\lambda \equiv G_{AA}$)[113]:

$$\Pi_{\lambda_3\lambda_4\lambda_2\vec{q}'s'}(t) = -i\theta(t)\left\langle [A_{\lambda_3}(t)A_{\lambda_4}(t)A_{\lambda_2}(t), A^\dagger_{\vec{q}'s'}]\right\rangle \approx$$
$$-i\theta(t)\left(\left\langle [A_{\lambda_3}(t), A^\dagger_{\vec{q}'s'}]A_{\lambda_4}A_{\lambda_2}\right\rangle + \left\langle A_{\lambda_3}[A_{\lambda_4}(t), A^\dagger_{\vec{q}'s'}]A_{\lambda_2}\right\rangle + \left\langle A_{\lambda_3}A_{\lambda_4}[A_{\lambda_2}(t), A^\dagger_{\vec{q}'s'}]\right\rangle\right)$$
$$\approx N_2\left(G_{\lambda_3}(t) + G_{\lambda_4}(t)\right).$$

Here $N_2 = 2n_{\lambda_2} + 1$ (n_{λ_2} is the number of phonons) is the harmonic approximation to the correlation function G_{AA}. Substituting the result above in Eq. (2.34) and after some (not necessarily trivial) algebra, we obtain [114]:

$$G_{AA}(\Omega) = \frac{\omega_{\vec{q}s}\delta_{\vec{q},\vec{q}'}\delta_{s,s'}}{\pi}\frac{1}{\Omega^2 - \omega^2_{\vec{q}s} - 2\omega_{\vec{q}s}\Sigma_{\vec{q}s}(\Omega)}. \tag{2.35}$$

$\Sigma_{\vec{q}s}(\Omega + i\epsilon) = \Delta_{\vec{q}s}(\Omega) - i\Gamma_{\vec{q}s}(\Omega)$ is the self-energy of phonon with the wave vector $\vec{q}$ and branch s [120, 121, 113, 122]:

$$\Gamma_\lambda(\Omega) = \frac{\hbar\pi}{16}\sum_{\lambda_1,\lambda_2}|\Phi_{\lambda,\lambda_1,\lambda_2}|^2\{(n_{\lambda_1} + n_{\lambda_2} + 1)\delta(\Omega - \omega_{\lambda_1} - \omega_{\lambda_2}) +$$
$$(n_{\lambda_1} - n_{\lambda_2})(\delta(\Omega - \omega_{\lambda_1} + \omega_{\lambda_2}) + \delta(\Omega + \omega_{\lambda_1} - \omega_{\lambda_2}))\}. \tag{2.36}$$

The real part of the self-energy can be then obtained as the Kramers-Kronig transformation of the imaginary part [113]:

$$\Delta_\lambda(\Omega) = \frac{\hbar\pi}{16}\mathcal{P}\sum_{\lambda_1,\lambda_2}|\Phi_{\lambda,\lambda_1,\lambda_2}|^2\{(n_{\lambda_1} + n_{\lambda_2} + 1)\frac{\omega_{\lambda_1} + \omega_{\lambda_2}}{\Omega^2 - (\omega_{\lambda_1} + \omega_{\lambda_2})^2} +$$
$$(n_{\lambda_2} - n_{\lambda_1})\frac{\omega_{\lambda_1} - \omega_{\lambda_2}}{\Omega^2 - (\omega_{\lambda_1} - \omega_{\lambda_2})^2}\}. \tag{2.37}$$

Knowing this Green's function, we can calculate the correlation function [117]:

$$J_{AA} = \frac{4\omega^2_{\vec{q}s}}{((e^{\frac{\hbar\Omega}{k_BT}} - 1)\pi}\frac{\Gamma_{\vec{q}s}(\Omega)}{(\Omega^2 - 2\omega_{\vec{q}s}\Delta_{\vec{q}s}(\Omega) - \omega^2_{\vec{q}s})^2 + 4\omega^2_{\vec{q}s}\Gamma^2_{\vec{q}s}(\Omega)}.$$

The other correlation functions in Eq. (2.32) are straightforwardly obtained if we re-

member $i\mathrm{d}/\mathrm{d}tA_{\vec{q}s}(t) = \omega_{\vec{q}s}B_{\vec{q}s}$. We can show [113]:

$$J_{BB} = \frac{\Omega^2}{\omega^2_{\vec{q}s}} J_{AA},$$
$$J_{AB} = \frac{\Omega}{\omega_{\vec{q}s}} J_{AA}. \tag{2.38}$$

Substituting these correlation functions in Eq. (2.32) and observing the Kronecker symbols, we finally obtain:

$$\kappa^{\alpha\beta} = \frac{4\hbar^2}{\pi NVk_BT^2} \sum_{\vec{q},s,s'} \int_{-\infty}^{\infty} \omega^2_{\vec{q}s}(\omega^2_{\vec{q}s'} + \omega^2_{\vec{q}s}) v^{\alpha}_{\vec{q}ss'} v^{\beta}_{\vec{q}s's} \frac{\Omega^2 e^{\frac{\hbar\Omega}{k_BT}}}{(e^{\frac{\hbar\Omega}{k_BT}} - 1)^2} \times$$
$$\frac{\Gamma_{\vec{q}s}(\Omega)}{\epsilon^2_{\vec{q}s}(\Omega) + 4\omega^2_{\vec{q}s}\Gamma^2_{\vec{q}s}(\Omega)} \frac{\Gamma_{\vec{q}s'}(\Omega)}{\epsilon^2_{\vec{q}s'}(\Omega) + 4\omega^2_{\vec{q}s'}\Gamma^2_{\vec{q}s'}(\Omega)} \mathrm{d}\Omega. \tag{2.39}$$

Here we used the following shorthand notation: $\epsilon_{\vec{q}s}(\Omega) = \Omega^2 - 2\omega_{\vec{q}s'}\Delta_{\vec{q}s'}(\Omega) - \omega^2_{\vec{q}s'}$.

Now we will show that, in the limit of small anharmonicity, Eq. (2.39) for the diagonal terms ($s = s'$) is identical to the solution of the Boltzmann transport equation in the relaxation time approximation. We set $\Delta_{\vec{q}s} = 0$ and assume $\Gamma_{\vec{q}s} \ll \omega_{\vec{q}s}$ and constant with Ω. First we recognize the Lorentzian in one of the spectral functions:

$$\frac{1}{4\omega_{\vec{q}s}\pi} \frac{\Gamma_{\vec{q}s}}{(\frac{\Omega^2 - \omega^2_{\vec{q}s}}{2\omega_{\vec{q}s}})^2 + \Gamma^2_{\vec{q}s}}.$$

If $\Gamma_{\vec{q}s} \ll \omega_{\vec{q}s}$, this Lorentzian peaks around $\Omega = \omega_{\vec{q}s}$ and thus acts as the Dirac delta function, since only that term will have a major influence in the integral. We substitute $\omega_{\vec{q}s}$ instead of Ω and obtain:

$$\kappa^{\alpha\beta} = \frac{1}{NV} \sum_{\vec{q},s} v^{\alpha}_{\vec{q}s} v^{\beta}_{\vec{q}s} c(\omega_{\vec{q}s}) \frac{1}{2\Gamma_{\vec{q}s}}. \tag{2.40}$$

Here $c(\omega_{\vec{q}s})$ is the heat capacity of the phonon mode $(\vec{q}s)$ and we recognize the phonon relaxation time $\tau_{\vec{q}s} = \frac{1}{2\Gamma_{\vec{q}s}}$. We used notation $v^{\alpha}_{\vec{q}s}$ for $v^{\alpha}_{\vec{q}ss}$ to emphasize the similarity with the conventional solution of the BTE in relaxation time approximation, see Eq. (2.29).

In the low anharmonicity case, the off-diagonal terms in thermal conductivity equation are zero, since when one Lorentzian function peaks the other one is zero. If anharmonicity is not low, then there is no way of analytically dealing with the above integral

(to yield any meaningful result) and we have to evaluate it directly. However, we can notice that the value of the integral will be different from zero only in the case when there is substantial overlap between the power spectra of two phonon branches. This is to be expected in high anharmonicity materials, but even more in alloys or amorphous materials. In the second case, the large broadening of the phonon power spectra is due to disorder and this method gives us an elegant way of dealing with it without resorting to molecular dynamics simulations.

Chapter 3

Negative thermal expansion of GeTe close to the phase transition

3.1 Introduction

3.1.1 General comments

Most materials expand upon heating, while those that shrink are much less common. Recent interest in these materials with negative thermal expansion (NTE) is also driven by technological applications that require materials with zero thermal expansion across a desired temperature range [123, 124, 125]. Even though NTE is an unusual phenomenon, it is relatively common for materials near structural phase transitions and is typically associated with soft phonons and strong anharmonicity [123, 124, 125].

To understand the origin of thermal expansion in materials, we consider the example of the solid with the Lenard-Jones type bonding. The Lenard-Jones potential is one of the simplest models of chemical bonding that captures a lot of essential physics and is the perfect toy model to explain why bodies expand while heated up. This potential has the following functional form (for simplicity we disregard the energy and spatial constants):

$$V(x) = -\frac{4}{x^6} + \frac{4}{x^{12}}.$$

It is simple to calculate that this potential has a minimum at $x_0 = 2^{1/6}$. At zero temperature this system has no thermal energy so the lattice constant (the distance between atoms and the measure of the size of the system) is equal to this value. If we slightly

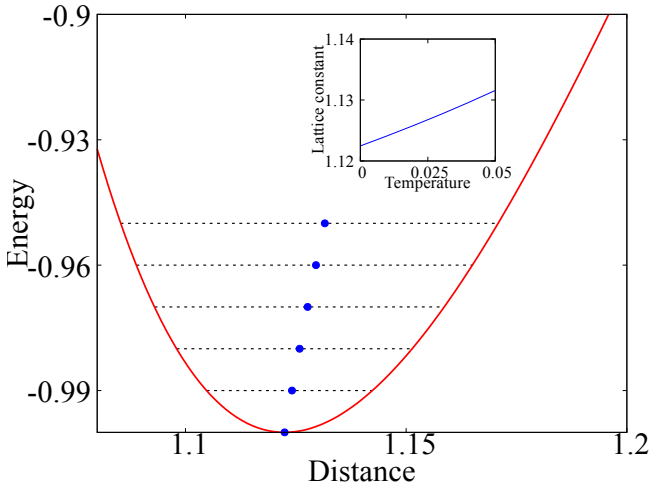

Figure 3.1: Thermal expansion in Lennard-Jones potential. Equipotential points are shown as dashed lines and the average of them is the blue point. The temperature dependence of the bond length is shown in the inset.

increase the temperature, let us say $T = 0.01/k_B$ in these units, the atoms gain thermal energy and will be able to oscillate around the potential well with the depth of 0.01 as shown in Fig. 3.1. This means that the average position of the atom is shifted slightly to the larger values as shown in Fig. 3.1 by a blue point corresponding to the energy of 0.99. If the temperature is doubled, this shift of the lattice constant or the average atomic position is even larger. This model, although extremely simple, gives us a clear picture of why thermal expansion happens in solids.

Imagine for a moment that the interaction between nuclei is described by a harmonic potential rather than that of Lenard-Jones. In this case, the atomic oscillations would be perfectly symmetrical around the original equilibrium position x_0 and the average position would not change as we increase the temperature. So we conclude that the primary reason for thermal expansion is the anharmonicity of the atomic interactions.

Anharmonicity is very important in real materials and it leads to a number of different phenomena besides thermal expansion, most notably finite thermal conductivity. There is a certain ambiguity regarding the term anharmonicity, which sometimes creates confusion among physicists. Usually, anharmonicity means that something can not be described by a harmonic interaction. The Lenard-Jones potential is anharmonic since it can not be expanded or replaced by only a harmonic potential. A different type of anharmonicity which is usually discussed in terms of phonon transport is the interaction between different phonon modes. This type of anharmonicity does have an origin in the non-harmonicity of the atom-atom interaction, but it is hard to map it back to the simple picture explained above. In the rest of this chapter, we will use the term

anharmonicity to describe a non-harmonic shape of the atom-atom interaction and will refrain from commenting on the interaction between different phonon modes unless it is specifically mentioned.

The Grüneisen theory [126, 127, 128, 129, 130, 131] is the standard approach of calculating thermal expansion from first principles, using density functional theory. In this method, anharmonicity of the crystal potential is described via mode Grüneisen parameters (GP's) $\gamma_{\vec{q}s}$, which represent the changes of phonon frequencies with volume [126, 127, 128, 129, 130, 131]:

$$\gamma_{\vec{q}s} = -\frac{V}{\omega_{\vec{q}s}} \frac{\partial \omega_{\vec{q}s}}{\partial V}.$$

Negative GP's of certain phonon modes are commonly identified as the source of NTE [132, 133, 134, 134, 131]. Phonon frequencies and mode GP's are usually calculated using the harmonic approximation. First principles methods that describe phonon frequency renormalization due to anharmonicity have been recently developed, such as the self consistent harmonic approximation (SCHA) [135] and temperature dependent effective potentials (TDEP) [136]. These and related approaches were recently used to describe the negative thermal expansion of ScF_3 [137] and Si [138]. In principle, these methods are capable of modeling the thermal expansion of materials near phase transitions. However, to the best of our knowledge, no previous work has investigated this possibility.

In this section, we present a first principles method to compute the thermal expansion of the rhombohedral phase of GeTe up to the Curie temperature. We calculate the structural parameters by minimizing the total free energy with respect to each structural parameter in the spirit of the Grüneisen theory. We explicitly include the internal atomic position as an independent variable in the minimization process. Although this effect was included to some extent in previous calculations of thermal expansion [126, 128, 129, 130, 131] by relaxing atomic positions due to applied strain, this may not be sufficient for materials near phase transitions. Our approach enables us to determine the temperature dependence of the static elastic energy variations with structural parameters, which we find is the key to correctly describing the thermal expansion of GeTe near the phase transition. We show that our calculated thermal evolution of the structural parameters of GeTe agrees well with experiments. Negative volumetric thermal expansion of GeTe near the phase transition is also well described in our model. We find that the coupling between acoustic and soft TO modes is the dominant mechanism leading not only to the low lattice thermal conductivity of GeTe, as shown

previously [55], but also to its NTE.

3.1.2 Quasiharmonic theory of thermal expansion close to the ferroelectric phase transition

We start with an overview of the zero temperature structure of GeTe (see Fig. 3.2). GeTe crystallizes in rhombohedral structure [7, 8, 139], which can be visualized as a slightly elongated rocksalt structure along one of the body diagonals of the rocksalt cube. This elongation is followed by an offset of the Te sublattice along the same direction, making GeTe ferroelectric. The structure of rhombohedral GeTe is defined by a set of lattice vectors:

$$\begin{aligned} \vec{r}_1 &= a(b, 0, c), \\ \vec{r}_2 &= a(-\frac{b}{2}, \frac{b\sqrt{3}}{2}, c), \\ \vec{r}_3 &= a(-\frac{b}{2}, -\frac{b\sqrt{3}}{2}, c). \end{aligned} \tag{3.1}$$

Here a is the lattice constant and b and c are defined as:

$$\begin{aligned} b &= \sqrt{\frac{2}{3}(1-\cos\theta)}, \\ c &= \sqrt{\frac{1}{3}(1+2\cos\theta)}, \end{aligned} \tag{3.2}$$

where θ is the angle between the rhombohedral lattice vectors. The atomic positions in this structure are taken to be (0,0,0) for the Ge atom and (τ, τ, τ) for the Te atom. At the phase transition (which happens around 700 K) the rhombohedral angle becomes 60° and τ becomes 0.5, giving the rocksalt structure. The lattice constant, rhombohedral angle, and interatomic displacement τ are the structural parameters referred to in the following section. We would also like to note that in this system τ is the primary order parameter and the direct measure of the ferroelectric polarization.

To obtain a microscopic theory of thermal expansion, we start from the premise that a structure at certain temperature minimizes the total free energy. We define the total free energy F of the system as follows [109]:

$$F = F_{el} + F_{vib} = E_{el} + F_{vib}.$$

In the equation above we disregarded the entropy part of the electron free energy (the

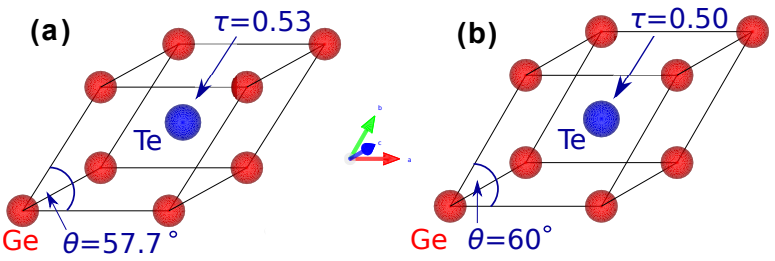

Figure 3.2: Primitive unit cell of GeTe at (a) 0 K and (b) above the Curie temperature, generated using VESTA software [2]. The low-temperature rhombohedral structure becomes more similar to the rocksalt structure as temperature increases: the angle between the primitive lattice vectors θ becomes closer to 60° and the Te internal atomic position τ approaches 0.5.

system remains semiconducting in the entire temperature range of interest). E_{el} is the total energy of the electron-ion system, treating the electrons quantum mechanically with fixed atomic positions specified by the lattice parameters - this is usually called the elastic energy and we will refer to it as such in what follows. F_{vib} is the free energy of atomic vibrations. To find the values of the structural parameters that minimize the total free energy, we take the first derivative of F with respect to each one of them ($u = a, \theta, \tau$):

$$\frac{\partial F}{\partial u} = \frac{\partial E_{el}}{\partial u} + \frac{\partial F_{vib}}{\partial u} = 0. \tag{3.3}$$

Within the harmonic approximation, the vibrational free energy is given as [109]:

$$F_{vib} = \sum_{\vec{q},s} \left\{ \frac{\hbar\omega_{\vec{q},s}}{2} + k_B T \ln\left[1 - \exp\left(\frac{\hbar\omega_{\vec{q},s}}{k_B T}\right)\right] \right\}, \tag{3.4}$$

where $\omega_{\vec{q},s}$ is the phonon frequency of the mode s and wave vector $\vec{q}$, k_B is the Boltzmann constant and T is the temperature. The derivative of the vibrational free energy with respect to one of the structural parameters u reads:

$$\frac{\partial F_{vib}}{\partial u} = -\frac{1}{u} \sum_{\vec{q},s} \hbar\omega_{\vec{q},s} \left(n(\omega_{\vec{q},s}) + \frac{1}{2} \right) \gamma^u_{\vec{q},s}, \tag{3.5}$$

where $n(\omega_{\vec{q},s})$ is the Bose-Einstein occupation factor at temperature T for a phonon with frequency $\omega_{\vec{q},s}$. We define the generalized Grüneisen parameters with respect to each structural parameter as:

$$\gamma^u_{\vec{q},s} = -\frac{u}{\omega_{\vec{q},s}} \frac{\partial \omega_{\vec{q},s}}{\partial u}. \tag{3.6}$$

Here we use a slightly different definition of the generalized Grüneisen parameter com-

pared to most of the previous work [126, 127, 128, 129, 130, 140]. The calculation of the derivative in Eq. (3.6) is done using the finite difference method. When we make a displacement of the structural parameter for the calculation of the Grüneisen parameter, we do not relax the atomic positions, or more specifically we do not relax the internal atomic displacement τ. We track the change of the phonon frequencies with τ directly, by accounting for it as one of the structural parameters. This is the first improvement we made compared to the previous works on the thermal expansion of solids, which allows us to track the temperature evolution of the order parameter τ. A similar approach has been implemented using density functional perturbation theory for calculating thermal evolution of the surfaces of Be and Mg [141, 142]. It might be possible to generalize this approach for any type of phase transition, by substituting τ with the order parameter of the given system. However, the implementation of the above equations might be more difficult and not immediately straightforward.

Now we will tackle the second part of the total free energy, the static elastic energy. To properly describe this part we will expand it to the Taylor series:

$$E_{el} = E_0 + \sum_u K_u \Delta u + \sum_{u,v} K_{uv} \Delta u \Delta v. \tag{3.7}$$

Δu and Δv represent small deviations of the structural parameters u and v from their equilibrium values for temperature T ($u, v \in \{a, \theta, \tau\}$, $u \geq v$). We define the first and second order coefficients as the changes of E_{el} with respect to the changes of structural parameters: $K_u = \frac{\partial E_{el}}{\partial u}$ and $K_{uv} = (1 - \frac{1}{2}\delta_{uv})\frac{\partial^2 E_{el}}{\partial u \partial v}$ (δ_{uv} is the Kronecker delta).

The second order coefficients $\hat{K}$ resemble elastic constants and indeed we can trace the relationship between the two. To do this, we change the lattice vectors by changing one of the structural parameters $u + \Delta u$ (here we are only taking into account θ and a since changing τ does not change the lattice vectors) and track the change of the projection of the lattice vectors onto one of the Cartesian axes. For example, the projection of the lattice vectors onto the z axis is the parameter c (see Eq. (3.2)) and its change while changing θ is:

$$\begin{aligned} c + \Delta c &= \sqrt{\frac{1}{3}(1 + 2\cos(\theta + \Delta\theta))} = \sqrt{\frac{1}{3}(1 + 2\cos\theta\cos\Delta\theta - 2\sin\theta\sin\Delta\theta)} \\ &= \sqrt{\frac{1}{3}(1 + 2\cos\theta - 2\sin\theta\Delta\theta)}. \end{aligned}$$

Here we used the limits $\Delta\theta \to 0$: $\sin\Delta\theta = \Delta\theta$ and $\cos\Delta\theta = 1$. Dividing both sides of

the above equation with c, we obtain:

$$\frac{\Delta z}{z} = \frac{\Delta c}{c} = \frac{\sin\theta}{1+2\cos\theta}\Delta\theta = Q_2\Delta\theta. \tag{3.8}$$

From the equation above it is obvious that the coefficient Q_2 represents the dilatation of the hexagonal structure parameter (the lattice constant parallel to the [111] axis) for the unit dilatation of angle. A similar reasoning follows for the axes x and y for the change in θ which gives us the coefficient Q_1:

$$\frac{\Delta x,y}{x,y} = \frac{\Delta b}{b} = \frac{\sin\theta}{2(1-\cos\theta)}\Delta\theta = Q_1\Delta\theta. \tag{3.9}$$

For the case of change in the lattice constant a, the derivation is similar. The final relations between elastic constants and our second order coefficients are:

$$\begin{aligned} K_{aa} =& C_{11}+C_{12}+2C_{13}+C_{33}/2, \\ K_{\theta\theta} =& Q_1^2(C_{11}+C_{12})-2Q_1Q_2C_{13}+Q_2^2C_{33}/2, \\ K_{a\theta} =& 2Q_1(C_{11}+C_{12})+2(Q_1-Q_2)C_{13}-Q_2C_{33}. \end{aligned} \tag{3.10}$$

Here C_{ij} are the elements of the clamped ion elastic matrix in the Voigt notation [143].

The second order coefficients $\hat{K}$ with respect to τ and a and/or θ tell us about the coupling of strain and the atomic positions within the unit cell. In this regard, they resemble the elements of the force-response internal strain tensor. Alternatively, we can say that they are measures of strain-order parameter coupling as defined in the Ginzburg-Landau-Devonshire theory.

$K_{\tau,\tau}$ measures the energy curvature with respect to the soft mode coordinate and hence determines the phonon frequency of the soft mode:

$$\omega_{TO}^2 = \frac{2K_{\tau,\tau}}{\mu a_{\|}^2}, \tag{3.11}$$

where μ is reduced mass of the unit cell and $a_{\|}$ is the length of the unit cell in the [111] direction.

Now we can take the first derivative of the static elastic energy with respect to the structural parameters:

$$\frac{\partial E_{el}}{\partial u} = K_u + \sum_v (1+\delta_{vu})K_{vu}\Delta v. \tag{3.12}$$

To properly track the temperature dependence of the structural parameters we should take the elastic coefficients in Eq. (3.12) at different temperatures. If we disregard the impact of electron-phonon coupling to the electronic band structure, we can associate the temperature dependence of the derivatives with the change in structure only. If we label the changes of the structural parameters at temperature T with respect to their values at zero temperature as:

$$\begin{aligned}\delta a &= a - a_0,\\ \delta\theta &= \theta - \theta_0,\\ \delta\tau &= \tau - \tau_0,\end{aligned} \tag{3.13}$$

we can expand static elastic energy as:

$$\begin{aligned}E_{el} = &\sum_{u,v} K^0_{uv}(\Delta u + \delta u)(\Delta v + \delta v) + \sum_{u,v,w} K^0_{uvw}(\Delta u + \delta u)(\Delta v + \delta v)(\Delta w + \delta w) + \\ &\sum_{u,v,w,t} K^0_{uvwt}(\Delta u + \delta u)(\Delta v + \delta v)(\Delta w + \delta w)(\Delta t + \delta t).\end{aligned} \tag{3.14}$$

K^0_{uv}, K^0_{uvw} and K^0_{uvwt} are the second, third and fourth order coefficients defined for the changes of structural parameters calculated at 0 K, and $\delta u \in \{\delta a, \delta\theta, \delta\tau\}$ ($u \geq v \geq w \geq t$). From Eqs. (3.12) and (3.14), we obtain the coefficients K_u and K_{uv} that depend on the changes δu from the 0 K values, e.g.:

$$\begin{aligned}K_a =& 2K^0_{aa}\delta a + K^0_{a\tau}\delta\tau + K^0_{a\theta}\delta\theta + 3K^0_{aaa}\delta a^2 + 2(K^0_{aa\tau}\delta\tau + K^0_{aa\theta}\delta\theta)\delta a + \\ & K^0_{a\tau\tau}\delta\tau^2 + K^0_{a\theta\theta}\delta\theta^2 + K^0_{a\theta\tau}\delta\theta\delta\tau + \text{terms with 4th order } K^0,\\ K_{aa} =& K^0_{aa} + 3K^0_{aaa}\delta a + K^0_{aa\theta}\delta\theta + K^0_{aa\tau}\delta\tau + 6K^0_{aaaa}\delta a^2 + \\ & 3(K^0_{aaa\theta}\delta\theta + K^0_{aaa\tau}\delta\tau)\delta a + K^0_{aa\theta\theta}\delta\theta^2 + K^0_{aa\tau\tau}\delta\tau^2 + K^0_{aa\theta\tau}\delta\theta\delta\tau.\end{aligned} \tag{3.15}$$

Taking into account the temperature dependence of the elastic coefficients $K_u v$ is the second improvement to the standard Grüneisen theory of thermal expansion introduced in this work. This, together with explicitly tracking the temperature dependence of internal atomic position, is important for the accurate description of thermal expansion near the phase transition, as we will show. Substituting Eqs. (3.5) and (3.12) into Eq. (3.3), we obtain:

$$\Delta u = \sum_v S_{vu}\left[\sum_{\vec{q},s}\hbar\omega_{\vec{q},s}\left(n(\omega_{\vec{q},s}) + \frac{1}{2}\right)\frac{\gamma^v_{\vec{q},s}}{v} - K_v\right]. \tag{3.16}$$

S_{vu} are the elements of the matrix defined as an inverse of the matrix of coefficients $\hat{K}$:

$$\hat{K} = \begin{bmatrix} 2K_{aa} & K_{a\theta} & K_{a\tau} \\ K_{a\theta} & 2K_{\theta\theta} & K_{\theta\tau} \\ K_{a\tau} & K_{\theta\tau} & 2K_{\tau\tau} \end{bmatrix}. \tag{3.17}$$

One should keep in mind that in Eq. (3.16) Δu does not represent the difference from the 0 K structure as in the standard approach, but the difference from the equilibrium values of the structural parameter at certain temperature. Considering that the right hand side of the same equation depends on δu implicitly through S_{uv} and K_u, we need to implement an iterative approach to solve this equation. At each iteration we make a change as $\delta u_i = \delta u_{i-1} + \Delta u_i(\delta a_{i-1}, \delta\theta_{i-1}, \delta\tau_{i-1})$ and iterate until $\Delta u_i \approx 0$ given by Eq. (3.16).

We note that this method to calculate thermal expansion is inexpensive and straightforward to implement. Its implementation requires: (i) the density functional theory (DFT) calculations of the phonon frequencies and generalized Grüneisen parameters for the 0 K values of the structural parameters, (ii) the calculation of the DFT energy surface for a range of structural parameter values, whose fitting gives coefficients K^0 Eq. (3.16), and (iii) the iterative solution for δa, $\delta\theta$ and $\delta\tau$ (i.e. where Δa, $\Delta\theta$ and $\Delta\tau$ in Eq. (3.16) are all zero) for a range of temperatures.

3.1.3 Computational details

DFT calculations were performed using the plane wave basis set, the generalized gradient approximation with Perdew-Burke-Ernzerhof [86] parametrization (GGA-PBE) for the exchange-correlation potential and the Hartwigsen-Goedecker-Hutter (HGH) pseudopotentials [144] as implemented in the ABINIT code [87]. For the ground state and static elastic energy calculations, we used a 32 Hartree energy cutoff for plane waves and a four shifted $12\times12\times12$ $\vec{k}$-point grid for Brillouin zone sampling of electronic states. Harmonic interatomic force constants at zero temperature were calculated from Hellmann-Feynman forces obtained by the finite difference supercell approach using the PHONOPY code [145]. Forces were computed using 128-atom supercells ($4\times4\times4$ rhombohedral unit cells) with a 24 Hartree cutoff and a four shifted $3\times3\times3$ $\vec{k}$-point grid. Phonon frequencies were calculated using a $20\times20\times20$ $\vec{q}$-point grid for vibrational modes. We obtained generalized Grüneisen parameters using a finite difference method, taking the finite displacement to be smaller than 1% for a, and smaller than 1% of the difference between the 0 K rhombohedral and high temperature rocksalt struc-

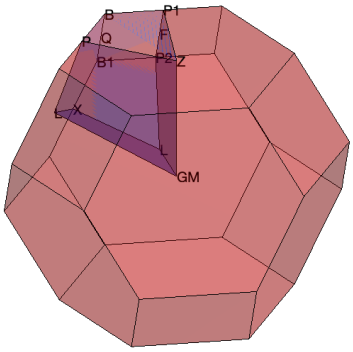

Figure 3.3: The first Brillouin zone of GeTe with notation of high symmetry points.

tures for θ and τ. For the calculation of coefficients K^0 in Eq. (3.14), we parametrized the energy surface on uniform grids for the values of structural parameters a, θ and τ from the 0 K rhombohedral structure to the high temperature rocksalt structure.

3.2 Results

We calculated the structural parameters of GeTe at 0 K using DFT and two different exchange-correlation functionals, the local density approximation (LDA) [144] and GGA-PBE, see Table 3.1. To our knowledge, the measured values of the structural parameters at zero temperature are not available. Nevertheless, it is likely that, as the temperature is reduced from 295 K to 0 K, the angle and the internal atomic position would deviate further from the high-symmetry (rocksalt) values, and would agree better with the GGA-PBE calculation than with the LDA. Since our goal is to describe the temperature dependence of structural parameters near the phase transition, where the internal atomic position plays a crucial role, we use the GGA-PBE functional in all further calculations. Our values of structural parameters are also in good agreement with previous DFT calculations [146, 5].

Table 3.1: Lattice parameters of GeTe at 0 K, calculated using the LDA and GGA-PBE functionals, and compared with experimental results [7]. a stands for the lattice constant, θ for the angle, τ for the internal atomic coordinate, and V_0 is the volume of the primitive unit cell.

	a [Å]	θ [deg]	τ	V_0 [Å^3]
LDA	4.207	58.788	0.524	51.193
GGA-PBE	4.381	57.776	0.530	56.420
Experiment (295 K)	4.299	57.931	0.525	53.513

Table 3.2: Calculated elastic constants of GeTe using density functional perturbation theory (DFPT), and density functional theory (DFT) combined with a finite difference method. $C_{11}+C_{12}$, C_{13} and C_{33} were calculated directly using DFPT and expressed in GPa, and transformed into K_{aa}, $K_{a\theta}$ and $K_{\theta\theta}$ using Eq. (3.10). K_{aa}, $K_{a\theta}$ and $K_{\theta\theta}$ were computed using DFT and expressed in eV, and transformed into $C_{11}+C_{12}$, C_{13} and C_{33} by inverting Eq. (3.10).

	$C_{11}+C_{12}$	C_{13}	C_{33}	K_{aa}	$K_{a\theta}$	$K_{\theta\theta}$
DFPT	114.756	29.962	63.899	72.764	74.514	27.243
Finite diff. DFT	116.555	29.942	60.543	72.789	76.133	27.667

We computed the elastic constant matrix $\hat{C}$ using density functional perturbation theory (DFPT) in the ABINIT code, and transformed them into K_{aa}, $K_{a\theta}$ and $K_{\theta\theta}$ using Eq. (3.10). We also calculated K_{aa}, $K_{a\theta}$ and $K_{\theta\theta}$ using DFT and a finite difference method, and converted them into $\hat{C}$ by inverting Eq. (3.10). All elastic constants and the coefficients $\hat{K}$ obtained from DFPT and the finite difference method are in very good agreement, see Table 3.2. To the best of our knowledge, there are no reported experimental values for the elastic constants of GeTe. If we use the Voigt average for calculating the bulk modulus as:

$$9B = 2(C_{11}+C_{12})+4C_{13}+C_{33} = 2K_{aa}, \tag{3.18}$$

we obtain the value of $B = 45.92$ GPa at 0 K, which is in a good agreement with the experimental value of 49.9 GPa at 300 K [147].

The phonon dispersion of GeTe at 0 K is given in Fig. 3.4(a) (the notation for high-symmetry points is in Fig. 3.3), together with the experimental results for the frequencies of the Raman active zone center modes [3, 4]. Large intrinsic concentrations of charge carriers in real GeTe samples (1- 20×10^{20} cm^{-1}[148]) completely screen long range interactions [3]. We roughly estimate this effect by setting the Born effective charges to zero in the calculation of phonon frequencies (see dashed red lines in Fig. 3.4(a)). To evaluate the importance of screening, we also neglect this effect in the phonon calculation by using the Born effective charge values obtained using density functional perturbation theory (DFPT) (solid black lines in Fig. 3.4(a)). Using both approaches, our calculated phonon frequencies at the zone center agree very well with experimental results [3, 4]. Fig. 3.4(b) illustrates that our computed phonon densities of states (DOS) of GeTe at 0 K compare fairly well with experiments [5, 6]. Since there are no appreciable differences in the calculated phonon DOS if we exclude or roughly include screening effects, we neglect screening in all further calculations [1].

[1] We verified explicitly that our treatment of screening produces a very small effect on the values of structural parameters with respect to the unscreened case. We expect that a more sophisticated treatment

Our phonon dispersions of GeTe also agree well with a previous DFPT calculation [146].

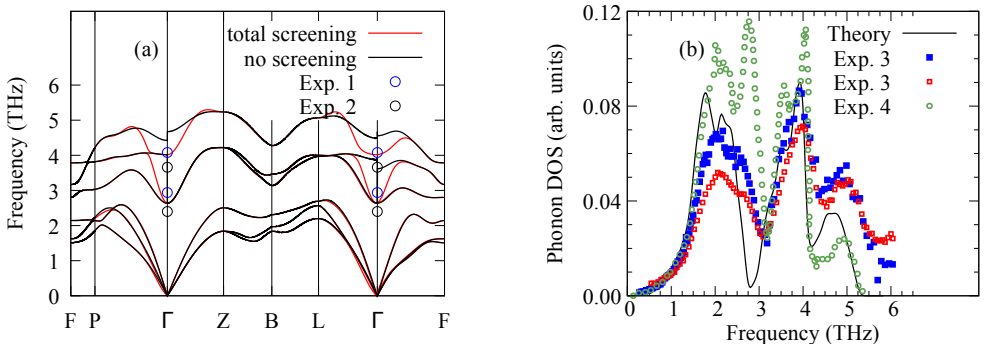

Figure 3.4: (a) Phonon dispersion of GeTe calculated using the GGA-PBE exchange-correlation functional neglecting and accounting for carrier screening (solid black lines and red lines, respectively). The frequencies of the zone centre Raman active modes were taken from the measurements of Ref. [3] (blue circles) and Ref. [4] (black circles). (b) Phonon density of states of GeTe calculated excluding screening (solid black line) and measured by Ref. [5] (blue filled squares and red empty squares) and Ref. [6] (green circles).

The temperature dependence of all structural parameters of rhombohedral GeTe (the lattice constant, angle and internal atomic coordinate τ) are illustrated in Fig. 3.5. Solid lines represent our calculations, while symbols show the measurements of Refs. [7, 8]. The experimental values were transformed from the pseudocubic to the rhombohedral unit cell for comparison with our results. The computed temperature variation of structural parameters is in good agreement with experiments, despite the small discrepancy between the GGA-PBE and the room temperature experimental structural parameters (see Table 3.1). Dashed lines in Fig. 3.5 represent our calculations shifted by the difference between our values and the experimental values of Ref. [7] at 300 K.

We can also explicitly track the softening of the TO mode in the quasiharmonic approximation close to the ferroelectric phase transition through changes in $K_{\tau\tau}$ (see Eq. (3.11)). The temperature dependence of the coefficient $K_{\tau\tau}$ (through the dependence on the structural parameters) is given by:

$$\begin{aligned} K_{\tau\tau} = {} & K^0_{\tau\tau} + 3K^0_{\tau\tau\tau}\delta\tau + K^0_{\tau\tau\theta}\delta\theta + K^0_{\tau\tau a}\delta a \\ & + 6K^0_{\tau\tau\tau\tau}\delta\tau^2 + 3(K^0_{\tau\tau\tau\theta}\delta\theta + K^0_{\tau\tau\tau a}\delta a)\delta\tau \\ & + K^0_{\tau\tau\theta\theta}\delta\theta^2 + K^0_{\tau\tau aa}\delta a^2 + K^0_{\tau\tau\theta a}\delta\theta\delta a. \end{aligned} \tag{3.19}$$

Here we omit the coupling of the soft TO mode with the phonon bath throughout the Brillouin zone and actually track its coupling only to the long wavelength modes (strain

of screening will change these values more substantially, as observed experimentally in GeTe samples with different carrier concentrations [149, 150].

and itself). We find that this level of approximation is sufficient to get the qualitative behavior of the phonon frequency close to the ferroelectric phase transition, as shown in Fig. 3.5 (d). Both the experiment [3] and our calculation show the softening of the TO mode with a similar power law dependency. We highlight that all these agreements are obtained fully from first principles, without any empirical parameters.

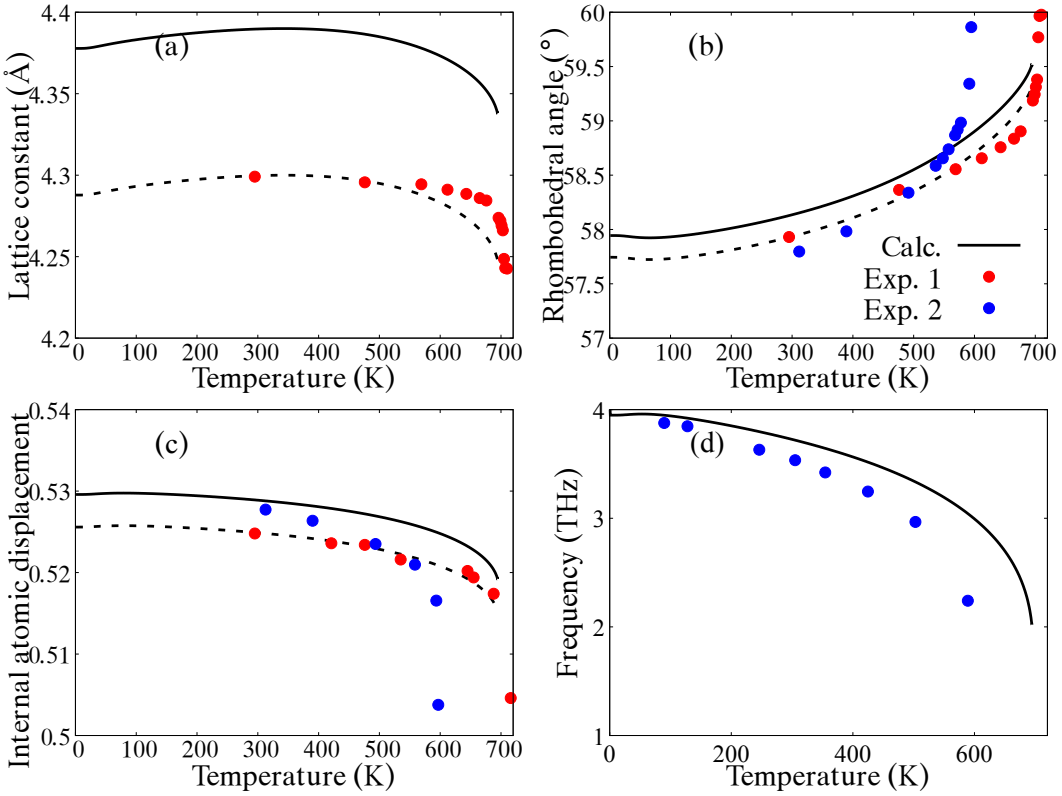

Figure 3.5: Structural parameters of GeTe as a function of temperature: (a) the lattice constant a, (b) the angle θ, and (c) the internal atomic coordinate τ. Solid black lines represent our calculations. Red and blue circles correspond to the measurements of Refs. [7] and [8], respectively. Dashed black lines represent our calculations shifted by the difference between our calculated values and the experimental values of Ref. [7] at 300 K. (d) TO mode frequency versus temperature: our calculation (solid black line) and experiment [3] (blue circles).

Our calculated structural parameters and the zone center transverse optical phonon frequency of rhombohedral GeTe show clear indications of the ferroelectric phase transition near 700 K, see Fig. 3.5. As temperature increases, the angle θ and the internal atomic coordinate τ tend to their high symmetry values, 60° and 0.5, respectively. Moreover, the temperature dependence of all structural parameters diverges from a linear behavior at high temperatures (500-700 K), which signals the proximity to the phase transition.

The thermal evolution of the structural parameters of GeTe is correctly captured only when the total free energy is minimized with respect to all structural parameters, and

the temperature dependence of coefficients K_u and K_{uv} defined in Eq. (3.12) is taken into account. Figure 3.6 shows the comparison between the calculations obtained using our approach and the standard approach [126, 127], where the free energy is not minimized with respect to the internal atomic coordinate τ and elastic constants do not vary with temperature. Even though the internal atomic position is relaxed as strain is applied in the standard method, this approach gives qualitatively very different trends compared to our model and experiments [7, 8]. These results highlight the importance of improving the standard method, to include the critical physical effects occurring near the phase transition, as shown here.

To further justify the importance of including the explicit dependence of the phonon frequency and elastic properties on the order parameter, rather than accounting for it through the relaxation of the structure with strain, we perform the following analysis. Mode Grüneisen parameters in the standard approach are computed as:

$$\frac{d\omega_{\vec{q}s}}{d\epsilon_{de}} = \frac{\partial\omega_{\vec{q},s}}{\partial\epsilon_{de}} + \frac{\partial\omega_{\vec{q},s}}{\partial\tau}\frac{\partial\tau}{\partial\epsilon_{de}} \tag{3.20}$$

where ϵ_{de} is a component of the strain tensor [126, 127]. We consider a simplified expression for the total free energy of a rhombohedral system:

$$F_{tot} = K_{\tau\tau}\tau^2 + K_{a\tau}a\tau + K_{\theta\tau}\theta\tau. \tag{3.21}$$

To find the value of τ at thermal equilibrium, we minimize this function with respect to τ:

$$\frac{\partial F_{tot}}{\partial\tau} = 2K_{\tau\tau}\tau + K_{a\tau}a + K_{\theta\tau}\theta = 0, \tag{3.22}$$

$$\tau = -\frac{K_{a\tau}a + K_{\theta\tau}\theta}{2K_{\tau\tau}}. \tag{3.23}$$

We estimate the terms that correspond to the term $\partial\tau/\partial\epsilon_{de}$ in Eq. (3.20) by replacing ϵ_{de} with a (or θ):

$$\frac{\partial\tau}{\partial a} = -\frac{K_{a\tau}}{2K_{\tau\tau}}. \tag{3.24}$$

The coefficient $K_{\tau\tau}$ corresponds to the zone center soft TO mode, and becomes zero at the phase transition. Our calculations show that $K_{a\tau}$ is finite at the phase transition. Consequently, the factor $\partial\tau/\partial a$ diverges at the phase transition. Our method captures the temperature dependence of the elastic coefficients K_{uv}, $u, v \in \{a, \theta, \tau\}$, and thus the temperature dependence of the terms $\partial\tau/\partial a$ and $\partial\tau/\partial\theta$. In contrast, the standard

method gives the corresponding terms only at 0 K. Both methods ignore the temperature dependence of the terms $\partial\omega_{\vec{q},s}/\partial\epsilon_{de}$ and $\partial\omega_{\vec{q},s}/\partial\tau$ in Eq. (3.20). We stress that the temperature dependence of elastic coefficients is critical for the description of the NTE of GeTe near the phase transition. This can be obtained straightforwardly by explicitly accounting for τ in the free energy minimization, as done in our method.

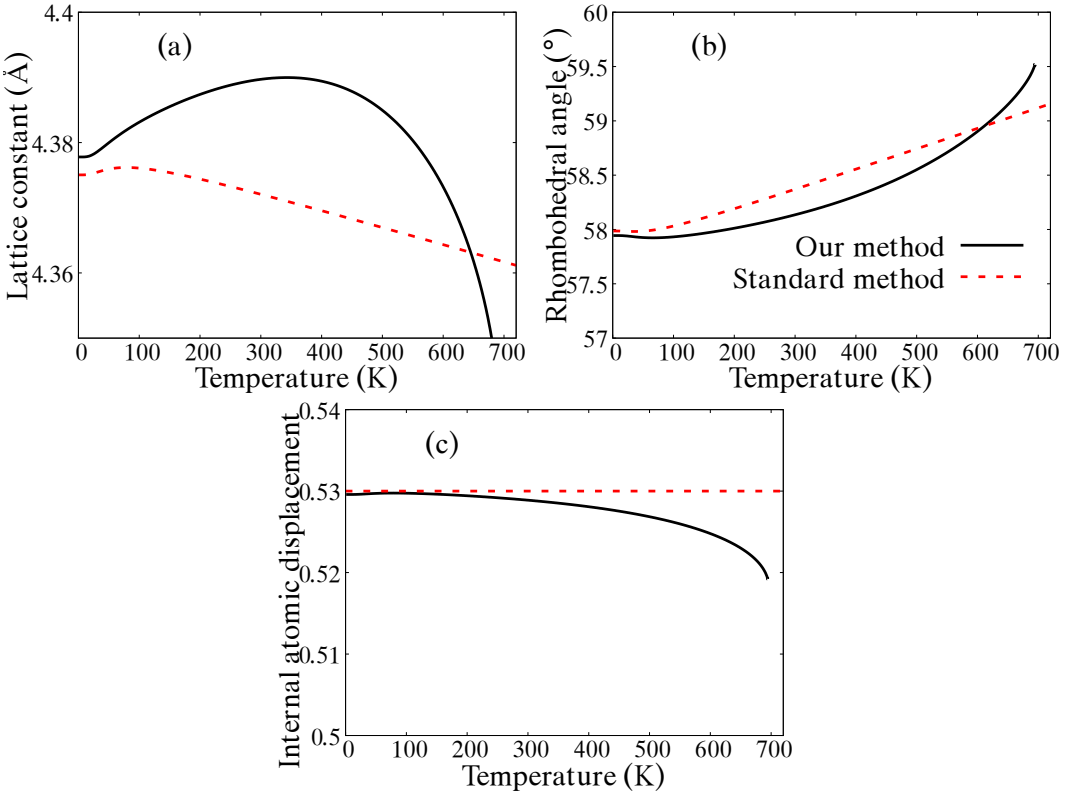

Figure 3.6: Structural parameters of GeTe as a function of temperature: (a) lattice constant, (b) angle, and (c) internal atomic coordinate. Solid black lines represent the results obtained using our approach, while dashed red lines correspond to the standard method (see text for full explanation).

In our calculations, GeTe exhibits negative volumetric thermal expansion near the phase transition at ~ 700 K, which has been also observed experimentally [7, 8, 150, 149] and reproduced in our calculations, see Fig. 3.7(a). In contrast, the standard approach gives a positive volume expansion of GeTe in the whole temperature range considered. The volumetric contraction close to the phase transition is due to the NTE of the lattice constant shown in Fig. 3.5(a). We note that the sign of the volumetric thermal expansion depends strongly on the exact composition of samples, as does the Curie temperature. Positive volumetric thermal expansion occurs in samples with more than 50.6% Te, as measured in Refs. [149, 150]. Samples with less than 50.6% of Te exhibit NTE at the phase transition [149, 150], which is in agreement with our calculation for stoichiometric GeTe (50% Te).

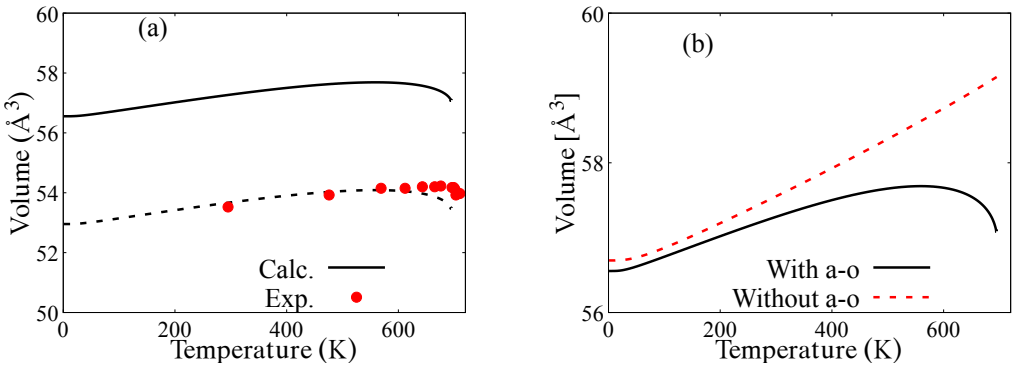

Figure 3.7: (a) Volumetric thermal expansion of GeTe: our calculation (solid black line), experiment [7] (red circles), and our calculation shifted by the difference between our and the experimental value at 300 K (dashed black line). (b) Computed volumetric thermal expansion including and neglecting acoustic-soft optical mode coupling, shown in solid black and dashed red lines, respectively.

To understand the reason behind the negative thermal expansion at the phase transition in GeTe, we will analyze separately all of the physical properties influencing thermal expansion as determined by Eq. (3.16). The second order elastic coefficients entering the equation can be cast as the standard elastic constants by inverting Eq. (3.10). In our calculations, the values of all elastic constants have a steep change at the phase transition, which is in agreement with experimental observations in $Sn_xGe_{1-x}Te$ [151] and $Pb_xGe_{1-x}Te$ [152]. Figure 3.8 shows how $C_{11}+C_{12}$, C_{13} and C_{33} vary with temperature. $C_{11}+C_{12}$ increases rapidly at the phase transition, as observed in [152, 151]. Experimental values of C_{13} and C_{33} were not reported, but our calculations correctly capture their expected behaviour. In the high symmetry rocksalt phase, $C_{33} = C_{11}$ and $C_{12} = C_{13}$. In the low symmetry rhombohedral phase, C_{33} has lower value than C_{11} (Table 3.2), so we would expect that C_{33} will increase towards the phase transition to become equal to C_{11}. On the other hand, C_{13} is larger than C_{12}, and it will decrease towards the phase transition to become equal to C_{12}. Both of these trends are observed in our results.

Although elastic constants show considerable change at the phase transition, the magnitude of these changes is not large. We found that only $K_{a\tau}$, $K_{\theta\tau}$ and $K_{\tau\tau}$ change substantially near the phase transition. $K_{a\tau}$ and $K_{\theta\tau}$ reflect static elastic energy variations with respect to simultaneous changes of the structural parameters related to acoustic strain (a and θ) and the TO mode (τ). Consequently, $K_{a\tau}$ and $K_{\theta\tau}$ quantify coupling between the acoustic and transverse optic (TO) vibrational modes, and indicate its large variation close to the phase transition.

The acoustic-soft TO mode coupling that increases considerably near the phase transition causes the negative thermal expansion of GeTe. In our computational method,

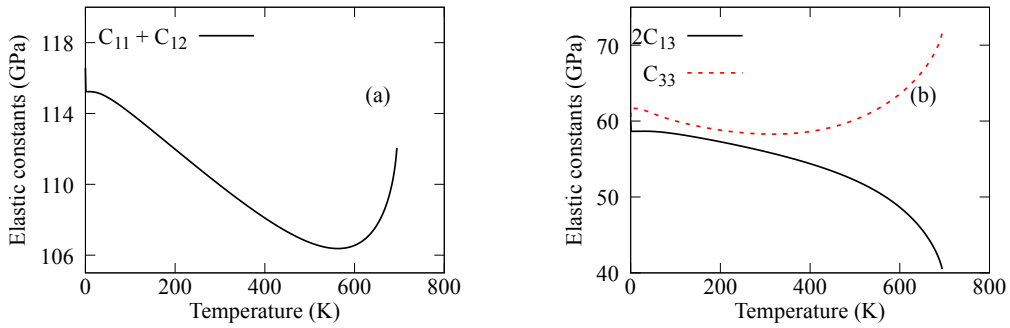

Figure 3.8: Elastic constants of GeTe as functions of temperature: (a) $C_{11}+C_{12}$, (b) C_{13} (solid black line) and C_{33} (dashed red line).

we can artificially turn off this coupling by setting $K_{a\tau}$ and $K_{\theta\tau}$ to zero, as shown in Fig. 3.7(b). The volume calculated by neglecting acoustic-TO coupling does not exhibit a negative thermal expansion. We thus conclude that strong acoustic-TO phonon coupling is the origin of the NTE of GeTe at the phase transition.

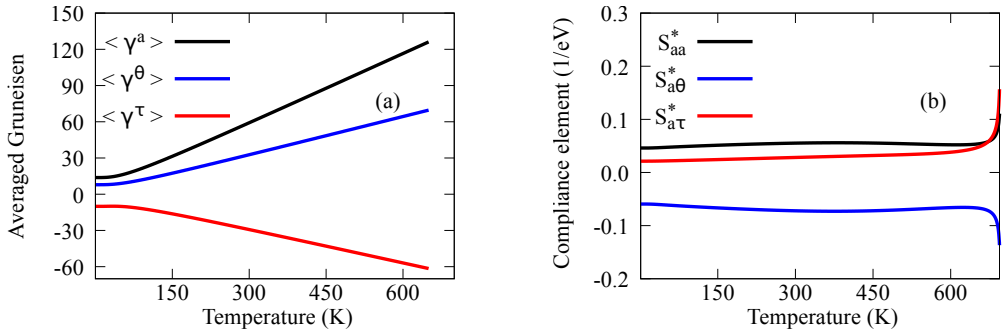

Figure 3.9: Temperature dependence of: (a) average generalized Grüneisen parameters defined for each structural parameter (a - lattice constant, θ - angle, τ - internal atomic coordinate), and (b) normalized compliance matrix elements (see text for full explanation).

The most commonly cited cause of negative thermal expansion in the literature is a negative mode Grüneisen parameter [132, 133, 134, 153]. Here we investigate the role of generalized Grüneisen parameters in establishing the NTE of GeTe. We define the average generalized Grüneisen parameters for $u \in \{a, \theta, \tau\}$ as:

$$\langle \gamma^u \rangle = \frac{1}{\hbar\omega_D} \sum_{\vec{q},s} \hbar\omega_{\vec{q},s} \left(n(\omega_{\vec{q},s}) + \frac{1}{2} \right) \gamma^u_{\vec{q},s}, \tag{3.25}$$

where ω_D is the Debye frequency [2]. The temperature dependence of $\langle \gamma^u \rangle$ is shown

[2] We calculated the Debye frequency of GeTe by fitting the analytical expression for the specific heat capacity obtained using the Debye model to that calculated using the phonon dispersion computed using density functional theory. Our calculated value of the Debye frequency is 3.8 THz.

in Fig. 3.9(a). Figure 3.9(b) illustrates the compliance elements that determine the value of the lattice constant in Eq. (3.16), normalized as $S^*_{aa} = S_{aa}/a^2$, $S^*_{a\tau} = S_{a\theta}/a\theta$, and $S^*_{a\tau} = S_{a\tau}/a\tau$. The linear temperature dependence of the average generalized Grüneisen parameters stems from the Bose-Einstein occupation factor. In contrast, the compliance elements change dramatically with temperature near the phase transition, due to large temperature variations of $K_{a\tau}$, $K_{\theta\tau}$ and $K_{\tau\tau}$. Since the lattice constant expansion is proportional to $S_{aa}\langle\gamma^a\rangle + S_{a\theta}\left\langle\gamma^\theta\right\rangle + S_{a\tau}\langle\gamma^\tau\rangle$ (Eq. (3.16)), its negative sign is partially due to negative $\langle\gamma^\tau\rangle$, which physically corresponds to the anharmonicity of the TO mode. Nevertheless, negative $\langle\gamma^\tau\rangle$ is not the main reason for NTE: it has to be accompanied by a large change of $S_{a\tau}$ i.e. large acoustic-TO coupling so that the expansion becomes negative. Furthermore, $S_{a\theta}$ is also negative and its absolute value increases more rapidly at the phase transition, resulting in an additional negative contribution to thermal expansion. This analysis confirms the important role of acoustic-TO coupling in establishing the NTE of GeTe near the phase transition. We expect that this conclusion will remain valid even when the temperature dependence of phonon frequencies and generalized Grüneisen parameters $\gamma^u_{\vec{q},s}$ is accounted for. This would make the temperature changes of $\langle\gamma^\tau\rangle$ near the phase transition somewhat larger than those calculated here, due to the temperature variations of the frequencies of soft TO modes close to the zone center.

There is an ongoing debate in the literature about the true nature of the phase transition in GeTe (displacive vs order-disorder). Our method directly applies only to the displacive phase transition. The experimental support for the displacive transition in GeTe was reported in Ref. [7, 8, 154]. This is challenged by recent works of Fons *et al.* [4] and Matsunaga *et al.* [155], whose findings support the order-disorder picture. Our calculations show that the thermal expansion near the phase transition in GeTe can be well described with a purely displacive model. However, further investigation of order-disorder effects is needed for the complete description of the phase transition of GeTe.

3.3 Conclusion

In conclusion, we developed a first principles method that accurately describes the temperature dependence of all structural parameters for the rhombohedral phase of GeTe up to the Curie temperature of ~ 700 K. The key new features of our approach with respect to the standard method based on the Grüneisen theory are the minimization of free energy with respect to all structural parameters, including internal atomic dis-

placement, and the temperature dependence of static elastic coefficients. Our computed thermal expansion is in very good qualitative agreement with experiment. We showed that the coupling between acoustic and soft transverse optical modes is the main reason for the negative volumetric thermal expansion of GeTe near the phase transition.

Chapter 4

Phonon spectral functions of GeTe close to the ferroelectric phase transition

4.1 Introduction

We commented on the differences between harmonic and TDEP phonon frequencies in Chapter 2. In this section we would like to expand on that discussion.

First we would like to elucidate the physical meaning of TDEP frequencies and how they correspond to the physical observables. Experiments can not directly measure phonon frequencies. What experiments actually measure (for example neutron scattering) are the scattering cross sections. In neutron scattering, the lowest contribution to the scattering cross section is the displacement autocorrelation function [121] (we expect a similar expression for Raman scattering, the difficulty being whether the polarizability operator is linearly dependent on the displacement operator [156]). We can directly calculate this quantity (subject to some approximations) using second and third order force constants. In the experiment one recognizes a peak of the signal (the scattering cross section for the incident neutron) in the energy space as the phonon frequency. We do the exact same thing when we determine the anharmonic frequency. We calculate the displacement autocorrelation function, find at which frequency it peaks and assign that frequency as the anharmonic frequency.

In perfectly harmonic materials (which do not exist), the peak of the displacement autocorrelation function (DAF), and hence the peak of the measured cross section, will

be at the value of harmonic frequency. In weakly anharmonic materials, the peak of DAF will slightly shift from the harmonic frequency, approximately by the value of the real part of the self energy at the harmonic frequency. In TDEP method, the harmonic frequency is automatically renormalized to the TDEP frequency, and although this TDEP frequency will be less shifted from the peak of the DAF, it still will not fully match the actual observable.

Now let us discuss the nature of the phase transition in a model system described by a double well potential as defined in Ref. [54]. The total energy of this system (Φ) is given by:

$$\Phi = \Phi_0 + Ap^2 + Bp^4, \tag{4.1}$$

where we dropped the explicit dependence of A and B on thermodynamic quantities and the order parameter is denoted as p. Ref. [54] assumes A and B are temperature and pressure dependent. With that in mind one can interpret Eq. 4.1 as the best possible fit of the true energy to the functional form expressed above. This reasoning is identical to the TDEP method.

The important detail is that p is the order parameter. In the ferroelectric system, the order parameter is the polarization, $p = \frac{1}{\Delta V}\sum_{\Delta V} p_i$, we sum local dipole moments in some volume ΔV. In the lowest approximation, the local (unit cell) polarization p_i is directly proportional to the interatomic displacement parameter (this is the definition of Born effective charge). In the displacive phase transition, the polarization and the interatomic displacement parameter μ are the same ($p \equiv \mu$), since all of the local dipole moments point in the same direction (μ are all in the same minimum of the double well). However, in the order - disorder phase transition, the polarization and interatomic displacement parameter are not the same thing. The interatomic displacement parameter is the local minimum of the energy (a degenerate quantity), while the polarization is the average over them. If the interatomic displacement parameters are unformly distributed between two or more minima, the polarization is likely to be zero, even while the distribution of μ is not peaked at zero.

In the low symmetry phase, the parameter A in Eq. 4.1 is negative. In the high symmetry phase, it is positive. The phase transition is defined as a point where this parameter changes sign [54]. If the phase transition is displacive, and the polarization is the same as μ, one can recognize that A is proportional to the square of the phonon frequency of the high-symmetry phase (for A to be related to a phonon frequency, p must be equal to the small perturbation from the equilibrium position, and if the system is in

the low symmetry phase, μ is not the perturbation from the equilibrium position, it is the equilibrium position). This frequency can be interpreted as the TDEP frequency due to the similar nature of A and the TDEP force constants. A has to pass through zero at the phase transition (both displacive and order disorder), meaning that in the displacive phase transition the TDEP frequency must pass through zero as well. In the order - disorder phase transition, however, the order parameter (the polarization p) is not the same as μ, it is actually the average of all local μ-s. This means that we can not associate A with the TDEP phonon frequency of the high symmetry phase. The parameter A still has to become zero at the phase transition, but it is not related to the TDEP phonon frequency. In the order-disorder phase transition, we can not make any claims, whether the TDEP phonon frequency goes to zero or not. On the other hand, the connection between the "anharmonic" frequency and the parameter A is not obvious at all.

Finally, we note that scattering experiments used to measure phonon frequencies do not measure the TDEP frequencies (they measure the peak of the power spectrum), so they can not conclusively tell if the phase transition is of the displacive type or not.

In this chapter we study the vibrational properties of GeTe close to the ferroelectric phase transition. We find that the TDEP frequencies of the soft modes soften at the phase transition, but do not become zero. However, the large anharmonicity of these phonon modes causes spectral functions to collapse and peak at zero frequency. Furthermore, the strong anharmonicity causes spectral functions of these phonon modes to drastically deviate from expected Lorentzian lineshapes, even at lower temperatures. We find that this behavior of phonon spectral functions originates due to the coupling of the soft modes to the entire phonon bath rather than specific phonon branches.

4.2 Computational details

We obtained the temperature dependent vibrational properties of GeTe using the temperature dependent effective potential (TDEP) method [106, 107, 108]. The atomic positions and forces needed for fitting the interatomic force constants in TDEP method were sampled along molecular dynamics trajectories. First we calculated the temperature dependence of the GeTe structure using molecular dynamics (MD) simulations (see Chapter 7 of the thesis for more details). We then fixed the lattice parameters at each temperature according to the MD thermal expansion data and ran an MD simulation in the NVT ensemble. The MD simulations were performed on 512 atoms

supercells ($4\times4\times4$ supercell of the pseudocubic (conventional) unit cell of GeTe) with a timestep of 1 fs. The initial atomic positions were chosen to be equilibrium positions of atoms at a given temperature. Initial velocities are randomly chosen from a Gaussian distribution with a variance according to the given temperature. After a 50 ps equilibration time, we ran a 300 ps MD simulation along which trajectory we sampled 24 atomic configurations.

The forces for the atomic configurations sampled in this way were calculated using density functional theory (DFT). Since the MD and DFT zero temperature structural parameters are different, we used the temperature dependent MD structural parameters to calculate GeTe thermal expansion coefficients. We then used these thermal expansion coefficients to calculate DFT structural parameters of GeTe at different temperatures. Using these DFT structural parameters and atomic positions from the MD simulations we calculated the forces needed to fit the TDEP force constants using DFT.

DFT calculations were performed using the ABINIT software package [87, 88]. We use a generalized gradient approximation with the Perdew-Burke-Ernzerhof parametrization (GGA-PBE) [86] for the exchange-correlation functional and the Hartwigsen-Goedecker-Hutter (HGH) pseudopotentials [144]. Wave functions are represented in a plane wave basis set with the cutoff of 16 Ha, and the Γ point is used for sampling of electronic states. Sampling of phonon states for the calculations of phonon spectral functions is carried out using a $30\times30\times30$ $\vec{q}$-point grid. The phonon self-energy in the calculation of the spectral functions is sampled at 2000 values, equally separated up to $2.1\times\omega_D$. ω_D is the Debye frequency, corresponding to the largest frequency on a $30\times30\times30$ $\vec{q}$-point grid (see Appendix A for more details).

4.3 Results

4.3.1 Soft phonon mode at the phase transition

GeTe is a ferroelectric material, exhibiting a spontaneous polarization below 600 – 700 K [157, 158, 159, 160]. The critical temperature strongly depends on the free charge carrier concentration. Spontaneous polarization occurs due to a slight offset of the Te sublattice along one of the body diagonals of the rocksalt structure. At temperatures higher than 600 – 700 K, GeTe transforms to the rocksalt structure, losing its ferroelectric nature [7, 8, 4, 155]. The GeTe structure can be described by the following

set of lattice vectors:

$$\begin{aligned}\vec{r}_1 &= a(b, 0, c),\\ \vec{r}_2 &= a(-\frac{b}{2}, \frac{b\sqrt{3}}{2}, c),\\ \vec{r}_3 &= a(-\frac{b}{2}, -\frac{b\sqrt{3}}{2}, c),\end{aligned} \tag{4.2}$$

where a is the lattice constant, $b = \sqrt{2(1-\cos\theta)/3}$, $c = \sqrt{(1+2\cos\theta)/3}$, and θ is the angle between the primitive lattice vectors. The atomic positions in this structure are taken to be: Ge (0.0,0.0,0.0) and Te ($0.5+\mu$, $0.5+\mu$, $0.5+\mu$) in reduced coordinates. If the phase transition is displacive, as assumed in Refs. [50, 55], the angle θ becomes 60° at the phase transition, while the interatomic displacement parameter μ becomes zero [7, 8]. In this type of the phase transition, the TDEP frequency of the soft mode also collapses to zero [3]. Here we define the TDEP frequency of the phonon mode as the square root of the eigenvalue of the dynamical matrix for that phonon mode at a certain temperature. In the order-disorder phase transition, both the TDEP frequency of the soft mode and the local interatomic displacement are non-zero [4, 155, 161]. It is still under debate which type of the phase transition occurs in GeTe [3, 7, 8, 4, 155].

We have calculated the phonon dispersion of GeTe at different temperatures using the TDEP method and neglecting LO/TO splitting due to high hole concentration in experimental GeTe samples. The TDEP method allows us to calculate TDEP frequencies of phonon modes at different temperatures. In these calculations, we used the structural parameters calculated at appropriate temperatures (see Chapter 7 for more details). Figure 4.1 shows the TDEP frequencies of the two TO modes at the Brillouin zone centre in GeTe as we approach Γ from the $\Gamma - X$ direction (corresponding to the non-degenerate A_1 mode and the E mode which is degenerate with the longitudinal optical (LO) mode). The phase transition temperature obtained in our MD calculations is $T_C \approx 634$ K. The TDEP frequencies of both phonon modes are strongly renormalized by anharmonic interaction and lattice thermal expansion. The TDEP frequencies of these phonon modes soften drastically at the phase transition, but they do not become zero, indicating that the phase transition in GeTe might not be of the displacive type.

The observed phonon frequency in experiments is not the TDEP frequency, but what we will call in the rest of the paper the anharmonic frequency i.e. the peak of the phonon mode power spectrum, see Eq. (4.3). Blue squares in Fig. 4.1 represent the computed anharmonic frequencies of both TO modes at the zone centre, which do fall to zero at the phase transition, in contrast to the TDEP frequencies. Our results thus

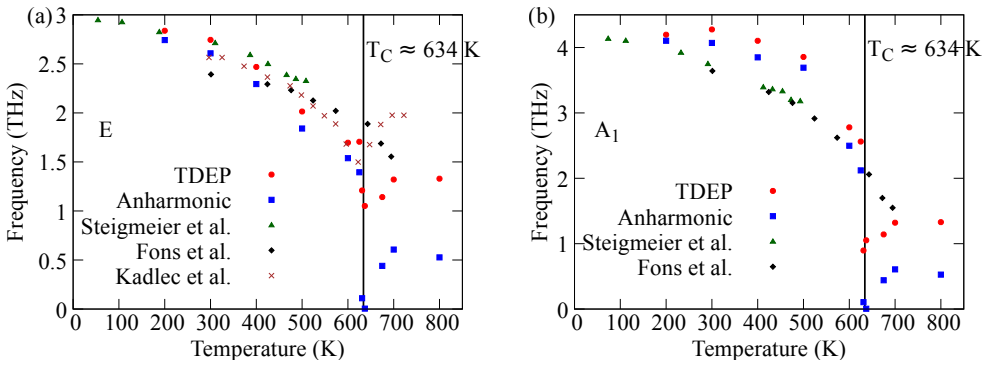

Figure 4.1: Temperature dependence of the zone centre transverse optical phonon frequencies. (a) The lower transverse optical (TO) mode (E) and (b) the higher TO mode (A_1) at the zone centre (as we approach Γ in the $X-\Gamma$ direction, which is perpendicular to the anisotropy axis). Red circles and blue squares represent the calculated TDEP and anharmonic phonon frequencies respectively, while other symbols represent the experimental results from Refs. [3, 9, 4]. The TDEP frequency is the square root of the eigenvalue of the dynamical matrix for $\vec{q} = 0$ at a particular temperature, while the anharmonic frequency is the peak of the phonon mode power spectrum, defined in Eq. (4.3). The black vertical line represents the phase boundary between the rhombohedral and rocksalt structures in our calculations (≈ 634 K).

suggest that the observation of phonon mode softening is not a conclusive proof of the displacive type of the phase transition, as previously argued in the case of GeTe [3]. The calculated phonon frequencies (both TDEP and anharmonic) are very similar in the two different phases for the temperatures closest to the phase transition (at 631 K and 637 K).

Our computed anharmonic TO frequencies at the zone centre agree fairly well with those measured in experiments, see Fig. 4.1. This agreement highlights the accuracy of the TDEP method even for the challenging cases of materials undergoing structural phase transitions. We note that the critical temperature in Ref. [3] is around 600 K, in Ref. [4] approximately 700 K and in Ref. [9] 650 K. This difference in the calculated and measured critical temperature is expected since the critical temperature strongly depends on the number of free charge carriers [150, 149].

4.3.2 Phonon spectral function

Harmonic frequencies are a valid description of lattice dynamics only in the absence of phonon-phonon interaction. In the inelastic neutron scattering experiments that measure phonon spectral functions, harmonic phonons would produce zero linewidth signals, revealing infinitely long lived quasiparticles. However, in real materials phonons interact with each other, thus broadening phonon spectral functions, with linewidths

inversely proportional to phonon lifetimes. This effect can be described using the concept of phonon self-energy that quantifies the strength of phonon-phonon interaction [121, 120, 122].

The probability of an incoming neutron to interact with a phonon system acquiring/losing energy $\hbar\Omega$ and momentum $\hbar\vec{q}$ is proportional to the spectral function [121, 120, 122]:

$$S(\vec{q},\Omega) \sim \sum_s \left\langle u^{\dagger}_{\vec{q},s} u_{\vec{q},s} \right\rangle = \sum_s \frac{4\omega^2_{\vec{q},s}}{\pi(e^{\beta\hbar\Omega}-1)} \times \frac{\Gamma_{\vec{q},s}(\Omega)}{(\Omega^2 - \omega^2_{\vec{q},s} - 2\omega_{\vec{q},s}\Delta_{\vec{q},s}(\Omega))^2 + 4\omega^2_{\vec{q},s}\Gamma^2_{\vec{q},s}(\Omega)}, \tag{4.3}$$

where $u_{\vec{q},s}$ is the phonon displacement operator, $\omega_{\vec{q},s}$ is the harmonic/TDEP frequency of the phonon mode with wave vector $\vec{q}$ and phonon branch s, β is $1/k_BT$ with k_B being the Boltzmann constant and T the temperature, and $\hbar$ is the reduced Planck constant. $\Delta_{\vec{q},s}$ and $\Gamma_{\vec{q},s}$ are the real and imaginary part of the phonon-self energy, respectively. In a weakly anharmonic material, the self-energy is approximately independent of energy and this expression can be reduced to a Lorentzian with a half-width of $\Gamma_{\vec{q},s}$ and the position of the peak at $\omega_{\vec{q},s} + \Delta_{\vec{q},s}$. In this case the phonon lifetime can be calculated as $\tau_{\vec{q},s} = \frac{1}{2\Gamma_{\vec{q},s}}$. However, in materials with strong anharmonicity, phonon spectral functions can exhibit exotic behaviour with satellite peaks, shoulders etc. [52, 162, 163, 164, 165, 166].

In Fig. 4.2 we show the phonon spectral function of GeTe near the phase transition (631 K) along a high symmetry path. The black lines represent the TDEP frequencies $\omega_{\vec{q},s}$ calculated at 631 K and the cyan dashed lines are the TDEP frequencies at 300 K. The TDEP frequencies of optical modes soften from 300 to 631 K. The acoustic mode frequencies soften as well in the F - Γ and the in plane (Γ - X) directions. This is the consequence of the overall softening of the second order force constants with temperature. On the other hand, the acoustic modes along the Γ - Z direction (the direction along the trigonal axis) stiffen because of the negative thermal expansion, as we will discuss in the next chapter. The spectral function shows further softening of the phonon frequencies due to anharmonic phonon-phonon interaction. As expected, the TO phonon at Γ can not be clearly resolved in the graph of the phonon spectral function.

Figure 4.3 (a) shows the unusual features of the spectral function for the higher frequency transverse optical mode (A_1) of GeTe at the zone centre for several different temperatures. A non-Lorentzian behavior of the phonon spectral function is evident

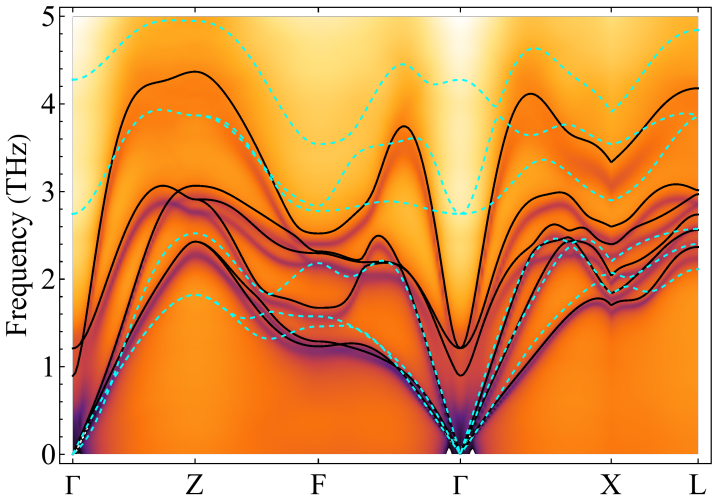

Figure 4.2: Phonon spectral function defined in Eq. (4.3) along high symmetry lines in GeTe at phase transition. Black lines represent the TDEP frequencies calculated at 631 K (close to the critical temperature 634 K) and dashed cyan lines are the TDEP phonon band structure at 300 K. The darker shades of purple show regions with higher phonon spectral function values, while pale yellow regions have the lowest values of phonon spectral function.

even at 300 K, very far from the phase transition. The broadening of the power spectrum is large, revealing the short lifetime of this phonon mode. The distortion of the power spectrum is stronger at 625 K, with a very large shift of the peak of the spectral function compared to the TDEP frequency. For temperatures near the phase transition, the power spectrum peaks around 0 THz as expected at the phase transition (see Fig. 4.1). At temperatures higher than the phase transition temperature, the peak of the power spectrum is at non-zero frequencies, but is still strongly renormalized compared to the TDEP frequency.

Non-Lorentzian shapes of the phonon power spectra of optical modes in GeTe at the phase transition are the consequence of the coupling of these phonon modes to the entire phonon bath, rather than coupling to specific phonons. We test this by calculating the power spectrum of the A_1 phonon mode (where atomic displacements are along the trigonal axis, as defined in Section 4.3.1) disregarding the coupling to specific phonon branches. We do this by setting the anaharmonic coupling strength ($|\Phi_{\lambda,\lambda_1,\lambda_2}|^2$ in Eq. (2.36)) to zero if λ_1 or λ_2 is the branch we want to exclude. We find that the change in the power spectrum does not substantially vary depending which phonon branch we disregard.

Figure 4.3 (b) shows the spectral function of the zone centre A_1 phonon mode at 631 K, computed including and excluding transverse acoustic-A_1 mode coupling. When we

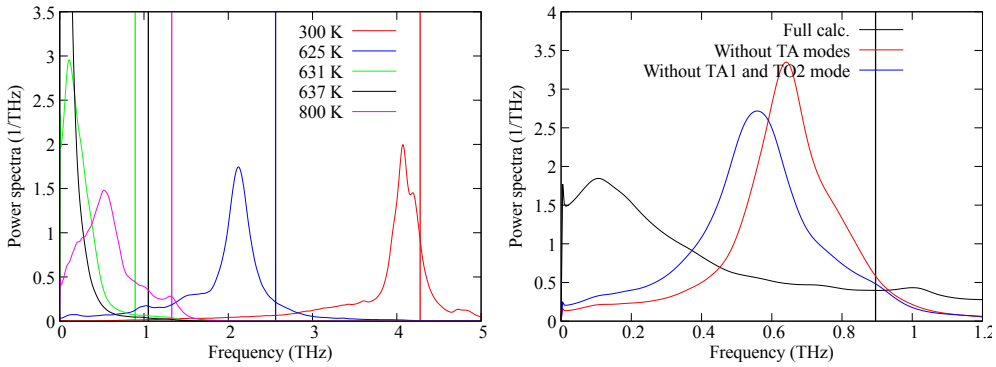

Figure 4.3: (a) Spectral function for the zone centre higher transverse optical mode (A_1) in GeTe at different temperatures. Vertical lines represent the values of the TDEP $A_1(\Gamma)$ frequencies at different temperatures. A drastic deviation from the Lorentzian shape is evident for the entire temperature range and most prominent in the vicinity of the phase transition (at 631 and 637 K). (b) Spectral function of the zone centre A_1 mode at 631 K including all phonon-phonon interactions ("Full calc."), excluding the coupling to transverse acoustic (TA) modes ("Without TA modes"), and excluding the interaction with the first transverse acoustic mode and the second transverse optical mode ("Without TA1 and TO2 mode"). The vertical line represents the TDEP frequency of the A_1 (Γ) mode at 631 K.

neglect the coupling of the A_1 mode with two lowest modes in our calculation (which we will call transverse acoustic (TA) modes), the peak of the spectral function shifts closer to the TDEP frequency. A similar behaviour is observed if we disregard the coupling of the A_1 zone centre mode with TA1 (the transverse acoustic mode with lowest frequency) and the second (mostly transverse) optical (TO2) mode. This illustrates that although coupling to TA modes is strong, it is not the sole source of the exotic behaviour of the soft A_1 phonon power spectrum.

The spectral function of the zone centre E mode (with atomic displacements perpendicular to the trigonal axis, as defined in Section 4.3.1) in GeTe is illustrated in Fig. 4.4 (a) for several temperatures. We can see a secondary peak in the E spectral function at 625 K, indicating that anharmonicity of this mode is even larger than that of the A_1 mode. This is somewhat to be expected since the TDEP frequency of the E mode is lower than that of the A_1 mode, leading to larger coupling to the rest of the modes. At 631 K the spectral function of this mode has a peak at almost 0 THz. In the rocksalt phase, the E and A_1 modes are degenerate and have the same lineshapes.

In Fig. 4.4 (b) we show the spectral function of the zone centre E mode at 631 K with full anharmonicity, excluding the coupling of E mode with transverse acoustic modes and excluding the coupling to the TA2 mode and the first (mostly transverse) optical (TO1) mode. We can see that the Lorentzian shape of the spectral function is not regained after excluding different types of interaction and thus we conclude that

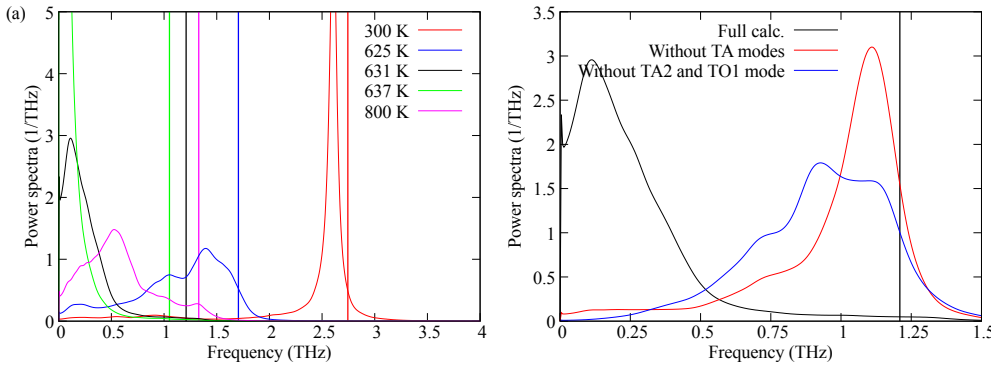

Figure 4.4: (a) Spectral function of the zone centre E mode at different temperatures. (b) Spectral function of the E (Γ) mode at 631 K including all phonon-phonon interactions ("Full calc."), excluding the coupling to transverse acoustic modes ("Without TA modes") and excluding the coupling between the second transverse acoustic and first transverse optical modes ("Without TA2 and TO1 modes"). The vertical lines represent the TDEP frequencies of the E (Γ) mode at various temperatures.

the non-Lorentzian shape of the E mode power spectrum and the softening of the E frequency is due to coupling to the entire phonon bath, rather than a particular phonon branch. However, here we can say that the coupling to the acoustic modes is dominant, as evidenced by the strongest renormalization of the E mode spectral function.

4.4 Conclusion

We performed detailed calculations of phonon frequencies and spectral functions of GeTe close to the ferroelectric phase transition. The TDEP frequencies of the soft modes, although dramatically softened, do not become zero at the phase transition. On the other hand, strong anharmonicity causes the spectral functions of the soft modes to collapse and effectively peak at zero frequency. Additionally, strong anharmonicity causes spectral function of soft phonon modes to deviate dramatically from the expected Lorentzian shape. This is a consequence of the soft mode coupling to the entire phonon bath, rather than specific phonon branches. The strong deviation of the phonon spectral functions at the ferroelectric phase transition questions the applicability of the Boltzmann transport equation for modeling lattice thermal conductivity in this system.

Chapter 5

Lattice thermal conductivity of GeTe close to the ferroelectric phase transition

5.1 Introduction

Reducing the lattice thermal conductivity κ is one of the most successful ways of improving the efficiency of thermoelectric materials [167, 168, 169, 59, 56, 170, 171]. Many of the best thermoelectric materials have intrinsically low lattice thermal conductivity. This is usually related to the large anharmonicity of phonon modes, which can stem from weak bonding, as in van der Waals materials [168, 170, 172, 173, 174, 175]. Weak bonding usually leads to low phonon group velocities which further reduces phonon mean free paths and consequently lattice thermal conductivity. Rattling modes [45, 42, 46, 43, 44, 176] are known to exhibit very flat phonon dispersions (with low phonon group velocities) which increase phonon scattering phase space, thus reducing phonon lifetimes. Introducing phonon scattering centers, such as grain boundaries or point defects, is another extremely succesful way of reducing lattice thermal conductivity [169, 59, 56].

Another source of large anharmonicity in good thermoelectric materials can be the proximity to structural phase transitions, as in the case of IV-VI materials [162, 177, 52, 178, 50, 55, 105]. For example, germanium telluride (GeTe) undergoes the ferroelectric phase transition at $\sim$ 700 K, and has intrinsically low lattice thermal conductivity and high thermoelectric efficiency [10, 11, 12].

Recent computational work has predicted that driving IV-VI materials closer to the ferroelectric phase transition via strain or alloying can lead to a drastically lower lattice thermal conductivity [50, 55]. Under the assumption of a displacive phase transition, it was found that coupling between soft transverse optical (TO) modes and heat carrying acoustic modes is the main reason for the κ reduction. At the displacive transition, the frequency of the soft TO mode collapses, becoming effectively zero. Since scattering rates are inversely proportional to phonon frequencies, the lifetimes of the acoustic modes that couple to soft TO modes decrease dramatically leading to a considerable reduction in κ [50, 55].

Surprisingly, experimental studies have shown that the lattice thermal conductivity increases at the ferroelectric phase transition in GeTe [10, 11, 179, 13, 14, 15, 16, 17]. This is at odds with measurements in some other materials going through ferroelectric phase transitions, where a drastic decrease in κ is observed [180]. The reason for the anomalous behaviour of κ at the phase transition in GeTe remains unknown. Understanding the microscopic origin of the κ increase at the ferroelectric phase transition may facilitate the design of improved thermoelectric materials.

In this chapter, we study how driving GeTe near the ferroelectric phase transition via temperature affects its lattice thermal conductivity, making no assumptions about the nature of the phase transition. Unlike the previous work [50, 55], we calculate interatomic force constants at different temperatures using the state-of-the art, temperature dependent effective potentials (TDEP) method [106, 107, 108]. We find that the increase of the lattice thermal conductivity of GeTe at the phase transition in the rhombohedral phase comes from negative thermal expansion that enhances the phonon group velocities. In the cubic phase phonon lifetimes increase, leading to even more substantial increase of κ. Large anharmonicity of phonon modes minimizes the phonon lifetimes at the phase transition in the rhombohedral phase and leads to non-Lorentzian power spectra of phonon modes.

We implement a new method of calculating κ based on the formalism first derived in Ref. [111] that includes these non-Lorentzian lineshapes of the phonon power spectra near the phase transition. This approach further increases κ at the phase transition, which can be attributed to further softening of the phonon frequencies due to phonon-phonon interaction.

5.2 Computational details

The details of the procedure on how we sampled interatomic force constants are given in Chapter 4. Here we additionally note that the sampling of phonon states for the lattice thermal conductivity calculations in BTE approach is carried out using a 30×30 $\vec{q}$-point grid. The same grid is used for the evaluation of the phonon self energy. The phonon self-energy in the calculation of the spectral functions for the evaluation of the integral in Eq. (2.39) is sampled at 2000 values, equally separated up to 2.1 ω_D. ω_D is the Debye frequency, the largest frequency on a $30\times30\times30$ $\vec{q}$-point grid (see Appendix A for more details).

5.3 Results

5.3.1 Lattice thermal conductivity in the Boltzmann transport approach

We calculated the lattice thermal conductivity of GeTe for a range of temperatures including both rhombohedral and rocksalt phases (see Fig. 5.1), combining the TDEP method with the Boltzmann transport approach. Overall, the lattice thermal conductivity is inversely proportional to temperature, as a result of the linear dependence of phonon populations with temperature above the Debye temperature (200 K for GeTe). The calculated κ deviates from the 1/T law near the phase transition, where there is a large κ increase at the phase transition and in the cubic phase. At high temperatures, the κ in the cubic phase regains the 1/T dependence.

There is an anisotropy in the lattice thermal conductivity in the rhombohedral phase (Fig. 5.1), as a consequence of the van der Waals gaps formed due to the Te sublattice offset. The direction perpendicular to the van der Waals gaps (i.e. parallel to the trigonal [111] axis) has weaker bonding, leading to the lower phonon group velocities and κ in that direction. Anisotropy of the lattice thermal conductivity disappears close to the phase transition and is not present in the rocksalt phase.

The agreement between the computed and experimental κ values is very good in the whole temperature range of the rhombohedral phase, especially if we consider the average κ (dashed line in Fig. 5.1). Almost all experiments show an increase in the lattice thermal conductivity in the vicinity of the phase transition [10, 11, 12, 13, 14, 15, 16, 17], similarly to our results. The range of values for κ from experiments (shown in

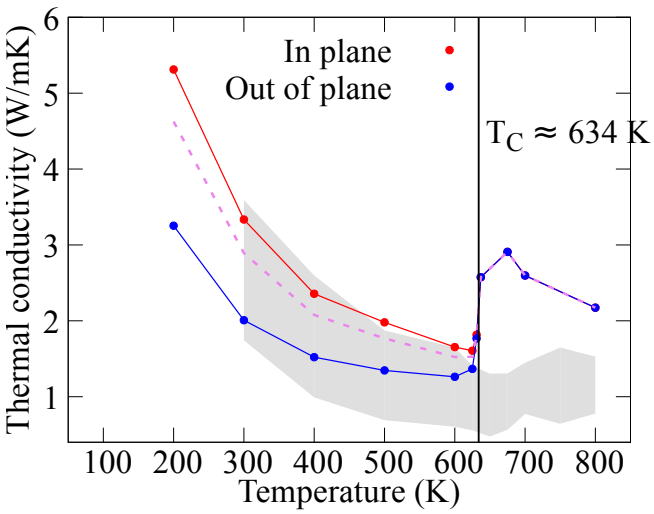

Figure 5.1: Temperature dependence of the lattice thermal conductivity of GeTe. Red and blue lines represent the calculated values using the Boltzmann transport approach in the directions perpendicular and parallel to the trigonal [111] axis, respectively. Dashed line represents the average values of the computed lattice thermal conductivity. Grey region represents the experimental results collected from Refs. [10, 11, 12, 13, 14, 15, 16, 17].

Fig. 5.1 as a grey region) was taken so that it is bounded by a maximum and minimum value from all available experiments at a certain temperature. Different experiments have different critical temperatures. There is no scaling of experimental data with respect to the experimental phase transition temperature in Fig. 5.1. The discrepancy between our results and experiments increases as we get closer to the phase transition and particularly in the cubic phase. Our results consistently overestimate κ compared to experiments. In the rhombohedral phase we would expect scattering from lattice imperfections, such as ferroelectric domain walls [82, 80, 181, 182, 183], to further reduce the computed lattice thermal conductivity, but this is not the case in the cubic phase.

The differences between our calculated κ values and experiments could also arise from the fact that GeTe has a large number of Ge vacancies. Several recent publications that report calculations of κ in GeTe stress the importance of including point defect scattering in the calculation [105, 184]. Additionally, the experimental investigation of the phase transition in GeTe [20] noted a huge increase of Ge vacancies in the cubic phase. These point defects scatter higher frequency phonons more effectively [58]. Considering this and the fact that the main contribution to the lattice thermal conductivity shifts to the phonons with higher frequencies at higher temperatures (see Fig. 5.2), we conclude that the lack of point defect scattering in our calculations might be one of the possible reasons for the larger discrepancy in κ in the cubic phase between our

calculated values and experiments.

The discrepancies between theory and experiments could also stem from omitting the higher order terms in the Taylor expansion of the interatomic forces (we include the second and third order terms only). However, to the lowest approximation, the fourth order anharmonic terms would only affect the real part of the self-energy [120] and not imaginary part, which would mean that the phonon lifetimes should remain unchanged. Additionally, since the force constants in TDEP are obtained through a fitting procedure, the fourth order force constants should be smaller than the third order ones. Therefore, higher order anharmonicity should not be the reason for the differences in the calculated and experimental κ values.

Experimental values of lattice thermal conductivity are usually extracted from the total thermal conductivity measurements using the Wiedemann-Franz law to eliminate the electronic contribution to the thermal conductivity, whose validity at structural phase transitions is not well understood. Additionally, most references use the single parabolic band Kane model to extract the Lorenz factor from measurements of the Seebeck coefficient, which is not appropriate in GeTe due to the intrinsically complicated Fermi surface [16]. Such lattice thermal conductivity values can differ widely near structural phase transitions, and sometimes an increase in the total thermal conductivity is assigned to the electronic contribution. Here we have shown that the increase in the thermal conductivity of GeTe at the phase transition, at least partially, comes from the lattice thermal conductivity. The difference between our theoretical and experimental results in the cubic phase might be due to an inaccurate estimation of the electronic contribution to the total thermal conductivity in experiments. Measuring the thermal conductivity of GeTe in an applied magnetic field (to exclude the electronic thermal conductivity) would test our predictions of the increased lattice thermal conductivity at the phase transition.

To analyze the contribution of specific phonon modes to the total lattice thermal conductivity, we calculated the spectral thermal conductivity at different temperatures by convolving the total lattice thermal conductivity with a Gaussian of an appropriate width:

$$\kappa^{x,y}(\Omega) = \frac{\mathrm{d}\kappa^{x,y}}{\mathrm{d}\Omega} = \frac{1}{NV}\sum_{\vec{q}s} c_{\vec{q}s} v^x_{\vec{q}s} v^y_{\vec{q}s} \tau_{\vec{q}s} \delta(\Omega - \omega_{\vec{q}s}). \tag{5.1}$$

Here N is the number of $\vec{q}$ points in the sum, V is the volume of the primitive cell, $c_{\vec{q}s}$ is the harmonic heat capacity, $v^x_{\vec{q}s}$ is the group velocity of $(\vec{q}s)$ phonon mode in the Cartesian direction x and $\tau_{\vec{q}s}$ is the phonon lifetime. We have found that acoustic

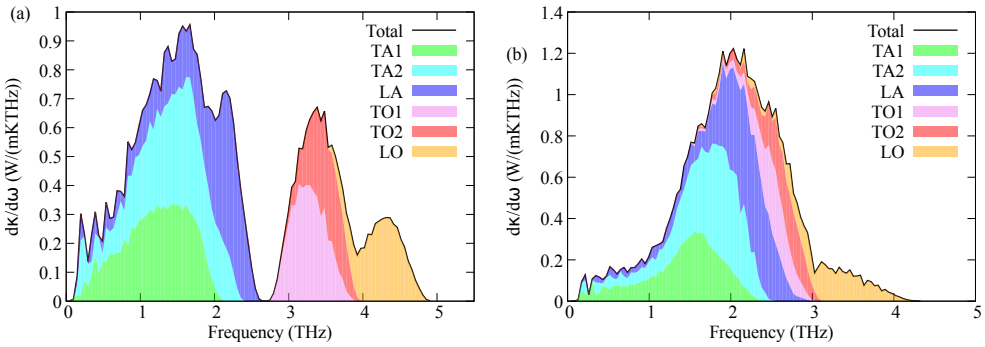

Figure 5.2: Spectral lattice thermal conductivity (see Eq. (5.1)) of GeTe at (a) 300 K and (b) 631 K. Shaded regions show the contribution of a particular phonon branch.

modes give the dominant contribution to the lattice thermal conductivity, as one would expect (see Fig. 5.2). At temperatures near the phase transition, the overall contribution of transverse modes (acoustic and optical) to the lattice thermal conductivity of GeTe diminishes. At the phase transition, the largest contribution to κ comes from the phonon modes in the frequency range between 1 and 3 THz.

To understand the anomalous behaviour of κ near the phase transition, we calculate the average phonon lifetimes and group velocities at different temperatures, see Fig. 5.3. For example, the average values of the phonon lifetimes in the vicinity of the phonon frequency ω_0 are given as:

$$\bar{\tau}(\omega_0) = \frac{\sum_\lambda \tau(\omega_\lambda) \exp(-\frac{(\omega_0-\omega_\lambda)^2}{\sigma^2})}{\sum_\lambda \exp(-\frac{(\omega_0-\omega_\lambda)^2}{\sigma^2})}, \tag{5.2}$$

where the sum goes over all phonon modes λ, and σ is the smearing parameter taken to be $\sigma = \omega_D/(N+1)$, where ω_D is the Debye frequency and N is the number of ω_0 frequencies.

The phonon group velocities of GeTe are mostly independent of temperature, except very close to the phase transition, see Fig. 5.3 (a). In this temperature region (600 – 675 K), there is an increase in the phonon group velocities across most of the frequency range and most noticeably for phonons between 1 and 3 THz. This is the frequency region that contributes most to the thermal conductivity (see Fig. 5.2). We thus conclude that the anomalous increase of the thermal conductivity at the phase transition is partially due to this rise in the phonon group velocities. We find that the increase in group velocities originates from the lattice contraction near the critical temperature [79, 7, 8]. This can be understood from the observation that the increase of phonon group velocities happens most prominently along out of the plane direction, where

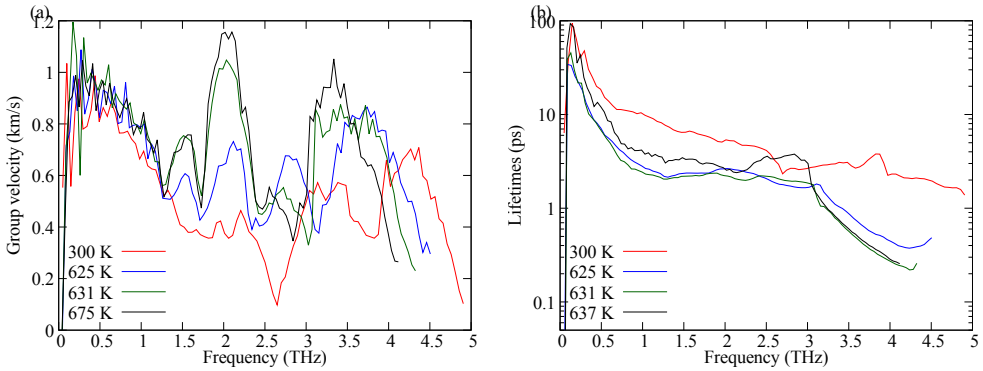

Figure 5.3: Frequency dependence of phonon transport properties. (a) Average phonon group velocities and (b) average phonon lifetimes of GeTe versus phonon frequency for different temperatures. Averaging is carried out by convolving the calculated values of these quantities with a Gaussian (see Eq. (5.2)).

negative thermal expansion occurs [79] as discussed in Chapter 3.

Phonon lifetimes in weakly anharmonic materials usually follow the 1/T law, similar to thermal conductivity. This is the case in our calculations in the rhombohedral phase far from the phase transition. At the phase transition, however, the phonon lifetimes of acoustic modes decrease more than expected from the 1/T scaling. This is a signature of stronger anharmonicity of acoustic phonon modes closer to the phase transition in the rhombohedral phase. Optical modes have more complicated behaviour. While soft transverse optical modes near the zone centre have much lower lifetimes at the phase transition, this is not the case for transverse optical modes in the rest of the Brillouin zone. Even more intriguing is the behaviour of longitudinal optical modes. At low temperatures, they usually have frequency independent lifetimes, but at the phase transition they decrease dramatically with frequency.

In the cubic phase there is a substantial increase in the phonon lifetimes with respect to the rhombohedral phase(see Fig. 5.3 (b)). The phonon lifetimes at 637 K are larger in most of the frequency range compared to the temperatures closest to the phase transition in the rhombohedral phase (625 K and 631 K). Interestingly, the phonon lifetimes at 675 K are larger than the phonon lifetimes at 300 K rescaled by temperature (i.e. by 675 K/300 K), revealing stronger intrinsic anharmonicity of the rhombohedral phase.

To understand the role of anharmonicity in the intriguing behavior of GeTe at the phase transition, we show the average phonon lifetimes of GeTe at different temperatures scaled by $T/300$ K, where T is the temperature, in Fig. 5.4. This enables us to see whether the decrease in the phonon lifetimes near the phase transition is due to phonon populations or increased anharmonicity of the material. Phonon lifetimes scale inversely with temperature for the temperatures far from the phase transition temperature

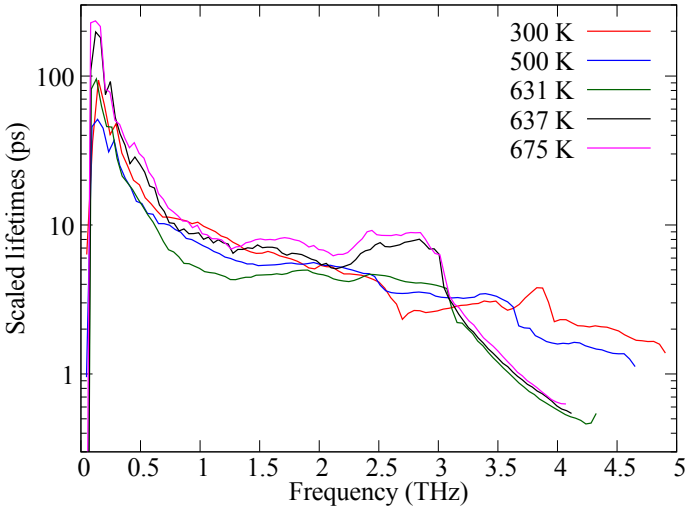

Figure 5.4: Average phonon lifetimes of GeTe scaled by T/300 K, where T is the temperature. Averaging is carried out by convolving the calculated phonon lifetimes with a Gaussian, see Eq. (5.2).

($T_C \approx 634$ K), which indicates that anharmonicity is not increased for those temperatures. However, close to the phase transition (631 K) in the rhombohedral phase, we can see a dip in the phonon lifetimes for most of the frequency range, revealing increased anharmonicity near the ferroelectric phase transition in the rhombohedral phase.

In the cubic phase, however, we see an increase in the scaled phonon lifetimes compared to the rhombohedral phase. Further from the phase transition (675 K), the scaled lifetimes are larger than the scaled phonon lifetimes at 300 K, which we attribute to lower intrinsic anharmonicity of the cubic phase.

To investigate in detail the reason for this behaviour of phonon lifetimes, we checked the change in anharmonic force constants with temperature (see Fig. 5.5). To compare anharmonic force constants, we define a norm of the anharmonic force constant matrix as: $N^{AFC}(i,j,k) = \sum_{\alpha,\beta,\gamma} |\Phi_{ijk}^{\alpha\beta\gamma}|$, where i,j,k denote atoms in triplet and α,β,γ are the Cartesian directions. Surprisingly, most of the anharmonic force constants decrease with temperature, in both rhombohedral and cubic phases. There is a sudden drop in the norm of the anharmonic force constants at the phase transition. The anharmonic force constants are drastically smaller in the cubic phase, explaining higher scaled phonon lifetimes in this phase.

However, the temperature dependence of anharmonic force constants does not explain the increased anharmonicity of the transverse acoustic modes at the phase transition in the rhombohedral phase (see Fig. 5.4). It is the scattering phase space (SPS) that

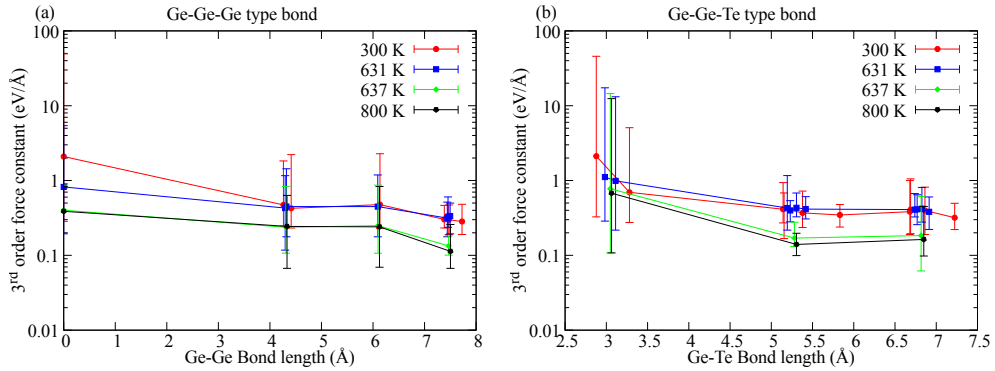

Figure 5.5: Change of the anharmonic force constants of (a) Ge-Ge-Ge and (b) Ge-Ge-Te triplets with temperature. The bars in the figure show the maximum and minimum norm of the force constants for the specific temperature and bond length.

increases at the phase transition appreciably, which leads to higher anharmonicity in the rhombohedral phase. We show this in Fig. 5.6 by calculating the scattering phase space for phonons at different temperatures. We do this by setting the matrix element $\Phi_{\lambda\lambda'\lambda''}$ in Eq. (2.36) to 1 and calculating the imaginary part of self-energy at the TDEP frequency for each phonon mode. The results are then scaled by temperature to minimize the effect of phonon population on the calculated value of the scattering phase space. We can notice that for the phonons in the frequency region around 1 THz the SPS increases dramatically near the phase transition, which explains the lower contribution of transverse optical modes to total κ at the phase transition compared to 300 K (see Fig. 5.2) and prominent dip in the scaled phonon lifetimes for this frequency region (see Fig. 5.4). Phonons in the frequency region around 2 THz have a smaller SPS, which again is consistent with the results presented in Fig. 5.4 (the scaled phonon lifetimes at the phase transition and 300 K are comparable in this frequency region). However, this can not be the reason for the increased lattice thermal conductivity at the phase transition, because this effect is noticeable only due to the temperature scaling of phonon lifetimes and SPS and does not exist if one takes phonon populations into account (see Fig. 5.3 (b)). Finally, the available scattering phase space of longitudinal optical (the highest frequency) phonons increases dramatically with temperature, which explains their unusual frequency dependence.

In the cubic phase, the SPS of the majority of phonons (except LO phonons) increases linearly with temperature, which balances out the decrease in the anharmonic force constants and leads to almost constant phonon lifetimes with temperature. The decrease in κ in the cubic phase between 700 K and 800 K comes primarily from a decrease in phonon group velocities.

In conclusion, the increase of the lattice thermal conductivity near the phase transition

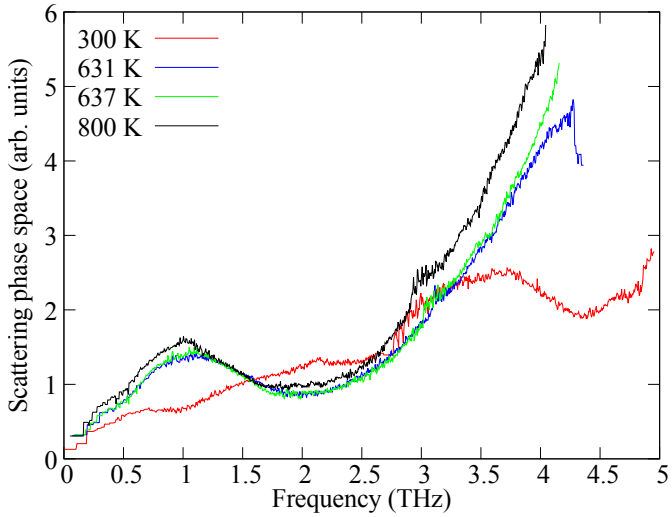

Figure 5.6: Phonon scattering phase space scaled by T/300 as a function of TDEP frequency at different temperatures.

can be attributed to two phenomena, depending on the structure of GeTe. In the rhombohedral phase, the increase in the thermal conductivity is due to negative thermal expansion that causes phonon group velocities to increase, increasing phonon mean free paths. On the other hand, in the cubic phase, phonon lifetimes increase dramatically compared to the rhombohedral phase due to lower intrinsic anharmonicity in this phase.

5.3.2 Lattice thermal conductivity using the Green-Kubo method

The non-Lorentzian behaviour of the phonon spectral function raises the question whether the Boltzmann transport equation employed in the calculation of the κ values in Fig. 5.1 is valid close to the phase transition. It is assumed in the derivation of the Boltzmann equation that phonons are well defined quasiparticles with unique frequencies and lifetimes. This implies that their spectral weights are Lorentzian functions centred at the harmonic frequencies and with widths equal to the phonon lifetimes. However, evidently this does not hold close to the phase transition, see Fig. 4.3 (a).

We include the effect of non-Lorentzian lineshapes on lattice thermal conductivity following the Green-Kubo approach derived in section 2.6. We can separate Eq. (2.39) into two parts. The first part is diagonal ($s = s'$). In the limit of small anharmonicity ($\Delta_{\vec{q},s} = 0$ and $\Gamma_{\vec{q},s} \ll \omega_{\vec{q},s}$), this part reduces to the standard solution of the Boltzmann equation in the relaxation time approximation, as we have shown (see Eq. (2.40) in Chapter 2). The second, non-diagonal part ($s \neq s'$), can be reduced in the limit of small

anharmonicity to the expressions similar to the ones given in Refs. [185, 186]. The non-diagonal contribution to the lattice thermal conductivity will become prominent only if there is a substantial overlap in the spectral functions of two phonon modes with the same wave vector. This is only true in the case of strong anharmonicity or when spectral peaks broaden substantially due to disorder.

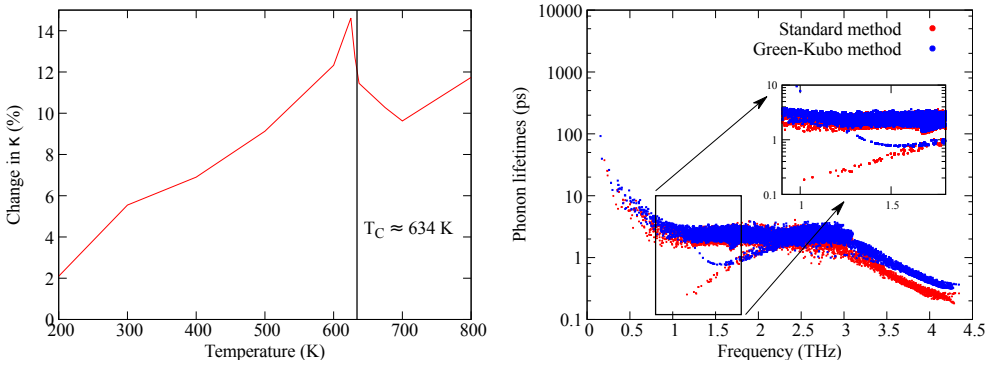

Figure 5.7: Green-Kubo lattice thermal conductivity. (a) Difference in the calculated lattice thermal conductivity using the Green-Kubo method (Eq. (2.39)) and the Boltzmann transport equation. (b) Phonon lifetimes of GeTe (see text for explanation) in the Green-Kubo and Boltzmann transport equation approach plotted versus TDEP frequencies of phonon modes. Inset shows the region of soft phonon modes where the change is most noticeable.

We have implemented the expression given by Eq. (2.39) with the TDEP method. Figure 5.7 (a) shows the difference between our results obtained using Eq. (2.39) and BTE (see Fig. 5.1). We can see that the BTE underestimates the thermal conductivity in the whole temperature range. Additionally, we can see that the underestimation is not large, around 10% even at high temperatures. Overall, the difference scales linearly with temperature. We can also see that the difference is largest at the phase transition, which is expected considering large deviations from the Lorentzian shape of the phonon spectral functions in this region (see Fig. 4.2). The contribution of the non-diagonal part of the lattice thermal conductivity is comparable to the overall enhancement of the diagonal part due to non-Lorentzian shapes of the phonon spectral functions.

To understand the reason for the increased difference in κ at the phase transition obtained by the standard BTE method and using the Green-Kubo relation (Eq. (2.39)), we show the phonon lifetimes of GeTe calculated using the two methods in Fig. 5.7 (b). We define the phonon lifetimes in the Green-Kubo method as:

$$\tau^{GK}_{\vec{q},s} = 8\frac{\hbar^2 k_B \beta^2 \omega^4_{\vec{q},s}}{\pi c_{\vec{q},s}} \int_{-\infty}^{\infty} \mathrm{d}\Omega \frac{\exp(\beta\hbar\Omega)}{(\exp(\beta\hbar\Omega)-1)^2} \frac{\Omega^2 \Gamma^2_{\vec{q},s}(\Omega)}{\left[\epsilon^2_{\vec{q},s} + 4\omega^2_{\vec{q},s}\Gamma^2_{\vec{q},s}(\Omega)\right]^2}, \tag{5.3}$$

where $c_{\vec{q},s}$ is the harmonic heat capacity of the phonon mode $(\vec{q}, s)$. The increase of the phonon lifetimes in the Green-Kubo method is visible in the whole Brillouin zone. It is, however, most prominent in the region of soft phonon modes, where the phonon lifetimes, defined in this way, increase by a factor of 100.

This result is counter-intuitive, why would stronger anharmonicity lead to higher phonon lifetimes? In the following we will try to show where this increase is coming from. To further investigate this, we calculate the phonon spectral function as previously defined (see Eq. (4.3)). We performed the inverse Fourier transform of the phonon spectral function and defined a time dependent phonon population operator:

$$n_{\vec{q},s}(t) = \frac{\langle u^{\dagger}_{\vec{q},s}(0) u_{\vec{q},s}(t)\rangle - 1}{2}. \tag{5.4}$$

This quantity describes the relaxation process where we excite a phonon $(\vec{q}, s)$ at time $t = 0$ and annihilate it at time t. The rate of the change of this quantity is what we usually associate with the phonon relaxation time. Further, the value of this quantity (in Eq. (5.4)) at time $t = 0$ is the phonon equilibrium population adjusted due to phonon-phonon interaction (the term $\langle u^{\dagger}_{\vec{q},s}(0) u_{\vec{q},s}(t)\rangle$ is the Fourier transform of Eq. (4.3) which explicitly accounts for third order anharmonicity). By tracking the behavior of these two quantities (phonon relaxation time and populations as defined in this paragraph), we will explain the intriguing results presented in Fig. 5.7 (b).

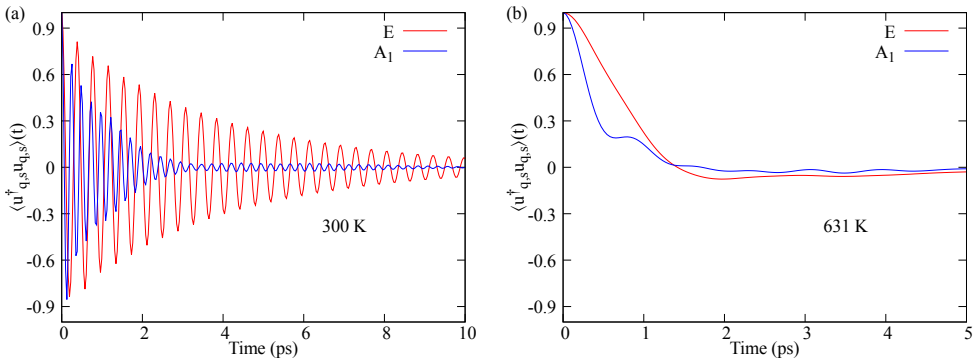

Figure 5.8: Displacement autocorrelation function of optical modes at the zone center at (a) 300 K and (b) 631 K. Displacement autocorrelation function has been normalized to be 1 at time 0.

First we show the time dependent displacement autocorrelation function for the soft modes at the zone center at 300 K and 631 K in Fig. 5.8. We can fit these profiles to the damped oscillator function to extract the phonon frequency and relaxation time. Phonon lifetimes and frequencies defined in this way are a true analog of what we actually think of when we consider phonon lifetimes and frequencies in the BTE. At 300

K, the TDEP frequency and relaxation time obtained from Eq. (2.36) agree extremely well with the fitted values. The TDEP (fitted) frequency of the E mode at the zone center is 2.42 (2.27) THz, and for the A_1 mode 3.61 (3.46) THz. The TDEP and fitted relaxation times are in similar agreement, for the E mode 1.59 (1.16) ps, and for the A_1 mode 0.87 (0.78) ps. At 631 K, however, it is hard to see any oscillatory behavior. The fitting procedure does not seem appropriate in this case. It does, however, give us an estimate of frequencies and lifetimes which are not far from the ones obtained through standard methods. [1]

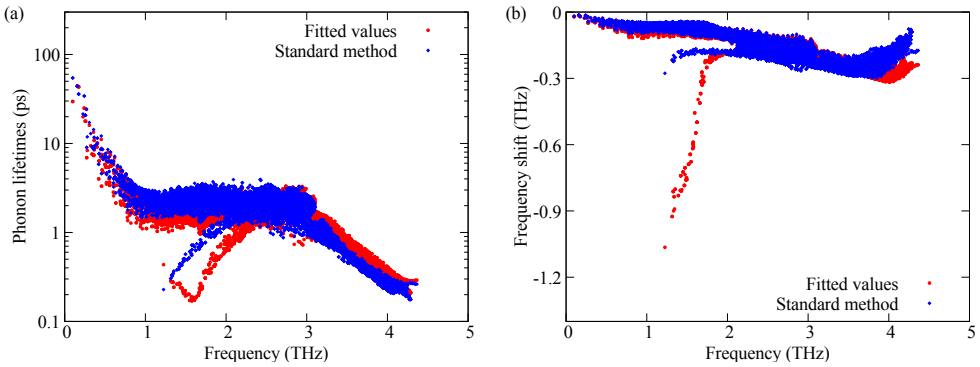

Figure 5.9: (a) Phonon lifetimes and (b) phonon frequency shifts obtained through the fitting procedure compared to the ones obtained by the standard method at 631 K (see text for more information).

Next, we show relaxation times at 631 K obtained through the fitting procedure and compared with those obtained via standard definition of relaxation time in Fig. 5.9 (a). By the standard definition of relaxation time and phonon frequency shift, we mean the values extracted from the phonon self-energy (imaginary and real part respectively) at the TDEP frequency. We can see that, contrary to Fig. 5.7 (b), phonon lifetimes obtained through the fitting procedure are smaller than the ones obtained by the standard method. This holds mostly for low frequency modes and most prominently for soft modes. On the other hand, longitudinal optical modes have in fact higher phonon relaxation times compared to the standard method.

Figure 5.9 (b) shows the phonon frequency shifts obtained with the fitting procedure and compared to ones obtained by the standard method. We can see that the shift is overall linear in frequency and most prominent for the region of soft modes, as we would expect (see Fig. 4.3). This means that phonon frequencies are mostly lower in the Green-Kubo approach compared to BTE.

Finally, in Fig. 5.10 (a) we show phonon populations calculated from displacement

[1] The TDEP anharmonic frequencies at 631 K agree fairly well with the fitted ones, while the TDEP relaxation time is not far from the fitted one (the agreement similar to the results at 300 K).

autocorrelation function at time zero to explain the behavior shown in Fig. 5.7 (b). We can see that the phonon populations seem to diverge for the soft phonons and depart from the expected Bose-Einstein factor. This is mostly due to the softening of the peak of the phonon spectral function and this is the source of the intriguing result of Fig. 5.7 (b). The increased phonon populations increase the phonon heat capacity in the Green-Kubo method. This increase of heat capacity (compared to the harmonic heat capacity) is the reason why phonon lifetimes in the Green-Kubo method (as defined in Eq. (5.3)) increase compared to BTE. Furthermore, this means that the increase in the lattice thermal conductivity in Green-Kubo method compared to the Boltzmann transport equation is due to the softening of the phonon modes due to phonon-phonon interaction, which is correctly captured in the Green-Kubo method.

To gain more insight in how the phonon populations increase due to the phonon softening, we calculated the difference between anharmonic phonon populations (phonon population renormalized due to phonon-phonon interaction) and the Bose-Einstein occupation factor along a high symmetry line, see Fig. 5.10 (b). We can see that large majority of the phonon modes show increase in the phonon population due to phonon-phonon interaction. Interestingly enough, a small percentage of phonons close to the zone center actually have a decrease in the phonon populations. This is even more intriguing considering that these modes are expected to soften the most.

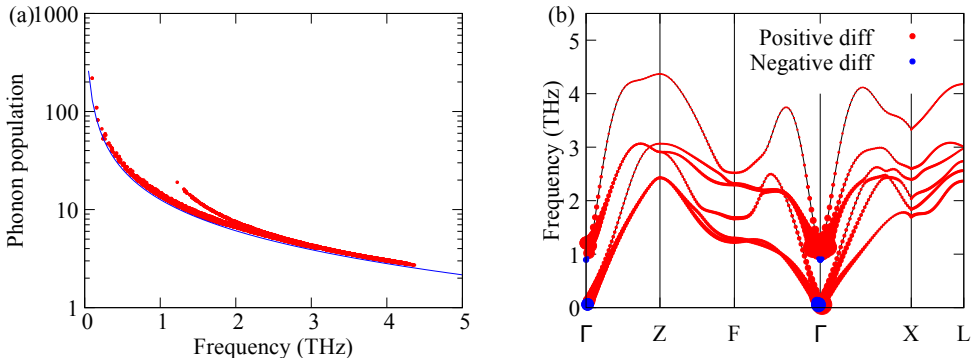

Figure 5.10: (a) Phonon populations obtained using the phonon displacement autocorrelation function at 631 K. The line represents the Bose-Einstein factor at 631 K. (b) Differences between the calculated values of phonon populations and the Bose-Einstein factor along the high symmetry lines. The size of the point is proportional to the log of the difference.

Finally, we highlight the advantages of the Green-Kubo method we implemented here over the standard approaches for computing κ in strongly anharmonic materials. Unlike the Boltzmann transport equation, the Green-Kubo method accounts for non-Lorentzian shapes of phonon spectral functions. It is possible to include these effects also by running long molecular dynamics (MD) simulations. Compared to MD, the Green-Kubo method presented here is faster and easier to converge, which is particu-

larly important if these methods are combined with first principles calculations. The results obtained using this approach are easier to interpret and analyze compared to traditional MD approaches. Unlike MD simulations, the Green-Kubo method uses the Bose-Einstein statistics for phonons. Additionally, this method gives the non-diagonal part of lattice thermal conductivity, accounting explicitly for the whole phonon power spectra. The method of Refs. [185, 186] includes only the values of the phonon self-energy at the harmonic frequency in the evaluation of the non-diagonal contribution to κ and are not applicable to strongly anharmonic materials.

5.4 Conclusion

In conclusion, we have performed a detailed first principles study of the lattice thermal conductivity κ of GeTe close to the ferroelectric phase transition. Strong anharmonicity minimizes the acoustic phonon modes lifetimes at the phase transition. However, using the Boltzmann transport equation, we calculate an increase in the lattice thermal conductivity at the phase transition, in agreement with experiments. In the rhombohedral phase, this effect is due to negative thermal expansion that increases phonon group velocities. In the cubic phase, the increase in κ is primarily driven by increased phonon lifetimes due to smaller anharmonicity of phonon modes compared to the rhombohedral phase.

We implement a novel approach to compute lattice thermal conductivity that includes the observed non-Lorentzian power spectra of phonon modes. Using the new approach, we find that the calculated κ increases even further at the phase transition, which is the consequence of larger phonon populations due to softening of the phonon modes caused by phonon-phonon interaction.

Chapter 6

Structural, electronic and transport properties of ferroelectric domain walls in GeTe

6.1 Introduction

Optimizing thermoelectric properties of materials has been proven to be a very difficult task [1, 33, 32]. One must reduce the thermal conductivity of the material, while simultaneously improving, or at least not degrading, the power factor (the product of the electrical conductivity and the square of the Seebeck coefficient $PF = \sigma S^2$).

Reducing the lattice thermal conductivity κ_L seems like a most promising path, since κ_L is the phonon transport phenomena that can be somewhat decoupled from electronic transport properties. One way of achieving reduced κ_L is the inclusion of crystallographic defects, such as vacancies, dopant ions, grain boundaries etc [167, 59, 56, 171]. A less explored route for lowering κ_L in ferroelectric materials (for example GeTe) is the domain structure formation. Domains (regions with collinear polarization) are separated by domain walls, which could be efficient phonon scatterers [187]. These 2D structures could complement existing phonon scattering centers (point defects) to achieve a maximum reduction of κ_L. The additional benefit of these structures is that they are easily manipulated, i.e. they can be created, erased, or moved by applying an external electric field, light, strain etc [182, 188].

Increasing the power factor of a material is an even more challenging task. One must increase either the Seebeck coefficient S or the electrical conductivity σ, without sub-

stantially decreasing the other. A promising route of enhancing the power factor is reducing the dimensionality of the system [62, 189, 63, 64] which increases the electronic density of states close to the band edges. This is usually achieved by trapping free charge carriers at the interfaces or surfaces of a material [67]. This could be achieved at charged domain walls (domain walls at which the polarization discontinuity induces the bound charge).

GeTe is a ferroelectric material below 700 K and as such can have a domain structure. Available experimental data agree that herringbone domain structures are present in GeTe samples, but they disagree on the predominant types of domain walls (DWs). Ref. [80] reported (001), $(1\bar{1}0)$ and $(11\bar{1})$ DWs, while other studies [181, 183] found (001) and (110) DWs. The most recent work [190] claims that the herringbone structure is bounded by the (110) and (111) planes, stabilizing $(11\bar{1})$ DWs after doping GeTe with Sb and Si. In the light of these contradictory experimental findings, computational investigation of ferroelectric DWs in GeTe gains in importance.

In this chapter, we will investigate the influence of specific domain wall types on the thermoelectric properties of GeTe. First, we will give a short introduction about the domain wall phenomena, with a classification notation that we will be using to distinguish different types of domain walls. Second, we will explain how to construct different domain walls, with special emphasis on twinned domain wall structures. Thirdly, we will present the structural properties of DWs in GeTe, as obtained in DFT. Following that, we will estimate the influence of different domain walls on the electronic properties of GeTe. Finally, we will estimate the influence of DWs on the phonon and electrical transport properties of GeTe.

6.1.1 Domain walls - general comments

We discussed some of the physical properties of GeTe close to the ferroelectric phase transition in Chapters 3 to 5. We noted in the introduction that the phase transition in GeTe occurs due to the offset of the Te sublattice along the body diagonal of the conventional unit cell of GeTe. This cell is a cube, meaning there are four equivalent body diagonals along which the Te sublattice can distort. Consequently, there are eight local minima of the ground state of the rhombohedral structure of GeTe.

Since the symmetry breaking is spontaneous, none of these eight directions is preferential and the order parameter can take any of these eight values during the phase transition. According to this simplified picture, we will have a random distribution of the order parameter throughout the crystal, with the order parameter still zero on

average. This resembles an order-disorder type of the phase transition [155, 4], where we have local distortions of the high symmetry phase, while the order parameter is still zero for the global structure. However, the local interaction between order parameters (dipole-dipole interaction in the case of ferroelectric materials) will make a collinear orientation of the local order parameters more energetically favorable and will drive the system to a lower symmetry phase (with the order parameter different from zero). This is true for infinite lattices. Finite, real-world, lattices will have surfaces and the divergence of the polarization at these surfaces would make a huge electric field along the crystal, making this structure unstable. To counter this effect, the crystal will spontaneously form a domain structure [188]. Domains are regions with collinear order parameter (in our case polarization). These regions are separated by domain walls where the polarization suddenly changes orientation from one domain to another (an example of the domain structure is given in Fig. 6.1).

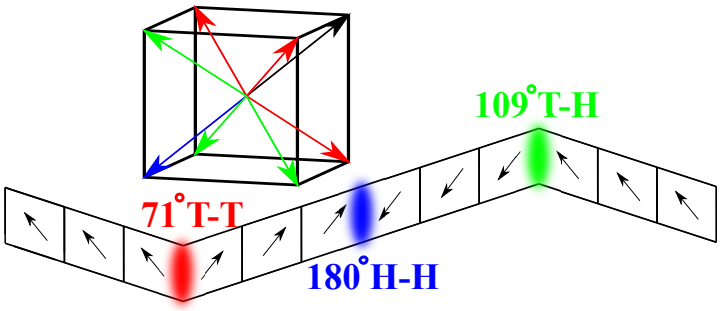

Figure 6.1: An example of the domain structure in a ferroelectric material. Different polarization directions in a single domain are color coded (top) and the boundaries between these domains correspond to different types of domain walls (bottom). The domain wall boundary for this configuration of domains is one of the faces of the cube, (001) plane. Tail-to-tail, head-to-head and tail-to-head domain walls are labeled as T-T, H-H and T-H, respectively.

The polarization change along the domain wall can be derived by minimizing the total free energy of the system (Φ) with respect to polarization. We start from the definition of the free energy similar to the Ginzburg-Landau theory, without the coupling to external fields or strains to the lowest order sufficient to describe phase transition in order to keep the picture simple:

$$\Phi = \Phi_0 + \frac{a}{2}P^2 + \frac{b}{4}P^4 + \frac{c}{2}(\frac{\partial P}{\partial x})^2. \tag{6.1}$$

If $a < 0$, the first two polarization (P) dependent terms give us a double well potential used in the Ginzburg-Landau theory of second order phase transitions [54]. The final term containing a derivative of the polarization with respect to the spatial coordinate (x) gives us the local mode coupling discussed above as the reason for a collinear orientation of the polarization in the low symmetry phase. This term is similar to the

exchange interaction term in the Ising model. To find the minimum of the total energy, we take the first derivative of Φ with respect to polarization [191]:

$$\frac{\partial \Phi}{\partial P} = aP + bP^3 + c\frac{\partial P}{\partial x}\frac{\partial}{\partial P}\frac{\partial P}{\partial x} = \\ = aP + bP^3 + c\frac{\partial^2 P}{\partial x^2} = 0. \tag{6.2}$$

The solution of the above equation is the soliton which we call a domain wall (DW):

$$P(x) = P_0 \tanh(\frac{x}{w}). \tag{6.3}$$

Here the coefficients $P_0 = \sqrt{-\frac{a}{b}}$ and $w = \sqrt{-\frac{c}{a}}$ are chosen to satisfy the boundary conditions $P(0) = 0$ (the center of the domain wall as suggested by Eq. (6.3)) and $P(\infty) = P_0$. P_0 is the polarization inside the domain far from the domain wall, while w is the half of the domain wall width.

We can systematize ferroelectric domain walls according to several criteria. The first criterion is the nature of the polarization change along the domain wall. In the example above (see Eq. (6.3)), polarization can only change in magnitude along the domain wall. This type of domain wall is the Ising domain wall and it is the most common among the ferroelectric materials. Polarization can also change its orientation along the domain wall. This can be represented with the potential in Eq. (6.2) by including two spatial dimensions in the definition of polarization, meaning that the interaction parameters become a tensor rather than a scalar. The solution for the components describing the rotation of the polarization vector has a kink like solution, rather than the soliton-like in Eq. (6.3) [192]. Depending on how orientation occurs in relation to the domain wall plane, domain walls can be of Bloch or Néel character [193]. If the polarization rotates in the domain wall plane, DW is of Bloch type and if the rotation is perpendicular to DW plane, it is of Néel type. Due to large strain-order parameter coupling, these types of domain walls are far less common in ferroelectrics compared to magnetic materials. If they occur, they are of the mixed type, Néel/Bloch with a large Ising character.

Considering the orientation of the polarization inside the domain with respect to the domain wall plane gives us another way to systematize domain walls. Namely, if polarizations point to the domain wall plane in both domains, that domain wall is called head-to-head (H-H). Similarly, if they point away from the domain wall plane, they are called tail-to-tail (T-T). In the mixed case, where polarization in one domain points towards and in another away from the DW plane, the domain wall is called

head-to-tail (H-T), or alternatively tail-to-head (T-H). These orientations will have a large influence on the structure and the electronic properties of the domain wall.

The final property by which we will distinguish domain walls is the crystallographic plane they occur on. To characterize domain walls in GeTe by the domain wall plane, we will use Miller indices of the crystallographic planes parallel to the DW plane for the cubic structure. Not every crystallographic plane can host a domain wall, or rather not all of the domain walls will have reasonable domain wall energies. The main condition for the mechanical stability of the domain wall is that there is no excess stress at the domain wall plane due to different spontaneous strain in the neighboring domains [194, 195]. The easiest way to visualize this condition is to imagine if any geometrical figure inside the DW plane is being distorted due to the difference between spontaneous deformations in the neighboring domains. From this, it is intuitive to see that if the domain wall plane is a mirror plane, it will fulfill this condition. Spontaneous strain due to a structural phase transition can be represented by the strain tensor S_{ij} that converts the high symmetry structure to the low symmetry one. To ensure there is no change of volume between two structures, the trace of $\hat{S}$ is zero. Now let's say that some vector $\vec{l}$ with components (l_1, l_2, l_3) is subjected to this strain field. It will be displaced by the vector:

$$dl_i = \sum_j S_{i,j} l_j. \tag{6.4}$$

Now let us say that there is some equivalent domain state characterized by the strain tensor S'_{ij}. These two domain states can share a crystallographic plane (the crystallographic plane can be the domain wall plane) if the magnitude of the displacement of the vector $\vec{l}$ in both domains is equal. So the condition that some crystallographic plane can host a domain wall between certain domains characterized by the spontaneous strain tensors S_{ij} and S'_{ij} is:

$$(S_{ij} - S'_{ij}) l_i l_j = 0. \tag{6.5}$$

We will show that this condition is satisfied for the case of $(11\bar{1})$ 39° domain walls for GeTe (here the 39° is the angle between polarizations in the neighbouring domains). This type of domain walls is not in the usual libraries of allowed domain walls for this phase transition, but nonetheless it satisfies the above condition. The spontaneous strain field for the transition from the cubic to the rhombohedral structure (Fm3m →

F$\bar{3}$m) is [196]:

$$S = \begin{pmatrix} 0 & t & t \\ t & 0 & t \\ t & t & 0 \end{pmatrix}. \tag{6.6}$$

This strain field induces distortion along the [111] direction. For the domain on the other side of (11$\bar{1}$) 39° DW, the spontaneous strain tensor is:

$$S' = \begin{pmatrix} 0 & t & t \\ t & 0 & t \\ -\frac{t}{3} & -\frac{t}{3} & \frac{4t}{3} \end{pmatrix}. \tag{6.7}$$

Using Eq. (6.5) we get:

$$(S_{ij} - S'_{ij}) l_i l_j = \frac{-4t}{3} l_3 (l_1 + l_2 - l_3) = 0. \tag{6.8}$$

From the equation above we can see that two crystallographic planes satisfy the condition, (001) and, the one we were expecting, (11$\bar{1}$) [194].

Depending on how polarization changes at the domain wall, some domain walls can be charged, meaning they host bound charge. If we follow the Gauss law for the polarization we can see that the change in polarization can create bound charge (ρ_b) [188]:

$$div\vec{P} = -\rho_b. \tag{6.9}$$

Since domain walls are 2D objects, the above equation is more commonly written as:

$$\sigma_b = (\vec{P}_1 - \vec{P}_2) \cdot \vec{n}, \tag{6.10}$$

where $\vec{P}_{1,2}$ are the polarization vectors in the first and the second domain, $\vec{n}$ is the unit vector of the domain wall plane, and σ_b is the surface-bound charge density. As one can imagine, the bound charge induces large electrostatic energy, so charged domain walls are not very common. However, the electrostatic energy can be reduced by screening from free charge carriers, electrons and holes. The system of two consecutive charged domain walls (which have to be oppositely charged due to the law of charge conservation) effectively form a parallel plate capacitor type of configuration, inducing an electric field along the domain (for illustration see Fig. 6.2). This electric field

attracts electrons and holes to opposite domain walls. Because of this, charged domain walls are usually doped, n or p-type depending on the polarization change with respect to the domain wall orientation.

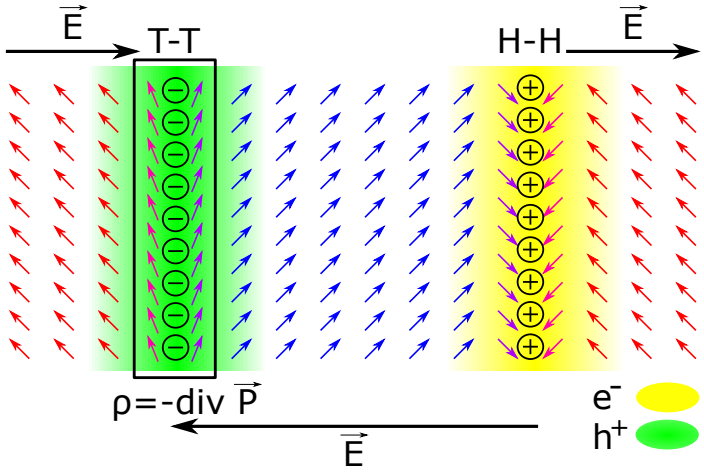

Figure 6.2: Illustration of a ferroelectric material containing charged domain walls (DWs). Coloured arrows denote the polarization orientations. DWs are the interfaces between domains with different polarization orientations. There are head-to-head (H-H) and tail-to-tail (T-T) charged DWs, depending on the polarization orientation with respect to the DW plane. In this figure, different polarization changes at DWs only give a qualitative illustration of the actual polarization differences between DWs. The polarization changes at these DWs form bound charge (labelled by plus and minus). The direction of the electric field induced by the bound charge is given with the black arrow. The electric field localizes free charge carriers on the DWs (green - holes, yellow - electrons). In the 39° $(11\bar{1})$ DWs considered here, the angle between the polarizations in neighbouring domains is 39°, and the DWs are in the $(11\bar{1})$ plane.

6.2 Results

6.2.1 Construction of domain walls in germanium telluride

As we saw in Chapter 3, germanium telluride (GeTe) crystallizes in the rhombohedral structure below 700 K. This means it exhibits a spontaneous polarization in this phase due to an offset of the tellurium sublattice from the high symmetry position. This distortion is usually taken to be along the z-direction (the [111] direction in the Miller indices) and it determines the anisotropy of the system.

Due to the relative simplicity of GeTe (only two atoms per primitive unit cell), we have a large number of possible choices for the unit cell with a relatively small number of atoms. This is important since any crystallographic plane that is also a mirror plane for two domains can be a host for a domain wall (see the previous section). Any of the

bounding planes of the unit cell can be a mirror plane, leading to the conclusion that any of these planes can host a domain wall. Possible choices for the unit cell of GeTe are the conventional rhombohedral unit cell (2 atoms), the pseudocubic unit cell (8 atoms), and the hexagonal unit cell (6 atoms). We can construct larger unit cells, like the orthorhombic one, but we will not consider them in this study. The rhombohedral cell is bounded by the crystallographic planes of $(11\bar{1})$ type, the pseudocubic one by the (001) plane, and the hexagonal one due to the anisotropy is bound by the (111) and $(1\bar{1}0)$ planes. The possible angles between polarization in different domains for these domain walls are 39°, 141° and 180° for $(11\bar{1})$ DWs, 71°,109° and 180° for (001) DWs (these domain walls are shown in Fig. 6.1) and 180° for the hexagonal ones. Head-to-tail type domain walls are 141° $(11\bar{1})$, 109° (001) and 180° $(1\bar{1}0)$ domain walls. The rest of the domain walls can be either head-to-head or tail-to-tail. All of the considered H-T and T-H domain walls are charge neutral, while H-H are positively and T-T DW are negatively charged. In the following section, we will explain how to construct each of these domain walls and define some of the properties we will use later.

First-principles calculations of 71° and 109° domain walls have already been attempted for $BaTiO_3$ [193] and $BiFeO_3$ [197]. Authors in these papers took advantage of the fact that in both cases the rhombohedral distortion is vanishingly small, so the cubic approximation of the unit cell is valid. However, this is not the case in GeTe. The low temperature value of the rhombohedral angle in GeTe is 57.825° [20], which is well captured with our density functional theory (DFT) calculation yielding 57.776°. Such a large value of the rhombohedral distortion makes the task of constructing GeTe supercells that contain DWs more difficult than that for cubic materials [193, 197, 198, 199, 200], since we need to realistically represent twinning due to lattice orientation mismatch at the DW boundary. Twinning does not occur for 180° DWs and their construction is straightforward.

The construction of 39° and 141° twinned domain walls in GeTe for the purposes of our DFT calculations is as follows. The primitive unit cell of rhombohedral GeTe is defined by the translation vectors:

$$\begin{aligned} \vec{r}_1 &= a(b, 0, c), \\ \vec{r}_2 &= a(-\frac{b}{2}, \frac{b\sqrt{3}}{2}, c), \\ \vec{r}_3 &= a(-\frac{b}{2}, -\frac{b\sqrt{3}}{2}, c), \end{aligned} \tag{6.11}$$

where a is the lattice constant, $b = \sqrt{2(1-\cos\theta)/3}$, $c = \sqrt{(1+2\cos\theta)/3}$, and θ is the

rhombohedral angle of GeTe. We choose one of the crystallographic planes in the primitive unit cell to be our domain wall boundary, for example $(11\bar{1})$. In this case, we keep the first and second lattice vectors unchanged prior to the structural relaxation and they are identical in both domains. The $(11\bar{1})$ plane will be a mirror symmetry of our domain structure. We calculate the third primitive lattice vector of the second domain $\vec{r''}_3$ using the fact that the plane $(11\bar{1})$ is the mirror plane:

$$\vec{r''}_3 = a(K_1\frac{b}{2}, K_1\frac{b\sqrt{3}}{2}, K_1 c - \frac{4c}{1+3c^2}),$$

where $K_1 = \frac{9c^2-1}{1+3c^2}$. The calculation of ground state properties of rhombohedral GeTe with this constructed lattice vector $\vec{r''}_3$ yields the same results as the calculation with $\vec{r'}_3$, proving we have the identical structure with different orientations of the polarization vector. The graphic representation of this structure is given in Fig. 6.3. We defined the third lattice vector $\vec{r}_3$ for the entire structure, see Fig. 6.3, as:

$$\vec{r}_3 = N(\vec{r'}_3 \cdot \vec{n})\vec{n} = Na(-K_2 c, -K_2\sqrt{3}c, K_2 a), \tag{6.12}$$

where N is the number of primitive unit cells in the supercell containing domain walls, $K_2 = \frac{3bc}{1+3c^2}$ and $\vec{n}$ is the unit vector normal to the plane $(11\bar{1})$:

$$\vec{n} = \frac{\vec{r}_1 \times \vec{r}_2}{|\vec{r}_1 \times \vec{r}_2|}. \tag{6.13}$$

After constructing the supercells described above, we relax the atomic positions and structure using DFT. First we relax the positions of Te atoms, keeping Ge atoms and the global structure (the unit cell vectors $\vec{r}_1$, $\vec{r}_2$ and $\vec{r}_3$) fixed. In this case, forces after relaxation are around 10^{-4} eV/Å inside the domains and can be as large as 0.1 eV/Å at the DW. The second step is the relaxation of the local structure through the relaxation of Ge atomic positions and the supercell lattice vectors, along with further optimization of Te atomic positions. After this step, atomic forces are lower than 10^{-6} eV/Å even for atoms at the DW. We used these structures for the calculation of DW energies and widths, and local structure distortions.

Next we define local structure parameters, which are descriptive of one primitive unit cell within the constructed supercell. We describe the local lattice constant for the ith primitive cell away from the DW as the distance between two neighboring Ge atoms:

$$a_i = |\vec{a}_i| = |\vec{r}_{Ge,i} - \vec{r}_{Ge,i+1}|. \tag{6.14}$$

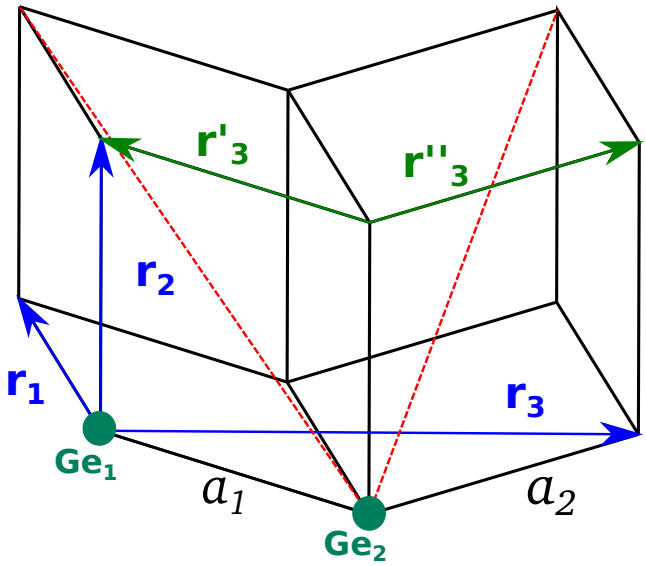

Figure 6.3: Geometry of GeTe domain structure containing 39° or 141° (11$\bar{1}$) domain walls for the case where domains are one unit cell long. Blue lines are the unit cell vectors of the domain structure, while green vectors represent the third primitive lattice vectors of individual domains. Red dashed lines represent polarization directions in different domains. The positions of Ge atoms are labeled as Ge_1 and Ge_2. The lattice constants of the two primitive unit cells that constitute this supercell are labeled as a_1 and a_2.

The local rhombohedral angle for the same primitive cell is calculated from the scalar product of $\vec{a}_i$ with the first supercell translation vector $\vec{r}_1$ (using $\vec{r}_2$ yields the same result):

$$\theta_i = \arccos \frac{\vec{a}_i \cdot \vec{r}_1}{|\vec{a}_i||\vec{r}_1|}. \tag{6.15}$$

We define the local polarization vector for each primitive cell as the vector between Te atom and the high symmetry point (0.5,0.5,0.5) inside the same primitive cell and normalize its value so that the polarization magnitude along the trigonal axis inside the domain is one. Polarization profiles are taken along different directions illustrated in Fig. 6.4. The first direction is along the trigonal axis inside a particular domain, $P_{\parallel}$ (red color in Fig. 6.4). This direction changes from one domain to another (from $P_{\parallel}$ to $P'_{\parallel}$). The second direction is along the vector normal to the plane defined by the trigonal axes in neighbouring domains P_n (black vector in Fig. 6.4), which corresponds to the Bloch component of polarization. The third direction is chosen to form the orthogonal coordinate system with the first two directions inside individual domains (blue vectors labeled as $P_{\perp}$ and $P'_{\perp}$ in Fig. 6.4), representing the Néel components of polarization.

To extract domain wall widths, we fit the polarization profiles along the trigonal axes

to the expression:

$$p(d) = P_0 \tanh \frac{2(d - d_0)}{w}. \tag{6.16}$$

Here w is the DW width, d_0 is the position of the DW boundary and P_0 is the polarization value inside domains.

Domain wall energies are calculated as:

$$E_{DW} = \frac{E_1 - E_0}{2S}, \tag{6.17}$$

where E_1 is the total energy of the relaxed domain structure, E_0 is the total energy of bulk GeTe with the same number of atoms as the supercell containing DWs, and S is the area of the DW boundary. Due to periodic boundary conditions, our supercells with a H-H DW must also contain a T-T DW. Therefore we can only calculate an average domain wall energy for a certain DW angle.

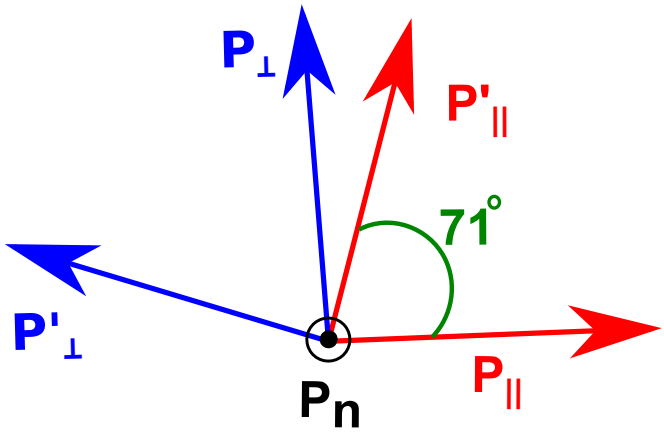

Figure 6.4: Polarization directions inside each domain for GeTe structures containing 71° or 109° $(11\bar{1})$ domain walls (illustration for 39°/141° DW is the same with appropriate angle between $P_{||}$ and $P'_{||}$). Polarization directions in two neighboring domains are labeled as primed and non-primed. $P_{||}$ is the direction along the trigonal axis. P_n is the direction normal to the plane of the trigonal axes in neighboring domains and corresponds to the Bloch character of polarization. The third direction, $P_{\perp}$, is perpendicular to the other two directions and quantifies the Néel character of polarization.

In the case of 180° $(11\bar{1})$ DWs, there is no twinning at the domain boundary and the construction of supercells containing these DWs is trivial. The definition of the polarization directions for these supercells is somewhat ambiguous, since the polarization vectors in neighboring domains are collinear. We choose the supercell in which the polarization directions inside domains are along the z Cartesian axis. We define the Bloch component of polarization along the direction perpendicular to the z axis and the vector of the DW boundary. This allows us to define the Néel component along the

direction perpendicular to the z axis and the Bloch component.

We construct supercells containing 180° (111) and $(1\bar{1}0)$ DWs from the hexagonal unit cell of GeTe. The hexagonal unit cell is defined with the following set of lattice vectors:

$$\begin{aligned}\vec{h}_1 &= a(\frac{\sqrt{3}b}{2}, -\frac{3b}{2}, 0),\\ \vec{h}_2 &= a(\frac{\sqrt{3}b}{2}, \frac{3b}{2}, 0),\\ \vec{h}_3 &= a(0, 0, 3c).\end{aligned} \tag{6.18}$$

The definition of parameters a, b and c are the same as in the case of the rhombohedral cell. The positions of atoms in this unit cell are: Ge ((0.0, 0.0, 0.0), (2/3, 1/3, 1/3), (1/3, 2/3, 2/3)) and Te ((0.0, 0.0, 0.5+τ), (2/3, 1/3, 5/6+τ), (1/3, 2/3, 1/6+τ)). (111) DWs are perpendicular to the trigonal axis, while $(1\bar{1}0)$ DW boundary contains the trigonal axis. For (111) DWs, the trigonal axis is oriented along the z Cartesian axis, and polarization directions correspond to the Cartesian axes. For $(1\bar{1}0)$ DWs, the Néel component of polarization is the vector of the DW plane, while the Bloch component is perpendicular to it and the trigonal axis.

(001) DWs are constructed in a similar manner as $(11\bar{1})$ DWs, but using the pseudocubic unit cell (conventional rocksalt structure) vectors:

$$\begin{aligned}\vec{p}_{c1} &= a(-2b, 0, c),\\ \vec{p}_{c2} &= a(b, -b\sqrt{3}, c),\\ \vec{p}_{c3} &= a(b, b\sqrt{3}, c).\end{aligned} \tag{6.19}$$

Parameters a, b, and c are the same as for the rhombohedral cell. We have tried performing relaxation of these domain walls as well. The relaxation of these structures proved to be very computationally expensive, mostly because these domain walls have approximately four times more atoms per domain length compared to $(11\bar{1})$ DWs. In the case of charged DWs, polarization discontinuity induced bound charge is larger at the (001) DWs making them harder to relax. However, we expect similar structural and electronic properties for (001) DWs as for $(11\bar{1})$ and (111) DWs.

6.2.2 Technical details of electronic structure calculations

DFT calculations were performed using the plane wave basis set, the generalized gradient approximation with Perdew - Burke - Ernzerhof parametrization (GGA-PBE) for the exchange-correlation potential [86] and Hartwigsen - Goedecker - Hutter (HGH) pseudopotentials [144] as implemented in the ABINIT code [87, 88]. We used the energy cutoff of 16 Ha for plane waves in all cases. We performed a convergence study of the DW widths and energies with respect to the domain size for all considered DWs (see Appendix B). We carried out DFT calculations on $1\times1\times N$ supercells containing $(11\bar{1})$ DWs, where N is 32 for 39° and 141° DWs (64 atoms) and 40 for 180° DWs (80 atoms). We used a $4\times4\times1$ $\vec{k}$-point grid for the Brillouin zone sampling of the electronic states of $(11\bar{1})$ DWs. For (111) and $(1\bar{1}0)$ DWs, we used $1\times1\times24$ and $24\times1\times1$ supercells formed from the hexagonal unit cell (144 atoms). We used $4\times4\times1$ and $1\times12\times4$ $\vec{k}$-point grids for sampling the Brillouin zone for (111) and $(1\bar{1}0)$ DWs, respectively. We used "cold smearing" for electronic states [201] due to the existence of metallic states in some of the structures. All calculations were done excluding spin-orbit coupling.

6.2.3 Structural properties of domain walls

6.2.3.1 Structural properties of $(11\bar{1})$ domain walls

The domain wall energies and widths of $(11\bar{1})$ DWs are presented in Table 6.1 [1]. The energy cost of DW formation is the largest for 39° DWs, and the lowest for 180° DWs. Compared to $BaTiO_3$ neutral DWs [193], GeTe DWs can have up to 100 times larger DW energies. However, compared to charged DWs in perovskite materials [192, 197], DWs in our calculations have comparable energies. GeTe $(11\bar{1})$ DW energies and widths exhibit a few obvious trends. Charged DWs (39°) usually have larger energies than the neutral one (141°). Twinning also gives a large contribution to the DW energy (compare the DW energies of twinned 39° and 141° DWs with those of 180° DWs). The DW energies of 180° and 141° DWs are similar because 180° DW is charged and 141° DW is neutral, but twinned.

We now discuss the polarization profiles along GeTe structures containing $(11\bar{1})$ domain walls. Bulk GeTe has a spontaneous polarization of 63 μC/cm^2, which is similar to that of perovskite materials [192, 197, 193]. The polarization along the trigonal axis

[1] For 39° tail-to-tail domain wall, polarization values along the trigonal axis in one of the domains were taken as negative to obtain the $\tanh(x)$ dependence of polarization, see Fig. 6.5(a).

Table 6.1: Domain wall (DW) widths and energies for (11$\bar{1}$) DWs. H-H and T-T denote head-to-head and tail-to-tail DWs, respectively. H-T and T-H denote head-to-tail and tail-to-head DWs, respectively.

	H-H width [Å]	T-T width [Å]	Average DW energy [mJ/m^2]
39° DW	3.4	4.4	547
180° DW	14.8	13.4	376
	H-T width [Å]	T-H width [Å]	Average DW energy [mJ/m^2]
141° DW	4.0	4.0	404

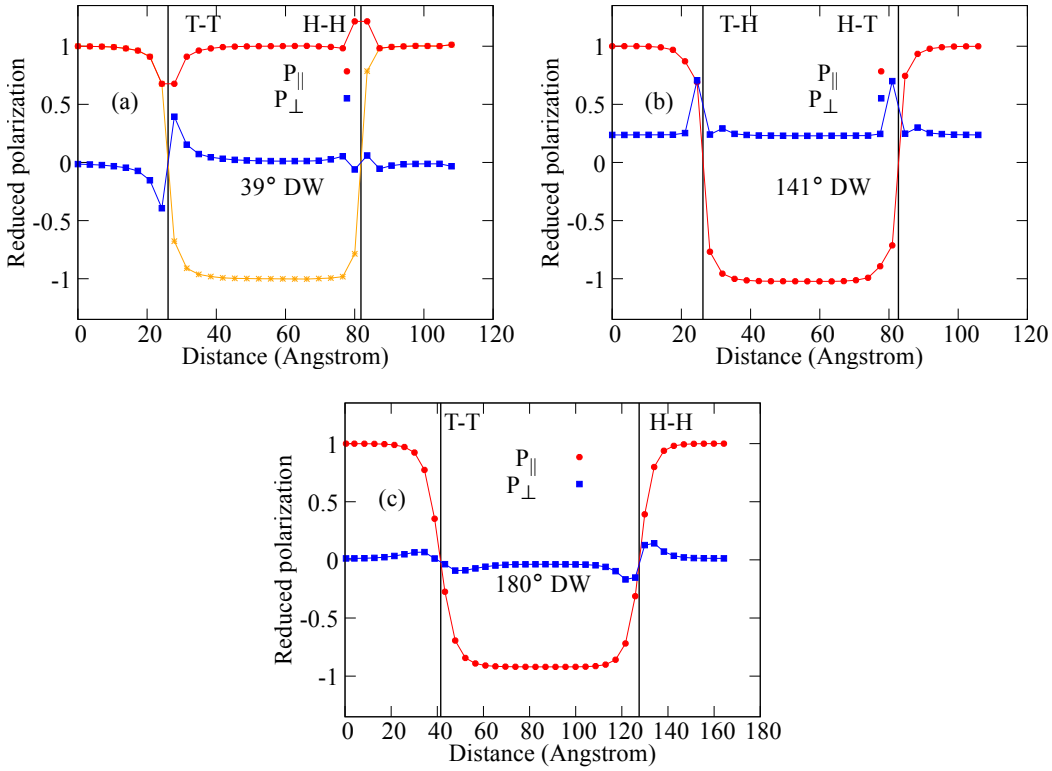

Figure 6.5: Polarization profiles for GeTe structures containing (a) 39°, (b) 141° and (c) 180° (11$\bar{1}$) domain walls (DWs). Red line represents polarization in the direction of trigonal axes of each domain ($P_{||}$), and blue line red shows the Néel component of polarization ($P_{\perp}$). DW boundaries are indicated by black vertical lines and labeled T-T for tail-to-tail, H-H for head-to-head, H-T for head-to-tail and T-H for tail-to-head DWs. For 39° T-T DW, $P_{||}$ values in one of the domains are plotted as negative (orange line) to aid visualization.

($P_{||}$) and the Néel component of polarization ($P_{\perp}$) for (11$\bar{1}$) DWs are given in Fig. 6.5. For all these DWs, the Bloch component of polarization is zero. The Néel character is stronger for T-T DWs with respect to H-H DWs with the same polarization angle. 141° DW has the strongest Néel character and 180° DWs have the strongest Ising character. Both 141° DWs have the same polarization profiles since they are of the H-T type, in contrast to 39° and 180° DWs.

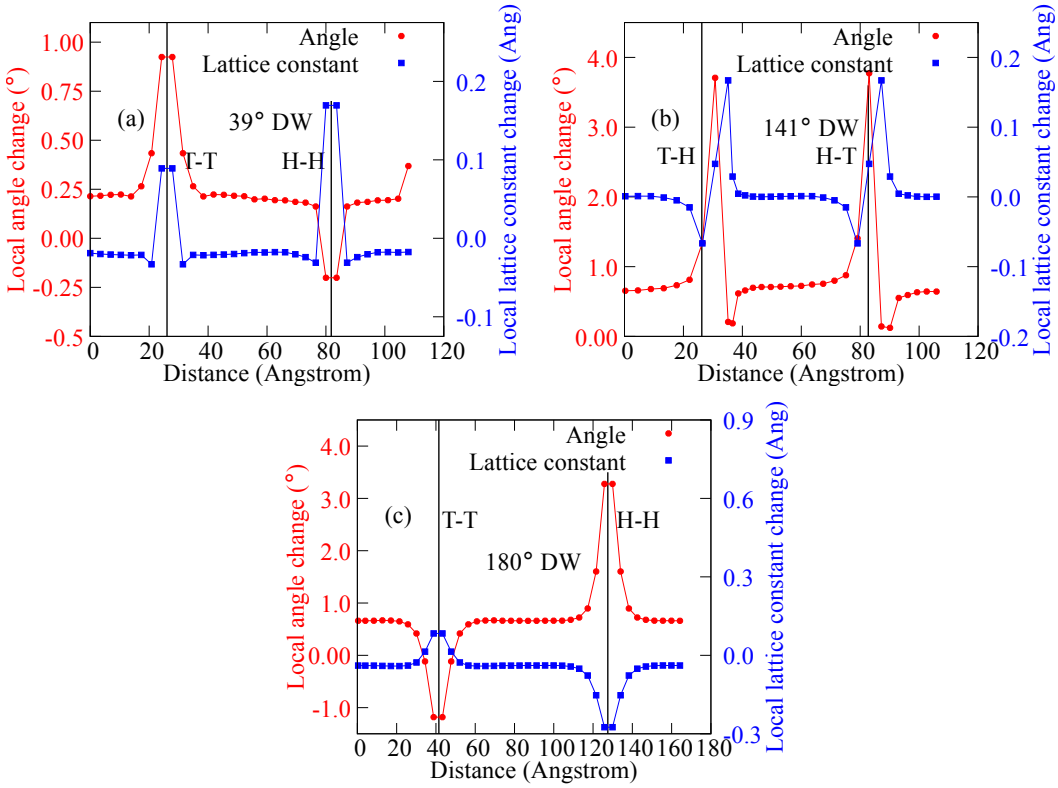

Figure 6.6: Local lattice constant (blue line) and local rhombohedral angle (red line) for GeTe structures containing (a) 39°, (b) 141° and (c) 180° $(11\bar{1})$ domain walls (DWs). DW boundaries are indicated by black vertical lines and labeled T-T for tail-to-tail, H-H for head-to-head, H-T for head-to-tail and T-H for tail-to-head DWs.

Next we illustrate large local structural distortions in the vicinity of $(11\bar{1})$ DWs. The local lattice constant and rhombohedral angle changes for supercells incorporating $(11\bar{1})$ DWs with respect to the bulk GeTe values are shown in Fig. 6.6. The structural distortions are the smallest in the case of 39° DWs, and are considerably larger for 141° and 180° DWs. We note that, even in the middle of each domain, there is a slight renormalization of the lattice constant and rhombohedral angle compared to the bulk values [79]. This is probably due to the small size of domains that do not perfectly screen the depolarizing field. Also, we point out the asymmetry of structural distortions for 141° DW with respect to the DW boundary, which is non-existent in other four types of $(11\bar{1})$ DWs, due to the difference in geometry.

It is interesting to compare the trends related to local structural changes near DWs to those observed in single crystalline GeTe near the ferroelectric phase transition. In GeTe undoped single crystals, the lattice constant and the internal atomic displacement decrease as the material approaches the phase transition with increasing temperature, while the angle increases [7, 8, 79]. For 39° H-H DW, the local lattice constant and polarization along the trigonal axis increase while the local rhombohedral angle de-

creases closer to the DW. Consequently, the local structure of 39° H-H DW exhibits the opposite trends to that of the single crystal near the phase transition. 180° H-H DW displays the same trends for the local structure as the single crystal near the phase transition, with decreasing lattice constant and polarization along the trigonal axis and increasing angle closer to the DW.

6.2.3.2 Structural properties of (111) and (1$\bar{1}$0) domain walls

Table 6.2 shows the domain wall energies and widths of 180° (111) and (1$\bar{1}$0) DWs. Their DW widths are larger compared to (11$\bar{1}$) DWs. We note that there is a difference in the DW widths for individual H-T and T-H (1$\bar{1}$0) DWs. It is unclear whether this is due to the finite size of domains, or there is a symmetry breaking we are not aware of. (1$\bar{1}$0) DW has the smallest energy among all investigated DWs. This is because (1$\bar{1}$0) DW is neutral and its electrostatic energy is small, its Néel component of polarization is small and there is no twinning at the DW boundary. On the other hand, (111) DWs have the highest energy among all considered DWs and this is mostly due to a large depolarization field caused by bound charge at the DW boundaries.

Table 6.2: Domain wall (DW) widths and energies for 180° (111) and (1$\bar{1}$0) DWs. H-H and T-T denote head-to-head and tail-to-tail DWs, respectively. H-T and T-H denote head-to-tail and tail-to-head DWs, respectively.

	H-H width [Å]	T-T width [Å]	Average DW energy [mJ/m^2]
(111) DW	22.6	19.4	686
	H-T width [Å]	T-H width [Å]	Average DW energy [mJ/m^2]
(1$\bar{1}$0) DW	9.7	8.4	25

Although our results suggest that the (1$\bar{1}$0) DW is much more energetically favorable than other DWs considered, we stress that this study is carried out on perfect crystals, without any imperfections. Including vacancies or interstitial atoms could considerably change the energetics of particulars domains, making other types of DWs more stable. This is somewhat confirmed by a recent experimental study [190], which shows that including impurities stabilizes (11$\bar{1}$) DWs.

The polarization profiles for (111) and (1$\bar{1}$0) DWs are given in Fig. 6.7. (111) DWs walls have pure Ising character, exhibiting only changes of the magnitude of polarization and not of the direction. This is primarily due to its geometry: the depolarization field is parallel to the polarization, and changing the direction of polarization would be energetically very expensive. The (1$\bar{1}$0) DW has a small but noticeable Bloch-Néel character. The existence of the Bloch component of polarization at this DW is unique

among the DWs considered. However, the Bloch and Néel components are too small to have a substantial effect on the electronic states.

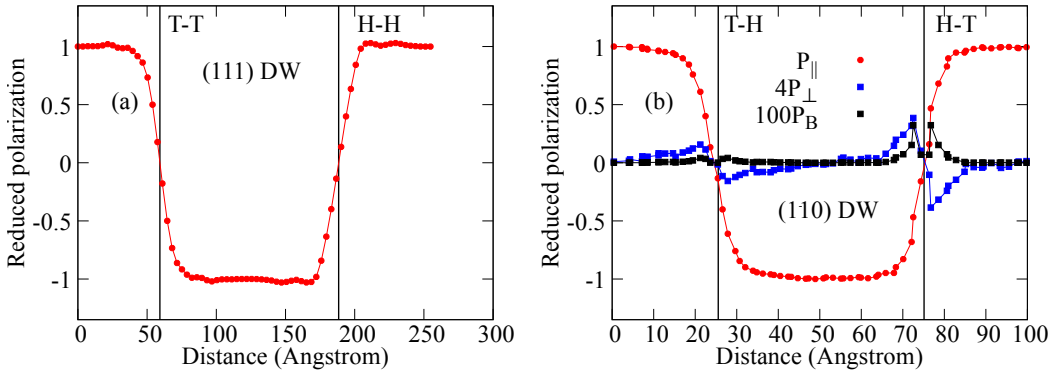

Figure 6.7: Polarization profiles for GeTe structures containing (a) (111) and (b) $(1\bar{1}0)$ domain walls (DWs). Red line represents polarization in the direction of the trigonal axis ($P_{\parallel}$), while blue and black lines represent the Néel ($P_{\perp}$) and Bloch (P_B) components of polarization (multiplied by constant values to make them visible on the graph). DW boundaries are indicated by black vertical lines and labeled T-T for tail-to-tail, H-H for head-to-head, H-T for head-to-tail and T-H for tail-to-head DWs.

Figure 6.8 illustrates local structural distortions for (111) and $(1\bar{1}0)$ DWs. Both (111) DWs have comparatively large changes of the local angle and lattice constant, similarly to $(11\bar{1})$ DWs. They exhibit the same trend as single crystalline GeTe near the phase transition [7, 8, 79]: increasing angle and decreasing lattice constant and polarization closer to the DW. This is expected due to the pure Ising character of this DW and the fact that the depolarizing field is collinear with polarization. Local structural distortions of $(1\bar{1}0)$ DW resemble numerical noise, since the structural changes along domains are smaller than the renormalization from the bulk values in the middle of domains. These effects as well as the differences in the polarization profiles and DW widths in $(1\bar{1}0)$ DWs may come from a small domain size used in our calculations. Using larger supercells is computationally expensive and the properties of $(1\bar{1}0)$ DW are not of significant immediate interest.

6.2.4 Electronic properties of domain walls

We have already commented on the occurrence of charged ferroelectric domain walls and how those can influence the electronic properties of these structures. In this section, we will give a detailed analysis of this effect.

In the case of $(11\bar{1})$ domain walls in GeTe, 39° and 180° domain walls are charged, while the 141° domain wall is neutral. H-H domain walls are positively charged, T-T

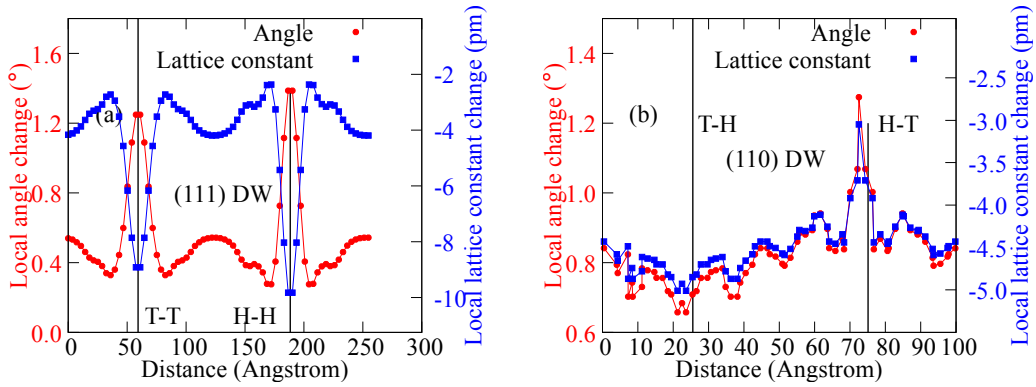

Figure 6.8: Local lattice constant (blue line) and local rhombohedral angle (red line) for GeTe structures containing (a) (111) and (b) $(1\bar{1}0)$ domain walls (DWs). DW boundaries are indicated by black vertical lines and labeled T-T for tail-to-tail, H-H for head-to-head, H-T for head-to-tail and T-H for tail-to-head DWs.

are negatively charged, while H-T (141°) DW are neutral [188]. This is easily confirmed by applying Eq. (6.10) to these cases. For example for 39° DW, the polarization vectors in two neighboring domains are in the directions [0,0,1] and [0.302, 0.523, 0.797] (Cartesian coordinates), while the vector of the domain wall plane is [0.474, 0.821, -0.319]. All of the numbers are taken for the 0 K structure of GeTe. Using the Gauss law, we conclude that the bound charge at the H-H 39° $(11\bar{1})$ DW is $\sigma_{39} = 0.64P_0$. In the case of 141° DW, the bound charge is zero as expected, and in the case of 180° H-H DW it is the same as for the 39° DW case. In the case of the T-T domain walls, we get the same numbers with the opposite sign.

The bound charge that occurs on these domain walls induces an electric field along the domains. If we use the Gauss law for the charged plane, we get that the electric field is given by $E = \sigma/\epsilon$, where σ is the surface charge of the domain wall and ϵ is the dielectric constant of the domain GeTe. This electric field will give another term in the external potential in DFT and will be visible in the graph of the total potential calculated in these structures. This is shown in Fig. 6.9 for 141° and 180° $(11\bar{1})$ DWs and Fig. 6.10 (a) for 39° $(11\bar{1})$ DW.

We have calculated the total potential of the domain structure for 20 planes per unit cell of the structure parallel to the domain wall plane. We sampled each plane using a uniform grid with the point density of 0.1 Bohr^{-2}. We then averaged the potential inside each plane (red line) and unit cell (blue line). Referring to Eq. (6.10), one would expect a slope only in the total potential for 39° and 180° domain walls, but no slope in the total potential for 141° DWs. However, the real picture is more complicated due to structural and atomic relaxation in the vicinity of the domain wall which induces a change in the potential even for neutral 141° domain wall. It is worth pointing out for

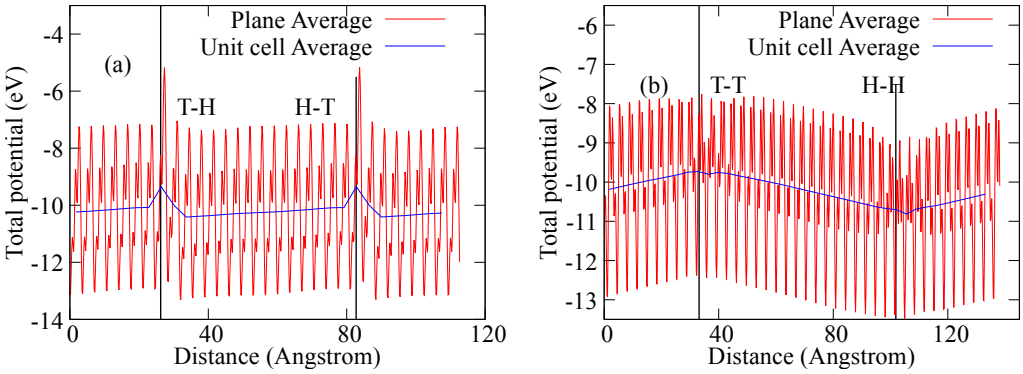

Figure 6.9: Total potential along the domain structure for (a) 141° and (b) 180° (11$\bar{1}$) domain walls. The red lines represent the plane average of the local potential in the plane parallel to the domain wall plane and blue lines are the unit cell average. Positions of the domain walls are represented by the vertical black lines and noted H-H for head-to-head, T-T for tail-to-tail and H-T for head-to-tail domain wall.

sufficiently large domains even charged domain walls (without structural relaxation) should not have the appreciable slope in the total potential. This is due to the screening by free charge carriers (electrons and holes) that would negate the influence of the bound charge. We can confirm this by calculating the total potential for the relaxed domain wall structure where we force the semiconducting occupation of electronic states, simulating a situation where there is no screening by free charge (see Fig. 6.10 (b)). We can see that the slope of the total potential and hence the electric field is larger for the case of semiconducting filling of electronic states, ie. without screening by free charge (16.6 meV/Å for the fully relaxed structure, 24.1 meV/Å for the structure with semiconducting occupation of electronic states).

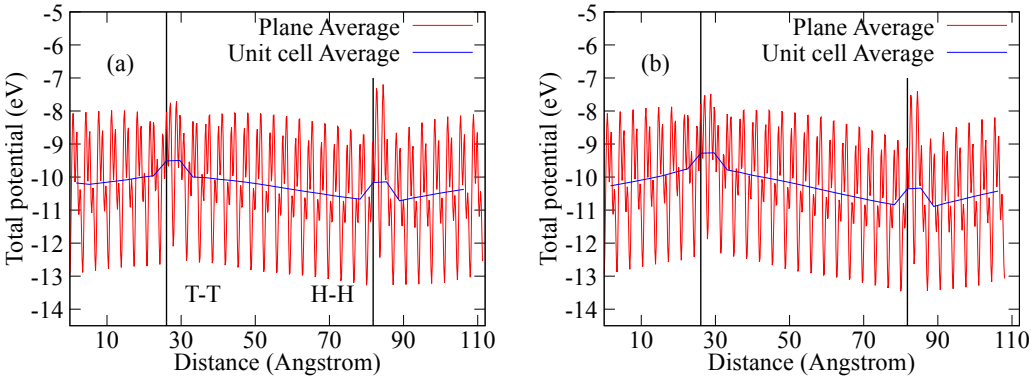

Figure 6.10: Total potential along the 39° (11$\bar{1}$) domain structure for (a) relaxed electronic occupations and (b) semiconducting electronic occupations. Red lines represent the plane average of the local potential in the plane parallel to the domain wall plane and blue lines are the unit cell average. Positions of the domain walls are represented by the vertical black lines and noted H-H for head-to-head and T-T for tail-to-tail.

Screening due to free charge carriers can be seen in the local electronic density of states (DOS) (the electronic density of states projected to specific atoms). We will define the domain wall density of states as the DOS projected to four-unit cells on each side of the domain wall (eight unit cells closest to the domain wall plane). The results for these three types of domain walls are shown in Fig. 6.11. Firstly, as we would expect from Fig. 6.9 and Fig. 6.10 H-H DWs are n-type doped, while T-T DWs are p-type doped. An interesting feature is that doping is contained to the domain walls, while the domain of GeTe stays semiconducting (the Fermi level is on the top of the valence band). This means that the charge and thus the electronic states are localized at the domain wall. Charged domain walls in GeTe could be regarded as a 2D electron gas, whose wavefunctions decay rapidly in the domain. The density of states of free 2D electron gas (described using the parabolic band model) has a step function dependence on energy. This is the feature that we can observe in the n-type doped domain walls (H-H 39° and 180° DW). Surprisingly, the p-type doped domain walls exhibit different types of energy dependence close to the band edge. A prominent peak in the local density of the state is observed for these types of domain walls. This peak resembles a resonant doping level in PbTe and GeTe that are experimentally shown to increase the Seebeck coefficient [68, 69].

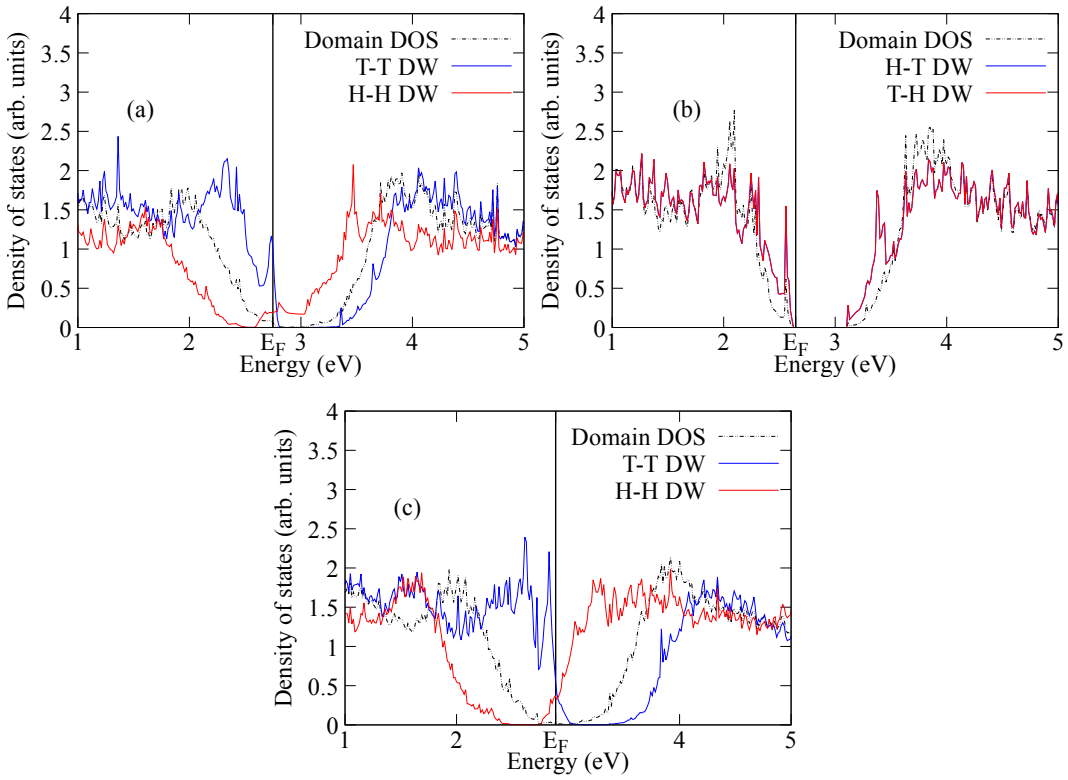

Figure 6.11: Local density of states for the structures with (a) 39°, (b) 141° and (c) 180° domain walls. Black vertical lines represent the intrinsic value of the Fermi level.

H-T and T-H 141° domain walls are not doped (see Fig. 6.11 (b)), as we would expect from the fact that they are neutral. The energy dependence of the DOS of these two domain walls is identical. However, this energy dependence is different compared to the unit cell (domain) DOS. Partially this could be expected due to large structural relaxation at the domain walls, however, the very narrow peaks in the DOS at the 141° domain walls could suggest that there might be a different origin. These very narrow peaks, similar to the Dirac delta function, are characteristic for 0D or 1D states.

To better understand the behavior of the electronic states close to the Fermi level, we calculated the electronic band structure of GeTe supercells with domain walls, projected onto the domain wall plane. The first Brillouin zone of this surface resembles a hexagon, with three distinctive high symmetry points (Γ (0, 0), X (0.5, 0.5) and K$(0.5 - 0.5\frac{\tan\left(\frac{180-\beta}{2}\right)}{\tan(180-\beta)}, 0.5\frac{\tan\left(\frac{180-\beta}{2}\right)}{\tan(180-\beta)} - 0.5)$). Here β is the angle between the reciprocal lattice vectors in that plane, which represent the projections of the reciprocal vectors of the real structure onto the DW plane. First, we find the set of points along the $X - \Gamma - K$ line so that their projection onto the vector of the domain wall plane is zero and then shift them along the first Brillouin zone parallel to the domain wall plane.

The electronic band structures obtained along the high symmetry lines described above are shown in Fig. 6.12 for twinned domain walls (39° and 141° DWs) and Fig. 6.13 (for 180° DWs). The blue lines represent the energies of the electronic states along the specified line for the zero projection of the reciprocal vector $\vec{k}_3$ onto the domain wall plane vector. The broadening of these lines is shown in red and represents the dispersion along the direction perpendicular to the domain wall plane (the $z \| \vec{k}_3$ direction). This means that the width of the red line corresponds to the bandwidth along the mentioned direction. Immediately it is obvious that states for the charged domain walls do not have broadening along the z direction. This means they are not dispersive along that direction and it is another proof of localization of these states[2]. For 39° DW, the conduction and valence states are strictly separated and the band structure of the full structure (H-H and T-T DWs) resembles a semimetal. This allows us to identify the top valence bands (the ones without dispersion in the z direction) as the T-T DW bands and bottom conduction bands as the H-H DW bands.

The simple resolution of the tail-to-tail and head-to-head domain walls' electronic band structures is not possible for 180° DW due to the large number of band crossings in the vicinity of the Fermi level. The crossings are especially prominent in the vicinity of the Γ point. To resolve the electronic band structure of each of the domain walls,

[2]The first hint of the localization of electronic states is given by the calculation of the DOS, which shows doping only at the charged domain walls and not in the domain.

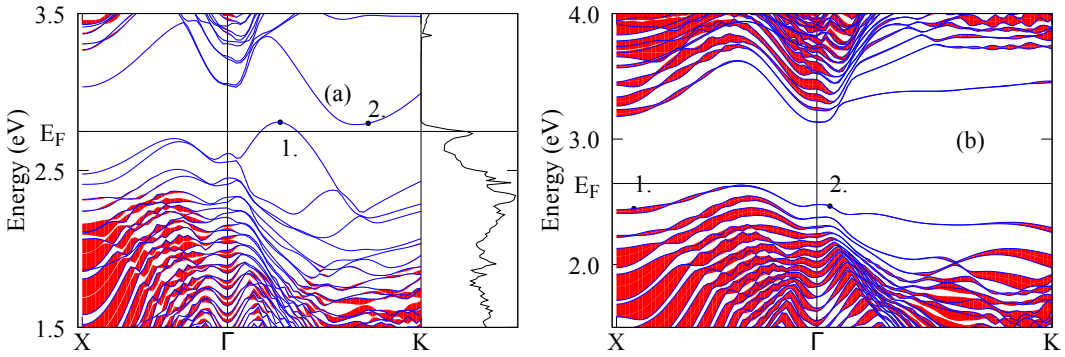

Figure 6.12: Projected electronic band structure along specific lines in the Brillouin zone for the structures with (a) 39° and (b) 141° domain walls. Blue lines are energies of electronic states with $k_3 = 0$, while the red broadening represents the dispersion of these states in the direction perpendicular to the domain wall. Horizontal lines are the values of the intrinsic Fermi level. The side plot in figure (a) represents local density of states for 39° T-T domain wall.

we calculated the wave function of each electronic state along the path in question (X-Γ-K). We calculated the charge density associated with each electronic state as the function of the coordinate perpendicular to the domain wall. We integrate the charge density over the regions belonging to H-H and T-T domain walls. We compare the integrated charge densities for a specific electronic state. If the charge density at the H-H DW is fifty times larger than at the T-T DW, we will attribute that state to the H-H DW and vice versa. When we do this for each electronic state, we obtain Fig. 6.13 (b). The red points denote the electronic states that belong to the H-H domain wall and the blue ones the states that are localized at the T-T DW. As expected, most of the conduction states are confined to the H-H domain wall and most valence states are confined to the T-T DW.

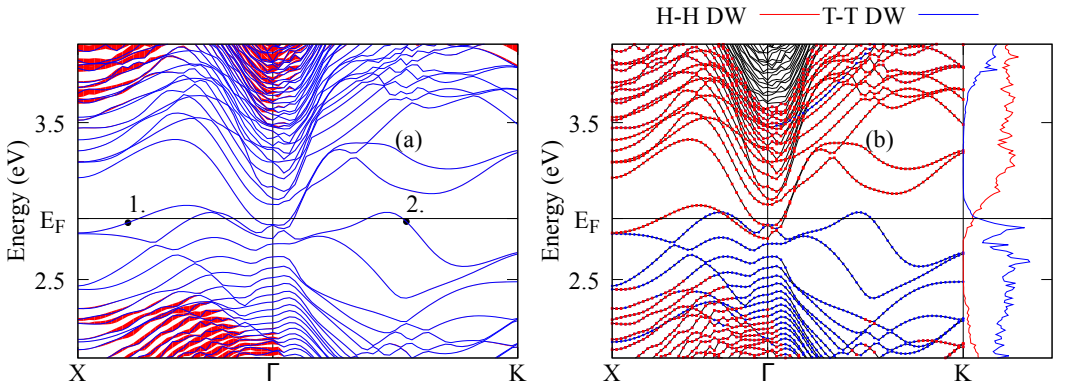

Figure 6.13: (a) Projected electronic band structure along specific lines in the Brillouin zone for the structures with 180° domain wall. Blue lines are energies of electronic states with $k_3 = 0$, while the red broadening represents the dispersion of these states in the direction perpendicular to the domain wall. (b) Electronic band structure of the same domain system resolved by a domain wall. The left side shows the 180° domain wall local density of states.

Neutral domain wall (141°) shows decreased broadening of the states close to the Fermi level (see Fig. 6.12 (b)), but the states are still somewhat dispersive along the z direction. Interestingly enough, the bandwidth of states close to Fermi level at this domain wall is smaller than for charged domain walls (here we mean bandwidth along the in-plane directions). This implies that the localization of these states (along the domain wall plane) is even stronger compared to charged domain walls. What causes a small localization length in these structures is up for discussion. One possible reason is that the Néel component of the polarization change, exceptionally strong at this type of domain walls, is actually causing a partial localization of states. Another possible reason is that the localization due to a mismatch of the Brillouin zones at the twinned domain walls weakly confines states. This is already experimentally observed for domain walls in 2D SnTe [202]. However, the localization occurs for the Γ point as well that should not be mismatched at this boundary.

We have calculated charge densities associated with some representative states for each domain wall (see Fig. 6.14). We can see that the states for the structures with charged domain walls close to the Fermi level that appear localized (through reduced dispersion along the z direction) are indeed localized at the domain walls. These states quickly decay away from the domain wall. For 141° neutral domain walls we have similar behavior. The states that we assumed are localized due to lack of dispersion along the z direction (Γ - K) line are localized at the domain walls. In this case, they are localized at both domain walls and decay only in the domain.

The electronic states localized at 39° (11$\bar{1}$) T-T DW have a sharp peak in the LDOS near the top of the valence band, as opposed to the step characteristic for 2D systems (see Fig. 6.11 (a)). Such distortion of the LDOS resembles those stemming from the resonant impurity levels in PbTe doped with Tl [68] and GeTe doped with In [69], which lead to an experimentally observed increase of the Seebeck coefficient. We will show that the LDOS peak of the T-T DWs also enhances the Seebeck coefficient even though its physical origin is very different from that of resonant impurities. The large increase of the LDOS near the Fermi level also occurs in 180° (11$\bar{1}$) T-T and 180° (111) DWs and may be a general feature for these systems.

To uncover the origin of the LDOS peak for 39° (11$\bar{1}$) T-T DW, we plot the LDOS of this DW together with the interface projected electronic band structure in Fig. 6.12 (a). We can see that the LDOS peak occurs at similar energy as the valence band maximum on the X - Γ line just below the Fermi level. The 2D dispersion of the electronic states of this particular band is given in Fig. 6.15. This figure shows that the states on the X - Γ line shown by blue points are actually saddle points in the electronic band structure:

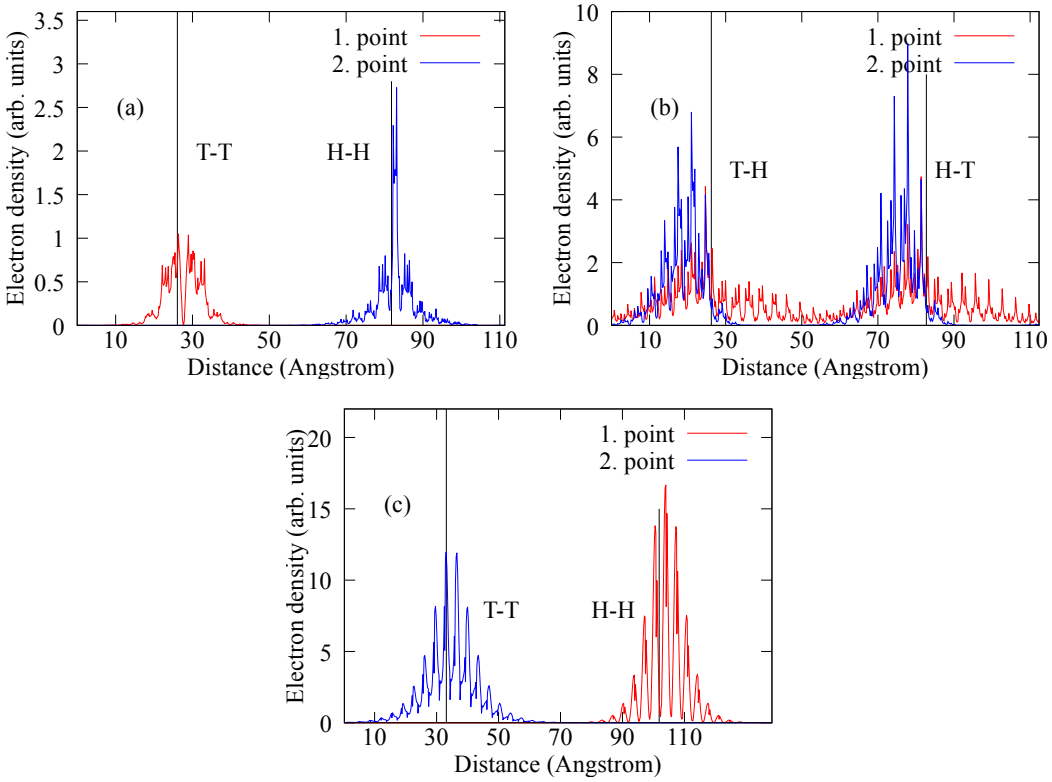

Figure 6.14: (a) Charge densities for the states labeled 1. and 2. in the electronic band structures Fig. 6.12 (a). (b) Charge densities for the states labeled 1. and 2. in the electronic band structures Fig. 6.12 (b). (c) Charge densities for the states labeled 1. and 2. in the electronic band structures Fig. 6.13 (a). Localization of electronic states at the domain walls is clearly shown in these figures. The x-axis is the coordinate perpendicular to the domain wall.

the energies of the electronic states decrease along the X - Γ direction away from the saddle points, and increase in the perpendicular direction. These are well-known Van Hove singularities that give a logarithmic divergence for the density of states in 2D systems [203], which explain the LDOS peak in our calculations.

Similar Van Hove singularities (i.e. saddle points) are also present in the electronic band structure of bulk GeTe (see Fig. 6.15 (b)). However, they are further from E_F than those of the T-T DW and do not lead to the logarithmic divergence of the DOS in three dimensions (3D) [203]. In the T-T DW, the electric field pushes the Van Hove singularities much closer to the Fermi level, thus making them contribute to electronic transport. Furthermore, the 2D nature of DWs makes the effect of the Van Hove singularities on the LDOS much larger than in bulk.

We note that the T-T DW has a very anisotropic valence band surface (see Fig. 6.15), which is beneficial for thermoelectric transport properties. The direction parallel to the projection of the polarization change along the DW given by the blue arrow (X - Γ) has much lower group velocities compared to the perpendicular direction in the DW

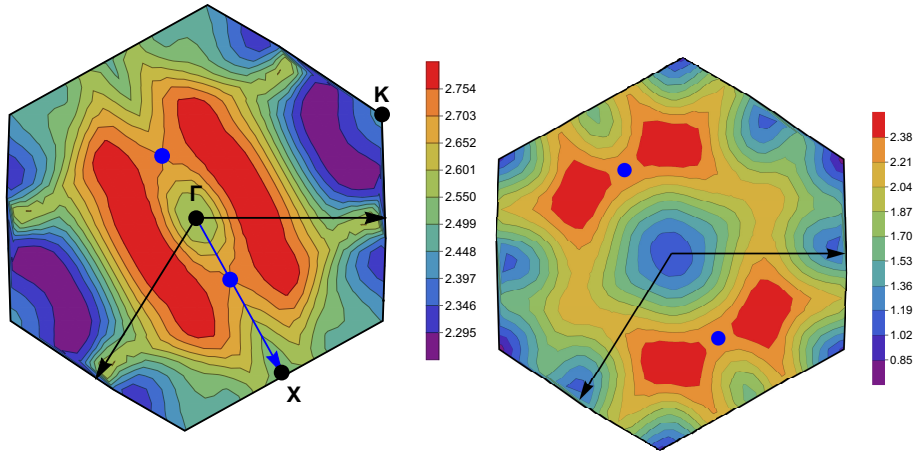

Figure 6.15: (a) 2D electronic band structure and Van Hove singularities of the tail-to-tail domain wall. Energy of the top valence band for 39° (11$\bar{1}$) tail-to-tail domain wall (in eV) in the interface Brillouin zone. Black arrows represent the directions of the in-plane reciprocal lattice vectors. The blue arrow corresponds to the projection of the polarization change onto the domain wall plane. Van Hove singularities are indicated by blue points. (b) Energy (in eV) of the top valence band of bulk GeTe projected onto the (11$\bar{1}$) domain wall (DW) plane, with the reciprocal lattice vector normal to the DW plane set to zero. Black arrows represent the directions of the in-plane reciprocal lattice vectors. Van Hove singularities are indicated by blue points.

plane (Γ - K). This is a consequence of the layered structure of bulk GeTe because the direction with low group velocities is perpendicular to van der Waals gaps in GeTe, making the states along that direction more confined. The 1D cigar like states in the X - Γ direction (red color in Fig. 6.15) gives an additional contribution to the peak of the density of states, which should be beneficial to the Seebeck coefficient as we show later. The Γ - K direction, on the other hand, has higher group velocities, which should result in higher electrical conductivity values for this direction.

6.2.5 Lattice thermal conductivity

Large local changes of the lattice constant and angle in the vicinity of DWs driven by large polarization changes indicate the presence of strong strain-order parameter coupling. This mechanism is similar to acoustic-soft TO mode coupling in bulk GeTe [55], and will likely reduce the lattice thermal conductivity of GeTe samples containing DWs. Alternatively, we can view DWs as grain boundaries which would effectively scatter phonons [204, 205]. Domain size will also determine the strength of phonon scattering. 39° and 141° DWs may be more effective in reducing the lattice thermal conductivity due to the larger lattice orientation mismatch (twinning of the structure) at the DW boundary.

We compute phonon scattering rates due to strain-order parameter coupling and lattice orientation mismatch caused by DWs as follows. First we define the scattering potential [206] with respect to structural deformations:

$$V_u^j(\vec{k},x) = \hbar\Delta\omega^j(\vec{k},x) = \hbar\omega^j(\vec{k})\gamma_u^j(\vec{k})\epsilon_u(x). \tag{6.20}$$

Here u represents one of the structural parameters: $u = a, \theta, \tau$ (a - lattice constant, θ - angle, τ - internal atomic displacement), $\omega^j(\vec{k})$ is the frequency of the phonon mode with the wave vector $\vec{k}$ and the branch j, $\Delta\omega^j(\vec{k},x)$ is the change of $\omega^j(\vec{k})$ at position x along the structure, and $\epsilon_u(x)$ is the relative change of the structural parameter u at x with respect to bulk. $\gamma_u^j(\vec{k})$ is the generalized mode Grüneisen parameter defined as:

$$\gamma_u^j(\vec{k}) = -\frac{u}{\omega^j(\vec{k})}\frac{\partial\omega^j(\vec{k})}{\partial u},$$

which we also used to accurately describe the thermal expansion of GeTe [79].

To account for the lattice orientation mismatch at the domain wall boundaries in 39° and 141° $(11\bar{1})$ DWs, we consider the cases of phonon reflection and transmission that conserve the phonon momentum inside the DW plane [207]. A phonon with certain Cartesian components of the momentum corresponds to different parts of the Brillouin zone, depending on which side of the DW that phonon is. The frequency mismatch at this boundary acts as the perturbation potential. The corresponding perturbation potential can then be defined as:

$$V_m^j(\vec{k},x) = \hbar\Delta\omega^j(\vec{k})\delta(x-d_0), \tag{6.21}$$

where $\Delta\omega^j(\vec{k})$ is the phonon frequency difference for phonons with the same momenta on the opposite sides of domain wall, and d_0 is the position of the DW in the structure.

Using Fermi's golden rule, we define the scattering rate induced by the presence of a DW as [206]:

$$\Gamma(\vec{k}) = \frac{n}{v_g\hbar^2}\frac{2k_x^2}{k^2}|g(2k_x)|^2, \tag{6.22}$$

where $n = 1/2L$ is the density of DWs, $2L$ is the domain size, v_g is the group velocity in the direction of the DW vector (perpendicular to the domain wall plane), k_x is the projection of the phonon wave vector in same direction and $|g(2k_x)|$ is the Fourier

transform of the scattering potential:

$$g(2k_x) = \int_{-L}^{L} V(x) e^{-i2k_x x} dx. \tag{6.23}$$

We have made the following approximations in the implementation of the outlined approach. The polarization change in each calculation is taken to be purely Ising, so there is no phonon scattering due to rotation of polarization. Grüneisen parameters do not accurately quantify phonon frequency changes for large structural distortions. We do not account for the structural renormalization in the middle of domains. We assume that this effect arises due to finite size effects in our calculations and should be zero for domain sizes of ~100 nm. For $(1\bar{1}0)$ DW, we do not account for the observed small changes in the lattice constant and angle. We do not take into account diffusive scattering at DWs, since this effect may not be important [187, 204]. The results obtained with our model should represent a lower bound for the lattice thermal conductivity reduction due to DWs.

We calculate the lattice thermal conductivity of GeTe including domain walls in the direction perpendicular to DW planes as:

$$\kappa_L = \frac{1}{NV} \sum_{\vec{k},j} c(\omega^j(\vec{k}))(v^j(\vec{k}))^2 / (\Gamma^j_{anh} + \Gamma^j_{DW}(\vec{k})),$$

where $c(\omega^j(\vec{k}))$ is the specific heat capacity of the phonon mode with the wave vector $\vec{k}$ and the branch j, $v^j(\vec{k})$ is its group velocity, and Γ^j_{anh} and $\Gamma^j_{DW}(\vec{k})$ are the phonon scattering rates due to anharmonic processes and DWs, respectively. Here we used the constant relaxation time approximation for Γ^j_{anh}. We calculated this value at several different temperatures from our previous calculations of the lattice thermal conductivity of GeTe [55].

Figure 6.16 (a) shows the contribution of each type of scattering to the lattice thermal conductivity reduction in GeTe structure with 39° H-H DWs and the domain size of 160 nm (approximately the value observed in experiment [80]) with respect to bulk. We assume that the perturbation potential is the sum of the contributions from lattice orientation mismatch and local changes of the structural parameters. This allows us to check the individual contributions of each perturbation potential (see Eqs. (6.20) and (6.21)). The largest contributions to κ_L come from local changes of the lattice constant and internal atomic displacement near the DWs, thus confirming that strong strain-order parameter coupling at DWs indeed reduces the κ_L of GeTe. Local angle distortions have a weak effect on κ_L due to relatively small values of the generalized

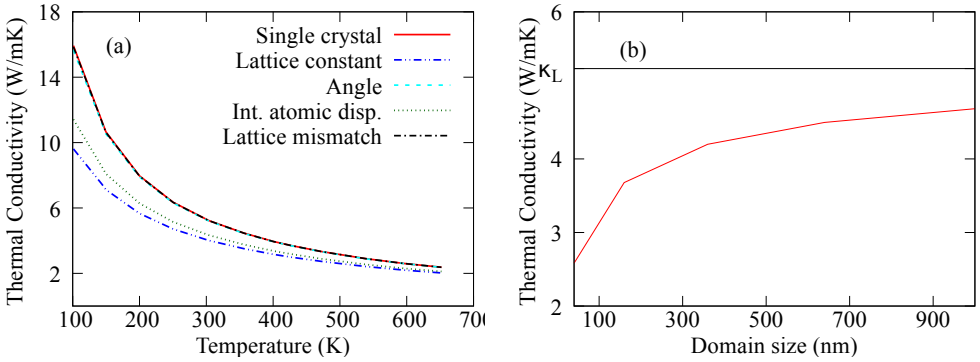

Figure 6.16: (a) Lattice thermal conductivity of bulk GeTe and GeTe structure with 39° head-to-head (H-H) domain walls (DWs) and the domain size of 160 nm at 300 K, showing the contribution of each scattering mechanism due to the DW. (b) Dependence of the lattice thermal conductivity of GeTe with 39° H-H DWs on the domain size at 300 K. Black horizontal line represents the bulk value of lattice thermal conductivity in GeTe.

mode Grüneisen parameters for the angle. The contribution of lattice orientation mismatch to the κ_L reduction is also small since the domain size is much larger than the average phonon mean free path in GeTe. At higher temperatures, the difference between the κ_L values for single crystal and domain structure becomes smaller since anharmonic processes become dominant. Fig. 6.16(b) illustrates the effect of the domain size on the lattice thermal conductivity at room temperature. For large domain sizes, κ_L tends towards the bulk value. For smaller domain sizes, there is a steep decline of the lattice thermal conductivity, driven by an increased density of local structural distortions.

Table 6.3: Lattice thermal conductivity of GeTe structure with a particular type of domain walls (DWs) at 300 K and DW density of 1/160 nm^{-1}, given as a percentage of the bulk value. H-H and T-T denote head-to-head and tail-to-tail DWs, respectively. 141° and (1$\bar{1}$0) DW only have head-to-tail DWs.

Charged DW	39° (11$\bar{1}$)	180° (11$\bar{1}$)	180° (111)
H-H DW	70%	71%	65%
T-T DW	79%	53%	64%
Neutral DW	141° (11$\bar{1}$)	180° (1$\bar{1}$0)	
H-T DW	75%	79%	

Table 6.3 shows considerable reductions of the lattice thermal conductivity of GeTe structure with one particular type of considered DWs and the domain size of 160 nm with respect to bulk at 300 K. (111) DWs have large thermal resistance since they are the widest DWs considered and have sizeable structural distortions. Similarly, 180° (11$\bar{1}$) T-T DW has the largest thermal resistance due to large structural deformations in the vicinity of this relatively wide DW. The smallest reduction of κ_L is obtained for

$(1\bar{1}0)$ DW, where local changes of the lattice constant and angle are taken to be zero. Consequently, the larger the amount of local distortions near the DW, the larger the κ_L reduction. Our results clearly illustrate the potential of domain walls for substantially reducing the lattice thermal conductivity of GeTe.

6.2.6 Electronic transport properties

An accurate calculation of the scattering rates $1/\tau$ (τ is the electronic state lifetime) of the electronic states localized on DWs is very challenging because of the complicated electronic band structure and the enormous computational cost involved in extracting electron-phonon matrix elements for large supercells containing DWs. Therefore, we have developed a model for the energy and momentum dependent scattering rates of the electronic states localized on DWs, whose all parameters can be obtained from DFT calculations. In our model, we account for scattering due to electron-phonon coupling. Scattering due to ionized impurities is neglected due to the large static dielectric constant of GeTe [208].

The transport relaxation time of the electronic state with the band number n and the wave vector $\vec{k}$ at the domain wall due to electron-phonon interaction can be obtained from first order perturbation theory as [209]:

$$\frac{1}{\tau_{n,\vec{k}}} = \sum_{m,\vec{k'}} \sum_{\lambda,\vec{q}} \frac{2\pi}{\hbar} \left| \left\langle \psi_{m,\vec{k'}} \left| H_{\lambda,\vec{q}} \right| \psi_{n,\vec{k}} \right\rangle \right|^2 \left(n_{\lambda,\vec{q}} + \frac{1}{2} \mp \frac{1}{2} \right) \times \delta(E_{m,\vec{k'}} - E_{n,\vec{k}} \pm \hbar\omega_{\lambda,\vec{q}})(1 - \cos\theta),$$

where $\hbar$ is the reduced Planck constant, $\psi_{n,\vec{k}}$ is the wave function of the electronic state $\left|n\vec{k}\right\rangle$ with energy $E_{n,\vec{k}}$, $n_{\lambda,\vec{q}}$ and $\omega_{\lambda,\vec{q}}$ are the equilibrium Bose-Einstein distribution and the frequency of phonons for the branch λ and the crystal momentum $\vec{q}$, and $H_{\lambda,\vec{q}}$ is the electron-phonon perturbation potential. The term $1 - \cos\theta = 1 - \frac{\vec{v}_{n,\vec{k}} \cdot \vec{v}_{m,\vec{k'}}}{|\vec{v}_{n,\vec{k}}||\vec{v}_{m,\vec{k'}}|}$ represents the scattering angle which accounts for the momentum relaxation rate. We neglect phonon frequencies in the energy conservation condition, but they are partially accounted via Gaussian broadening (standard deviation of 5 meV). We use $n_{\lambda,\vec{q}} + \frac{1}{2} \mp \frac{1}{2} \approx \frac{k_B T}{\hbar\omega_{\lambda,\vec{q}}}$, where k_B is the Boltzmann constant. This is a good approximation at 300 K since the Debye temperature of GeTe is ≈ 180 K.

We assume that the dominant electron-phonon interactions are non-polar since we consider systems with high doping concentrations where polar interactions are largely screened by free carriers, as shown in first principles calculations for bulk GeTe [210].

We thus consider the electron-phonon perturbation of the form:

$$H_{ac,\vec{q}} = \sqrt{\frac{\hbar}{2M'\omega_{\vec{q}}}} U_1 q e^{-i\vec{q}\cdot\vec{r}},$$

for long-wavelength acoustic phonons with linear dispersions, and:

$$H_{opt,\vec{q}} = \sqrt{\frac{\hbar}{2\bar{M}\omega}} U_2 e^{-i\vec{q}\cdot\vec{r}},$$

for long-wavelength optical dispersionless phonons [209, 208] (M' is the total mass and $\bar{M}$ is the reduced mass of the unit cell). Considering the dispersion relations for acoustic and optical modes, we can further write:

$$H_{ac,\vec{q}} \sqrt{\frac{2\pi k_B T}{\hbar^2 \omega_{\lambda,\vec{q}}}} = \left(\sqrt{\frac{\pi k_B T}{\hbar M'}} \frac{1}{v} U_1 \right) e^{-i\vec{q}\cdot\vec{r}} = \bar{U}_1 e^{-i\vec{q}\cdot\vec{r}},$$
$$H_{opt,\vec{q}} \sqrt{\frac{2\pi k_B T}{\hbar^2 \omega_{\lambda,\vec{q}}}} = \left(\sqrt{\frac{\pi k_B T}{\hbar \bar{M}}} \frac{1}{\omega} U_2 \right) e^{-i\vec{q}\cdot\vec{r}} = \bar{U}_2 e^{-i\vec{q}\cdot\vec{r}}.$$

Here v is the speed of sound and ω is the characteristic frequency of optical modes. The final expression for the total relaxation time including both scattering mechanisms can be written as:

$$\frac{1}{\tau_{n,\vec{k}}} = U^2 \sum_{m,\vec{k'}} I^2_{n,m,\vec{k},\vec{k'}} \, \delta(E_{m,\vec{k'}} - E_{n,\vec{k}})(1 - \cos\theta), \tag{6.24}$$

where the coefficient $U^2 = \bar{U}_1^2 + \bar{U}_2^2$ contains all the physical constants and material parameters described above and temperature (kept constant at 300 K in all our calculations). $\vec{k}$ corresponds to the wave vector component in the DW plane, and the momentum is conserved only in the DW plane [211]. The quantity $I_{n,m,\vec{k},\vec{k'}}$ is defined as [211]:

$$I_{n,m,\vec{k},\vec{k'}} = \frac{1}{N_\perp V} \sum_{\vec{q}_\perp} \int u^*_{m,\vec{k'}} \, e^{-i\vec{q}_\perp \cdot \vec{r}} \, u_{n,\vec{k}} \, \mathrm{d}\vec{r},$$

where the integration over $\mathrm{d}\vec{r}$ is within the unit cell, $\vec{q}_\perp$ is the wave vector component perpendicular to the DW and $N_\perp$ is the number of $\vec{q}_\perp$ vectors. $u_{n,\vec{k}}$ is the periodic part of the Bloch wave function of the state $\left|n\vec{k}\right\rangle$, and V is the unit cell volume. Here we assume that the phonon band structure and the strength of electron-phonon interaction do not change at the DW with respect to bulk.

We can derive the expressions for the scattering rates in bulk GeTe in a similar manner. In this case, the total momentum is conserved in Eq. (6.24), and $I_{n,m,\vec{k},\vec{k'}}$ is the overlap of the wave functions of the states $\left|n\vec{k}\right\rangle$ and $\left|m\vec{k'}\right\rangle$. To compare our conductivity and power factor values for bulk GeTe to experiments, we fit the value of U to the first principles calculations of the bulk electronic conductivity for p-type GeTe at 300 K [210].

In the case of bulk GeTe, the thermoelectric transport properties are obtained along the trigonal [111] axis and two directions perpendicular to it, and using their average. In the DW case, we calculate the transport quantities along the Γ - X and Γ - K directions in the DW plane and in the direction perpendicular to the DW plane. We have performed convergence studies of the transport properties with respect to the number of $\vec{k}$-points. We did this by calculating electronic transport properties of GeTe in constant relaxation time approximation for a several $\vec{k}$-point grids and found the smallest one for which the electronic transport coefficients do not change appreciably upon increasing the grid (see Appendix B). For the bulk calculation, we use a $70\times70\times70$ grid, while for the DW calculation we use a uniform 2D grid with 1806 $\vec{k}$-points in the first Brillouin zone. To make the calculation of the wave function overlaps more computationally tractable, we reduce the energy cutoff for plane waves from 16 Ha to 8 Ha when calculating wave functions. For small $\vec{k}$-point grids this method gives a very small error (much smaller compared to fitting procedure which would be an alternative) compared to the calculation with the converged energy cutoff of 16 Ha.

We compute the free charge concentration at the T-T domain wall as follows. We assume that the separation between the T-T and H-H DWs is equal to the domain size in our DFT calculation (5.6 nm). We calculate the local density of states (LDOS) of the T-T DW in the supercell containing both H-H and T-T DWs by summing the LDOS contributions from the atoms belonging to the half of the supercell that contains only the T-T DW. We normalize the LDOS of these atoms so that the LDOS integral up to the top of the valence band for each Ge atom is 4 and for each Te atom is 6, meaning 10 electrons per unit cell. We then obtain the surface and volume charge densities of the T-T DW as:

$$p_{S,V} = \frac{1}{S,V}\int_{-\infty}^{E_\mathrm{V}} (1 - f(E, E_\mathrm{F}, T))\, N(E) dE,$$

where S is the DW plane surface, V is the volume of the half of the supercell, E_V is the top of the valence band, and $N(E)$ is the LDOS of the T-T DW structure. We note that the DW volume carrier concentration (p_V) depends on the size of the domain, unlike the surface charge density (p_S).

6.2.6.1 Results

We compute the Seebeck coefficient of 39° T-T DW in the X - Γ and Γ - K directions in the DW plane and in the direction perpendicular to the DW plane using the Boltzmann transport equation (see Fig. 6.15). S is plotted in Fig. 6.17 (a) as a function of the extrinsic free charge density on the DWs. Our calculations show at least a two-fold enhancement of the Seebeck coefficient of 39° T-T DW with respect to bulk GeTe in all directions. To compare the free charge densities of the DW (2D) and bulk (3D), we obtain the volume charge concentration of the T-T DWs by assuming that the separation between the T-T and H-H DWs corresponds to one in our DFT calculation (5.6 nm) (see Methods). The intrinsic DW charge density due to charge transfer between the H-H and T-T DWs and the related volume charge concentration are indicated by the black vertical line in Fig. 6.17.

An increase of the domain size (the separation between the domain walls) will lead to an increase in the DW free charge carrier density. We use the domain size for which the electronic states at the head-to-head and tail-to-tail domain walls are decoupled and their band structures are converged. As the separation between domain walls increases, the increased free charge carrier density will more completely screen the bound charge caused by the polarization change at the DWs, leading to a decrease in the electric field along the domains. However, the increase of the domain size does not have a significant effect on the electronic band structure of domain walls. Consequently, we expect that the major effect of the increased domain size would be a shift of the black vertical line in Fig. 5 to higher free charge carrier surface densities.

Our BTE results for 39° T-T DW show that the Seebeck coefficient is the largest in the direction perpendicular to the DW plane (Fig. 6.17 (a)). The enhancement of S is smaller in the in-plane directions, where the electronic states are more dispersive and more conductive. We explain these trends for the Seebeck coefficient using the Mott expression [60]:

$$S = \frac{\pi^2 k_B^2 T}{3e} \left(\frac{N'(E)}{N(E)} + \frac{\left\langle v^2(E) \right\rangle'}{\left\langle v^2(E) \right\rangle} + \frac{\tau'(E)}{\tau(E)} \right) \Bigg|_{E=\mathrm{E_F}}, \tag{6.25}$$

where k_B is the Boltzmann constant, T is the temperature, e is the electron charge, $N(E)$ is the density of states, $\left\langle v^2(E) \right\rangle$ is the squared group velocities average, and $\tau(E)$ is the relaxation time. Primed quantities represent the first derivatives with respect to energy.

To disentangle the individual contributions of the three terms in Eq. (6.25), we calculate

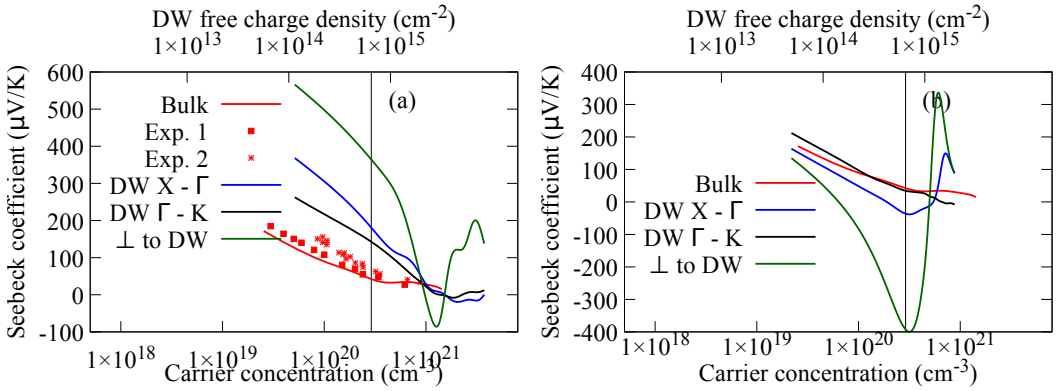

Figure 6.17: a) Calculated Seebeck coefficient for p-type bulk GeTe and 39° $(11\bar{1})$ tail-to-tail (T-T) domain walls (DWs) for various directions at 300 K. Experimental data for bulk GeTe from Refs. [18, 12] are shown by red squares and stars, respectively. The top x-axis shows the DW interface free charge density, while the bottom x-axis corresponds to the volume charge concentration for the DW separation of 5.6 nm. Black vertical line shows the intrinsic doping concentration of DWs for this DW separation due to charge transfer between the head-to-head and T-T DWs. b) Calculated Seebeck coefficient along same directions for the H-H DWs.

the Seebeck coefficient using three levels of approximation (see Fig. 6.18 a)). Firstly, we set group velocities and relaxation times to constant values, and account only for the energy dependence of DOS in the S calculation. This approximation (the constant group velocities approximation - CGVA) gives an isotropic Seebeck coefficient for the DW that is enhanced compared to bulk. This increase comes from the LDOS peak near the Fermi level at the DW, which arises due to Van Hove singularities. Secondly, including the energy dependence of group velocities in addition to that of DOS in the S calculation gives rise to an anisotropic Seebeck coefficient for the DW (the constant relaxation time approximation - CRTA). S increase is larger in the directions of lower group velocities and stronger localization (perpendicular to the DW plane and X - Γ) compared to the direction with higher group velocities (Γ - K), see Fig. 6.15. Finally, including the energy and momentum dependent relaxation times in the S calculation further increases the Seebeck coefficient of the DW in all three directions with respect to bulk, see Fig. 6.17. Therefore, the increased energy dependence of the DOS, group velocities and relaxation times near the Fermi level induced by the presence of 2D Van Hove singularities is the key to the S enhancement in the T-T DW. Confirmation of this can be seen in Fig. 6.18 b). Here we plot the averaged values of $v^2(E)\tau(E)$ close to the band edge for three different directions. We can see that close to the band edge the direction perpendicular to the domain wall has the largest slope resulting in the largest S in that direction, followed by the X - Γ direction.

Next we calculate the electrical conductivity and the power factor of 39° T-T DWs (see Fig. 6.19 (a) and Fig. 6.20 (a)). Even though there is a local increase of the free charge

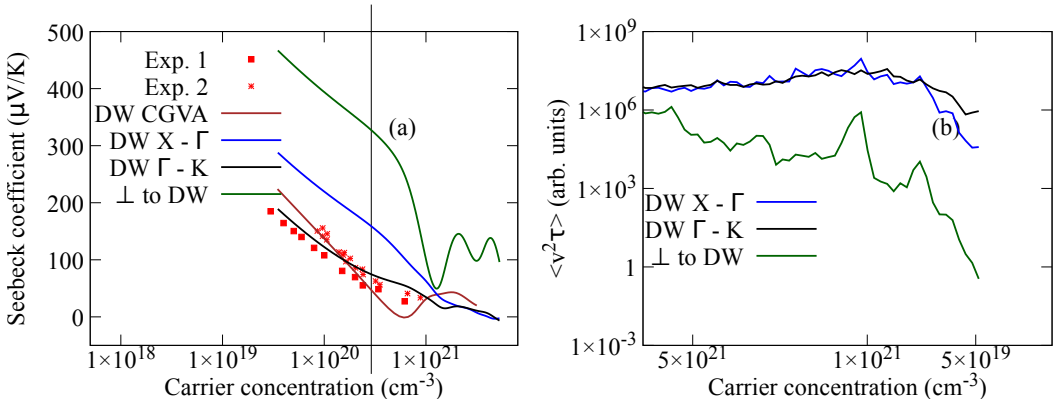

Figure 6.18: (a) Seebeck coefficient of p-type 39° $(11\bar{1})$ tail-to-tail (T-T) domain walls at 300 K calculated using the constant relaxation time approximation and the constant group velocity approximation (CGVA). Experimental data from Refs. [18, 12] are shown by red squares and stars, respectively. The bottom x-axis corresponds to the volume charge concentration for the DW separation of 5.6 nm. Black vertical line shows the intrinsic doping concentration of the T-T DW for this DW separation due to charge transfer between the head-to-head and T-T DWs. (b) Average value of transport coefficient $v^2(E)\tau(E)$ at T-T DW for three directions noted in the figure (a). Maximum value of the Seebeck coefficient strongly correlates with the relative slope of this transport coefficient.

concentration at the DWs compared to bulk, the electrical conductivity in the in-plane directions (Γ - K and X - Γ) is somewhat reduced at the DW for some extrinsic doping concentrations. The reason for this decrease are the increased electron scattering rates due to Van Hove singularities. Nevertheless, there is more than a five-fold increase of the in-plane power factor across the whole doping range due to the large S enhancement. Most importantly, the maximum of the power factor for the T-T DW in the Γ - K and X - Γ directions is five times larger than that for bulk. Consequently, the combination of the increased energy dependence of the transport quantities that enhance S and the increased local charge concentration that prevents σ reduction lead to a large increase of the in-plane power factor in the T-T DWs.

In the direction perpendicular to the T-T DW, the electrical conductivity and the power factor of the DW are both significantly decreased with respect to bulk. This occurs because the electronic states near the Fermi level are localized on the DW and have low group velocities in the direction perpendicular to the DW. As a result, the thermoelectric transport properties of DWs in the out-of-plane direction are inferior to those in the DW plane.

We have also computed the thermoelectric transport properties of 39° $(11\bar{1})$ head-to-head domain walls in GeTe. We compare the values of the calculated Seebeck coefficient of the bulk and H-H DWs GeTe in Fig. 6.17 (b). The bulk results are for p-type GeTe, but the difference between the transport properties for p- and n-type bulk GeTe

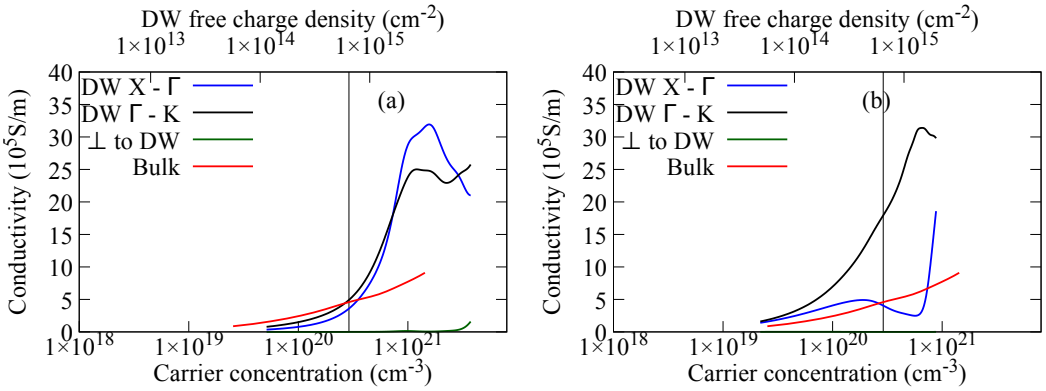

Figure 6.19: Calculated electrical conductivity of p-type bulk GeTe and (a) 39° $(11\bar{1})$ tail-to-tail (T-T) domain walls (DWs) and (b) n-type head-to-head DW for various directions at 300 K. The top x-axis shows the DW interface free charge density, while the bottom x-axis corresponds to the volume charge concentration for the DW separation of 5.6 nm. Black vertical line shows the intrinsic doping concentration of the T-T DW for this DW separation due to charge transfer between the head-to-head and T-T DWs.

is not large [210]. Since the H-H DW is n-type, the Seebeck coefficient of this DW is multiplied by -1. The Seebeck coefficient for the H-H DW is smaller than that for the T-T DW, but it is still improved in one of the in-plane directions (Γ - K) with respect to bulk GeTe. The in-plane Seebeck coefficient of the H-H DW exhibits the opposite behaviour compared to the T-T DW: the more dispersive direction (Γ - K) has a larger S than the less dispersive direction (X - Γ). This is due to the fact that the group velocities in the X - Γ direction decrease with doping (and thus the derivative of the average squared velocities has a negative sign), while this trend is the opposite in the case of the Γ - K direction for the H-H DW and for both of these directions in the T-T DW.

The out-of-plane Seebeck coefficient for the H-H DW exhibits an unusual behaviour with doping. It changes sign from negative to positive for the doping concentration of $\sim 10^{20}$ cm^{-3}. This is the consequence of the band inversion near the L points that are at the edge of the bottom conduction band for the H-H DW. This band inversion leads to Van Hove singularities in the electronic band structure of the H-H DW (see the small peak in the local density of states of the H-H DW below the Fermi level at 0 K in Fig. 6.11 (a)) and non-zero group velocities in the out-of-plane direction. This band inversion is deep in the valence band of the T-T DW ($p \sim 10^{21}$ cm^{-3}) and also has an effect on its transport properties. There is another change of sign from positive to negative of the out-of-plane S for the H-H DW at $\sim 3\times10^{20}$ cm^{-3}. This is caused by saddle points in the electronic band structure of the H-H DW, which result in Van Hove peaks in the local density of states of the H-H DW above the Fermi level at 0 K (Fig. 6.11 (a)). The Van Hove singularities for the H-H DW are not as large and not as near the Fermi level as for the T-T DW, which explains the lower Seebeck coefficient

values for the H-H DW.

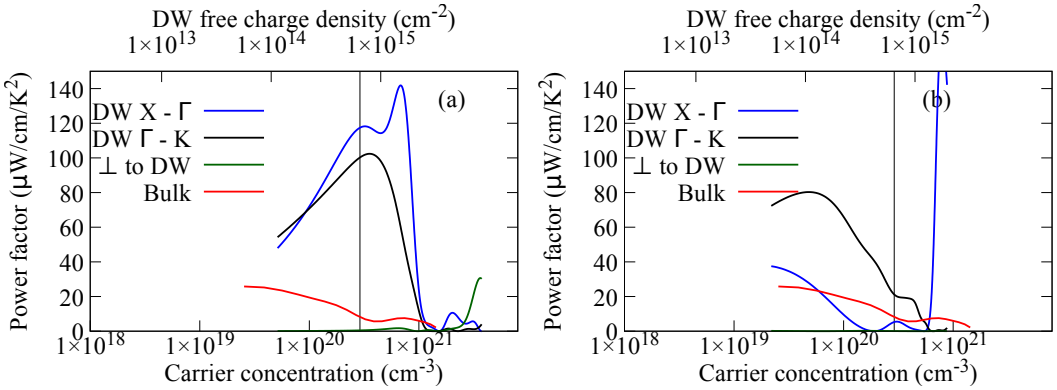

Figure 6.20: Calculated power factor of p-type bulk GeTe and (a) 39° $(11\bar{1})$ tail-to-tail (T-T) domain walls (DWs) and (b) n-type head-to-head DW for various directions at 300 K. The top x-axis shows the DW interface free charge density, while the bottom x-axis corresponds to the volume charge concentration for the DW separation of 5.6 nm. Black vertical line shows the intrinsic doping concentration of the T-T DW for this DW separation due to charge transfer between the head-to-head and T-T DWs.

The computed values of the electrical conductivity for bulk GeTe, and the H-H domain walls are shown in Fig. 6.19(b). The conductivity at the H-H DW is increased compared to the T-T DW, which is a consequence of the lower scattering rates at the H-H DW. The higher scattering rates at the T-T DW are the result of the large Van Hove singularities close to the band edge that provide large scattering phase space. The conductivity at the H-H DW appears to be increased even with respect to the bulk material. This is partly due to our method of computing the free charge concentration of the domain walls: we take the volume to be the half of the domain structure, rather than the domain wall volume. The conductivity of the H-H DW in the direction perpendicular to the domain wall is small as a result of very low group velocities in that direction. The power factor of the H-H DW in the Γ - K direction is increased compared to bulk and is the largest of all considered structures for low doping (see Fig. 6.20 (b)). The enhanced power factor of the H-H DW indicates that it would be possible to realize the nano-thermoelectric device based on ferroelectric domain walls described in the following paragraph.

In GeTe samples with charged DWs, both n- and p-type DWs will contribute to the Seebeck coefficient, thereby suppressing its overall enhancement. To harness the predicted outstanding thermoelectric properties of ferroelectric DWs, we propose a nano-thermoelectric device consisting of H-H and T-T DWs acting as n- and p-type legs of the thermoelectric couple [32], separated by electrically insulating domains (see Fig. 6.21). The temperature gradient would be applied along DWs, rather than perpendicular to them. The proposed device could be used for nanoscale energy harvesting

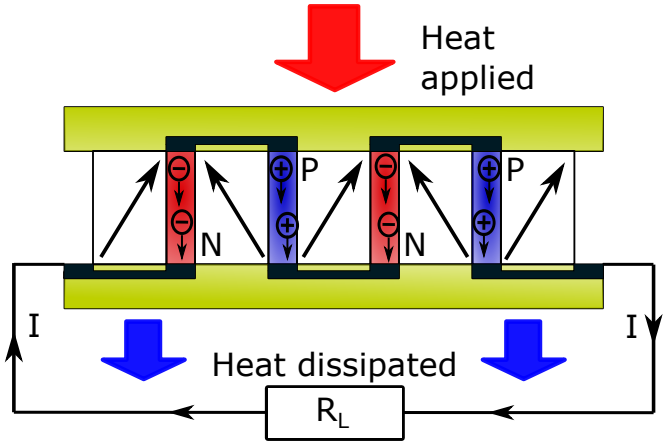

Figure 6.21: Proposed design of the nano-thermoelectric device based on domain walls. White regions represent domains with different polarization orientations, acting as electrical insulators. Head-to-head and tail-to-tail domain walls, shown by red and blue regions, act as an n- and p-type leg of the thermoelectric device, respectively. Electrodes and insulating parts are shown in black and green, respectively. Heating up the top electrodes causes electron and hole diffusion in n- and p-type domain walls, respectively, which produces electrical current.

or cooling. Since DWs already exist in GeTe forming an ordered herringbone structure [181, 182, 157, 80, 212, 190], it should be possible to realize such device with an appropriate placing of contact electrodes. Another important advantage of using DWs as nano-thermoelectric couples is that we can write or erase them by applying an electric field (or light) [182]. For example, we could grow a pristine GeTe film without domains and then pole it to form desired types of DWs that will act as active device elements [157]. Manipulating the domain wall separation would also allow us to tune the doping concentrations at the domain walls [213], in addition to vacancies and dopants.

6.3 Conclusion

In summary, we presented a first-principles structural characterization of $(11\bar{1})$, (111), and $(1\bar{1}0)$ domain walls in GeTe, which included calculations of domain wall energies and widths, local polarization, and local structure distortions. (111) domain walls exhibit the Ising character of polarization change, while all other domain walls show mixed Ising-Néel character. Large local structure distortions and strong strain-order parameter coupling are present at most of the domain walls investigated. We have shown that the lattice thermal conductivity of GeTe can be substantially lowered by these domain walls, particularly by those with large structural changes and large widths. At high domain wall densities, phonon scattering from strain fields becomes

dominant, and lattice thermal conductivity can be dramatically suppressed.

Furthermore, we have shown that the thermoelectric power factor of charged ferroelectric domain walls in GeTe can be enhanced up to a factor of five compared to the bulk values. The bound charge arising from polarization discontinuity on these interfaces causes localization of electronic states close to the Fermi level on the domain walls. The local density of these two-dimensional states diverges logarithmically near the Fermi level due to the presence of saddle points in their electronic band structure. This significantly increases the Seebeck coefficient in the domain wall plane without considerably reducing the electrical conductivity. Our results clearly show the potential of ferroelectric domain walls for nanoscale thermoelectric applications.

Chapter 7

Molecular dynamics simulation of the ferroelectric phase transition in GeTe

7.1 Introduction

In the previous chapters, we presented the results for different physical properties of GeTe close to the ferroelectric phase transition. These results, however, depend on several approximations whose validity is questionable close to the phase transition. For example, our thermal expansion calculation rests on the premise that the elastic energy of GeTe can be expanded to the Taylor series that depends only on the macroscopic properties of the system (lattice constant, angle, and interatomic displacement). We do not take into account the temperature dependence of the phonon band structure in that study, either through the quasiharmonic or fully anharmonic approach. This is not well justified since we know that the temperature renormalization of the phonon band structure in GeTe is large. Similarly, our study of the lattice thermal conductivity of domain wall structures in GeTe rests on the assumption that the scattering potential is proportional to the Grüneisen parameter. Considering large deviations of the structural parameters close to domain walls, this definition of the scattering potential is questionable. Finally, in our study of the lattice thermal conductivity close to the phase transition, we take into account only three phonon processes. There is a large number of recent publications that claim fourth-order anharmonic coupling is important in this and similar materials [105, 214, 215, 216]. Going beyond the lowest anharmonic order in the expansion of the Hamiltonian (to describe the contribution of higher-order anharmonicity to phonon lifetimes) makes the problem almost numerically intractable and the validity of using Fermi's golden rule questionable.

Most of these problems can be resolved by the use of molecular dynamics (MD) simulations [217, 218]. MD simulations explicitly track the time evolution of the atomic system by integrating classical Newton's equations at discrete time steps [91]. Thermal expansion can be obtained by running the system in the NPT ensemble, which keeps the number of particles, pressure, and temperature constant and changes the volume of the simulation cell to accommodate these restrictions [127, 219, 220]. If we set our target pressure to be zero at different temperatures, we obtain thermal expansion by averaging the volume of the simulation cell over an appropriately long MD trajectory. Equilibrium molecular dynamics (EMD) simulations utilize the Green-Kubo result from the linear response theory to obtain lattice thermal conductivity from the heat autocorrelation function [217, 221, 222]. In principle, this allows us to calculate lattice thermal conductivity by accounting for all orders in anharmonic interaction. Finally, non-equilibrium molecular dynamics (NEMD) simulations would allow us to calculate the thermal resistance of ferroelectric domain walls [217]. This method mimics the experimental setup by setting a constant thermal current through the simulation cell and measures the resulting thermal gradient.

To integrate Newton's equation one needs to calculate forces on individual atoms in the simulation cell. Ideally, these forces would come from density functional theory (DFT) calculations. However, DFT is relatively slow and, more importantly, does not scale well with the increased size of the simulation cell. This is why the most common approach for MD simulations is to fit some parametric form of the interatomic potential, either to experiment or DFT calculations. However, most traditional interatomic potentials are too simple to capture equally accurately different phases of the material or different bonding environments. Recent developments in applying machine learning techniques in material science give us an opportunity to construct extremely transferable and accurate force fields [99, 100, 97, 98]. The only assumption that comes into building these interatomic potentials is that the interaction is short-ranged. This means that the force on an atom depends only on the local environment of that atom. The accurate description of the local environment might be the most important part of the potential fitting procedure and there are several ways to do this [97, 100, 101].

Finally, MD simulations provide us with an opportunity to directly study the dynamics of the system. The phonon mode frequency renormalization can be obtained from the velocity autocorrelation function [223]. The properties such as phonon number or phonon lifetime can also be inferred directly from MD simulations. Most importantly, we will be able to track the behavior of the order parameter as we approach the phase transition temperature. There is still confusion in the community whether this phase transition is of displacive or order-disorder type, and even if it is of the first or second-

order kind [8, 4]. We hope to directly probe the order parameter properties at the phase transition and deduce the nature of the ferroelectric phase transition in GeTe.

However, MD simulations are very hard to converge and interpret. Very long calculations are needed to integrate out the intrinsic noise of an MD simulation. This is problematic for us, since the downside of the interatomic potential we used is its complexity, which makes it much slower than the ordinary interatomic potential. Additionally, sampling of the vibrational properties of a material is determined by the size of the supercell, which means one has to be particularly careful about convergence with respect to the size of the simulation cell.

This chapter is organized as follows. The first section will be devoted to details of the fitting procedure to obtain the parameters of our model interatomic potential. We will justify our choice of the interatomic potential by comparing it to DFT. We find that the fitted interatomic potentials reproduces a large number of DFT results with large accuracy. The second part will be the temperature evolution of GeTe. Our results on lattice thermal expansion show lattice contraction at the phase transition. We also notice an increase in the volume-order parameter correlation at the phase transition, which we interpret as a sign of stronger acoustic-soft phonon mode coupling. We try to elucidate the nature of the phase transition by tracking the order parameter behavior at the phase transition and find that the phase transition exhibits both displacive and order-disorder behavior. Finally, in the last section we use equilibrium molecular dynamics simulations to calculate the lattice thermal conductivity of GeTe close to the ferroelectric phase transition. We again notice the increase of the lattice thermal conductivity at the phase transition and assign it to the increase of the group velocities and heat capacity at the phase transition.

7.1.1 Fitting of the Gaussian Approximation Potential

We fitted the GAP potential using QUIP code with an iterative procedure as follows. We created the first training set of atomic forces and energies using randomly displaced atoms at different temperatures for different sizes of supercells (128 - 512 atoms). The temperature for these structures was defined through the average square of atomic displacements from equilibrium positions. Additional datasets are taken from ab initio MD simulations of GeTe at temperatures above the melting point ($\approx$ 1500 K). Ab initio MD simulations were done using ABINIT with a 128 atom supercell ($4\times4\times4$ supercell of the primitive cell) with a timestep of $\approx$ 2fs for 10 000 timesteps. We trained an initial version of GAP and ran a MD simulation using it as a force field. The MD

simulation fails at some temperature (some atoms would leave a simulation box) and we sample a number of atomic configurations along that MD trajectory. Atoms leaving a simulation box is a common error in LAMMPS code, usually associated with large timesteps, which means that atoms move too far in one timestep. We recalculate forces and energies for these structures in DFT and include them into the training set of the potential. We refit GAP with an updated training set. We repeat these steps (running MD, sampling configurations along the MD trajectory, adding them to the training set and training a new version of GAP) until we reach a sufficiently converged version of the interatomic potential. By this we mean the MD simulations are stable for a range of temperatures and structures, and the potential does not show a significant improvement upon adding new structures to the training set. The hyperparameters of the GAP model are given in Table 7.1. Definitions of hyperparameters can be found in Refs. [99, 100]

Table 7.1: The Gaussian Approximation Potential hyperparameters used to fit the interatomic potential for GeTe.

Cutoff radius	6.5 Å
Smooth cutoff transition	0.8 Å
Energy regularization	0.001 eV per atom
Force regularization	0.02 eV $Å^{-1}$ per atom
Kernel exponent	4
Sparse jitter	10^{-8}
(l_{max}, n_{max})	(6,8)

7.1.1.1 Comparison of GAP results with DFT

Figure 7.1 (a) shows the comparison between DFT and GAP energies. We can see that the data points lie on the $y = x$ line indicating that the error in energies is small compared to the range of energies that the configurations in the test sample have. The test configurations are chosen from rocksalt and rhombohedral structures along the MD trajectories we used to get interatomic force constants for our study of the lattice thermal conductivity (see Chapter 5). None of these configurations was in the training set used to fit the interatomic potential. The inset shows the number of configurations with the absolute value of error smaller than one indicated by the x-axis (expressed as a percentage of the total number of configurations). We can see that more than 90% of configurations have errors smaller than 1 meV/atom.

Figure 7.1 (b) shows the same study but for forces. We can see that the large majority of forces (around 90%) have errors less than 0.1 eV/Å. This error margin is comparable to

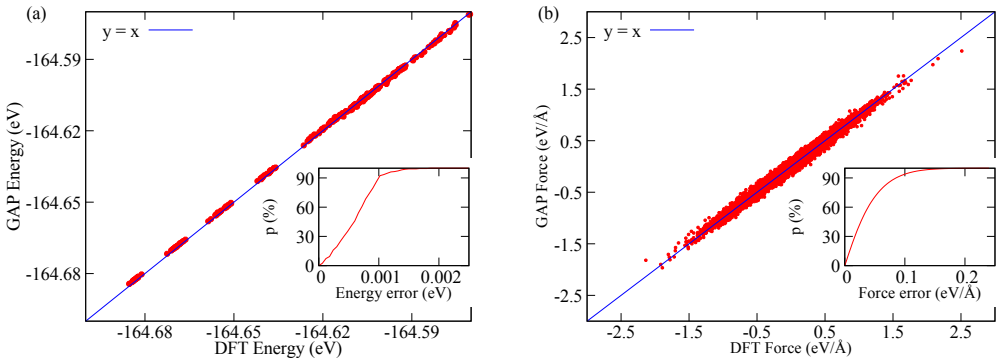

Figure 7.1: (a) Average atomic energies and (b) atomic forces, calculated using DFT and GAP. The test set in this case is the data we use to fit TDEP force constants in Chapter 5. The insets show the distributions of errors (differences of computed energies/forces with DFT and GAP.), where p is the percentage of the energies/forces with errors smaller than indicated by the x-axis.

that expected from the reduced accuracy (by reducing plane wave cutoff and the $\vec{k}$-point grid) DFT calculations that we would have to use for the ab initio MD simulations.

Next, we will compare the ground state properties of germanium telluride computed using DFT and GAP. Table 7.2 shows the structure of GeTe from GAP, DFT (GGA and LDA), and experiment. The agreement between DFT-GGA and GAP (we fitted GAP using DFT-GGA) is comparable to the agreement between different DFT flavors. Also, our results are similar to the other studies that used a neural network potential to model germanium telluride [224, 225]. Most importantly, we can see that our description of the order parameter (interatomic displacement τ) is very good, which gives us confidence that the phase transition behavior will be described appropriately.

Table 7.2: Lattice parameters of GeTe at 0 K, calculated using the GAP interatomic potential, DFT LDA and GGA-PBE functionals, and compared with experimental results [7]. a stands for lattice constant, θ for angle, and τ for internal atomic coordinate.

	a (Å)	θ (deg)	τ	V_0 (Å^3)
LDA	4.207	58.788	0.524	51.193
GGA-PBE	4.381	57.776	0.530	56.420
GAP	4.422	56.861	0.532	56.700
Experiment (295 K)	4.299	57.931	0.525	53.513
GAP (300 K)	4.453	56.850	0.532	57.903

To further justify the use of GAP, we compare the elastic constants ($\hat{C}$) and bulk modulus (B) calculated using GAP and density functional perturbation theory (DFPT). Here we will report the ion relaxed values[1] of these quantities. Bulk modulus was calcu-

[1]This is different from the study in the thermal expansion chapter where we report ion-clamped

lated using the Voigt average (see Eq. (3.18)). To check the stability of GeTe structure predicted by GAP, we calculated the stability conditions for rhombohedral structure:

$$K_1 = C_{11} - C_{12},$$
$$K_2 = \frac{1}{2}(C_{11} + C_{12})C_{33} - C_{13}^2,$$
$$K_3 = \frac{1}{2}(C_{11} - C_{12})C_{44} - C_{14}^2.$$

All of these coefficients should be larger than zero and they are in our model. As we can see from Table 7.3, all of the calculated values of elastic constants agree in the range of 20% error. However, the stability condition values can differ as much as 35%. This large discrepancy does not seem to have large effect at least on the qualitative results of thermal expansion (see next section).

Table 7.3: Elastic properties of germanium telluride calculated using the GAP interatomic potential and DFPT with the GGA-PBE exchange-correlation functional.

(GPa)	C_{11}	C_{12}	C_{13}	C_{33}	C_{14}	C_{44}	B	K_1	K_2	K_3
GAP	79	21	20	30	14	21	34	58	1100	413
GGA-PBE	87	18	18	36	15	25	35	69	1566	637

Additionally, we compare the vibrational properties of germanium telluride at 0 K calculated with DFT and GAP (we used the PHONOPY code to calculate the phonon band structure [145]). The phonon band structures of GeTe obtained with DFT and GAP agree very well in the entire frequency range (see Fig. 7.2 (a)). In these calculations, as well in the rest of the chapter, we do not take into account the long-range forces (we do not calculate LO/TO splitting). The zone center TO modes display the expected soft mode behavior for our fitted model of interatomic interaction. Figure 7.2 (b) shows the Grüneisen parameters calculated using Eq. (3.6) for the lattice constant. Considering this is a property that depends on the derivatives of force constants (third-order anharmonic force constants), the agreement between DFT and GAP is very good. These results give us confidence that calculations of the lattice thermal conductivity using GAP will be trustworthy.

Finally, we compare the energy profile of the interatomic displacement parameter calculated with GAP and DFT in Fig. 7.2 (c). In this case we fix the lattice parameters (lattice constant a and rhombohedral angle θ) to be the same for both calculations (we took values of a and θ for the ground state of GeTe at 0 K calculated with GGA-PBE). The agreement is excellent between two methods, which assures us that the simulation

elastic constants (there we do not relax atomic positions after straining the system).

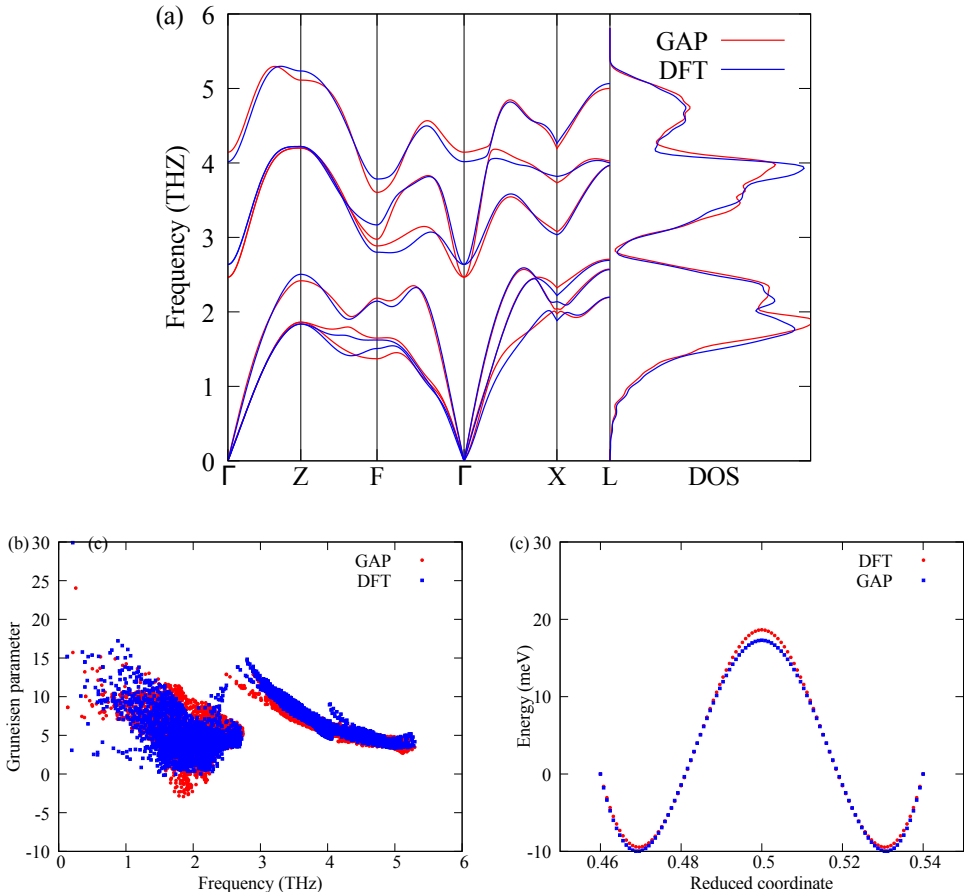

Figure 7.2: (a) Comparison of the phonon band structure and phonon density of states (side plot) of GeTe calculated using DFT and GAP. (b) Mode resolved Grüneisen parameters of GeTe calculated using DFT and GAP. (c) Comparison of the energy profile of the interatomic displacement parameter calculated with GAP and DFT

of the phase transition in GeTe will be successful.

7.2 Results

7.2.1 Thermal expansion of GeTe from molecular dynamics simulations

First, we will show the results for the thermal evolution of GeTe structure using MD simulations. To achieve this, we ran MD simulations using the LAMMPS code [93] in NPT ensemble, by fixing pressure at 0 Pa at the appropriate temperature. We ran the simulation using a supercell of 2000 atoms (the $10\times10\times10$ supercell)[2]. First, we

[2]We checked convergence with respect to the supercell size and found that the dependence of the critical temperature on the supercell size is weak

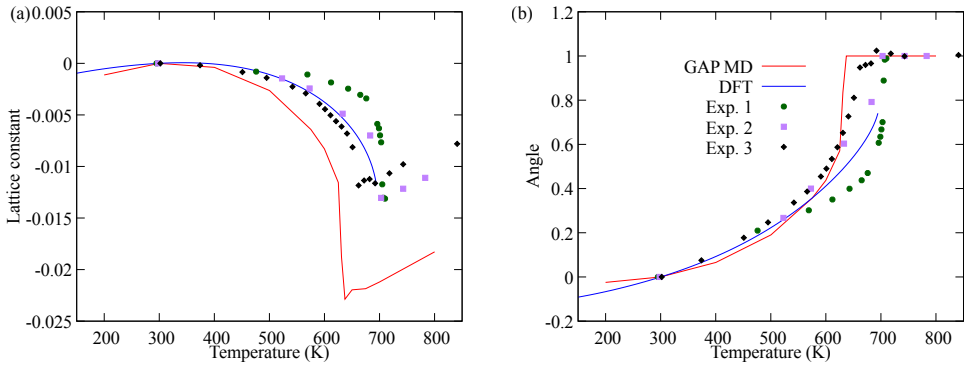

Figure 7.3: Thermal expansion of (a) lattice constant, and (b) rhombohedral angle using different methods. The error bars associated with the GAP model are not visible on the graph (smaller than experimental points). Experiments correspond to Refs. [7, 19, 20].

equilibrated the structure in the NVT ensemble for 10 ps, followed by a 20 ps NPT calculation for further equilibration. We used the 1 fs timestep for the integration of Newton's equations of motion. After the equilibration, we ran a 100 ps simulation collecting appropriate macroscopic quantities every 100 fs. For the calculation of the polarization (order parameter), we sampled atomic positions at every timestep. We calculated average quantities and standard errors by simple arithmetic averaging of obtained datasets (the ensemble averages[3] gave similar results).

Figures 7.3 and 7.4 show the thermal expansion of germanium telluride obtained by different methods and compared with experiment. Here we show the relative change of the structural parameters (α):

$$\alpha_u = \frac{u_T - u_{300}}{u_{300}} \quad \text{for } u = a, V,$$
$$\alpha_\theta = \frac{\theta_T - \theta_{300}}{60 - \theta_{300}}.$$

GAP in these figures denotes the results obtained by molecular dynamics simulation, DFT is our study of thermal expansion from Chapter 3, and experiments are from Refs. [7, 19, 20]. We can see that our results qualitatively track the experimental results really well. GAP mimics the experimental results for volume much better than DFT, while for lattice constant is the other way around.

The negative thermal expansion at the phase transition is present in both computational methods (see Fig. 7.4) and agrees qualitatively with experiments. In our previous computational study of negative thermal expansion, we recognized the acoustic-soft optical mode coupling as the reason behind negative thermal expansion. Molecular dynam-

[3] Sums weighted by the probability of the state, $\exp(-\frac{-E_i}{k_B T})$.

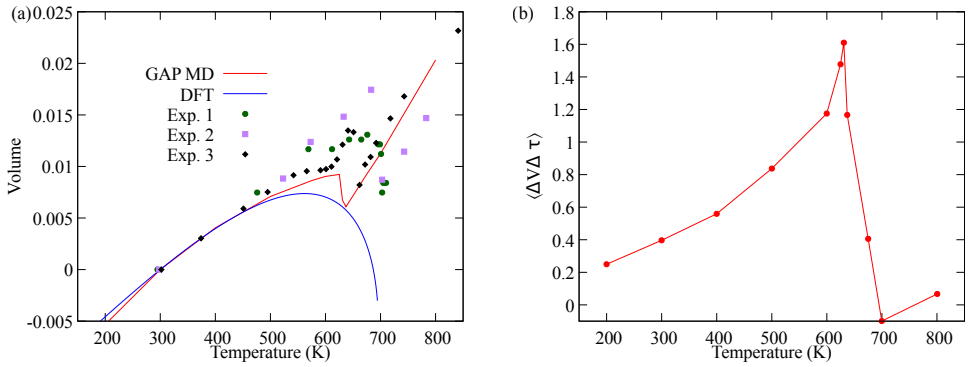

Figure 7.4: (a) Thermal expansion of volume in germanium telluride using different methods. Experiments correspond to Refs. [7, 19, 20]. (b) The volume-order parameter correlation coefficient at different temperatures. We can see a large increase at the phase transition, which is a sign of an increased coupling between strain and order parameter.

ics simulations do not provide us a direct measure of the acoustic-soft optical mode coupling. However, we can infer the behavior of this quantity by calculating the correlation coefficient between the volume and the order parameter τ (for definition of τ see the next section):

$$C_{V\tau} = \langle \Delta V \Delta \tau \rangle = \frac{1}{N} \sum_{i=1}^{N} (V_i - \langle V \rangle)(\tau_i - \langle \tau \rangle), \tag{7.1}$$

where $\langle V \rangle$ is the sample average of the volume and $\langle \tau \rangle$ is the sample average of the order parameter. We can see this quantity in Fig. 7.4 (b) as a function of temperature. This quantity peaks at the phase transition, as we would expect from our previous computational study in Chapter 3.

Some experimental studies claimed that the origin of the negative thermal expansion (NTE) in GeTe at the ferroelectric phase transition is the excess vacancy formation at the structural phase transition [20, 7]. Here we have shown, using two different, first principles models that the negative thermal expansion is not solely due to vacancies and is an intrinsic property of the ferroelectric phase transition. This is implicitly confirmed by the experimental observation of NTE at the phase transition in a large number of ferroelectric materials [226, 220, 227]. However, vacancies might have a role in the subtle differences between experiments and theoretical results in this work.

Another important detail is that the thermal expansion is hugely anisotropic in GeTe. The in-plane directions (perpendicular to the trigonal axis) experience positive thermal expansion in the entire temperature range, even at the phase transition. On the other hand, the direction parallel to the trigonal axis is contracting in most of the temperature range in the rhombohedral phase (except below room temperature). In the cubic

phase, this direction has a positive thermal expansion. This is in accordance with experiments [7, 19, 20] that observe the same effects.

7.2.2 Order parameter at the phase transition

Next, we look at the properties of the order parameter τ at the phase transition. We define the local order parameter as the instantaneous distance of the tellurium atom $\vec{x}_{Te,i}(t)$ from the center of the primitive unit cell (defined by the average primitive lattice vectors $\vec{r}_j$, which we use to define the initial structure in NVT ensemble, and the position of the germanium atom $\vec{x}_{Ge,i}(t)$). In this case, the order parameter is the average of the local order parameter over the entire simulation cell of N atoms:

$$\tau(t) = \frac{1}{N}\sum_{i}^{N}\tau_i(t) = \frac{1}{N}\sum_{i}^{N}\left(\vec{x}_{Te,i}(t) - \vec{x}_{Ge,i}(t) - 0.5\sum_{j}\vec{r}_j\right). \tag{7.2}$$

The order parameter at a given temperature was obtained by running a 300 ps long MD simulation in the NVT ensemble (keeping the number of particles, volume and temperature fixed) for a 512-atom large supercell with the structural parameters from Fig. 7.3. We sampled atomic positions every second time step (every 2 fs) and obtained the order parameter by averaging the local order parameter over all time steps and unit cells. Additionally, we calculated the absolute value of the local order parameter at each timestep and unit cell and averaged it in the same way. We present the results in Fig. 7.5 (a) and compare them to available experimental results and our previous DFT study. We find a satisfactory agreement between different methods, with the largest difference coming from the different estimations of the critical temperature. We can see that the average of the absolute value of the local order parameter and the polarization start diverging from each other, as we approach critical temperature. This could be the fingerprint of the order-disorder type of the phase transition. However, this is not conclusive since the absolute polarization in the other two directions (perpendicular to the trigonal axis) has similar values, so the difference appears to be due to the Debye-Waller factor. Alternatively, this could be the sign of the polarization switching between equivalent low symmetry positions (along the other three body diagonals of the conventional cubic rocksalt structure).

Alternatively, one might look at the frequency of the A_1 phonon mode (soft phonon mode) as an order parameter. This would be true in the displacive type of phase transition, where the frequency of this mode would depend quadratically on the order parameter value [54]. We show the calculated frequency values of the E and A_1 modes

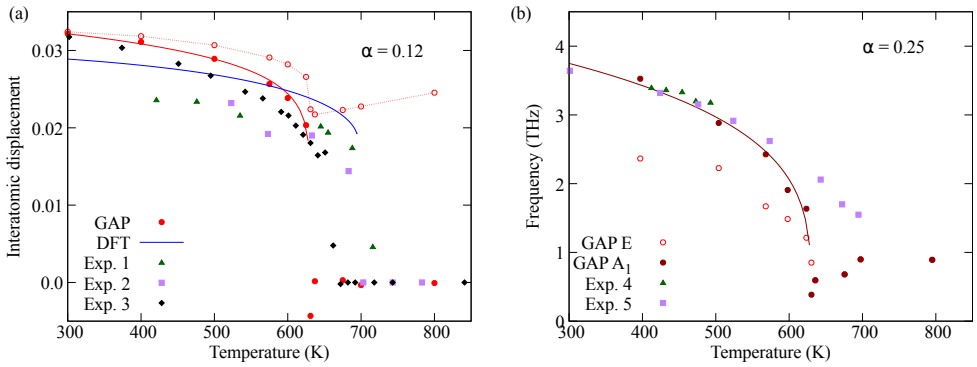

Figure 7.5: (a) Calculated temperature dependence of the polarization in GeTe compared to experiments. Full red points represent the average polarization at a certain temperature, while empty points are the average absolute values of the polarization. Experimental results are from Refs. [7, 19, 20]. (b) Calculated temperature dependence of the soft TO mode in GeTe compared to experiments [3, 9]. Full lines in both panels represent the function $f(T) = A(T_C - T)^{\alpha}$ fitted to the calculated values of polarization and soft TO mode.

using the temperature-dependent effective potential (TDEP) method with the data obtained from the GAP potential using atomic configurations from MD simulations in Fig. 7.5 (b). We compared them with the experimental values [3, 9] and found good agreement between the two methods. We fitted softening of the order parameter values and the soft mode to the simple functional form $f(T) = A(T_C - T)^{\alpha}$ and found that the α exponent is around two times larger for the soft phonon mode compared to the order parameter, as expected from the simple Landau model [54] of second-order phase transitions. This might be a good argument for the displacive nature of phase transition in GeTe.

To better understand the behavior of the order parameter at the phase transition, we calculate the polarization correlation function as:

$$G_{ij}(\vec{r},t) = \langle \tau_i(0,0)\tau_j(\vec{r},t)\rangle = \int\int \mathrm{d}\vec{r}'\,\mathrm{d}t'\,(\tau_i(\vec{r}',t') - \langle\tau_i\rangle)\Big(\tau_j(\vec{r}'+\vec{r},t'+t) - \langle\tau_j\rangle\Big). \tag{7.3}$$

$\langle\vec{\tau}\rangle$ is the value of the order parameter at a given temperature. We also define the Fourier transform of this function as $\Gamma_{ij}(\vec{q},\omega)$. Figure 7.6 (a) shows $\Gamma_{zz}(\vec{q}=0,\omega)$ for different temperatures. We can see that the polarization along the anisotropy axis oscillates with the identical frequency as that of the soft A_1 phonon mode, as one might expect. The two perpendicular directions oscillate with the frequencies of other two optical (E) phonon modes at Γ. We can see that the oscillations vanish at the phase transition and we only observe the exponential decay of the correlation function with time. This decay can be explained by the disappearance of temporal correlations of the

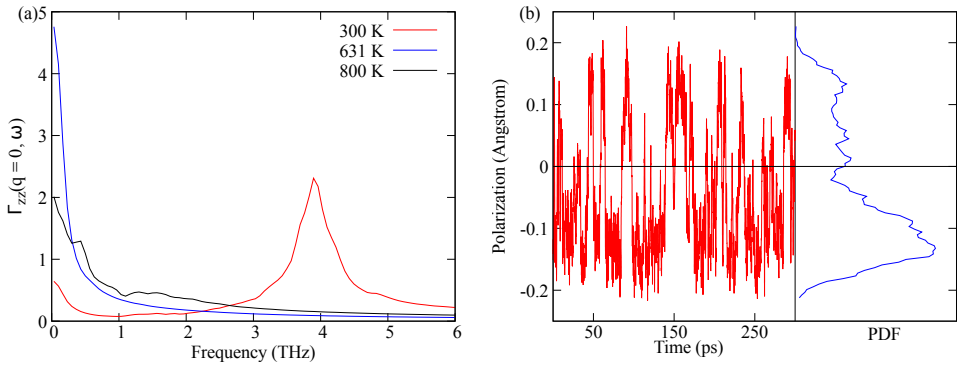

Figure 7.6: (a) Dynamical properties of the order parameter at different temperatures. The figure shows the Fourier transform of the polarization correlation function for different temperatures. (b) Switching behavior of the polarization close to the phase transition (631 K). The side plot shows the probability distribution function of the order parameter along the MD trajectory shown in the larger part of the figure.

order parameter at the phase transition and the appearance of switching phenomena (shown in Fig. 7.6(b)). The frequency of the switching between two equivalent order parameter positions depends strongly on the size of the simulation cell. The switching frequency is smaller for larger simulation cells.

Figure 7.6 (b) shows that while the instantaneous polarization remains correlated (hence non-zero), the polarization averaged over time will be zero. This, however, is not the order-disorder phase transition we usually think of. Order-disorder phase transition would involve a spatially decaying polarization correlation as well (we would expect the instantaneous polarization to be zero as well). The side plot of Fig. 7.6 (b) shows the probability distribution function (PDF) of the spatial average of the polarization at the phase transition (631 K). The PDF does not peak at zero but has the highest probability for non-zero polarization values. In the order-disorder phase transition this probability distribution function would peak at 0, while the PDFs of the local polarizations would have peaks at non-zero values (the peak's position would take $\pm\tau$ values to satisfy the conditional that the overall instantaneous polarization is zero).

To investigate these assumptions, we calculated the instantaneous probability distribution function of the local polarization (see Fig. 7.7). We expect the polarization to be normally distributed around some mean value which in the cubic phase should be zero in the displacive phase transition, and non zero for the order-disorder phase transition. However, this analysis might be clouded if the means of the polarization PDF in the order-disorder case of phase transition are sufficiently close to zero so their PDFs overlap. The peak of this sum of the PDFs would then be at zero mimicking the displacive phase transition.

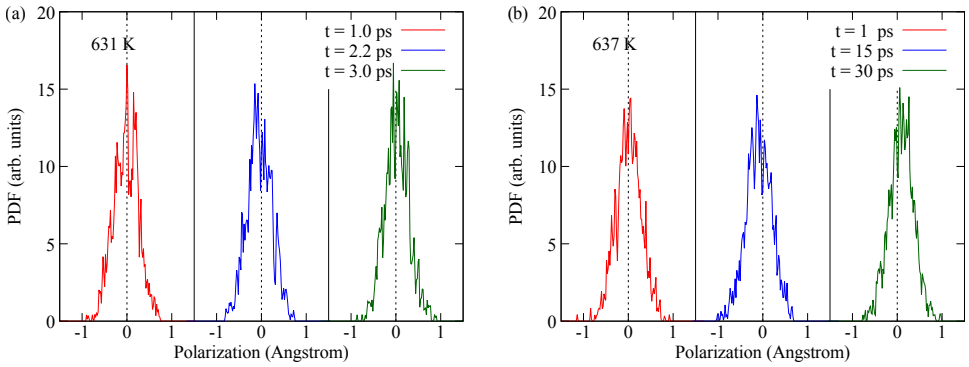

Figure 7.7: (a) Probability distribution function (PDF) of the local order parameter at 631 K at three different timesteps. (b) PDF of the local order parameter at 637 K at three different timesteps.

Figure 7.7 (a) shows the PDF of local polarization at 631 K. These PDFs can be fitted to the Gaussian function with a mean at non zero values, confirming the ferroelectric nature of GeTe at this temperature. At 637 K (Fig. 7.7 (b)), however, the PDFs can be fitted with a Gaussian that has the mean close to 0 (several times smaller than the mean for the PDFs in Fig. 7.7 (a)), indicating that the system is in the paraelectric state. As we said in the previous paragraph, the position of the mean of these PDFs can not conclusively tell us about the type of the phase transition. To gain more insight, we calculated these PDFs every ps, fitted them to a Gaussian and in the end averaged the fitted means and variances. We performed this for each temperature.

The results of this study are shown in Fig. 7.8 for the change of the variance of the order parameter PDFs with temperature (the means have the same functional dependence as the polarization, see Fig. 7.5). What we expect to see in the displacive phase transition is that the variance is a smooth function of temperature, without any odd behavior at the phase transition. For the order-disorder phase transition, due to the PDF being actually a sum of two Gaussians, we would expect variance to have a peak in the vicinity of the phase transition. What we actually observe is a combination of these two cases. Variance does not peak at the phase transition, but it does experience a small step, much larger then the standard error of the calculated values of the variance at that temperature (the standard error is too small to be visible on the graph). The step is however very small, indicating if there are two local minima at 637 K they are very close to the 0. From all of these results, we can conclude that the phase transition in GeTe has signatures of both displacive and order-disorder phase transitions.

We tried calculating the correlation length of the polarization in this system. We noticed an exponential decay of the polarization correlation with distance. The correlation length fitted from this decay increases at the phase transition. However, our sim-

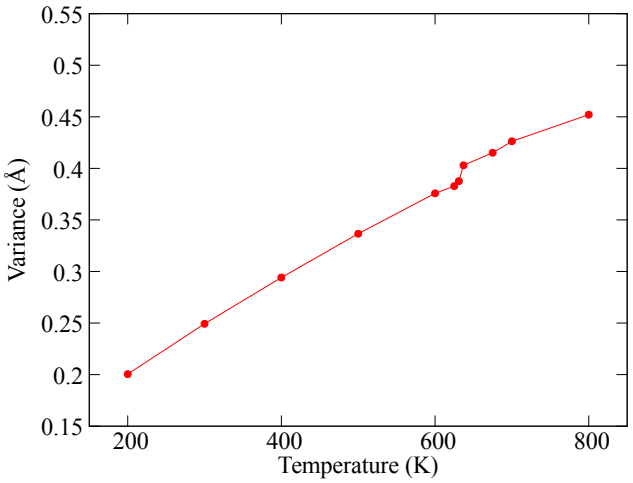

Figure 7.8: Variance of the local polarization averaged over time as a function of temperature.

ulation cells are too small to notice divergence of the correlation length at the phase transition, which would confirm the second-order nature of the phase transition.

7.2.3 Vibrational properties of GeTe from MD simulations

Molecular dynamics simulations allow us to easily extract temperature dependent vibrational properties of materials. Here we show the vibrational properties of GeTe at different temperatures computed using MD and compare them to the lattice dynamics simulations.

We have performed a MD simulation with GAP interatomic potential in the NVT ensemble for several temperatures to obtain the vibrational properties of GeTe. To sample a larger number of normal modes we used a 4096 atoms supercell. We first ran a 50 ps equilibration calculation, followed by a 150 ps long MD simulation to obtain data with a 1 fs timestep. We sampled atomic positions and velocities every 5 timesteps. We also sampled forces every picosecond. We used forces and atomic positions to fit TDEP force constants to obtain harmonic properties (TDEP frequencies and eigenvectors) at a given temperature.

First, we calculate the phonon density of states (PDOS) of GeTe at 300 K and 631 K (close to the phase transition). We obtain PDOS by calculating the Fourier transform of the velocity autocorrelation function [228]:

$$G(\Omega) = \frac{1}{2\pi} \sum_{l,\alpha,j} \int \langle v^j_{l\alpha}(0) v^j_{l\alpha}(\tau) \rangle e^{i\Omega\tau} d\Omega. \tag{7.4}$$

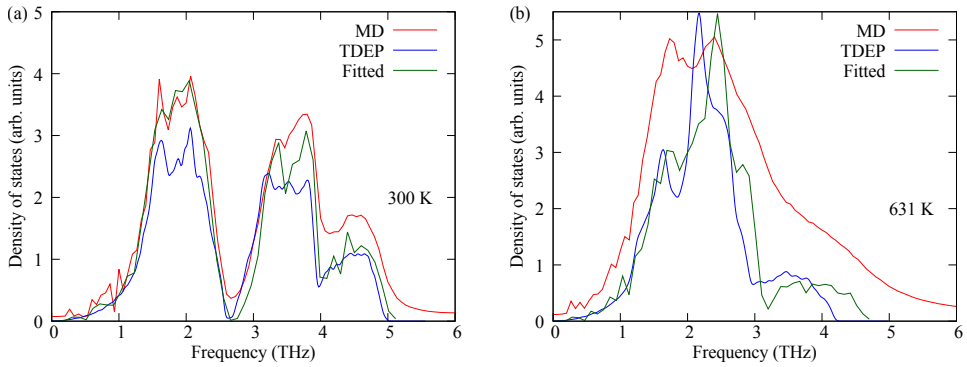

Figure 7.9: Phonon density of states in germanium telluride at (a) 300 K and (b) 631 K calculated with three different methods: the velocity autocorrelation function power spectrum from molecular dynamics (MD), lattice dynamics (TDEP), from frequencies obtained by fitting the velocity autocorrelation function (fitted).

Here, $v^j_{l\alpha}$ is the velocity of the α atom in the lth unit cell in the Cartesian direction j and τ is the correlation time. The correlation function is computed by:

$$\langle v^j_{l\alpha}(0) v^j_{l\alpha}(\tau)\rangle = \frac{1}{N}\sum_i v^j_{l\alpha}(t_i) v^j_{l\alpha}(t_i+\tau).$$

Here the sum is performed over N consecutive timesteps. We show the comparison between the MD results and the lattice dynamics calculations at two different temperatures in Fig. 7.9. We note that the lattice dynamics result is obtained with the temperature dependent effective potential (TDEP) method [106, 107, 108] using forces calculated with the GAP potential. We can see that the agreement is very good at both temperatures. We disregard the differences in the total number of modes since the normalization of the MD data is ambiguous. There is, however, a slight shift of the dip in the PDOS at 300 K (at around 2.6 THz, related to the acoustic-optical mode gap), which might be a consequence of the fourth-order anharmonicity not captured in our lattice dynamics calculations. We also show the calculated PDOS from the fitted frequencies (we will explain the fitting procedure further in the next section) and find that this method gives even better agreement with lattice dynamics calculations.

Secondly, we can project atomic velocities onto phonon mode eigenvectors and obtain spectral functions of the individual phonon modes (here we consider only $\vec{q}$-vectors that are commensurate for a given supercell). The phonon mode projected velocities are obtained with [228, 109]:

$$v_{\vec{q},s}(t) = \sum_\alpha \sqrt{\frac{m_\alpha}{N}} \sum_l \mathrm{e}^{-i\vec{q}\cdot\vec{r}_l} \vec{v}_{l\alpha}(t)\cdot\epsilon^\alpha_{\vec{q}s}.$$

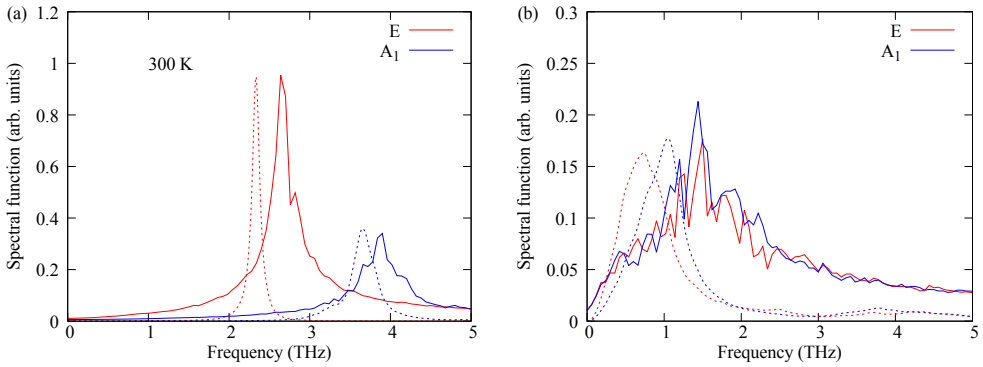

Figure 7.10: Zone center optical phonon mode spectral functions at (a) 300 K and (b) 631 K, calculated with two different methods (full lines are molecular dynamics simulations, while dashed lines are the lattice dynamics calculations implemented in the temperature dependent effective potential method).

Here m_α is the mass of the α-th atom in the unit cell, l counts the unit cell in the MD simulation cell, and $\epsilon_{\vec{q}s}$ is the eigenvector of the phonon with the wave vector $\vec{q}$ and branch s calculated from TDEP. We calculate the Fourier transform of the autocorrelation function of this quantity to obtain phonon spectral function [228]. Figure 7.10 shows the phonon spectral function of the zone center optical phonon modes at 300 K and 631 K. To compare these quantities with lattice dynamics, we calculated $\langle B^\dagger_{\vec{q}s} B_{\vec{q}s} \rangle$ ($B_{\vec{q}s}$ is the scaled Fourier transform of the velocity operator) using lattice dynamics, as shown in Chapter 5. These quantities in the harmonic limit are the same as the neutron scattering cross-section, which is proportional to $\langle A^\dagger_{\vec{q}s} A_{\vec{q}s} \rangle$, but in highly anharmonic materials, they are noticeably different. While $\langle A^\dagger_{\vec{q}s} A_{\vec{q}s} \rangle$ (or $\langle u^*_{\vec{q}s} u_{\vec{q}s} \rangle$ in MD) peaks at the zero frequency at the phase transition, the peak of the Fourier transform of the velocity autocorrelation function is at non-zero frequencies, as shown in Fig. 7.10 (b). Here we show the velocity autocorrelation function since it is much less noisy in MD simulations compared to the displacement autocorrelation function. We can see that the TDEP lattice dynamics always underestimates the peak of the spectral function compared to MD simulations, as well as the broadening of the lineshape. This could mean that the first-order perturbation theory in the expansion of the self-energy is not sufficient at the phase transition, even if it is implemented as in TDEP.

Finally, the average energy of each phonon mode can be regarded as a multiple of its frequency [223] $\langle E_{\vec{q}s} \rangle = n_{\vec{q}s} \hbar \omega_{\vec{q}s}$, where $n_{\vec{q}s}$ is the phonon population. We can calculate the average phonon mode energy as:

$$\langle E_{\vec{q}s} \rangle = \langle T_{\vec{q}s} \rangle + \langle V_{\vec{q}s} \rangle = \frac{1}{2N_t} \sum_i \left(|v_{\vec{q}s}(t_i)|^2 + \omega^2_{\vec{q}s} |u_{\vec{q}s}(t_i)|^2 \right).$$

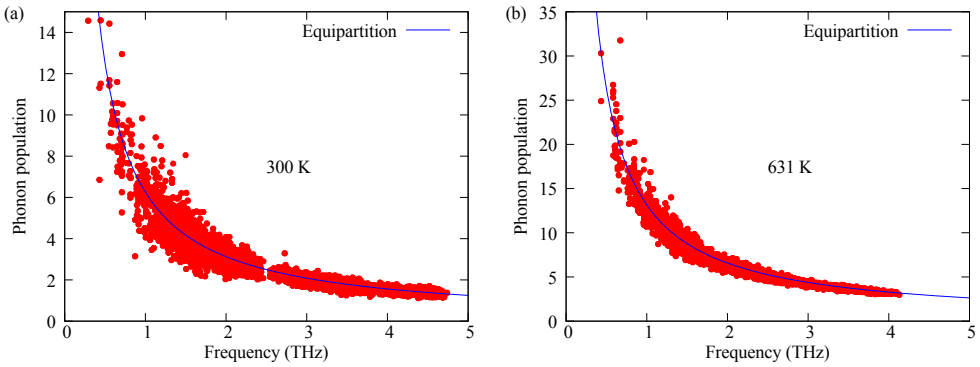

Figure 7.11: Phonon populations calculated from molecular dynamics simulations at (a) 300 K and (b) 631 K, and compared to the values extracted from the equipartition law ($n_{\vec{q}s} = \frac{k_B T}{\hbar \omega_{\vec{q}s}}$).

In molecular dynamics simulations, each phonon mode should have $k_B T$ energy. We show this in Fig. 7.11 for two different temperatures. Although we might expect that the phonon populations diverge from the equipartition law at the phase transition, this does not happen.

7.2.4 Lattice thermal conductivity from molecular dynamics

Lattice thermal conductivity can be calculated directly from molecular dynamics simulation utilizing the Green-Kubo theory [217, 218, 221, 222]. We connect the heat current autocorrelation function to the lattice thermal conductivity similarly as in the Chapter 5, see Eq. (2.30):

$$\kappa^{\alpha\beta} = \frac{1}{NVk_BT^2} \int_0^\infty \langle J^\alpha(0) J^\beta(t) \rangle \mathrm{d}t. \tag{7.5}$$

k_B is the Boltzmann constant and T is the temperature. Here the total volume of the simulation cell NV is in the denominator because the heat current is calculated in LAMMPS [93] as:

$$J^\alpha = \sum_i \left(e_i v_i^\alpha + \left[\hat{S}_i \cdot \vec{v}_i \right]^\alpha \right). \tag{7.6}$$

In the above equation e_i is the energy associated with the atom i and $\hat{S}_i$ is per atom stress of the atom i [229] and the *hat* symbol signifies the tensor nature of this variable. In Eq. (7.5) the integration can not be performed to infinity, so we have to choose some maximum correlation time to evaluate the integral. On top of that, we have to converge our results with respect to the total length of the simulation (in terms of timesteps) and the size of the supercell. For more information on the convergence study please refer

to Appendix C.

Figure 7.12 shows the comparison of the calculated lattice thermal conductivity values using molecular dynamics and the Boltzmann transport equation (BTE) with experimental results. The Boltzmann transport results here were obtained using force constants computed with the GAP potential and the TDEP method. The agreement between MD and the experiment is very good. More importantly, both computational methods (BTE and MD) show an increase of the lattice thermal conductivity at the phase transition. However, BTE agrees with MD only qualitatively and consistently overestimates the lattice thermal conductivity compared to experiment and MD. The difference between the MD and BTE results increases in the cubic phase.

We have also calculated the lattice thermal conductivity using the BTE with the phonon lifetimes obtained from MD through the fitting procedure (this will be explained later in the text), see green lines in Fig. 7.12. To mimic the MD setup, we used the equipartition theorem value for phonon mode heat capacity (constant k_B value). The group velocities are obtained from TDEP. At low temperatures, this approach and MD agree almost perfectly, but they deviate as temperature increases, with the MD Green Kubo method giving consistently larger values of lattice thermal conductivity. The difference is largest at the phase transition. Because of this behavior of the discrepancy, one might speculate that the difference is due to an additional mechanism of heat transport, maybe one described in Chapter 5. The BTE method with fitted MD lifetimes also shows a slight increase of the lattice thermal conductivity at the phase transition, but much smaller than the other two methods.

To evaluate the reason behind the lattice thermal conductivity enhancement at the phase transition, as well as to understand the differences between the MD and TDEP approaches, we calculated phonon lifetimes for both of them. We do this by explicitly calculating the phonon mode velocity autocorrelation function for each phonon mode. This time series is then fitted to the decaying oscillation:

$$\frac{\langle v^*_{\vec{q}s}(t)v_{\vec{q}s}(0)\rangle}{\langle v^*_{\vec{q}s}(0)v_{\vec{q}s}(0)\rangle} = \exp(-\frac{t}{2\tau_{\vec{q}s}})\cos(2\pi\nu_{\vec{q}s}t), \tag{7.7}$$

where $\tau_{\vec{q}s}$ is the relaxation time of the phonon with a wavevector $\vec{q}$ and branch s, while $\nu_{\vec{q}s}$ is the fitted frequency of the same mode. One can use the values $\langle v^*_{\vec{q}s}(0)v_{\vec{q}s}(0)\rangle$ to extract phonon populations ($\langle v^*_{\vec{q}s}(0)v_{\vec{q}s}(0)\rangle = \frac{h\nu_{\vec{q}s}}{2}(2n_{\vec{q}s}+1)$) and would get the similar result to the one shown in Fig. 7.11.

First, we show the comparison between the lattice dynamics (TDEP) and molecular

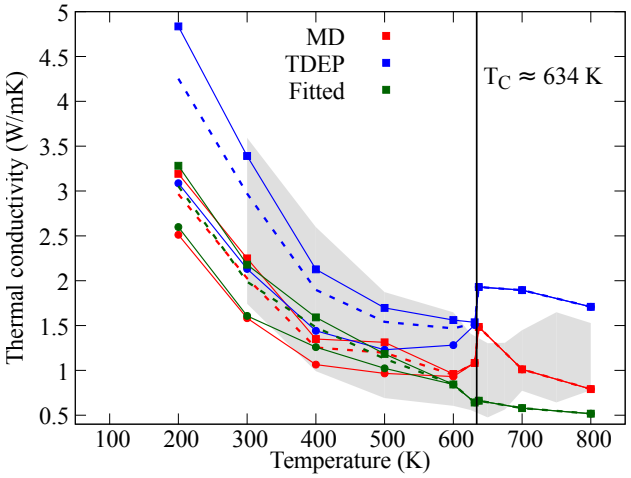

Figure 7.12: Lattice thermal conductivity of germanium telluride calculated using molecular dynamics (MD) (red lines and dots), the Boltzmann transport equation (BTE) with the temperature dependent effective potential (TDEP) method and the GAP forces (blue lines and dots), and BTE with phonon lifetimes fitted to MD simulations (green lines and dots) and compared to experiment (gray region). The lines with squares represent the lattice thermal conductivity along directions perpendicular to trigonal axis (in-plane directions), while lines with dots are results along direction parallel to trigonal axis. The dashed lines are average values of the lattice thermal conductivity.

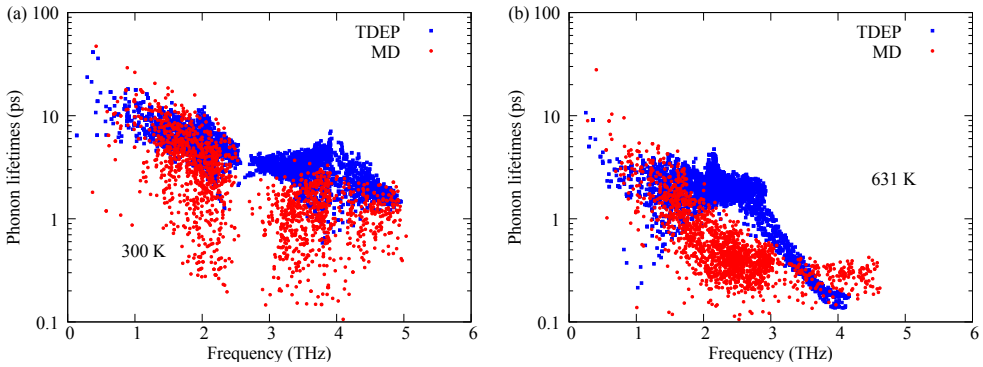

Figure 7.13: Phonon lifetimes calculated from molecular dynamics (see Eq. (7.7)) and the temperature dependent effective potential (TDEP) method at (a) 300 K and (b) 631 K.

dynamics results for phonon lifetimes in Fig. 7.13 for two different temperatures, 300 K and 631 K. At 300 K, the MD simulation gives smaller phonon lifetimes in the whole frequency region compared to TDEP and most prominently for optical phonons. For this region, the average MD phonon lifetime is several times smaller compared to the TDEP approach. In the acoustic branch region, MD gives smaller lifetimes as well for some phonon modes. In fact, these lifetimes are as small as those for the optical phonons. It is hard to pinpoint whether this anomalous behavior is due to the fitting procedure, insufficiently long MD simulation, or an actual physical effect.

At 631 K, the MD results for phonon lifetimes are again much smaller than the TDEP

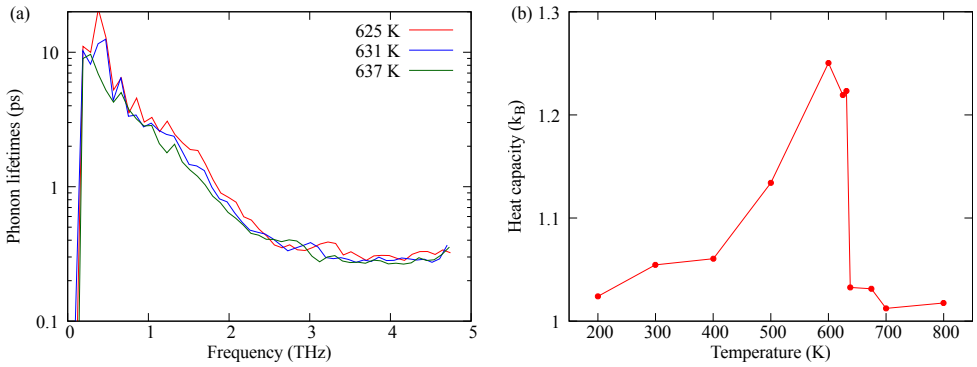

Figure 7.14: (a) Average phonon lifetimes from molecular dynamics at three different temperatures closest to the phase transition (see Eq. (7.7)). (b) The heat capacity of GeTe calculated from energy fluctuation at different temperatures (see Eq. (7.8)).

ones. Most strikingly, the region between 2 and 3 THz, which has been shown to carry most of the heat in the LD approach, has several times smaller phonon lifetimes in the MD approach compared to TDEP. This region also shows the largest density of states (see Fig. 7.9 (b)). One possible reason for this discrepancy might be the fourth order anharmonicity, which is neglected in the TDEP approach.

Finally, we reveal the reason behind the lattice thermal conductivity enhancement at the ferroelectric phase transition by calculating the phonon lifetimes at three temperatures closest to phase transition (625, 631, and 637 K) using the fitting procedure. We show the average of these lifetimes in Fig. 7.14. What is immediately noticeable is that the phonon lifetimes at 625 K are larger than the phonon lifetimes at two other temperatures. Since the MD lattice thermal conductivity increases from 625 K to 631 K and 637 K, while the phonon lifetimes decrease, we conclude that the phonon group velocities must have increased. This confirmes the conclusion from Chapter 5 that the increase of the phonon group velocities is the driving force behind the lattice thermal conductivity enhancement at the phase transition.

The fact that the values of phonon lifetimes between 631 and 637 K overall stay constant in MD represents another difference with respect to TDEP. In our TDEP study, there is a noticeable increase of phonon lifetimes between these two temperatures due to a decrease in the third-order anharmonic force constants (see Chapter 5). However, we do not notice that in our MD study, although the lattice thermal conductivity does increase at the phase transition.

Another possible reason for the increase of the lattice thermal conductivity at the phase transition might be the increase of the heat capacity. We recognized this increase of the heat capacity at the phase transition as the main reason for the discrepancy between Boltzmann transport and the Green-Kubo approach in Chapter 5. In the NVT ensem-

ble, we can calculate the heat capacity at constant volume of the system from energy fluctuations (here we consider only potential energy fluctuations, since kinetic energy is much more heavily influenced by the thermostat):

$$C_V = \frac{1}{Nk_BT^2N_{df}} \sum_i^N (U_i - \langle U \rangle)^2, \tag{7.8}$$

where N is the number of timesteps taken in the sum, N_{df} is the number of degrees of freedom, U_i is the potential energy of the system at timestep i, and $\langle U \rangle$ is the average potential energy. Heat capacity at constant volume for different temperatures is shown in Fig. 7.14 (b). We can see a drastic increase in the heat capacity at the phase transition, which can partially explain the increase of the lattice thermal conductivity. However, this does not resolve a large discrepancy between the MD and BTE results with fitted lifetimes in the cubic phase.

7.3 Conclusion

In conclusion, we performed a molecular dynamics simulation of the phase transition in GeTe. We fitted a very accurate interatomic potential using the Gaussian Approximation Potential framework. We were able to correctly track the lattice thermal expansion of GeTe and reproduce negative thermal expansion at the phase transition. We noticed an increase in the correlation between volume and internal atomic displacement, which we interpret as the enhancement of acoustic-soft optical phonon mode coupling, which we previously recognized as the reason behind lattice contraction at the phase transition. Investigation of the order parameter at the phase transition revealed both displacive and order-disorder signatures of the phase transition. We have calculated the lattice thermal conductivity of GeTe for a range of temperatures using equilibrium molecular dynamics simulations and the Green-Kubo formalism. The calculated κ showed an increase at the phase transition. Comparison of phonon lifetimes at different temperatures in the vicinity of the phase transition revealed that the increase of κ had to come partially due to an increase in the group velocities. The calculation of the heat capacity from energy fluctuations showed that a large contribution to the increase of κ might come from an increase of the heat capacity at the phase transition.

Chapter 8

Conclusions

8.1 Summary

This work was motivated by the previous computational prediction of the reduction of the lattice thermal conductivity at the ferroelectric phase transition in PbTe [50, 55]. We expanded the previous study to include higher-order anharmonicity in the calculation of the vibrational properties in a related material group, germanium telluride [230]. Additionally, we have investigated the influence of the phase transition on the mechanical properties of germanium telluride [79]. Finally, we determined the influence of the domain structure formation on the structural and transport properties of GeTe [82, 81].

It has been experimentally observed that germanium telluride experiences lattice contraction (negative thermal expansion) in the vicinity of the phase transition [7, 8, 20]. While fairly common in ferroelectrics [226, 220, 227] (and some ferromagnetic materials [231, 232]), this phenomenon has not been rigorously explained previously. Our first principles calculations on pristine single crystal GeTe showed negative thermal expansion at the phase transition with two completely different and unrelated methods. This shows that NTE is an intrinsic property of the ferroelectric phase transition in these materials and not induced by the presence of vacancies, as previously postulated [7, 20]. We have shown that the reason behind negative thermal expansion at the phase transition is the enhancement of the acoustic - soft transverse optical mode (strain - order parameter) coupling. This is in agreement with previous studies that showed that this type of coupling is responsible for the reduction of the lattice thermal conductivity at the phase transition in PbTe [50, 55].

Another intriguing feature of the phase transition in GeTe is the increase of the lattice thermal conductivity κ [10, 11, 179, 13, 14, 15, 16, 17]. We accurately model this phenomenon by two different and independent methods. We used a temperature dependent effective potential (TDEP) method to correctly capture the temperature dependent vibrational properties of GeTe [106, 107, 108]. We found that the enhancement of κ at the phase transition has two different origins depending on the phase of GeTe. In the rhombohedral, low temperature phase, κ increases due to negative thermal expansion which dramatically increases phonon group velocities. In the high symmetry, cubic, phase the phonon lifetimes increase as well, due to intrinsically lower anharmonicity of this phase compared to the rhombohedral phase. We confirmed this result by sampling the heat current autocorrelation function during equilibrium molecular dynamics simulation and using it in the Green-Kubo formula to obtain κ in the wide temperature range in GeTe.

The increased anharmonicity at the phase transition in germanium telluride causes phonon spectral functions to distort from the expected Lorentzian shape. Exotic behavior of phonon spectral functions at the phase transition lead us to question the applicability of the Boltzmann transport equation (BTE) used to model κ in this material. To correctly capture the contribution of non-Lorentzian phonon spectral functions, we implemented a novel method of calculating lattice thermal conductivity in highly anharmonic materials based on the Green-Kubo (GK) approach [109, 112, 111, 113]. We show that BTE consistently underestimates κ compared to the new method. The origin of this discrepancy between these two methods are phonon populations which are assumed to follow the Bose-Einstein distribution in BTE. The Green-Kubo approach, on the other hand, directly calculates the population of phonon modes accounting for phonon-phonon interactions. On the other hand, the estimated GK phonon lifetimes are smaller compared to the BTE ones. This cancellation of errors leads to a modest difference in the total lattice thermal conductivity of GeTe between the two methods.

The ferroelectric phase transition in germanium telluride is accompanied by the formation of domain structures, as observed in numerous experiments [80, 181, 182, 183]. We have performed a first principles computational study of structural, electronic, and transport properties of selected domain wall types in this material. We have found, as expected, that electrically neutral domain walls that are not twinned have the lowest domain formation energies and thus are most likely to be observed in real materials. All types of domain walls have structural distortions at the domain wall accompanying the polarization change. We have evaluated the thermal boundary resistance of these domain walls and found that the volume, rather than a shape, change at the domain wall is more important for the κ reduction. The domain wall (DW) size also has a large

effect on the boundary thermal resistance (larger DW size - larger resistance), as well as the domain wall density.

Depending on the nature of the polarization change between neighboring domains, some domain walls can be electrically charged. The bound charge at DWs can attract free charge carriers and trap them there, thus making these DWs intrinsically conductive. We have performed an investigation of the DW electronic properties and found that an electronic density of states of the p-doped tail-to-tail 39° $(11\bar{1})$ domain wall exhibits a strong peak close to the Fermi level. These peaks, that originate from the van Hove singularities in the electronic band structure, resemble ones observed in resonantly doped PbTe and GeTe where they substantially increase the thermoelectric power factor [68, 69]. We performed electronic transport calculations of these domain walls and showed that the power factor is approximately four times larger at the DW compared to the bulk material, due to the strong enhancement of the Seebeck coefficient. We also proposed a design of a nano-thermolectric device that fully utilizes the extraordinary electronic properties of GeTe DWs.

8.2 Outlook

Our results explained the origin of the enhancement of the lattice thermal conductivity at the phase transition but did not quantitatively describe the κ in the cubic phase. One possible reason for this might be the fact that we terminate the expansion of the potential energy at the third order, hence keeping only the leading order in anharmonic interaction. There are several recent publications that stress the importance of including higher order anharmonicity to describe highly anharmonic materials [105, 214, 215, 216]. A more detailed analysis of the influence of the higher order anharmonicity might be necessary to fully describe the κ in the cubic phase.

The Green-Kubo method of calculating the lattice thermal conductivity, as implemented in our work, reduces to BTE in the relaxation time approximation in the limit of low anharmonicity. Since we know that the relaxation time approximation is insufficient for some materials below the Debye temperature, there is an open question how to improve on the existing approach. Should we change the definition of the heat current [116]? Would higher orders in the perturbation expansion of Green's functions (equivalent to decoupling the system of equations at a later stage compared to our work) give rise to a momentum relaxation time, rather than a phonon mode relaxation time? Is it truly necessary to account for a two phonon Green's function to capture these effects,

as implied in some previous work [233]?

We have laid out a scheme for constructing different types of domain walls in the second chapter. However, due to an enormous computational cost, we did not consider domain walls based on the pseudocubic unit cell of GeTe. These domain walls have been observed in some of the experiments [80], so it would be very beneficial to actually model them from first-principles. The computational cost of relaxing these domain walls can be dramatically reduced using the interatomic potential we already constructed. This potential would allow us to explore an even larger set of possible domain walls and recognize those most suitable for thermoelectric applications.

Our results clearly showed that domain walls are effective phonon scatterers. However, our model is too simple to quantitatively capture the influence of DWs on thermal conductivity. This can be correctly modeled through the use of molecular dynamics simulations. Non-equilibrium MD simulations performed on GeTe supercells containing domain walls would give us a clear answer to what magnitude of the κ reduction is to be expected from these domain walls.

Our results on the Seebeck coefficient at the charged domain walls in GeTe are very promising. However, they are based on the model of electron-phonon interaction whose accuracy has not been properly evaluated. For a better estimation of transport properties, we should develop a more accurate representation of electron-phonon scattering. Additionally, DWs should attract vacancies or facilitate their formation. Another possible avenue of research would be to determine to what extent vacancies would modify electronic and structural properties of domain walls.

Appendix A

Convergence of the lattice thermal conductivity results

Figure A.1 (a) shows the convergence of the lattice thermal conductivity of GeTe with respect to the third order force constant cutoff. The second order force constant cutoff was always taken to be the maximum one that can fit in all of the structures (12 Å). We perform this study at 631 K, the temperature closest to the phase transition in the rhombohedral phase, where we expect the strongest anharmonicity. We can see clearly from the figure that the value of the lattice thermal conductivity converges for the cutoff of 8 Å.

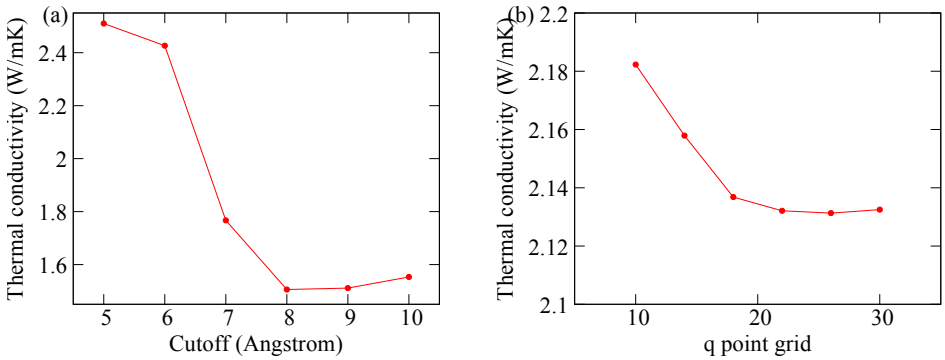

Figure A.1: Convergence study of lattice thermal conductivity with respect to (a) the third order force constant cutoff and (b) the $\vec{q}$ point grid.

Figure A.1 (b) shows the convergence of the lattice thermal conductivity of GeTe with respect to the $\vec{q}$ point grid. We performed this study for GeTe at 300 K. We chose the lower temperature, because we expect the lower temperature to be more sensitive to the $\vec{q}$-point grid sampling. At lower temperatures the populations of phonons vary more drastically, so a denser $\vec{q}$ point sampling is needed to converge results. The

convergence is reached for the $30\times30\times30$ $\vec{q}$ point grid.

The convergence of the lattice thermal conductivity using the Green-Kubo method is challenging due to the computational cost involved with calculating phonon self energy for different sampling of the frequency grid Ω. To determine a suitable density of the Ω sampling, we calculate the integral of the phonon spectral functions: $\langle A^{\dagger}_{\vec{q}s} A_{\vec{q}s}\rangle$ and $\langle B^{\dagger}_{\vec{q}s} B_{\vec{q}s}\rangle$ over frequency (Ω). These integrals are proportional to the values of the phonon displacement and velocity autocorrelation functions at the same time (and hence approximately to the phonon populations).

Figure A.2 shows the study explained above. The integrals were performed using the simple rectangular rule. The sampling of Ω always goes up to $2.1\times\omega_{\mathrm{D}}$, where ω_{D} is the maximum TDEP phonon frequency in the $30\times30\times30$ $\vec{q}$ point grid used in the evaluation of phonon self energy. We performed this study for the A_1 phonon mode close to the phase transition (631 K). The convergence is reached for 2000 points (the sampling density of $\frac{2.1\omega_{\mathrm{D}}}{2000}$).

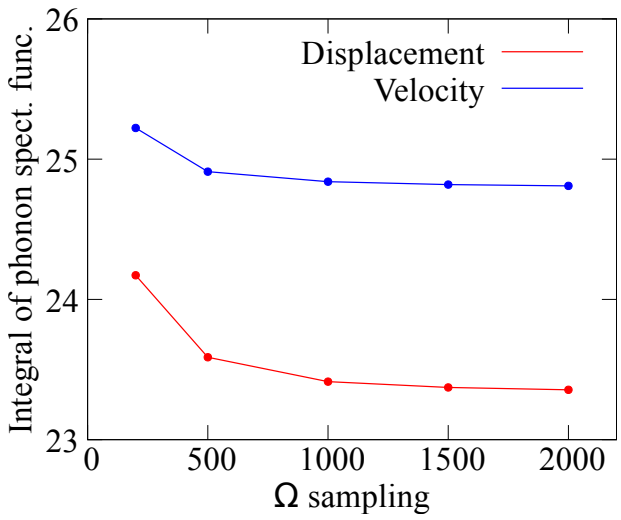

Figure A.2: Convergence study of the integral of the phonon spectral function of the A_1 phonon mode with respect to the number of points in the sampling of Ω.

Appendix B

Convergence of domain wall properties

B.1 Domain wall widths and energies

We have performed the convergence study for the structural properties of ferroelectric domain walls (DWs) in GeTe with respect to the domain size. To reduce the computational time needed for the study here we relax Te atoms only, keeping the lattice vectors and Ge atom positions fixed. The widths and energies of $(11\bar{1})$ domain walls are shown in Table B.1. We can see that the 64 atom supercell is sufficiently large for 39° and 141° DWs, since it gives the similar values of domain wall widths and energies compared to larger cells. For 180° DWs the convergence is reached for the 80 atoms supercell.

The same convergence study for the hexagonal domain walls is presented in Fig. B.1. Converging results for these domain walls was more challenging mostly due to the larger number of atoms in the hexagonal unit cell. Additionally, the bound charge at (111) domain walls is larger compared to $(11\bar{1})$ DWs, causing larger electrical field along the domain that makes the relaxation of these domain walls more challenging. We can see that the sufficient convergence was achieved for the 144 atoms supercells.

Table B.1: Domain wall (DW) widths and energies for different sizes of the simulation supercell relaxing only Te atom positions.

39° DW	H-H DW width [Å]	T-T DW width [Å]	DW energy [mJ/m^2]
64 atoms	2.47	6.13	1198
96 atoms	2.47	6.11	1170
104 atoms	2.70	6.13	1205
141° DW	H-T DW width [Å]	T-H DW width [Å]	DW energy [mJ/m^2]
64 atoms	4.03	4.33	1070
96 atoms	4.15	4.49	1056
104 atoms	4.14	4.40	1075
180° DW	H-H DW width [Å]	T-T DW width [Å]	DW energy [mJ/m^2]
64 atoms	11.44	12.45	772
80 atoms	16.11	13.60	966
104 atoms	16.16	13.75	955

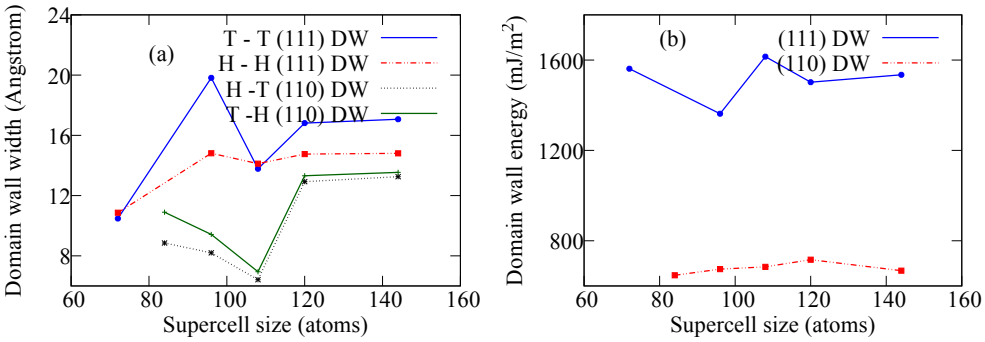

Figure B.1: (a) Domain wall width and (b) domain wall energy for (111) and (1$\bar{1}$0) domain walls (DWs) as a function of the supercell size.

B.2 Convergence of the Seebeck coefficient with respect to the number of k points

We performed a convergence study of the Seebeck coefficient with respect to the number of $\vec{k}$-points in the evaluation of the sum in Eq. (2.26). Since the calculation of the transport properties using the electron relaxation times defined through the overlap of the wave functions is very time consuming, we performed the convergence study using the constant relaxation time and for p-type GeTe.

Figure B.2 (a) shows the convergence study for bulk GeTe. We can see that the Seebeck coefficient values calculated with 60^3 and 70^3 $\vec{k}$-grids are very similar.

Figure B.2 (b) shows the convergence study for the T-T 39° (11$\bar{1}$) domain walls. We generated an equidistant grid of $\vec{k}$-points in the first Brillouin zone. We chose the points so they lie inside the Wigner-Seitz cell. We needed this for plotting Fig. 6.15 (a) and then we used the same method to sample points for the calculation of the transport properties. Since the grid is not square in the reciprocal lattice vectors space, we give the total number of points used in the sum. We see that for three grid sizes we used, the numbers are quite similar, so we chose the smallest grid to perform a transport study with energy and momentum dependent electron lifetimes.

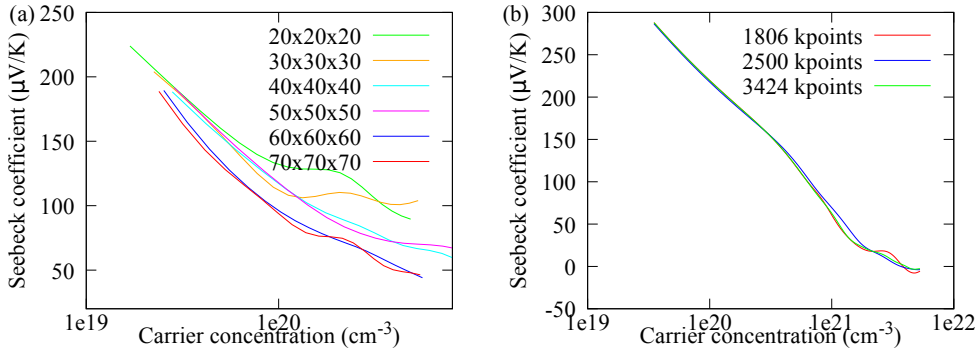

Figure B.2: Convergence study of transport properties with respect to the number of $\vec{k}$ points for (a) bulk GeTe and (b) T-T 39° (11$\bar{1}$) domain wall.

Appendix C

Convergence issues with molecular dynamics simulations

Molecular dynamics (MD) simulations, while extremely powerful at describing thermal properties of materials, are notoriously hard to converge. In our case, using the Gaussian Approximation Potential (GAP) represents an additional difficulty due to high computational cost associated with this force field. In this appendix, we will present our attempt to reduce intrinsic noise in MD calculations and show the convergence study with respect to correlation time and the size of the supercell.

The main result from our molecular dynamics simulations of GeTe is the lattice thermal conductivity κ at the phase transition. We calculate κ by using the Green-Kubo theory:

$$\kappa^{\alpha\beta} = \frac{1}{NVk_BT^2}\sum_{\tau}^{t_{corr}}\langle J^{\alpha}(0)J^{\beta}(\tau)\rangle. \tag{C.1}$$

Here we rewrote the original Green-Kubo relation in the form that we actually use in our calculation. NV is the volume of the simulation system, k_B is the Boltzmann constant, T is the temperature, $J^{\alpha}(t)$ is the heat current in the Cartesian direction α at time t. The $\langle\ldots\rangle$ represent a correlation function, while τ is the correlation time, and t_{corr} is the maximum correlation time, i.e. the upper limit of our sum. t_{corr} in the original definition is infinity, and since we can not run that long MD simulation, we choose t_{corr} as the time when the heat autocorrelation function becomes zero (or vanishingly small).

The heat autocorrelation function is calculated as follows:

$$\langle J^{\alpha}(0)J^{\beta}(\tau)\rangle = \frac{1}{N_{\tau}}\sum_{t_i}^{N_{\tau}} J^{\alpha}(t_i)J^{\beta}(t_i+\tau), \tag{C.2}$$

where $N_{\tau} = t_{tot} - \tau$. Now it becomes clear what are the quantities we have to converge our MD simulations against: the total simulation time t_{tot}, the maximum correlation time t_{corr} and the size of the simulation cell NV.

The most difficult part of this convergence study is to obtain reliable values of the heat autocorrelation function $\langle J^{\alpha}(0)J^{\beta}(\tau)\rangle$. To show why this is the case, we plot the probability distribution function (PDF) of the terms $J^{\alpha}(t_i)J^{\beta}(t_i+\tau)$ in the sum in Eq. (C.2). One might expect that this quantity would be the sum of two Gaussian distributions: the one we are trying to calculate and the zero mean one of the noise. We show this PDF for $\tau = 20$ ps at 300 K in Fig. C.1. We can see that this distribution function has heavier tails than the Gaussian distribution. We tried fitting this PDF with three types of functions: the sum of two Gaussians, the Cauchy distribution and the sum of the Cauchy distribution and a Gaussian. One of the Gaussians is always assumed to represent noise (its mean is fixed at zero). The best fit by far is achieved with the third function, the sum of the Cauchy distribution and the Gaussian. Now the obvious problem is that the Cauchy distribution does not have a mean, meaning even if we had large number of samples in the sum in Eq. (C.2), that sum would not converge. However, this particular PDF is only fitted best to the Cauchy distribution from the limited set of distributions we have tried, but it does not mean its values are distributed according to the Cauchy distribution. In either case, due to very long tails of this PDF, the sample mean is not a very efficient maximum likelihood estimator (MLE). If this PDF was indeed the Cauchy distribution, a more accurate MLE would be the sample median.

What complicates things further and does not allow us to use the sample median for estimating Eq. (C.2) is the fact that for the small values of τ, the PDF is not symmetrical, see Fig. C.1 (b). In this case the mode, the mean and the median of the PDF do not coincide and the median can not be used as an estimator of Eq. (C.2). We checked if this is true for other interatomic potentials as well. We found that the same problem appears regardless of the type of interatomic potential and this appears to be a general feature of the method.

To try to avoid possible issues with convergence of the heat autocorrelation with the total time of the simulation, we decided to do signal filtering in the frequency space. We employ the Wiener-Khinchin theorem[234, 235] to calculate the heat autocorrelation

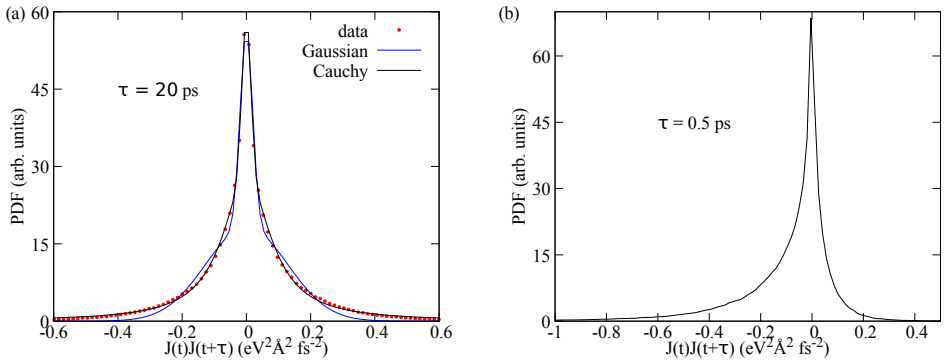

Figure C.1: Probability distribution function (PDF) of the elements in the sum in Eq. (C.2). (a) Calculated PDF and the Gaussian and Cauchy fits to the data with the Gaussian noise. (b) PDF of the same quantity at lower correlation times is a skewed distribution.

function. First, we calculate the fast Fourier transform (FFT) of the heat current. The Wiener-Khinchin theorem states that the power spectrum[1] of this quantity is equivalent to the FFT of the heat autocorrelation function. We then calculate the inverse FFT of the power spectrum of the heat current to obtain the heat autocorrelation function. Prior to that we apply a Gaussian filter to the power spectrum of the heat current:

$$W'(\Omega) = \frac{1}{N}\sum_{\omega} W(\omega)\exp(-\frac{(\Omega-\omega)^2}{\sigma}), \tag{C.3}$$

where $W'(\Omega)$ is the filtered power spectra, $W(\omega)$ is the original power spectra, σ is some smearing constant which we choose empirically (smallest possible that reduces the noise) and N is the normalization constant.

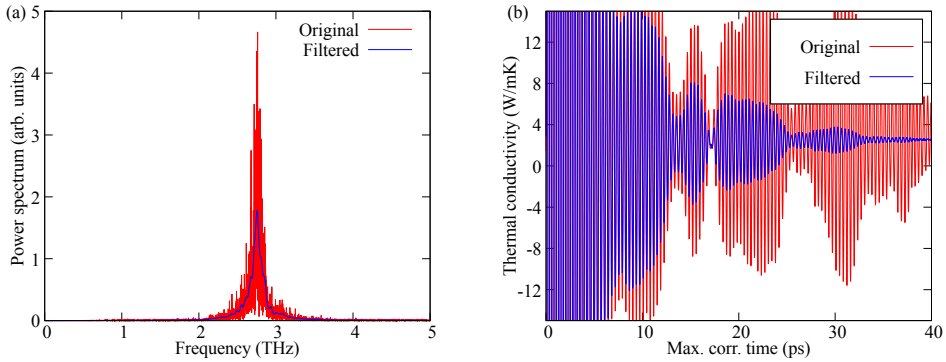

Figure C.2: (a) Original and filtered power spectrum of the heat current of GeTe at 300 K. (b) Lattice thermal conductivity of GeTe at 300 K as a function of the maximum correlation time, see Eq. (C.2).

The results of this approach are given in Fig. C.2. Figure C.2 (a) shows us the comparison of the original and filtered heat current power spectra of GeTe at 300 K. We

[1] Power spectrum is simply the square of the absolute value of the FFT.

can see that the noise in the signal is drastically reduced in the filtered signal. More importantly, Fig. C.2 (b) shows the calculated κ as a function of the maximum correlation time for the filtered and unfiltered signal. We can see that for the unfiltered signal κ varies drastically with the maximum correlation time and the convergence of this quantity can not be observed. On the other hand, the filtered κ shows much better behavior finally setting to a constant enough value for sufficiently large correlation times.

Convergence due to the maximum correlation time is obvious for Fig. C.2 (b) showing that the value of the κ for the filtered data does not change significantly after 40 ps. This is in accordance with our study of phonon lifetimes in this system showing the maximum phonon lifetimes to be of that order of magnitude.

Finally, let us comment on the convergence with the size of the supercell. We calculated lattice thermal conductivity of GeTe at 300 K using the cells of four different sizes: 288, 360, 672 and 720 atoms. The choices for the cell size make sense considering we used the orthorombic unit cell of GeTe for this study. The orthorombic unit cell is the most efficient in LAMMPS (due to the fact that all three directions are perpendicular to each other). On the other hand, the orthorombic unit cell has a large number of atoms (12 atoms). On top of that, the lengths of the unit cell are fairly different from each other. To check the convergence of κ with respect to the supercell size, we used following shapes of the orthorombic supercell: 288 - $3\times4\times2\times12$, 360 - $3\times5\times2\times12$, 672 - $4\times7\times2\times12$ and 720 - $4\times5\times3\times12$.

Table C.1: Dependence of the calculated lattice thermal conductivity on the size of the MD simulation cell. The errors are determined as the standard errors from the set of calculated values.

	288 atoms	360 atoms	672 atoms	720 atoms
$\kappa_\perp$	2.33 ± 0.34	2.26 ± 0.11	2.17 ± 0.13	2.36 ± 0.16
$\kappa_\parallel$	1.58 ± 0.16	1.54 ± 0.11	1.45 ± 0.13	1.35 ± 0.07

Table C.1 shows no appreciable difference between the results for κ calculated using these four cells. For the 288 atoms cell we ran five different calculations. For other cells we had 8 calculated values, but along 2 different MD trajectories. The total simulation time among all calculations was similar ($\approx$ 1.2 ns).

In the end, to obtain the results in Fig. 7.12, we ran 5 independent equilibrium molecular dynamics simulations on 288 atoms supercells in the NVE ensemble with 1 fs timestep for each temperature. We thermostat the temperature using Berendsen thermostat [236]. The choice of thermostat is somewhat arbitrary, we checked results for

κ of Si and Bi_2Te_3 with different thermostats and the results do not differ significantly depending on the choice of the thermostat. After 1 ns of equilibration, we sampled heat current every timestep for 1.2 ns long simulation (2.2 ns in total). The evaluation of the data is explained above.

Appendix D

Comparison of the results with two different heat current definitions

There is a difference between our results obtained in section 2.6 and the one described in the literature [112]. Besides obvious differences because of the different definition of the heat current, our results for the velocity-velocity autocorrelation current also differ. In this appendix we will comment on these differences and justify our approach.

The authors of Ref. [112] used Peierls definition of the heat current for the diagonal part of the lattice thermal conductivity. This leads to a different result for κ:

$$\kappa^{i,j} = \frac{\hbar^2 k_B \beta^2}{\pi N V} \sum_{\vec{q},s} \omega^2_{\vec{q},s} v^i_{\vec{q},s} v^j_{\vec{q},s} \int_{-\infty}^{\infty} \mathrm{d}\Omega \frac{e^{\beta\hbar\Omega}}{(e^{\beta\hbar\Omega}-1)^2} \frac{\Gamma^2_{\vec{q},s}(\Omega)}{\left[\left(\Omega - \omega_{\vec{q},s} - \Delta_{\vec{q},s}(\Omega)\right)^2 + \Gamma^2_{\vec{q},s}(\Omega)\right]^2}. \tag{D.1}$$

Here we used the same notation as in section 2.6. Relative difference between this result and the one presented in Chapter 5 is given in Fig. D.1. In the rhombohedral phase Eq. (D.1) overestimates the result obtained using Eq. (2.39). In the cubic phase the agreement between two equations is much better.

Although the difference is not large (max. 8 %), the result using equation Eq. (D.1) is troubling due to the following reason. In the case of soft modes the phonon spectral function peaks at almost zero frequency. That means that the spectral function part of the integrand in Eqs. (D.1) and (2.39) will be non-zero even for small values of Ω. On

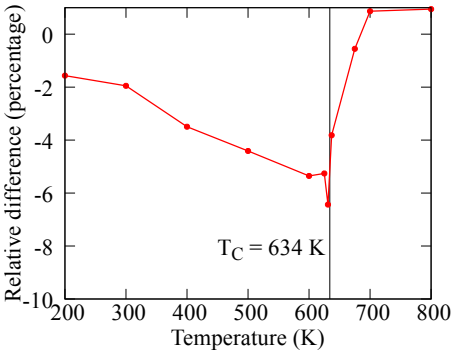

Figure D.1: Relative difference in the lattice thermal conductivity calculated using Eqs. (D.1) and (2.39)

the other hand the heat capacity term of the integrand diverges as Ω goes to zero:

$$\frac{e^{\frac{\hbar\Omega}{k_BT}}}{(e^{\frac{\hbar\Omega}{k_BT}}-1)^2} \approx \frac{1+\frac{\hbar\Omega}{k_BT}}{(\frac{\hbar\Omega}{k_BT})^2} = \frac{(k_BT)^2+\hbar\Omega k_BT}{(\hbar\Omega)^2}.$$

In the case of the equation we used (see Eq. (2.39)), there is Ω^2 term in the integrand to counteract this divergent term. In case of Eq. (D.1) there is no such cancellation and this might lead to unphysical results.

Another difference between the results presented in section 2.6 and Ref. [112] is in the definition of velocity-velocity autocorrelation function. The solution of the velocity-velocity Green's function presented in Ref. [112] would lead to the same expressions for the velocity-velocity and displacement-displacement autocorrelation functions. In the end this would lead to the same problem in the definition of the lattice thermal conductivity as stated in the first part of appendix (divergent contribution of the soft phonon modes). Here we will further justify our use of Eq. (2.38).

To find the definition for the velocity-velocity autocorrelation function we start from the Green's function:

$$G_{AB}(t) = -i\theta(t)\langle[A_{\vec{q}s}(t), B_{\vec{q}',s'}(0)]\rangle. \tag{D.2}$$

We find the equation of motion for this Green's function:

$$i\frac{\mathrm{d}}{\mathrm{d}t}G_{AB}(t) = i\frac{2}{\pi}\delta_{\vec{q},-\vec{q}'}\delta_{s,s'} + \omega_{\vec{q}s}G_{BB}(t). \tag{D.3}$$

The rest of the derivation follows almost identically as in section 2.6 and we reach the

result (which agrees with Ref. [112]):

$$G_{AB}(\Omega) = \frac{\Omega\delta_{\vec{q},-\vec{q}'}\delta_{s,s'}}{\pi}\frac{1}{\Omega^2 - \omega_{\vec{q}s}^2 - 2\omega_{\vec{q}s}\Sigma_{\vec{q}s}}.$$

From Eq. (D.3) we can get $G_{BB}(\Omega)$:

$$G_{BB}(\Omega) = -\frac{\delta_{\vec{q},-\vec{q}'}\delta_{s,s'}}{\pi}\frac{4\Sigma_{\vec{q}s} + 2\omega_{\vec{q}s}}{\Omega^2 - \omega_{\vec{q}s}^2 - 2\omega_{\vec{q}s}\Sigma_{\vec{q}s}}. \tag{D.4}$$

From this we obtain for the velocity-velocity autocorrelation function:

$$\begin{aligned} J_{BB}(\Omega) &= -\frac{2}{e^{\frac{\hbar\Omega}{k_BT}} - 1}\mathrm{Im}G_{BB}(\Omega \pm i\epsilon) \\ &= \frac{4\Omega^2}{\left(\exp(\frac{\hbar\Omega}{k_BT}) - 1\right)\pi}\frac{\Gamma_{\vec{q}s}(\Omega)}{(\Omega^2 - 2\omega_{\vec{q}s}\Delta_{\vec{q}s}(\Omega) - \omega_{\vec{q}s}^2)^2 + 4\omega_{\vec{q}s}^2\Gamma_{\vec{q}s}^2(\Omega)}, \end{aligned}$$

which agrees with Eq. (2.38).

References

[1] C. B. Vining, "An inconvenient truth about thermoelectrics," *Nature Materials*, vol. 8, pp. 83–85, Feb 2009.

[2] K. Momma and F. Izumi, "*VESTA3* for three-dimensional visualization of crystal, volumetric and morphology data," *J. Appl. Cryst.*, vol. 44, pp. 1272–1276, Dec 2011.

[3] E. Steigmeier and G. Harbeke, "Soft phonon mode and ferroelectricity in gete," *Solid State Commun.*, vol. 8, no. 16, pp. 1275 – 1279, 1970.

[4] P. Fons, A. V. Kolobov, M. Krbal, J. Tominaga, K. S. Andrikopoulos, S. N. Yannopoulos, G. A. Voyiatzis, and T. Uruga, "Phase transition in crystalline gete: Pitfalls of averaging effects," *Phys. Rev. B*, vol. 82, p. 155209, Oct 2010.

[5] U. D. Wdowik, K. Parlinski, S. Rols, and T. Chatterji, "Soft-phonon mediated structural phase transition in gete," *Phys. Rev. B*, vol. 89, p. 224306, Jun 2014.

[6] P. Bauer Pereira, I. Sergueev, S. Gorsse, J. Dadda, E. Müller, and R. P. Hermann, "Lattice dynamics and structure of gete, snte and pbte," *Phys. Status Solidi B*, vol. 250, no. 7, pp. 1300–1307, 2013.

[7] T. Chattopadhyay, J. X. Boucherle, and H. G. vonSchnering, "Neutron diffraction study on the structural phase transition in gete," *J. Phys. C: Solid State Phys.*, vol. 20, no. 10, p. 1431, 1987.

[8] T. Chatterji, C. M. N. Kumar, and U. D. Wdowik, "Anomalous temperature-induced volume contraction in gete," *Phys. Rev. B*, vol. 91, p. 054110, Feb 2015.

[9] F. Kadlec, C. Kadlec, P. Kužel, and J. Petzelt, "Study of the ferroelectric phase transition in germanium telluride using time-domain terahertz spectroscopy," *Phys. Rev. B*, vol. 84, p. 205209, Nov 2011.

[10] J. Li, Z. Chen, X. Zhang, H. Yu, Z. Wu, H. Xie, Y. Chen, and Y. Pei, "Simultaneous optimization of carrier concentration and alloy scattering for ultrahigh performance gete thermoelectrics," *Adv. Sci.*, vol. 4, no. 12, p. 1700341, 2017.

[11] S. Perumal, S. Roychowdhury, D. S. Negi, R. Datta, and K. Biswas, "High thermoelectric performance and enhanced mechanical stability of p-type ge1–xsbxte," *Chem. Mat.*, vol. 27, no. 20, pp. 7171–7178, 2015.

[12] J. Li, Z. Chen, X. Zhang, Y. Sun, J. Yang, and Y. Pei, "Electronic origin of the high thermoelectric performance of gete among the p-type group iv monotellurides," *NPG Asia Mater.*, vol. 9, p. e353, Mar 2017.

[13] T. Xing, Q. Song, P. Qiu, Q. Zhang, X. Xia, J. Liao, R. Liu, H. Huang, J. Yang, S. Bai, D. Ren, X. Shi, and L. Chen, "Superior performance and high service stability for GeTe-based thermoelectric compounds," *Natl. Sci. Rev.*, vol. 6, pp. 944–954, 04 2019.

[14] Y. Jin, Y. Xiao, D. Wang, Z. Huang, Y. Qiu, and L.-D. Zhao, "Realizing high thermoelectric performance in gete through optimizing ge vacancies and manipulating ge precipitates," *ACS Appl. Energy Mater.*, vol. 2, pp. 7594–7601, Oct 2019.

[15] E. Nshimyimana, S. Hao, X. Su, C. Zhang, W. Liu, Y. Yan, C. Uher, C. Wolverton, M. G. Kanatzidis, and X. Tang, "Discordant nature of cd in gete enhances phonon scattering and improves band convergence for high thermoelectric performance," *J. Mater. Chem. A*, vol. 8, pp. 1193–1204, 2020.

[16] Z. Liu, J. Sun, J. Mao, H. Zhu, W. Ren, J. Zhou, Z. Wang, D. J. Singh, J. Sui, C.-W. Chu, and Z. Ren, "Phase-transition temperature suppression to achieve cubic gete and high thermoelectric performance by bi and mn codoping," *PNAS*, vol. 115, no. 21, pp. 5332–5337, 2018.

[17] J. Li, Y. Xie, C. Zhang, K. Ma, F. Liu, W. Ao, Y. Li, and C. Zhang, "Stacking fault-induced minimized lattice thermal conductivity in the high-performance gete-based thermoelectric materials upon bi2te3 alloying," *ACS Appl. Mater. & Interfaces*, vol. 11, pp. 20064–20072, Jun 2019.

[18] E. M. Levin, M. F. Besser, and R. Hanus, "Electronic and thermal transport in gete: A versatile base for thermoelectric materials," *J. Appl. Phys.*, vol. 114, p. 083713, 2013.

[19] J. Gainza, F. Serrano-Sánchez, N. M. Nemes, J. L. Martínez, M. T. Fernández-Díaz, and J. A. Alonso, "Features of the high-temperature structural evolution

of gete thermoelectric probed by neutron and synchrotron powder diffraction," *Metals*, vol. 10, no. 1, 2020.

[20] M. Sist, H. Kasai, E. M. J. Hedegaard, and B. B. Iversen, "Role of vacancies in the high-temperature pseudodisplacive phase transition in gete," *Phys. Rev. B*, vol. 97, p. 094116, Mar 2018.

[21] J. Cook, D. Nuccitelli, S. A. Green, M. Richardson, B. Winkler, R. Painting, R. Way, P. Jacobs, and A. Skuce, "Quantifying the consensus on anthropogenic global warming in the scientific literature," *Environmental Research Letters*, vol. 8, p. 024024, may 2013.

[22] N. Oreskes, "The scientific consensus on climate change," *Science*, vol. 306, no. 5702, pp. 1686–1686, 2004.

[23] D. Beretta, N. Neophytou, J. M. Hodges, M. G. Kanatzidis, D. Narducci, M. Martin- Gonzalez, M. Beekman, B. Balke, G. Cerretti, W. Tremel, A. Zevalkink, A. I. Hofmann, C. Müller, B. Dörling, M. Campoy-Quiles, and M. Caironi, "Thermoelectrics: From history, a window to the future," *Materials Science and Engineering: R: Reports*, vol. 138, p. 100501, 2019.

[24] M. Hong, J. Zou, and Z.-G. Chen, "Thermoelectric gete with diverse degrees of freedom having secured superhigh performance," *Advanced Materials*, vol. 31, no. 14, p. 1807071, 2019.

[25] I. Petsagkourakis, K. Tybrandt, X. Crispin, I. Ohkubo, N. Satoh, and T. Mori, "Thermoelectric materials and applications for energy harvesting power generation," *Science and Technology of Advanced Materials*, vol. 19, no. 1, pp. 836–862, 2018. PMID: 31001364.

[26] A. Zevalkink, D. M. Smiadak, J. L. Blackburn, A. J. Ferguson, M. L. Chabinyc, O. Delaire, J. Wang, K. Kovnir, J. Martin, L. T. Schelhas, T. D. Sparks, S. D. Kang, M. T. Dylla, G. J. Snyder, B. R. Ortiz, and E. S. Toberer, "A practical field guide to thermoelectrics: Fundamentals, synthesis, and characterization," *Applied Physics Reviews*, vol. 5, no. 2, p. 021303, 2018.

[27] "Lead telluride alloy thermoelectrics," *Materials Today*, vol. 14, no. 11, pp. 526 – 532, 2011.

[28] C. Wood, "Materials for thermoelectric energy conversion," *Reports on Progress in Physics*, vol. 51, pp. 459–539, apr 1988.

[29] D. Champier, "Thermoelectric generators: A review of applications," *Energy Conversion and Management*, vol. 140, pp. 167 – 181, 2017.

[30] G. J. Snyder, E. S. Toberer, R. Khanna, and W. Seifert, "Improved thermoelectric cooling based on the thomson effect," *Phys. Rev. B*, vol. 86, p. 045202, Jul 2012.

[31] Y. Cai, Y. Wang, D. Liu, and F.-Y. Zhao, "Thermoelectric cooling technology applied in the field of electronic devices: Updated review on the parametric investigations and model developments," *Applied Thermal Engineering*, vol. 148, pp. 238 – 255, 2019.

[32] G. J. Snyder and E. S. Toberer, "Complex thermoelectric materials," *Nat. Mater.*, vol. 7, p. 105, Feb 2008.

[33] L.-D. Zhao, G. Tan, S. Hao, J. He, Y. Pei, H. Chi, H. Wang, S. Gong, H. Xu, V. P. Dravid, C. Uher, G. J. Snyder, C. Wolverton, and M. G. Kanatzidis, "Ultrahigh power factor and thermoelectric performance in hole-doped single-crystal snse," *Science*, vol. 351, no. 6269, pp. 141–144, 2016.

[34] G. J. Snyder and T. S. Ursell, "Thermoelectric efficiency and compatibility," *Phys. Rev. Lett.*, vol. 91, p. 148301, Oct 2003.

[35] D. A. der Wissenschaften zu Berlin., *Abhandlungen der Königlichen Akademie der Wissenschaften zu Berlin.*, vol. 1822-1823. Berlin :Realschul-Buchhandlung,, 1822. https://www.biodiversitylibrary.org/bibliography/41825 — Jahre 1869 (publ. 1870) issued in 2 vols.

[36] *Annales de chimie et de physique*. No. v. 56 in Annales de chimie et de physique, 1834.

[37] W. Thompson, "On a mechanical theory of thermo-electric currents," *Proceedings of the Royal Society of Edinburgh.*, vol. 3, pp. 91–98, 1851.

[38] A. Ioffe, *Semiconductor thermoelements, and Thermoelectric cooling*. Infosearch, ltd., 1957.

[39] C. Kittel, *Introduction to Solid State Physics*. Wiley, 2004.

[40] A. W, N. Ashcroft, N. Mermin, N. Mermin, and B. P. Company, *Solid State Physics*. HRW international editions, Holt, Rinehart and Winston, 1976.

[41] S. Simon, *The Oxford Solid State Basics*. OUP Oxford, 2013.

[42] M. A. Avila, K. Suekuni, K. Umeo, H. Fukuoka, S. Yamanaka, and T. Takabatake, "Ba8ga16sn30 with type-i clathrate structure: Drastic suppression of heat conduction," *Appl. Phys. Lett.*, vol. 92, no. 4, p. 041901, 2008.

[43] Y. Tang, Z. M. Gibbs, L. A. Agapito, G. Li, H.-S. Kim, M. Nardelli, S. Curtarolo, and G. J. Snyder, "Convergence of multi-valley bands as the electronic origin of high thermoelectric performance in cosb3 skutterudites," *Nature Mater.*, vol. 14, no. 12, pp. 1223–1228, 2015.

[44] M. K. Jana, K. Pal, U. V. Waghmare, and K. Biswas, "The origin of ultralow thermal conductivity in inte: Lone-pair-induced anharmonic rattling," *Angew. Chem. Int. Ed.*, vol. 55, no. 27, pp. 7792–7796, 2016.

[45] J. S. Tse, D. D. Klug, J. Y. Zhao, W. Sturhahn, E. E. Alp, J. Baumert, C. Gutt, M. R. Johnson, and W. Press, "Anharmonic motions of kr in the clathrate hydrate," *Nature Mater.*, vol. 4, p. 917, 2005.

[46] M. Christensen, A. B. Abrahamsen, N. B. Christensen, F. Juranyi, N. H. Andersen, K. Lefmann, J. Andreasson, C. R. H. Bahl, and B. B. Iversen, "Avoided crossing of rattler modes in thermoelectric materials," *Nature Mater.*, vol. 7, p. 811, 2008.

[47] C. Uher, "Chapter 5 skutterudites: Prospective novel thermoelectrics," in *Recent Trends in Thermoelectric Materials Research I* (T. M. Tritt, ed.), vol. 69 of *Semiconductors and Semimetals*, pp. 139 – 253, Elsevier, 2001.

[48] R. Robert, L. Bocher, B. Sipos, M. Döbeli, and A. Weidenkaff, "Ni-doped cobaltates as potential materials for high temperature solar thermoelectric converters," *Progress in Solid State Chemistry*, vol. 35, no. 2, pp. 447 – 455, 2007. International Conference on Perovskites at EMPA, 2005.

[49] S. Lee, K. Esfarjani, T. Luo, J. Zhou, Z. Tian, and G. Chen, "Resonant bonding leads to low lattice thermal conductivity," *Nature Communications*, vol. 5, p. 3525, Apr 2014.

[50] R. M. Murphy, É. D. Murray, S. Fahy, and I. Savić, "Broadband phonon scattering in pbte-based materials driven near ferroelectric phase transition by strain or alloying," *Phys. Rev. B*, vol. 93, p. 104304, Mar 2016.

[51] P. A. Fleury, J. F. Scott, and J. M. Worlock, "Soft phonon modes and the 110°k phase transition in $srtio_3$," *Phys. Rev. Lett.*, vol. 21, pp. 16–19, Jul 1968.

[52] C. W. Li, O. Hellman, J. Ma, A. F. May, H. B. Cao, X. Chen, A. D. Christianson, G. Ehlers, D. J. Singh, B. C. Sales, and O. Delaire, "Phonon self-energy and origin of anomalous neutron scattering spectra in snte and pbte thermoelectrics," *Phys. Rev. Lett.*, vol. 112, p. 175501, Apr 2014.

[53] T. P. Dougherty, G. P. Wiederrecht, K. A. Nelson, M. H. Garrett, H. P. Jensen, and C. Warde, "Femtosecond resolution of soft mode dynamics in structural phase transitions," *Science*, vol. 258, no. 5083, pp. 770–774, 1992.

[54] L. Landau and E. Lifshitz, *Statistical Physics*. No. v. 5, Elsevier Science, 2013.

[55] R. M. Murphy, É. D. Murray, S. Fahy, and I. Savić, "Ferroelectric phase transition and the lattice thermal conductivity of $pb_{1-x}ge_xTe$ alloys," *Phys. Rev. B*, vol. 95, p. 144302, Apr 2017.

[56] C. J. Vineis, A. Shakouri, A. Majumdar, and M. G. Kanatzidis, "Nanostructured thermoelectrics: Big efficiency gains from small features," *Adv. Mater.*, vol. 22, no. 36, pp. 3970–3980, 2010.

[57] M. G. Kanatzidis, "Nanostructured thermoelectrics: The new paradigm?," *Chemistry of Materials*, vol. 22, no. 3, pp. 648–659, 2010.

[58] J. Callaway, "Model for lattice thermal conductivity at low temperatures," *Phys. Rev.*, vol. 113, pp. 1046–1051, Feb 1959.

[59] K. Biswas, J. He, I. D. Blum, C.-I. Wu, T. P. Hogan, D. N. Seidman, V. P. Dravid, and M. G. Kanatzidis, "High-performance bulk thermoelectrics with all-scale hierarchical architectures," *Nature*, vol. 489, no. 7416, pp. 414–418, 2012.

[60] Y. Xia, J. Park, F. Zhou, and V. Ozoliņš, "High thermoelectric power factor in intermetallic CoSi arising from energy filtering of electrons by phonon scattering," *Phys. Rev. Appl.*, vol. 11, p. 024017, Feb 2019.

[61] L. D. Hicks and M. S. Dresselhaus, "Thermoelectric figure of merit of a one-dimensional conductor," *Phys. Rev. B*, vol. 47, pp. 16631–16634, Jun 1993.

[62] L. D. Hicks and M. S. Dresselhaus, "Effect of quantum-well structures on the thermoelectric figure of merit," *Phys. Rev. B*, vol. 47, pp. 12727–12731, May 1993.

[63] Y. Zhang, B. Feng, H. Hayashi, C.-P. Chang, Y.-M. Sheu, I. Tanaka, Y. Ikuhara, and H. Ohta, "Double thermoelectric power factor of a 2d electron system," *Nature Communications*, vol. 9, p. 2224, Jun 2018.

[64] H. Ohta, S. Kim, Y. Mune, T. Mizoguchi, K. Nomura, S. Ohta, T. Nomura, Y. Nakanishi, Y. Ikuhara, M. Hirano, H. Hosono, and K. Koumoto, "Giant thermoelectric seebeck coefficient of a two-dimensional electron gas in srtio3," *Nature Materials*, vol. 6, pp. 129–134, Feb 2007.

[65] Y. Mune, H. Ohta, K. Koumoto, T. Mizoguchi, and Y. Ikuhara, "Enhanced seebeck coefficient of quantum-confined electrons in srtio3/srti0.8nb0.2o3 superlattices," *Applied Physics Letters*, vol. 91, no. 19, p. 192105, 2007.

[66] H. Ohta, S. W. Kim, S. Kaneki, A. Yamamoto, and T. Hashizume, "High thermoelectric power factor of high-mobility 2d electron gas," *Advanced Science*, vol. 5, no. 1, p. 1700696, 2018.

[67] S. Shimizu, M. S. Bahramy, T. Iizuka, S. Ono, K. Miwa, Y. Tokura, and Y. Iwasa, "Enhanced thermopower in zno two-dimensional electron gas," *Proceedings of the National Academy of Sciences*, vol. 113, no. 23, pp. 6438–6443, 2016.

[68] J. P. Heremans, V. Jovovic, E. S. Toberer, A. Saramat, K. Kurosaki, A. Charoenphakdee, S. Yamanaka, and G. J. Snyder, "Enhancement of thermoelectric efficiency in pbte by distortion of the electronic density of states," *Science*, vol. 321, no. 5888, pp. 554–557, 2008.

[69] L. Wu, X. Li, S. Wang, T. Zhang, J. Yang, W. Zhang, L. Chen, and J. Yang, "Resonant level-induced high thermoelectric response in indium-doped gete," *NPG Asia Mater.*, vol. 9, p. e343, Jan 2017.

[70] Y. Pei, X. Shi, A. LaLonde, H. Wang, L. Chen, and G. J. Snyder, "Convergence of electronic bands for high performance bulk thermoelectrics," *Nature*, vol. 473, pp. 66–69, May 2011.

[71] T. Fu, X. Yue, H. Wu, C. Fu, T. Zhu, X. Liu, L. Hu, P. Ying, J. He, and X. Zhao, "Enhanced thermoelectric performance of pbte bulk materials with figure of merit zt >2 by multi-functional alloying," *Journal of Materiomics*, vol. 2, no. 2, pp. 141 – 149, 2016. Special Issue on Advances in Thermoelectric Research.

[72] A. Banik, U. S. Shenoy, S. Anand, U. V. Waghmare, and K. Biswas, "Mg alloying in snte facilitates valence band convergence and optimizes thermoelectric properties," *Chemistry of Materials*, vol. 27, pp. 581–587, Jan 2015.

[73] D. Vashaee and A. Shakouri, "Improved thermoelectric power factor in metal-based superlattices," *Phys. Rev. Lett.*, vol. 92, p. 106103, Mar 2004.

[74] M. Zebarjadi, K. Esfarjani, A. Shakouri, J.-H. Bahk, Z. Bian, G. Zeng, J. Bowers, H. Lu, J. Zide, and A. Gossard, "Effect of nanoparticle scattering on thermoelectric power factor," *Applied Physics Letters*, vol. 94, no. 20, p. 202105, 2009.

[75] J. Zhang, D. Wu, D. He, D. Feng, M. Yin, X. Qin, and J. He, "Extraordinary thermoelectric performance realized in n-type pbte through multiphase nanostructure engineering," *Advanced Materials*, vol. 29, no. 39, p. 1703148, 2017.

[76] J. Martin, L. Wang, L. Chen, and G. S. Nolas, "Enhanced seebeck coefficient through energy-barrier scattering in pbte nanocomposites," *Phys. Rev. B*, vol. 79, p. 115311, Mar 2009.

[77] E. K. Salje, "Ferroelastic materials," *Annual Review of Materials Research*, vol. 42, no. 1, pp. 265–283, 2012.

[78] H. Stanley, *Introduction to Phase Transitions and Critical Phenomena*. International series of monographs on physics, Oxford University Press, 1987.

[79] Đ. Dangić, A. R. Murphy, É. D. Murray, S. Fahy, and I. Savić, "Coupling between acoustic and soft transverse optical phonons leads to negative thermal expansion of gete near the ferroelectric phase transition," *Phys. Rev. B*, vol. 97, p. 224106, Jun 2018.

[80] H. S. Lee, B.-S. Kim, C.-W. Cho, M.-W. Oh, B.-K. Min, S.-D. Park, and H.-W. Lee, "Herringbone structure in gete-based thermoelectric materials," *Acta Materialia*, vol. 91, pp. 83 – 90, 2015.

[81] Đ. Dangić, S. Fahy, and I. Savić, "Giant thermoelectric power factor in charged ferroelectric domain walls of gete with van hove singularities," *npj Computational Materials*, vol. 6, p. 195, Dec 2020.

[82] D. Dangić, E. D. Murray, S. Fahy, and I. Savić, "Structural and thermal transport properties of ferroelectric domain walls in gete from first principles," *Phys. Rev. B*, vol. 101, p. 184110, May 2020.

[83] R. Martin, R. Martin, and C. U. Press, *Electronic Structure: Basic Theory and Practical Methods*. Cambridge University Press, 2004.

[84] P. Hohenberg and W. Kohn, "Inhomogeneous electron gas," *Phys. Rev.*, vol. 136, pp. B864–B871, Nov 1964.

[85] W. Kohn and L. J. Sham, "Self-consistent equations including exchange and correlation effects," *Phys. Rev.*, vol. 140, pp. A1133–A1138, Nov 1965.

[86] J. P. Perdew, K. Burke, and M. Ernzerhof, "Generalized gradient approximation made simple," *Phys. Rev. Lett.*, vol. 77, pp. 3865–3868, Oct 1996.

[87] X. Gonze, B. Amadon, P.-M. Anglade, J.-M. Beuken, F. Bottin, P. Boulanger, F. Bruneval, D. Caliste, R. Caracas, M. Côté, T. Deutsch, L. Genovese, P. Ghosez, M. Giantomassi, S. Goedecker, D. Hamann, P. Hermet, F. Jollet, G. Jomard, S. Leroux, M. Mancini, S. Mazevet, M. Oliveira, G. Onida, Y. Pouillon, T. Rangel, G.-M. Rignanese, D. Sangalli, R. Shaltaf, M. Torrent, M. Verstraete, G. Zerah, and J. Zwanziger, "Abinit: First-principles approach to material and nanosystem properties," *Comput. Phys. Commun.*, vol. 180, no. 12, pp. 2582 – 2615, 2009.

[88] X. Gonze, F. Jollet, F. A. Araujo, D. Adams, B. Amadon, T. Applencourt, C. Audouze, J.-M. Beuken, J. Bieder, A. Bokhanchuk, E. Bousquet, F. Bruneval, D. Caliste, M. Côté, F. Dahm, F. D. Pieve, M. Delaveau, M. D. Gennaro, B. Dorado, C. Espejo, G. Geneste, L. Genovese, A. Gerossier, M. Giantomassi, Y. Gillet, D. Hamann, L. He, G. Jomard, J. L. Janssen, S. L. Roux, A. Levitt, A. Lherbier, F. Liu, I. Lukačević, A. Martin, C. Martins, M. Oliveira, S. Poncé, Y. Pouillon, T. Rangel, G.-M. Rignanese, A. Romero, B. Rousseau, O. Rubel, A. Shukri, M. Stankovski, M. Torrent, M. V. Setten, B. V. Troeye, M. Verstraete, D. Waroquiers, J. Wiktor, B. Xu, A. Zhou, and J. Zwanziger, "Recent developments in the abinit software package," *Computer Physics Communications*, vol. 205, pp. 106 – 131, 2016.

[89] "www.abinit.org." `www.abinit.org`.

[90] D. R. Hamann, M. Schlüter, and C. Chiang, "Norm-conserving pseudopotentials," *Phys. Rev. Lett.*, vol. 43, pp. 1494–1497, Nov 1979.

[91] L. Verlet, "Computer "experiments" on classical fluids. i. thermodynamical properties of lennard-jones molecules," *Phys. Rev.*, vol. 159, pp. 98–103, Jul 1967.

[92] W. Shinoda, M. Shiga, and M. Mikami, "Rapid estimation of elastic constants by molecular dynamics simulation under constant stress," *Phys. Rev. B*, vol. 69, p. 134103, Apr 2004.

[93] S. Plimpton, "Fast parallel algorithms for short-range molecular dynamics," *Journal of Computational Physics*, vol. 117, no. 1, pp. 1 – 19, 1995.

[94] A. P. Bartók and G. Csányi, "Gaussian approximation potentials: A brief tutorial introduction," *International Journal of Quantum Chemistry*, vol. 115, no. 16,

pp. 1051–1057, 2015.

[95] J. Tersoff, "New empirical approach for the structure and energy of covalent systems," *Phys. Rev. B*, vol. 37, pp. 6991–7000, Apr 1988.

[96] F. H. Stillinger and T. A. Weber, "Computer simulation of local order in condensed phases of silicon," *Phys. Rev. B*, vol. 31, pp. 5262–5271, Apr 1985.

[97] J. Behler and M. Parrinello, "Generalized neural-network representation of high-dimensional potential-energy surfaces," *Phys. Rev. Lett.*, vol. 98, p. 146401, Apr 2007.

[98] J. Behler, "Constructing high-dimensional neural network potentials: A tutorial review," *International Journal of Quantum Chemistry*, vol. 115, no. 16, pp. 1032–1050, 2015.

[99] A. P. Bartók, M. C. Payne, R. Kondor, and G. Csányi, "Gaussian approximation potentials: The accuracy of quantum mechanics, without the electrons," *Phys. Rev. Lett.*, vol. 104, p. 136403, Apr 2010.

[100] A. P. Bartók, R. Kondor, and G. Csányi, "On representing chemical environments," *Phys. Rev. B*, vol. 87, p. 184115, May 2013.

[101] Y. Zuo, C. Chen, X. Li, Z. Deng, Y. Chen, J. Behler, G. Csányi, A. V. Shapeev, A. P. Thompson, M. A. Wood, and S. P. Ong, "Performance and cost assessment of machine learning interatomic potentials," *The Journal of Physical Chemistry A*, vol. 124, no. 4, pp. 731–745, 2020. PMID: 31916773.

[102] J. Quiñonero-Candela and C. E. Rasmussen, "A unifying view of sparse approximate gaussian process regression," *Journal of Machine Learning Research*, vol. 6, no. 65, pp. 1939–1959, 2005.

[103] A. V. Shapeev, "Moment tensor potentials: A class of systematically improvable interatomic potentials," *Multiscale Modeling & Simulation*, vol. 14, no. 3, pp. 1153–1173, 2016.

[104] A. Thompson, L. Swiler, C. Trott, S. Foiles, and G. Tucker, "Spectral neighbor analysis method for automated generation of quantum-accurate interatomic potentials," *Journal of Computational Physics*, vol. 285, pp. 316 – 330, 2015.

[105] Y. Xia and M. K. Y. Chan, "Anharmonic stabilization and lattice heat transport in rocksalt β-gete," *Appl. Phys. Lett.*, vol. 113, no. 19, p. 193902, 2018.

[106] O. Hellman, I. A. Abrikosov, and S. I. Simak, "Lattice dynamics of anharmonic solids from first principles," *Phys. Rev. B*, vol. 84, p. 180301, Nov 2011.

[107] O. Hellman and I. A. Abrikosov, "Temperature-dependent effective third-order interatomic force constants from first principles," *Phys. Rev. B*, vol. 88, p. 144301, Oct 2013.

[108] O. Hellman, P. Steneteg, I. A. Abrikosov, and S. I. Simak, "Temperature dependent effective potential method for accurate free energy calculations of solids," *Phys. Rev. B*, vol. 87, p. 104111, Mar 2013.

[109] G. P. Srivastava, *The Physics of Phonons*. Taylor & Francis Group, New York, U.S.A., 1990.

[110] J. Ziman, *Electrons and Phonons: The Theory of Transport Phenomena in Solids*. International series of monographs on physics, OUP Oxford, 2001.

[111] B. Deo and S. N. Behera, "Calculation of thermal conductivity by the kubo formula," *Phys. Rev.*, vol. 141, pp. 738–741, Jan 1966.

[112] B. S. Semwal and P. K. Sharma, "Thermal conductivity of an anharmonic crystal," *Phys. Rev. B*, vol. 5, pp. 3909–3914, May 1972.

[113] K. N. Pathak, "Theory of anharmonic crystals," *Phys. Rev.*, vol. 139, pp. A1569–A1580, Aug 1965.

[114] B. V. Thompson, "Neutron scattering by an anharmonic crystal," *Phys. Rev.*, vol. 131, pp. 1420–1427, Aug 1963.

[115] R. Kubo, "Statistical-mechanical theory of irreversible processes. i. general theory and simple applications to magnetic and conduction problems," *J. Phys. Soc. Jpn*, vol. 12, no. 6, pp. 570–586, 1957.

[116] R. J. Hardy, "Energy-flux operator for a lattice," *Phys. Rev.*, vol. 132, pp. 168–177, Oct 1963.

[117] D. N. Zubarev, "DOUBLE-TIME GREEN FUNCTIONS IN STATISTICAL PHYSICS," *Soviet Physics Uspekhi*, vol. 3, pp. 320–345, mar 1960.

[118] V. Bonch-Bruevich, S. Tyablikov, N. Bogolyubov, and D. Haar, *The Green Function Method in Statistical Mechanics*. Dover Books on Physics, Dover Publications, 2015.

[119] P. Gluck, "Green function decoupling and diagrams," *Proceedings of the Physical Society*, vol. 92, pp. 192–194, sep 1967.

[120] R. A. Cowley, "Anharmonic crystals," *Rep. Prog. Phys.*, vol. 31, pp. 123–166, jan 1968.

[121] A. A. Maradudin and A. E. Fein, "Scattering of neutrons by an anharmonic crystal," *Phys. Rev.*, vol. 128, pp. 2589–2608, Dec 1962.

[122] J. Kokkedee, "Anharmonic effects in the coherent scattering of neutrons by crystals: A formal treatment of shift and width of the peaks in the scattering spectrum," *Physica*, vol. 28, no. 4, pp. 374 – 408, 1962.

[123] R. Mittal, M. K. Gupta, and S. L. Chaplot, "Phonons and anomalous thermal expansion behaviour in crystalline solids," *Prog. Mater. Sci.*, vol. 92, p. 360, 2018.

[124] M. T. Dove and H. Fang, "Negative thermal expansion and associated anomalous physical properties: review of the lattice dynamics theoretical foundation," *Rep. Prog. Phys.*, vol. 79, no. 6, p. 066503, 2016.

[125] J. Chen, L. Hu, J. Deng, and X. Xing, "Negative thermal expansion in functional materials: controllable thermal expansion by chemical modifications," *Chem. Soc. Rev.*, vol. 44, no. 11, p. 3522, 2015.

[126] B. Arnaud, S. Lebègue, and G. Raffy, "Anisotropic thermal expansion of bismuth from first principles," *Phys. Rev. B*, vol. 93, p. 094106, Mar 2016.

[127] P. K. Schelling and P. Keblinski, "Thermal expansion of carbon structures," *Phys. Rev. B*, vol. 68, p. 035425, Jul 2003.

[128] N. Mounet and N. Marzari, "First-principles determination of the structural, vibrational and thermodynamic properties of diamond, graphite, and derivatives," *Phys. Rev. B*, vol. 71, p. 205214, May 2005.

[129] G. Liu, J. Zhou, and H. Wang, "Anisotropic thermal expansion of snse from first-principles calculations based on gruneisen's theory," *Phys. Chem. Chem. Phys.*, vol. 19, pp. 15187–15193, 2017.

[130] D. Bansal, J. Hong, C. W. Li, A. F. May, W. Porter, M. Y. Hu, D. L. Abernathy, and O. Delaire, "Phonon anharmonicity and negative thermal expansion in snse," *Phys. Rev. B*, vol. 94, p. 054307, Aug 2016.

[131] C. Ablitt, S. Craddock, M. S. Senn, A. A. Mostofi, and N. C. Bristowe, "The origin of uniaxial negative thermal expansion in layered perovskites," *npj Comp. Mat.*, vol. 3, p. 44, 2017.

[132] V. Gava, A. L. Martinotto, and C. A. Perottoni, "First-principles mode gruneisen parameters and negative thermal expansion in $\alpha-\mathrm{zrw_2o_8}$," *Phys. Rev. Lett.*, vol. 109, p. 195503, Nov 2012.

[133] C. W. Li, X. Tang, J. A. Muñoz, J. B. Keith, S. J. Tracy, D. L. Abernathy, and B. Fultz, "Structural relationship between negative thermal expansion and quartic anharmonicity of cubic $\mathrm{scf_3}$," *Phys. Rev. Lett.*, vol. 107, p. 195504, Nov 2011.

[134] Y.-C. Jiao, M. Li, B.-Y. Qu, M.-Y. Wu, N. Zhang, P. Guo, and J.-J. Wang, "First-principles study of the negative thermal expansion of pbtio3," *Comput. Mat. Sci.*, vol. 124, pp. 92 – 97, 2016.

[135] R. Bianco, I. Errea, L. Paulatto, M. Calandra, and F. Mauri, "Second-order structural phase transitions, free energy curvature, and temperature-dependent anharmonic phonons in the self-consistent harmonic approximation: Theory and stochastic implementation," *Phys. Rev. B*, vol. 96, p. 014111, Jul 2017.

[136] N. Shulumba, O. Hellman, and A. J. Minnich, "Intrinsic localized mode and low thermal conductivity of pbse," *Phys. Rev. B*, vol. 95, p. 014302, Jan 2017.

[137] A. van Roekeghem, J. Carrete, and N. Mingo, "Anomalous thermal conductivity and suppression of negative thermal expansion in $\mathrm{scf_3}$," *Phys. Rev. B*, vol. 94, p. 020303, Jul 2016.

[138] D. S. Kim, O. Hellman, J. Herriman, H. L. Smith, J. Y. Y. Lin, N. Shulumba, J. L. Niedziela, C. W. Li, D. L. Abernathy, and B. Fultz, "Nuclear quantum effect with pure anharmonicity and the anomalous thermal expansion of silicon," *Proc. Natl. Acad. Sci. U.S.A*, 2018.

[139] J. Goldak, C. S. Barrett, D. Innes, and W. Youdelis, "Structure of alpha gete," *J. Chem. Phys.*, vol. 44, no. 9, pp. 3323–3325, 1966.

[140] E. Bosoni, G. C. Sosso, and M. Bernasconi, "Grüneisen parameters and thermal conductivity in the phase change compound gete," *J. Comp. Electron.*, vol. 16, pp. 997–1002, Dec 2017.

[141] M. Lazzeri and S. de Gironcoli, "First-principles study of the thermal expansion of be $(11\bar{1}0)$," *Phys. Rev. B*, vol. 65, p. 245402, May 2002.

[142] M. Lazzeri, *A first principles study of the thermal expansion in some metallic surfaces*. PhD thesis, 1999.

[143] W. Voigt, *Lehrbuch der kristallphysik: (mit ausschluss der kristalloptik)*. B.G. Teubners Sammlung von Lehrbüchern auf dem Gebiete der mathematischen Wissenschaften ; Bd. XXXIV, B.G. Teubner, 1910.

[144] S. Goedecker, M. Teter, and J. Hutter, "Separable dual-space gaussian pseudopotentials," *Phys. Rev. B*, vol. 54, pp. 1703–1710, Jul 1996.

[145] A. Togo and I. Tanaka, "First principles phonon calculations in materials science," *Scr. Mater.*, vol. 108, pp. 1–5, Nov 2015.

[146] D. Campi, L. Paulatto, G. Fugallo, F. Mauri, and M. Bernasconi, "First-principles calculation of lattice thermal conductivity in crystalline phase change materials: Gete, $\mathbf{sb_2te_3}$, and $\mathbf{ge_2sb_2te_5}$," *Phys. Rev. B*, vol. 95, p. 024311, Jan 2017.

[147] A. Onodera, I. Sakamoto, Y. Fujii, N. Môri, and S. Sugai, "Structural and electrical properties of gese and gete at high pressure," *Phys. Rev. B*, vol. 56, pp. 7935–7941, Oct 1997.

[148] J. Li, Z. Chen, X. Zhang, Y. Sun, J. Yang, and Y. Pei *NPG Asia Mater.*, vol. 9, p. e353, 2017.

[149] E. A. Marchenkov and V. P. Shipul', "Thermal expansion of semiconductor materials," *J. Eng. Phys. Thermophys.*, vol. 66, pp. 547–551, May 1994.

[150] N. K. Abrikosov, V. F. Bankina, L. V. Poretskaya, L. E. Shelimova, and E. V. Skudnova, *Semiconducting II–VI, IV–VI, and V–VI Compounds*. Monographs in Semiconductor Physics, Springer US, 1969.

[151] W. Rehwald and G. K. Lang, "Ultrasonic studies of phase transitions in the tin telluride-germanium telluride system sn x ge 1-x te," *J. Phys. C: Solid State Phys.*, vol. 8, no. 20, p. 3287, 1975.

[152] S. Sugai, K. Murase, T. Tsuchihira, and H. Kawamura, "Interaction of the to-phonon with the acoustic phonons near the phase transition temperature in pb1-xgexte," *J. Phys. Soc. Jpn*, vol. 47, no. 2, pp. 539–546, 1979.

[153] T. Li, X. Fu, D. Chang, Q. Sun, and F. Wang, "Negative thermal expansion properties in tetragonal nbpo5 from the first principles studies," *AIP Adv.*, vol. 7, no. 3, p. 035202, 2017.

[154] U. D. Wdowik, K. Parlinski, S. Rols, and T. Chatterji, "Soft-phonon mediated structural phase transition in gete," *Phys. Rev. B*, vol. 89, p. 224306, Jun 2014.

[155] T. Matsunaga, P. Fons, A. V. Kolobov, J. Tominaga, and N. Yamada, "The order-disorder transition in gete: Views from different length-scales," *Appl. Phys. Lett.*, vol. 99, no. 23, p. 231907, 2011.

[156] R. A. Cowley, "The theory of raman scattering from crystals," *Proceedings of the Physical Society*, vol. 84, pp. 281–296, aug 1964.

[157] C. Rinaldi, S. Varotto, M. Asa, J. Slawińska, J. Fujii, G. Vinai, S. Cecchi, D. Di Sante, R. Calarco, I. Vobornik, G. Panaccione, S. Picozzi, and R. Bertacco, "Ferroelectric control of the spin texture in gete," *Nano Lett.*, vol. 18, no. 5, pp. 2751–2758, 2018.

[158] J. Krempaský, M. Fanciulli, N. Pilet, J. Minár, W. Khan, M. Muntwiler, F. Bertran, S. Muff, A. Weber, V. Strocov, V. Volobuiev, G. Springholz, and J. Dil, "Spin-resolved electronic structure of ferroelectric α-gete and multiferroic ge1−xmnxte," *Journal of Physics and Chemistry of Solids*, vol. 128, pp. 237 – 244, 2019. Spin-Orbit Coupled Materials.

[159] D. Di Sante, P. Barone, R. Bertacco, and S. Picozzi, "Electric control of the giant rashba effect in bulk gete," *Adv. Mater.*, vol. 25, no. 4, pp. 509–513, 2013.

[160] M. Liebmann, C. Rinaldi, D. Di Sante, J. Kellner, C. Pauly, R. N. Wang, J. E. Boschker, A. Giussani, S. Bertoli, M. Cantoni, L. Baldrati, M. Asa, I. Vobornik, G. Panaccione, D. Marchenko, J. Sánchez-Barriga, O. Rader, R. Calarco, S. Picozzi, R. Bertacco, and M. Morgenstern, "Giant rashba-type spin splitting in ferroelectric gete(111)," *Adv. Mater.*, vol. 28, no. 3, pp. 560–565, 2016.

[161] T. P. Dougherty, G. P. Wiederrecht, K. A. Nelson, M. H. Garrett, H. P. Jensen, and C. Warde, "Femtosecond resolution of soft mode dynamics in structural phase transitions," *Science*, vol. 258, no. 5083, pp. 770–774, 1992.

[162] O. Delaire, J. Ma, K. Marty, A. F. May, M. A. McGuire, M.-H. Du, D. J. Singh, A. Podlesnyak, G. Ehlers, M. D. Lumsden, and B. C. Sales, "Giant anharmonic phonon scattering in pbte," *Nature Mater.*, vol. 10, no. 8, pp. 614–619, 2011.

[163] C. W. Li, J. Hong, A. F. May, D. Bansal, S. Chi, T. Hong, G. Ehlers, and O. Delaire, "Orbitally driven giant phonon anharmonicity in?snse," *Nature Phys.*, vol. 11, no. 12, pp. 1063–1069, 2015.

[164] G. A. S. Ribeiro, L. Paulatto, R. Bianco, I. Errea, F. Mauri, and M. Calandra, "Strong anharmonicity in the phonon spectra of pbte and snte from first principles," *Phys. Rev. B*, vol. 97, p. 014306, Jan 2018.

[165] U. Aseginolaza, R. Bianco, L. Monacelli, L. Paulatto, M. Calandra, F. Mauri, A. Bergara, and I. Errea, "Phonon collapse and second-order phase transition in thermoelectric snse," *Phys. Rev. Lett.*, vol. 122, p. 075901, Feb 2019.

[166] U. Aseginolaza, R. Bianco, L. Monacelli, L. Paulatto, M. Calandra, F. Mauri, A. Bergara, and I. Errea, "Strong anharmonicity and high thermoelectric efficiency in high-temperature sns from first principles," *Phys. Rev. B*, vol. 100, p. 214307, Dec 2019.

[167] G. Tan, L.-D. Zhao, and M. G. Kanatzidis, "Rationally designing high-performance bulk thermoelectric materials," *Chem. Rev.*, vol. 116, pp. 12123–12149, Oct 2016.

[168] C. Chang, M. Wu, D. He, Y. Pei, C.-F. Wu, X. Wu, H. Yu, F. Zhu, K. Wang, Y. Chen, L. Huang, J.-F. Li, J. He, and L.-D. Zhao, "3d charge and 2d phonon transports leading to high out-of-plane zt in n-type snse crystals," *Science*, vol. 360, no. 6390, pp. 778–783, 2018.

[169] Z. Chen, Z. Jian, W. Li, Y. Chang, B. Ge, R. Hanus, J. Yang, Y. Chen, M. Huang, G. J. Snyder, and Y. Pei, "Lattice dislocations enhancing thermoelectric pbte in addition to band convergence," *Adv. Mater.*, vol. 29, no. 23, p. 1606768, 2017.

[170] L.-D. Zhao, S.-H. Lo, Y. Zhang, H. Sun, G. Tan, C. Uher, C. Wolverton, V. P. Dravid, and M. G. Kanatzidis, "Ultralow thermal conductivity and high thermoelectric figure of merit in snse crystals," *Nature*, vol. 508, no. 7496, pp. 373–377, 2014.

[171] M. Beekman, D. T. Morelli, and G. S. Nolas, "Better thermoelectrics through glass-like crystals," *Nature Mater.*, vol. 14, no. 12, pp. 1182–1185, 2015.

[172] Q. Tan, L.-D. Zhao, J.-F. Li, C.-F. Wu, T.-R. Wei, Z.-B. Xing, and M. G. Kanatzidis, "Thermoelectrics with earth abundant elements: low thermal conductivity and high thermopower in doped sns," *J. Mater. Chem. A*, vol. 2, pp. 17302–17306, 2014.

[173] M. R. Dirmyer, J. Martin, G. S. Nolas, A. Sen, and J. V. Badding, "Thermal and electrical conductivity of size-tuned bismuth telluride nanoparticles," *Small*, vol. 5, no. 8, pp. 933–937, 2009.

[174] K. Biswas, L.-D. Zhao, and M. G. Kanatzidis, "Tellurium-free thermoelectric: The anisotropic n-type semiconductor bi2s3," *Adv. Energy Mater.*, vol. 2, no. 6, pp. 634–638, 2012.

[175] O. Hellman and D. A. Broido, "Phonon thermal transport in bi_2te_3 from first principles," *Phys. Rev. B*, vol. 90, p. 134309, Oct 2014.

[176] P.-F. Lory, S. Pailhès, V. M. Giordano, H. Euchner, H. D. Nguyen, R. Ramlau, H. Borrmann, M. Schmidt, M. Baitinger, M. Ikeda, P. Tomeš, M. Mihalkovič, C. Allio, M. R. Johnson, H. Schober, Y. Sidis, F. Bourdarot, L. P. Regnault, J. Ollivier, S. Paschen, Y. Grin, and M. de Boissieu, "Direct measurement of individual phonon lifetimes in the clathrate compound ba7.81ge40.67au5.33," *Nature Commun.*, vol. 8, p. 491, 2017.

[177] T. Shiga, J. Shiomi, J. Ma, O. Delaire, T. Radzynski, A. Lusakowski, K. Esfarjani, and G. Chen, "Microscopic mechanism of low thermal conductivity in lead telluride," *Phys. Rev. B*, vol. 85, p. 155203, Apr 2012.

[178] A. H. Romero, E. K. U. Gross, M. J. Verstraete, and O. Hellman, "Thermal conductivity in pbte from first principles," *Phys. Rev. B*, vol. 91, p. 214310, Jun 2015.

[179] S. Roychowdhury, M. Samanta, S. Perumal, and K. Biswas, "Germanium chalcogenide thermoelectrics: Electronic structure modulation and low lattice thermal conductivity," *Chem. of Mater.*, vol. 30, pp. 5799–5813, Sep 2018.

[180] J. Philip, "Thermal conduction across ferroelectric phase transitions: Results on selected systems," in *Ferroelectrics* (M. Lallart, ed.), ch. 7, Rijeka: IntechOpen, 2011.

[181] P. A. Vermeulen, A. Kumar, G. H. ten Brink, G. R. Blake, and B. J. Kooi, "Unravelling the domain structures in gete and laalo3," *Cryst. Growth & Des.*, vol. 16, no. 10, pp. 5915–5922, 2016.

[182] P. Nukala, M. Ren, R. Agarwal, J. Berger, G. Liu, A. T. C. Johnson, and R. Agarwal, "Inverting polar domains via electrical pulsing in metallic germanium telluride," *Nat. Commun.*, vol. 8, pp. 15033 EP –, Apr 2017.

[183] M. J. Polking, H. Zheng, R. Ramesh, and A. P. Alivisatos, "Controlled synthesis and size-dependent polarization domain structure of colloidal germanium telluride nanocrystals," *J. Am. Chem. Soc.*, vol. 133, no. 7, pp. 2044–2047, 2011.

[184] D. Campi, L. Paulatto, G. Fugallo, F. Mauri, and M. Bernasconi, "First-principles calculation of lattice thermal conductivity in crystalline phase change materials: Gete, $\mathbf{sb_2te_3}$, and $\mathbf{ge_2sb_2te_5}$," *Phys. Rev. B*, vol. 95, p. 024311, Jan 2017.

[185] M. Simoncelli, N. Marzari, and F. Mauri, "Unified theory of thermal transport in crystals and glasses," *Nat. Phys.*, vol. 15, pp. 809–813, Aug 2019.

[186] L. Isaeva, G. Barbalinardo, D. Donadio, and S. Baroni, "Modeling heat transport in crystals and glasses from a unified lattice-dynamical approach," *Nature Communications*, vol. 10, p. 3853, Aug 2019.

[187] J. A. Seijas-Bellido, H. Aramberri, J. Íñiguez, and R. Rurali, "Electric control of the heat flux through electrophononic effects," *Phys. Rev. B*, vol. 97, p. 184306, May 2018.

[188] P. S. Bednyakov, B. I. Sturman, T. Sluka, A. K. Tagantsev, and P. V. Yudin, "Physics and applications of charged domain walls," *npj Computational Materials*, vol. 4, p. 65, Nov 2018.

[189] G. D. Mahan and J. O. Sofo, "The best thermoelectric," *PNAS*, vol. 93, no. 15, pp. 7436–7439, 1996.

[190] S. Kim and H. S. Lee, "Effects of addition of si and sb on the microstructure and thermoelectric properties of gete," *Met. Mater. Int.*, vol. 25, pp. 528–538, Mar 2019.

[191] M. Lines and A. Glass, *Principles and Applications of Ferroelectrics and Related Materials*. International series of monographs on physics, OUP Oxford, 2001.

[192] B. Meyer and D. Vanderbilt, "Ab initio study of ferroelectric domain walls in pbtio$_3$," *Phys. Rev. B*, vol. 65, p. 104111, Mar 2002.

[193] M. Taherinejad, D. Vanderbilt, P. Marton, V. Stepkova, and J. Hlinka, "Bloch-type domain walls in rhombohedral batio$_3$," *Phys. Rev. B*, vol. 86, p. 155138, Oct 2012.

[194] J. Erhart, "Domain wall orientations in ferroelastics and ferroelectrics," *Phase Transitions*, vol. 77, no. 12, pp. 989–1074, 2004.

[195] J. Fousek and V. Janovec, "The orientation of domain walls in twinned ferroelectric crystals," *Journal of Applied Physics*, vol. 40, no. 1, pp. 135–142, 1969.

[196] Boulesteix, C., Yangui, B., Ben Salem, M., Manolikas, C., and Amelinckx, S., "The orientation of interfaces between a prototype phase and its ferroelastic derivatives : theoretical and experimental study," *J. Phys. France*, vol. 47, no. 3, pp. 461–471, 1986.

[197] A. Lubk, S. Gemming, and N. A. Spaldin, "First-principles study of ferroelectric domain walls in multiferroic bismuth ferrite," *Phys. Rev. B*, vol. 80, p. 104110, Sep 2009.

[198] O. Diéguez, P. Aguado-Puente, J. Junquera, and J. Íñiguez, "Domain walls in a perovskite oxide with two primary structural order parameters: First-principles study of bifeo$_3$," *Phys. Rev. B*, vol. 87, p. 024102, Jan 2013.

[199] Y.-W. Chen, J.-L. Kuo, and K.-H. Chew, "Polar ordering and structural distortion in electronic domain-wall properties of bifeo3," *Journal of Applied Physics*, vol. 122, no. 7, p. 075103, 2017.

[200] J. Gong, C. Li, Y. Zhang, Y. Li, S. Zheng, K. Yang, R. Huang, L. Lin, Z. Yan, and J.-M. Liu, "Interactions of charged domain walls and oxygen vacancies in batio3: a first-principles study," *Materials Today Physics*, vol. 6, pp. 9 – 21, 2018.

[201] N. Marzari, *Ab-initio molecular dynamics for metallic systems*. PhD thesis, 1996.

[202] K. Chang, B. J. Miller, H. Yang, H. Lin, S. S. P. Parkin, S. Barraza-Lopez, Q.-K. Xue, X. Chen, and S.-H. Ji, "Standing waves induced by valley-mismatched domains in ferroelectric snte monolayers," *Phys. Rev. Lett.*, vol. 122, p. 206402, May 2019.

[203] L. Van Hove, "The occurrence of singularities in the elastic frequency distribution of a crystal," *Phys. Rev.*, vol. 89, pp. 1189–1193, Mar 1953.

[204] J. A. Seijas-Bellido, C. Escorihuela-Sayalero, M. Royo, M. P. Ljungberg, J. C. Wojdeł, J. Íñiguez, and R. Rurali, "A phononic switch based on ferroelectric domain walls," *Phys. Rev. B*, vol. 96, p. 140101, Oct 2017.

[205] M. Royo, C. Escorihuela-Sayalero, J. Íñiguez, and R. Rurali, "Ferroelectric domain wall phonon polarizer," *Phys. Rev. Materials*, vol. 1, p. 051402, Oct 2017.

[206] R. Hanus, A. Garg, and G. J. Snyder, "Phonon diffraction and dimensionality crossover in phonon-interface scattering," *Communications Physics*, vol. 1, no. 1, p. 78, 2018.

[207] E. T. Swartz and R. O. Pohl, "Thermal boundary resistance," *Rev. Mod. Phys.*, vol. 61, pp. 605–668, Jul 1989.

[208] J. Cao, J. D. Querales-Flores, A. R. Murphy, S. Fahy, and I. Savić, "Dominant electron-phonon scattering mechanisms in *n*-type pbte from first principles," *Phys. Rev. B*, vol. 98, p. 205202, Nov 2018.

[209] B. K. Ridley, *Quantum Processes in Semiconductors*. Oxford University Press, fourth ed., 1999.

[210] V. Askarpour and J. Maassen, "Unusual thermoelectric transport anisotropy in quasi-two-dimensional rhombohedral gete," *Phys. Rev. B*, vol. 100, p. 075201, Aug 2019.

[211] P. Harrison, *Quantum Wells, Wires and Dots*. Wiley, second ed., 2005.

[212] M. Snykers, P. Delavignette, and S. Amelinckx, "The domain structure of gete as observed by electron microscopy," *Mat. Res. Bull.*, vol. 7, no. 8, pp. 831 – 839, 1972.

[213] L. Chen, C. Paillard, H. J. Zhao, J. Íñiguez, Y. Yang, and L. Bellaiche, "Tailoring properties of hybrid perovskites by domain-width engineering with charged walls," *npj Comput. Mater.*, vol. 4, no. 1, p. 75, 2018.

[214] Y. Xia, K. Pal, J. He, V. Ozoliņš, and C. Wolverton, "Particlelike phonon propagation dominates ultralow lattice thermal conductivity in crystalline tl_3vse_4," *Phys. Rev. Lett.*, vol. 124, p. 065901, Feb 2020.

[215] Y. Xia, V. Ozoliņš, and C. Wolverton, "Microscopic mechanisms of glasslike lattice thermal transport in cubic $cu_{12}sb_4s_{13}$ tetrahedrites," *Phys. Rev. Lett.*, vol. 125, p. 085901, Aug 2020.

[216] Y. Xia, "Revisiting lattice thermal transport in pbte: The crucial role of quartic anharmonicity," *Applied Physics Letters*, vol. 113, no. 7, p. 073901, 2018.

[217] Y. He, I. Savić, D. Donadio, and G. Galli, "Lattice thermal conductivity of semiconducting bulk materials: atomistic simulations," *Phys. Chem. Chem. Phys.*, vol. 14, pp. 16209–16222, 2012.

[218] Z. Wang, S. Safarkhani, G. Lin, and X. Ruan, "Uncertainty quantification of thermal conductivities from equilibrium molecular dynamics simulations," *International Journal of Heat and Mass Transfer*, vol. 112, pp. 267 – 278, 2017.

[219] Y.-K. Kwon, S. Berber, and D. Tománek, "Thermal contraction of carbon fullerenes and nanotubes," *Phys. Rev. Lett.*, vol. 92, p. 015901, Jan 2004.

[220] H. Fang, Y. Wang, S. Shang, and Z.-K. Liu, "Nature of ferroelectric-paraelectric phase transition and origin of negative thermal expansion in $PbTio_3$," *Phys. Rev. B*, vol. 91, p. 024104, Jan 2015.

[221] A. J. H. McGaughey and M. Kaviany, "Quantitative validation of the boltzmann transport equation phonon thermal conductivity model under the single-mode relaxation time approximation," *Phys. Rev. B*, vol. 69, p. 094303, Mar 2004.

[222] P. K. Schelling, S. R. Phillpot, and P. Keblinski, "Comparison of atomic-level simulation methods for computing thermal conductivity," *Phys. Rev. B*, vol. 65, p. 144306, Apr 2002.

[223] M. Puligheddu, Y. Xia, M. Chan, and G. Galli, "Computational prediction of lattice thermal conductivity: A comparison of molecular dynamics and boltzmann transport approaches," *Phys. Rev. Materials*, vol. 3, p. 085401, Aug 2019.

[224] S. Gabardi, E. Baldi, E. Bosoni, D. Campi, S. Caravati, G. C. Sosso, J. Behler, and M. Bernasconi, "Atomistic simulations of the crystallization and aging of gete nanowires," *The Journal of Physical Chemistry C*, vol. 121, no. 42, pp. 23827–23838, 2017.

[225] G. C. Sosso, G. Miceli, S. Caravati, J. Behler, and M. Bernasconi, "Neural network interatomic potential for the phase change material gete," *Phys. Rev. B*, vol. 85, p. 174103, May 2012.

[226] K. Takenaka, "Progress of research in negative thermal expansion materials: Paradigm shift in the control of thermal expansion," *Frontiers in Chemistry*, vol. 6, p. 267, 2018.

[227] Z. Pan, X. Jiang, T. Nishikubo, Y. Sakai, H. Ishizaki, K. Oka, Z. Lin, and M. Azuma, "Pronounced negative thermal expansion in lead-free bicoo3-based ferroelectrics triggered by the stabilized perovskite structure," *Chemistry of Materials*, vol. 31, pp. 6187–6192, Aug 2019.

[228] A. Carreras, A. Togo, and I. Tanaka, "Dynaphopy: A code for extracting phonon quasiparticles from molecular dynamics simulations," *Computer Physics Communications*, vol. 221, pp. 221 – 234, 2017.

[229] T. W. Sirk, S. Moore, and E. F. Brown, "Characteristics of thermal conductivity in classical water models," *The Journal of Chemical Physics*, vol. 138, no. 6, p. 064505, 2013.

[230] Đ. Dangić, O. Hellman, S. Fahy, and I. Savić, "The origin of the lattice thermal conductivity enhancement at the ferroelectric phase transition in gete," 2020. to be published.

[231] F. Hu, F. Shen, J. Hao, Y. Liu, J. Wang, J. Sun, and B. Shen, "Negative thermal expansion in the materials with giant magnetocaloric effect," *Frontiers in Chemistry*, vol. 6, p. 438, 2018.

[232] R. Huang, Y. Liu, W. Fan, J. Tan, F. Xiao, L. Qian, and L. Li, "Giant negative thermal expansion in nazn13-type la(fe, si, co)13 compounds," *Journal of the American Chemical Society*, vol. 135, pp. 11469–11472, Aug 2013.

[233] J. LANGER, A. MARADUDIN, and R. WALLIS, "C15 - on the interaction between cubic anharmonicity and a second-order electric moment in the optical absorption of crystals," in *Lattice Dynamics* (R. WALLIS, ed.), pp. 411 – 419, Pergamon, 1965.

[234] A. Khintchine, "Korrelationstheorie der stationären stochastischen prozesse," *Mathematische Annalen*, vol. 109, pp. 604–615, Dec 1934.

[235] N. Wiener, "Generalized harmonic analysis," *Acta Math.*, vol. 55, pp. 117–258, 1930.

[236] H. J. C. Berendsen, J. P. M. Postma, W. F. van Gunsteren, A. DiNola, and J. R. Haak, "Molecular dynamics with coupling to an external bath," *The Journal of Chemical Physics*, vol. 81, no. 8, pp. 3684–3690, 1984.